Multi-impairment and multi-channel optical performance monitoring

Lamia Meflah

A thesis submitted to the University College London for the degree
of Doctor of Philosophy (Ph.D.)

Department of Electronic and Electrical Engineering

University College London

December 2008

I, Lamia Meflah, confirm that the work presented in this thesis is my own. Where information has been derived from other sources, I confirm that this has been indicated in this thesis.

To Tim and Isabelle

Abstract

Next generation optical networks will evolve from static to dynamically reconfigurable architectures to meet the increasing bandwidth and service requirements. The benefits of dynamically reconfigurable networks (improved operations, reduced footprint and cost) have introduced new challenges, in particular the need for complex management which has put pressure on the engineering rules and transmission margins. This has provided the main drive to develop new techniques for optical performance monitoring (OPM) without using optical-to-electrical-to-optical conversions. When considering impairments due to chromatic dispersion in dynamic networks, each channel will traverse a unique path through the network thus the channels arriving at the monitoring point will, in general, exhibit different amounts of residual dispersion. Therefore, in a dynamic network it is necessary to monitor all channels individually to quantify the degradation, without the requirement of knowing the data path history. The monitoring feature can be used in conjunction with a dispersion compensation device which can either be optical or electrical or used to trigger real-time alarms for traffic re-routing.

The proposed OPM technique is based on RF spectrum analysis and used for simultaneous and independent monitoring of power, chromatic dispersion (CD), polarisation mode dispersion (PMD) and optical signal-to-noise ratio (OSNR) in 40Gbit/s multi-channel systems. An analytical model is developed to describe the monitoring technique which allows the prediction of the measurement range. The experimental results are given for group velocity dispersion (GVD), differential group delay (DGD) and OSNR measurements. This technique is based on electro-optic down-conversion that simultaneously down-converts multiple channels, sharing the cost of the key components over multiple channels and making it cost effective for multi-channel operation. The measurement range achieved with this method is equal to 4742±100ps/nm for GVD, 200±4ps for DGD and 25±1dB for OSNR. To the knowledge of the author, these dispersion monitoring ranges are the largest reported to date for the bit-rate of 40Gbit/s with amplitude modulation formats.

Acknowledgements

I would first like to thank my first supervisor, Dr. John Mitchell, for his ongoing support and helpful advises in conducting and completing this work. I will also be ever indebted to my second supervisor, Professor Polina Bayvel, who interviewed me while I was still working in the USA and who was very successful in finding a funding for my PhD. I am deeply grateful to Dr. Benn Thomsen, who joined the ONG group only few months after my start. His presence and continuous technical guidance helped me achieve most of the results I am now presenting. Without him, this thesis would look drastically thinner! I would also like to thank Dr. Seb Savory for his guidance in some of the analytical work; Dr. Yannis Benlachtar for his initial contribution in helping me understand some of the techniques described in my transfer thesis; and last but not least, Dr. Michael Dueser, who helped me choose a PhD topic during the first months of my work at UCL. I have enjoyed being part of the 808 group, and will always remember all my colleagues from the Optical Networks Group. Finally, I can never thank enough my husband, Tim, who has always supported me throughout this adventure.

Glossary

ASE:	Amplified spontaneous emission.
ASK:	Amplitude shift key.
BER:	Bit-error-rate.
BPF:	Band pass filter.
CD:	Chromatic dispersion.
CM:	Cable modem.
CNR:	Carrier to noise ratio.
CSRZ:	Carrier-suppressed return to zero.
DCF:	Dispersion compensating fibre.
DGD:	Differential group delay.
DSB:	Dual sideband.
DSF:	Dispersion shifted fibre.
DSL:	Digital subscriber line.
DWDM:	Dense wavelength division multiplexing.
EAM:	Electro-absorption modulator.
EDFA:	Erbium doped fibre amplifier.
FBG:	Fibre Bragg grating.
FWHM:	Full width at half maximum.
GVD:	Group velocity dispersion.
IL:	Insertion loss.
LPF:	Low pass filter.
LSB:	Lower sideband.

MZI:	Mach-Zehnder interferometer.
NRZ:	Non-return to zero.
OBS:	Optical burst switching.
O-E-O:	Optical to electrical to optical.
OOK:	On-off keying.
OPS:	Optical packet switching.
OPM:	Optical performance monitoring.
OSNR:	Optical signal-to-noise ratio.
PBS:	Polarisation beam splitter.
PC:	Polarisation controller.
PDL:	Polarisation dependent loss.
PLC:	Planar Lightwave circuit.
PMD:	Polarisation mode dispersion.
PMDC:	Polarisation mode dispersion compensator.
PSP:	principal state of polarisation.
RCP:	Relative clock power.
RF:	Radio-frequency.
ROADM:	Reconfigurable optical add/drop multiplexer.
RZ:	Return to zero.
SDH:	Signal digital hierarchy.
SMF:	Single mode fibre
SNR:	Signal-to-noise ratio.
SONET:	Synchronous optical networks.
SSB:	Single sideband.

SSMF:	Standard single mode fibre.
TDC:	Tuneable dispersion compensator.
USB:	Upper sideband.
VIPA:	Virtually imaged phased array.
WDM:	Wavelength division multiplexing.

Table of content

Chapter 1: Introduction

Multimedia services have been the main drivers in the deployment of higher capacity optical networks. Recently, access optical networks have been exposed to substantial challenges with exponentially increasing per-user bandwidth demand and ever-increasing backbone capacity [MOR'07]. Although access technologies, such as digital subscriber line (DSL) and cable modem (CM), offer affordable solutions for residential data users, they pose fundamental distance and bandwidth limitations. It is expected that the next-generation optical networks will be able to support various emerging broadband applications as well as emulate many kinds of legacy services over the same infrastructure, with minimal engineering investment. Two main factors have emerged to satisfy this new demand. The first factor has been to increase the data channel bit-rate. With the explosive growth in demand for capacity in optical networks, high bit-rate fibre transmission has recently become an essential part of state-of-the-art communications. Modern optical networks are now primarily based on 2.5Gbit/s and 10Gbit/s channels. 40Gbit/s channels have begun to be implemented in new product offerings [HOF'05], while 100Gbit/s and even 160Gbit/s bit-rates are being tested in various labs [MOR'07]. The second factor has been the use of wavelength division multiplexing (WDM) which has dramatically increased the network capacity. This technology allows the transport of hundreds of gigabits of data on a single fibre for distances over thousands of kilometres, without the need of optical-to-electrical-to-optical (O-E-O) conversion [CHA'04].

As higher bit-rates and WDM technologies have evolved, the network bottleneck has moved from the optical-transport to the routing layer, as conventional electronic routers have not been capable of offering a cost-effective solution to the increasing bandwidth demand [NEI'05]. To cope with this, highly flexible and dynamic networks were envisioned a few years ago to provide virtually unlimited bandwidth with dynamic reconfiguration supported not only in the electrical layer, but also in the optical layer. Current research has shown that dynamically reconfigurable networks, with an optical plane consisting of optical transmission and optical switching capabilities, can yield a more efficient utilisation of network resources, however, at the cost of increased complexity of required components and routing. As a result, significant research has been carried out in the field of dynamic networks in the last decade, see for example [LEL06, DUS05, GER03, SEN03, MAH01, ZAN01, HUN00]. These networks require a number of novel technologies to ensure their dynamic reconfigurability. The WDM transport layer must now deliver advanced functionalities such as automatic wavelength routing and enhanced fault management. Reconfigurable optical add/drop multiplexers (ROADMs) have emerged as one of the mainstream cost-effective platforms to provide a dynamic wavelength-routing capability that enable network flexibility and connectivity [WAG'06, TAN'06]. The benefits of optically switched networks (improved operations, reduced footprint and cost) have introduced new challenges, in particular the need for complex management which has put pressure on the engineering rules and transmission margins. Optical performance monitoring (OPM) can potentially address this difficult balance by allowing fault management and transmission control improvements. New forms of physical layer functionalities, such as real-time impairment monitoring and compensation (i.e. monitoring and compensation performed on the network switching timescales) and dynamic reconfiguration, introduce greater complexity that may demand sophisticated OPM to monitor the quality of the optical signal throughout the network. OPM can therefore be seen as crucial to the success of next generation optical networks [KIL'04].

Performance monitoring and impairment mitigation are essential features in static and dynamic WDM networks. In a static network, the wavelength allocation is performed off-line and optical switches and wavelength routers, as well as transmitters and receivers, are configured accordingly [BAR'97]. When considering impairments due to chromatic dispersion in static networks, it is sufficient to monitor a single channel in a WDM system. This is the case since all channels travel through the same fixed path accumulating the same residual chromatic dispersion caused by link mismatch. In static networks, the impairment correction is performed at the network design stage. However, in dynamic networks, each channel will traverse a unique path through the network thus the channels arriving at the monitoring point will, in general, exhibit different amounts of residual dispersion. Therefore, in a dynamic network it is necessary to monitor all channels individually to quantify the degradation, without the requirement of knowing the data path history. The monitoring feature can be used in conjunction with a dispersion compensation device which can either be optical or electrical or used to trigger real-time alarms for traffic re-routing. Figure 1-1 depicts a dynamically reconfigurable network schematic using OPM. In this example, a dispersion compensation fibre (DCF) is typically incorporated in each link of the network to compensate for the chromatic dispersion due to single-mode fibre (SMF), leaving the signal subject to some residual dispersion. In this scheme, the OPM device is also deployed in each link and is connected to a tunable dispersion compensator (TDC). The combination of the OPM and TDC is used to monitor and compensate for residual dispersion. It can also be envisaged that the OPM device could be an integral part of the network management system, allowing for signal rerouting when monitoring a signal failure. The system manufacturers would then design and integrate the OPM function into the optical network sub-systems that would be deployed by network operators.

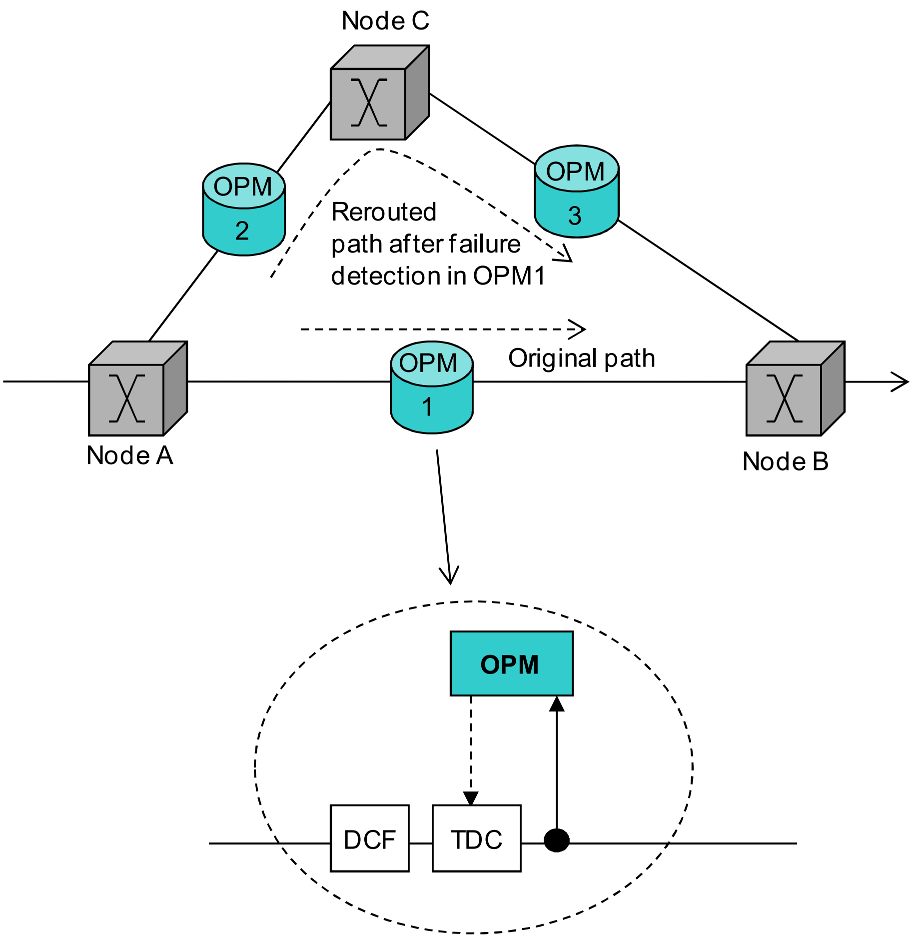

Figure 1-1: General schematic of a dynamically reconfigurable network, depicting the possible location of optical performance monitoring (OPM) and tunable dispersion compensation (TDC) devices. The rerouted path is performed after failure detection in OPM1.

Multiple definitions of OPM can be found in the literature. Some related to the measurements of a single performance parameter, such as that of the bit-error-rate (BER) [RAM'99], the Q-factor [FRI02] or the optical signal-to-noise ratio (OSNR) [KIL'03]. In this thesis, OPM takes the broad definition of physical layer monitoring for the purpose of determining the 'health' of the signal in the optical domain. Current performance monitoring, based on digital signals, relies on synchronous digital hierarchy/synchronous optical networking (SDH/SONET) line terminal elements to determine the BER or loss of signal from power measurements. Other degradations that may affect the signal-to-noise ratio (SNR) are calculated in advance by measuring the characteristics of the optical components (such as the optical amplifier noise figure). However, these simple monitoring techniques are inadequate in the case of dynamic networks. Traditionally, the primary application of performance monitoring was to certify service level agreements between the network operators and their clients. In a dynamic network, the desired applications have evolved to signal diagnosis for impairment compensation and fault management. An OPM device, deployed at each link, would allow for the physical layer fault management by identifying discontinuities in parameters such as

OSNR; whereas the diagnosis of impairments such as chromatic dispersion (CD) and polarisation mode dispersion (PMD) would provide a mechanism to trigger alarms or provide feedback for active dispersion compensation. Future dynamic networks will require dynamic compensators that are controlled using feedback from a performance monitoring system. In such networks, each channel is dynamically added and dropped, and has a different transport history which may include different paths and different optical elements, in addition to changes in environment such as temperature. This prevents network management based on statically mapped network elements and fibre properties, and drives the need for dynamic OPM and compensation. Other potential applications of OPM in dynamically reconfigurable networks may include routing capabilities where high capacity and priority-traffic that requires high-performance, can be dynamically tuned to the appropriate optical channels. As such, more targeted research on OPM is required, and is the topic of discussion in this thesis. The following section describes the optical impairments that are typically monitored within an OPM system.

Impairments in transmitted optical signals

Optical noise from erbium-doped fibre amplifiers (EDFAs) is the most common source of penalty and the primary limit on system performance [WAL'91]. Minimising penalties due to noise have been primarily achieved with the overall reduction of losses in the network and the use of low-noise optical amplifiers. Although the out-of-band optical noise can be suppressed by the filtering effects of the multiplexing/demultiplexing components, it is the in-band amplified spontaneous emission (ASE) noise that mainly determines the OSNR, defined as the ratio of the signal channel power to the power of the ASE in a specified optical bandwidth, usually equal to 0.1nm for transmission rates of 10Gbit/s. OSNR is often used as an indicator for the signal quality. Depending on the OSNR level (see Figure 2-7), an alarm could be triggered in real-time, achieved in the switching timescale, to check the EDFAs, the transmitters and used for intelligent path provisioning and traffic routing. Therefore, a technique that can precisely monitor the in-band OSNR is highly desirable for performance monitoring of optical networks [AND'07].

Chromatic dispersion (CD) plays a critical role in the propagation of short optical pulses in single mode fibre (SMF). CD manifests itself through the frequency dependence of the refractive index of the optical fibre causing the optical pulse shape to broaden, which in turn limits the maximum bit-rate that can be transmitted through the fibre. Chromatic dispersion has become a key issue with the increasing bit-rates. 40Gbit/s systems are 16 times less tolerant to the effects of chromatic dispersion than 10Gbit/s systems, due to the quadratic dependence of dispersion on signal bandwidth. Operating at wavelengths close to the zero dispersion, such as dispersion shifted fibre (DSF) with *D=0ps/(nm.km)*, would facilitate a decrease in CD limitations, however, this is not an option since most of the fibre deployed in the field is standard single mode fibre (SSMF), and would in any case give rise to nonlinear effects [WIL’02b].

PMD has its origins in the random variation of the birefringent orientation axes along the fibre, such that the optical power of the transmitted signal is split between two orthogonal polarisation states with different propagation velocities [KOG’02]. First-order PMD, resulting in differential group delay (DGD), is identified as the difference in arrival times between the two polarization states. PMD effects are stochastic, temperature dependent, time varying, and worsen with higher bit-rates. Proper PMD in-service monitoring is required in high-speed optical networks, especially in the next-generation dynamic reconfigurable WDM networks [LU05], where the monitoring information can also be used in conjunction with a compensation device and used to trigger real-time alarms for traffic re-routing.

Power monitoring is also a desirable feature. This has traditionally been implemented in current static networks and used for gain equalisation, where the power of each channel is tuned to obtain a flat spectrum. The literature review described in chapter 3 shows that most advanced OPM techniques can typically add such functionality using low-speed photo diodes.

Criteria for OPM

For OPM to be an enabling technology of dynamic networks a number of criteria should be met:

Maximum coverage of impairments: BER can be seen as the ultimate parameter to describe the optical signal quality and can readily be obtained at the termination point of each channel where error localisation can be achieved by implementing BER measurement at each node. However, this represents a very costly solution since it requires optical-to-electrical (OE) conversion in each monitor. In addition, BER does not give any indication of the cause of the channel degradation. The direct monitoring of the individual impairments that cause the signal degradation, allows signal diagnosis for impairment compensation and fault management. In order to achieve these functionalities, various impairments should be able to be monitored simultaneously and independently. These impairments typically include OSNR, CD, PMD and power. Other impairments such as crosstalk, jitter and non-linear effects can also be monitored, however, it is noted that monitoring these impairments is outside the scope of this thesis.

WDM: The second criterion of the monitoring technique is its ability to monitor various channels simultaneously with the minimum duplication of optical and electrical components, as this will reduce the OPM cost per channel.

Sufficient range and accuracy: A number of factors increase the impairment sensitivity of the optical link in WDM systems, these factors may include the bit-rate and the number of channels. Dynamic reconfiguration may add further sensitivity degradation by requiring the need to manage requests for transparent transmission of arbitrary distances. This has put new constraints on the OPM measurement range and accuracy which are dictated by the network architecture.

Response time: Static and dynamic networks may both require some OPM, although their requirements may be differentiated by the monitor's measurement time. In a static network, the measurement time can be of the same order of magnitude as the 50ms restoration time. In this case, if an impairment failure is detected, the OPM device would work in conjunction with a compensating device such that the impairment level is tuned to an acceptable threshold and this without altering the restoration time requirements. However, in a dynamic network, the OPM measurement time must be of the same order of magnitude as the network's switching time. Within dynamic networks, the switching time becomes faster when moving toward packet architectures, making the response time an important factor to consider when choosing an OPM technique.

Non-intrusive: The OPM device should be implemented in the network in a way where the optical signal is not terminated. This usually involves a tap where a small portion of the signal is routed into the monitoring device, which in turn is able to assess the signal performance. The monitor's power sensitivity is key in limiting the penalties introduced by the OPM into the system.

Network agnostic: All the features mentioned above come at a cost. It is envisaged that successful OPM techniques will be to an extent network agnostic, where the monitor is bit-rate and modulation format independent and does not require transmitter modification. Additionally, even if these conditions are met, the OPM technique should ensure that the benefits achieved by the technique are sufficient to compensate for the extra cost introduced by the components of the new technique.

State-of-the-art in OPM

In this thesis, I refer to advanced OPM techniques as techniques that meet some or all of the criteria mentioned above. These measurements can be divided into either time domain methods or spectral methods. Time domain monitoring includes synchronous and asynchronous sampling measurements, whilst spectral methods can be divided into techniques that involve the measurement of either the optical or electrical signal spectrum. Electrical spectrum techniques are also referred to as radio-frequency (RF) spectrum measurements. Figure 1-2 classifies the main OPM techniques developed to date.

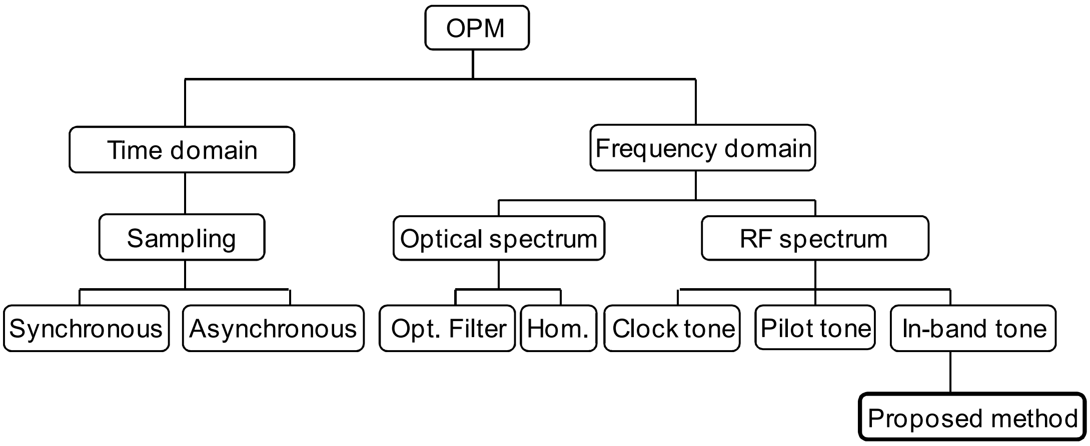

Figure 1-2: Diagram showing the main OPM techniques developed to date (Hom: homodyne techniques).

Sampling methods [HAN'99, MUE'98], aim at reconstructing the eye diagram, explore the statistical information of an optical signal to derive the histogram and the BER of a transmission channel. They are sensitive to CD, PMD and noise effects and can be integrated into a single electronic circuit. However, they may be costly in WDM networks when implemented in every network element since they need de-multiplexing and opto-electrical conversion of the signal. In addition, their response time is usually in the order of milliseconds, making these techniques inadequate for dynamic networks operating on shorter timescales. Sampling methods can be divided into two categories: synchronous and asynchronous. Synchronous sampling methods require clock recovery to acquire the samples at the bit-rate. Asynchronous sampling has the advantage of performing sampling without the need for a clock recovery but looses accuracy and impairment details.

The optical spectrum methods can provide carrier frequency and optical noise information. The optical spectrum can either be obtained using optical filtering or using homodyne detection (see chapter 3). These methods can monitor the OSNR and the wavelength drift and are suitable for multi-channel operation; however, they do not provide any information on the dispersion. In addition, these methods tend to be slow; it may take few seconds to obtain the full WDM scan. This is due to the tuning mechanism of the optical filters or of the tunable laser used in homodyne methods.

The RF spectrum is a better measure of signal quality since noise and distortion on the amplitude power spectrum will usually directly relate to impairments on the signal. Performance monitoring techniques based on RF spectrum analysis using clock detection are attractive compared to various other techniques such as the ones mentioned previously. They can monitor either CD or PMD. These techniques are applicable to the most widely used optical modulation formats such as non-return-to-zero (NRZ), return-to-zero (RZ) and carrier-suppressed return-to-zero (CS-RZ), and would be suitable for bit-rates beyond 40Gbit/s. One of the advantages of these methods is the fact that they are not intrusive and that they do not require transmitter modification. The monitor response time can be of a sub-microseconds order, which may allow for real-time monitoring and compensation in dynamic networks with comparable switching timescales. However, these methods have some key disadvantages: their implementations can only be used for single channels; which increases their cost for WDM systems as they use high speed electronics, in addition, they are bit-rate and modulation format dependent.

A pilot tone is defined as a frequency component that has been added to the modulated signal at the transmitter. Typically, this frequency component has a stronger amplitude than the adjacent tones of the signal (see section 6.5). In a WDM system, a different tone frequency can be attributed to each channel. Pilot tones can be added to and extracted from any node in the network. The pilot tone amplitude can be a measure of numerous parameters such as optical power, wavelength, OSNR, CD and PMD. The main advantages of the pilot tone techniques over the clock detection methods is the fact that the pilot tone frequency can be chosen (and is bit-rate independent), whereas the clock detection method relies on the clock frequency which is determined by the bit-rate and is format dependent. Choosing the tone frequency gives flexibility in finding a compromise between the dispersion monitoring range and the measurement sensitivity (see section 6.3.1). This is the case since the measurement accuracy is directly proportional to the monitoring range, where doubling the latter would double the former thus decreasing the measurement sensitivity. However, these techniques also present several limitations: the pilot tone can superimpose an unwanted modulation on the data and deteriorates the BER at the receiver; in addition, the method requires transmitter modification which has been the key drawback of these methods.

Figure 1-3 shows the routing timescale of dynamically reconfigurable networks and of OPM techniques developed to date. Within dynamic networks, two main architectures have emerged, the first one based on optical burst switching (OBS) and the second one based on optical packet switching (OPS). In OBS, the data traffic is aggregated in large data units (bursts) which travel to the destination without undergoing any optical-to-electrical conversion [LEL'06]. The burst aggregation-time can be as short as few microseconds to few milliseconds [MAL'05]. The latter time scale does not pose a particular challenge to OPM techniques. This is indeed the case since both sampling and RF spectrum methods are able to monitor within the millisecond timescale. However, only RF spectrum-based techniques are able to reach timescales of microseconds and below. In OPS, the optical packet comprises an optical label attached to a payload. Within OPS networks, the packet header or label is read, and the payload is transparently routed through the switch [MAH'01]. OPS requires very fast routing, in the nanosecond timescale [NEI'05], and is thus the most challenging to achieve from all technological aspects. It can be seen in Figure 1-3 that none of the OPM techniques developed to date reach the nanosecond timescale, which represent an interesting research area discussed in the future work section of chapter 7. It is however noted that such monitoring would only apply to impairments that develop in the nanosecond timescale, thus excluding PMD effects, which can evolve in timescales of the order of an hour (see section 2.3.2).

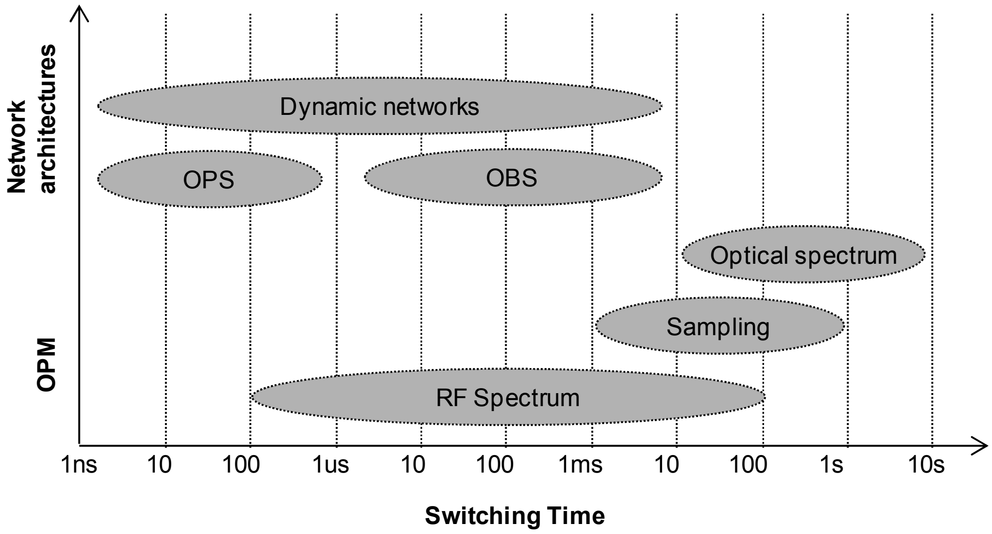

Figure 1-3: Switching time of dynamic reconfigurable networks with optical burst switched (OBS) and optical packet switched (OPS) architectures; and their applicable OPM techniques.

The proposed OPM technique

The shortcomings of the various advanced OPM techniques developed to date have prompted the research presented in this thesis. As shown in Figure 1-2, the proposed OPM technique is based on RF spectrum analysis but using in-band tone monitoring (see chapter 4). This technique allows for the retention of all advantages of the clock and pilot tone techniques, while resolving most of their limitations. As shown in Table 1.1, the proposed OPM technique presents a number of advantages compared to the existing proposals, published to date. A novel method for simultaneous and independent monitoring of power, OSNR, CD and PMD in 40Gbit/s multi-channel systems is proposed and experimentally demonstrated. An analytical model is developed to describe the monitoring technique which allows the prediction of the measurement range. The experimental results of the proposed monitoring technique are given for CD, first-order PMD and OSNR measurements and the impact that each impairment has on the measurement of the others is also investigated. It is shown that these three impairment measurements can be performed simultaneously and independently of each other. As a result, a single monitoring technique has been developed for multiple impairments including CD, PMD and OSNR. This technique is based on electro-optic down-conversion that simultaneously down-converts multiple WDM channels, sharing the cost of the key components over multiple channels and making it cost effective for multi-channel operation. The crosstalk from adjacent WDM channels is shown to have no impact on any of the three impairment measurements. The measurement range achieved with this method is equal to 4742±100ps/nm for CD, 200±4ps for DGD and 23±1dB for OSNR. To the knowledge of the author, the dispersion monitoring ranges are the largest reported to date for the bit-rate of 40Gbit/s using amplitude modulation formats. The impact of acquisition-time on the performance of the system has been demonstrated. As predicted by the theory, longer acquisition-time has no effect on the measurement range but reduces the measurement error for all impairments. The acquisition-time is then chosen as a compromise between the required measurement accuracy and the required measurement-time. This method is shown to be non-intrusive, with power levels of -40dBm reaching the detection system shown to be sufficient to maintain the stated measurement accuracies. Finally, the proposed method is network agnostic since it is bit-rate and amplitude modulation format independent and does not require transmitter modification.

	OPM				
	Time domain	**Frequency domain**			
	Sampling	**Opt. spectrum**	**RF spectrum**		
Criteria	**Sync. &** **Async.**	**Optical filter &** **Homodyne**	**Clock tone**	**Pilot tone**	**In-band tone (proposed method)**
Impairments	CD and PMD OSNR BER	OSNR Wavelength drift	CD and PMD	CD and PMD OSNR	CD and PMD OSNR
WDM	No	Yes	No	No	Yes
Dispersion Range	Bit-rate limited for PMD		Bit-rate limited	No fundamental limit	No fundamental limit
Speed	Slow (ms)	Very slow (s)	Very fast (μs)	Fast (μs-ms)	Fast (μs-ms)
Network agnostic	No Dependent on bit-rate	Yes	No Dependent on bit-rate and mod. format	No Need transmitter modification	Yes

Table 1.1: Diagram showing a non-exhaustive list of the main OPM techniques developed to date and their key characteristics.

1.1 Overview of the thesis

The theory needed to understand the various subsequent chapters is described in **chapter 2**. The first section discusses the fundamentals of the transmitted optical signal. The subsequent sections describe the fundamental concepts of the three key impairments that are monitored, which are CD, PMD and OSNR. Each section also provides the system's tolerance to these impairments.

Advanced OPM techniques reported to date are reviewed in **Chapter 3**. In this thesis, we refer to advanced OPM techniques as those techniques that are capable of multi-impairment monitoring. These techniques are based on RF spectrum analysis using clock detection, pilot tones and sampling methods. These techniques facilitate network management operations, including reporting degradations for alarm correlation and fault localisation [NOC'05], network optimisation, root cause analysis, prevention and for real-time control of compensation devices. However, none of the proposed methods to-date have addressed the major issue of network cost reduction.

In **Chapter 4**, the proposed novel technique for the simultaneous multi-channel monitoring of CD, PMD and OSNR is described. This technique is based on the conventional RF spectrum phase detection. The latter method uses electrical mixing providing a single-channel CD monitoring. In the course of the work, the proposed technique has evolved through three generations, each including an additional feature compared to the conventional method. The first generation provided a multi-channel operation through the use of optical mixing. The second generation has the added capability of simultaneous CD and OSNR monitoring, whereas the third generation retained all advantages of the previous implementation, but had included DGD monitoring. The three key advantages of the final implementation compared to the conventional method have been demonstrated, which are: (i) simultaneous and independent multi-impairment monitoring of CD, PMD and OSNR, (ii) multi-channel operation and (iii) bit-rate and modulation format independency.

In **Chapter 5,** an analytical model is developed to describe the proposed monitoring technique for group velocity dispersion (GVD), DGD and OSNR. The impact of filter detuning on the monitoring performance is investigated. It is shown that the analytical results presented in this chapter agree very well with the experimental results presented in chapter 6.

In **Chapter 6**, the experimental results of the proposed monitoring technique are presented for GVD, DGD and OSNR measurements. The impact of the measurement acquisition-time, filter detuning and WDM crosstalk as well as the effects of one impairment on the monitoring of the other impairments is also presented. The analysis of the results is based on the theory developed in the previous chapter.

Finally, **Chapter 7** provides a summary of the work performed in the course of this research and possible areas for further research are identified.

1.2 Original contributions

The following original contributions to the field of optical performance monitoring were made in the course of this research:

- First experimental results demonstrating a multi-channel monitoring of multi-impairments that include OSNR, CD and PMD. These impairments have been simultaneously and independently monitored [MEF'08].

- Largest chromatic dispersion monitoring range demonstrated to date of 4742ps/nm was achieved using the proposed method [MEF'07b].

- Largest DGD monitoring range of 200ps was achieved using the proposed method. Unlike previous techniques proposed in the literature, this monitoring range is not bit-rate limited to 25ps for 40Gbit/s systems [MEF'08].

- First experimental results presenting a novel method based on monitoring a high frequency in-band tone optically down-converted to an intermediate frequency tone of 10kHz for simultaneous and independent OSNR and chromatic dispersion monitoring [MEF'06b, MEF'07].

- First experimental results presenting the novel method for residual dispersion monitoring in 40Gbit/s systems. The measurement time of this implementation is in the order of 10µs, making this scheme the fastest RF spectrum monitoring technique published to date [MEF'06].

- Development and simulation verification of a novel technique for multi-channel chromatic dispersion monitoring. This proposed method utilises electro-optical mixing to dramatically decrease the number of high-bandwidth components required for a WDM 40Gbit/s chromatic dispersion monitoring system applicable in dynamically-reconfigurable optical networks [MEF'05c].

1.3 Publications and conference presentations arising as a result of the work described in this thesis

[MEF'05] Lamia Meflah, Benn Thomsen, John Mitchell, Polina Bayvel, "Chromatic Dispersion Monitoring using RF Spectrum Analysis," Proceedings London Communication Symposium (LCS), London, p251, 2005.

[MEF'05b] Lamia Meflah, Benn Thomsen, John Mitchell, Polina Bayvel, Gottfried Lehmann, Stefano Santoni, Bernd Bollenz, "Advanced Optical Performance Monitoring for Dynamically Reconfigurable Networks," Proceedings Networks Optical Communications (NOC) conference, London, 2005.

[MEF'05c] Lamia Meflah, Benn Thomsen, John Mitchell, Polina Bayvel, "Chromatic Dispersion Monitoring of a Multi-Channel 40 Gbit/s System for Dynamically Reconfigurable Networks," Proceedings European Conference on Optical Communication (ECOC2005), Glasgow, paper Th3.2.5, 2005.

[MEF'06] Lamia Meflah, Benn Thomsen, John Mitchell, Polina Bayvel, "Fast residual chromatic dispersion monitoring for dynamic burst networks," Proceedings Optical Fiber Communication Conf./National Fiber Optic Engineers Conf. (OFC/NFOEC), Anaheim, 2006.

[MEF'06b] Lamia Meflah, Benn Thomsen, Seb Savory, John Mitchell, Polina Bayvel, "Single Technique for Simultaneous Monitoring of OSNR and Chromatic Dispersion at 40Gbit/s," Proceedings European Conference on Optical Communication (ECOC2006), Cannes, 2006.

[MEF'07] Lamia Baker-Meflah, Seb Savory, Benn Thomsen, John Mitchell, Polina Bayvel, "In-band OSNR Monitoring Using Spectral Analysis After Frequency Down-Conversion," *IEEE Photon. Technol. Lett.,* vol. 19, no. 2, pp. 115-117, Jan. 2007.

[MEF'07b] Lamia Baker-Meflah, Benn Thomsen, John Mitchell, Polina Bayvel, "Chromatic dispersion and OSNR monitoring in a WDM 40Gbit/s system," Proceedings European Conference on Optical Communication (ECOC2007), Berlin, 2007.

[MEF'08] Lamia Baker-Meflah, Benn Thomsen, John Mitchell, Polina Bayvel, "Simultaneous chromatic dispersion, polarization-mode-dispersion and OSNR monitoring at 40Gbit/s," *Optics Express*, vol. 16, no. 20, pp. 15999-16004, 2008.

Chapter 2: Fibre propagation impairments

2.1 Introduction

In this chapter, the theory needed to understand the subsequent chapters is described. The first section discusses the fundamentals of the transmitted optical signal. The power spectrum of a non-return-to zero (NRZ) modulated signal is examined and the transmission bandwidth required for such format is estimated. A transmitted optical signal can be degraded by various impairments that are described in the following sections. These impairments include chromatic dispersion (CD), polarisation mode dispersion (PMD) and optical signal-to-noise ratio (OSNR). Each section also provides the system's tolerance to these impairments.

CD causes different spectral components of a propagating optical pulse to travel at different speeds, whereas PMD manifests itself through birefringence and the random variation of the birefringence axes orientation along the fibre and causes different polarisation modes to travel at different speeds. Both CD and PMD cause the optical pulse shape to broaden, which in turn limits the maximum bit-rate that can be transmitted through the fibre. Optical amplification is used to compensate for the fibre loss, but is not possible without the generation of amplified spontaneous emission (ASE), which gives rise to signal-spontaneous beat noise and can be characterized in terms of OSNR, which represents a severe impairment that limits the span length of such systems. In this thesis, optical performance monitoring (OPM) takes the broad definition of physical layer monitoring in the optical domain. Most OPM techniques falling in this description, described in chapter 3, in addition to the OPM technique proposed in this work aim at monitoring these three impairments, thus the need to understand the fundamental concepts but most importantly the system's tolerance to these impairments.

2.2 Optical pulse

2.2.1 Fundamental concepts

The electric field $E(t,L)$ of a propagating optical signal may be described in the time domain as [SAL'91]:

$$E(t,L) = A(t,L)\exp\left(i\left(\omega t - \beta L\right)\right) \tag{2.1}$$

where A is the complex envelop of the pulse, ω is the angular optical frequency, β is the mode-propagation constant and L is the propagation length.

The effects of fibre dispersion are accounted for by expanding the mode-propagation constant β in a Taylor series around the frequency ω_0 at which the pulse spectrum is centred [AGR'07]:

$$\beta(\omega) = \beta_0 + (\omega - \omega_0)\beta_1 + \frac{1}{2}(\omega - \omega_0)^2 \beta_2 + ... \tag{2.2}$$

where $\beta_0 = \beta(\omega_0)$ and other parameters are defined as:

$$\beta_m = \left(\frac{d^m \beta}{d\omega^m}\right)_{\omega=\omega_0} \quad (m = 1, 2, ...) \tag{2.3}$$

The envelop of an optical pulse travels at the group velocity v_g , and the parameter β_1 is defined such that:

$$\beta_1 = \frac{1}{v_g} \tag{2.4}$$

The parameter β_2 represents the dispersion of the group velocity and is defined in the section 2.3.1.

2.2.2 Optical pulse shape for NRZ signals

The amplitude of the optical signal can be modulated; if the modulating waveform consists of a non-return-to-zero (NRZ) rectangular pulse, then the modulated parameter will be switched or keyed from one discrete value to another which is often referred to as amplitude-shift keying (ASK). The binary ASK waveform can be generated simply by turning the carrier on and off, a process described as on-off keying (OOK).

In the time domain, the electric field of an NRZ waveform can be expressed as follows [CAR'02]:

$$E_{NRZ}(t) = E(t) \sum_k a_k p(t - kT) \tag{2.5}$$

where a_k represents the random data stream transmitted at a bit-rate of $B=1/T$ and p is the pulse shape.

The NRZ modulation format is considered in which the individual bits are modelled ideally as rectangular pulses occupying the full time slot of duration T. In the frequency domain, the power spectral density *S(f),* of the NRZ pulses of amplitude A, has a squared sinc function and is given by [CON'02]:

$$|S(f)|^2 = \frac{|A|^2}{4} T \,\mathrm{sinc}^2(fT) + \frac{|A|^2}{4} \delta(f) \tag{2.6}$$

where δ is the Dirac delta function.

The power spectral density function has nulls at ±NB where N is an integer and is illustrated in Figure 2-1. The transmission bandwidth, if measured between the first nulls, on either side of the zero frequency, is twice the bit-rate. It is noted that typically, the spectrum outside ±*1B* is filtered out.

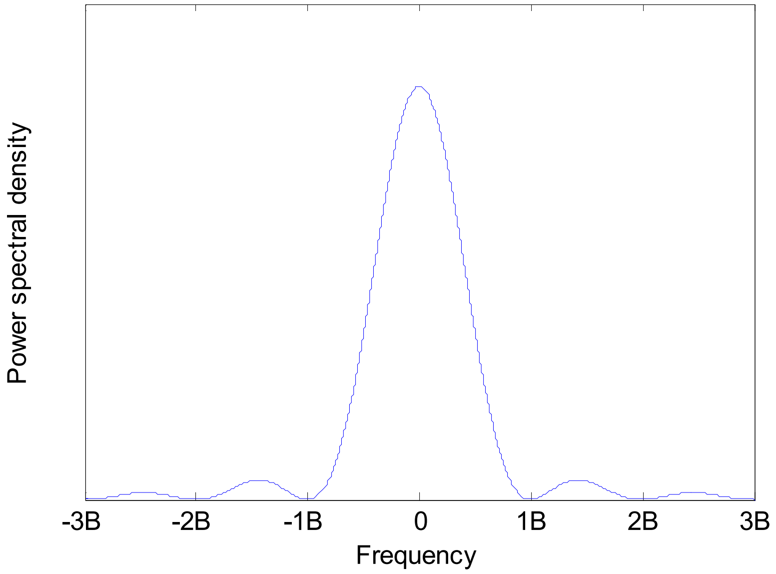

Figure 2-1: Illustration of the base-band power spectral density for an NRZ signal (B is the bit-rate).

2.3 Chromatic dispersion

2.3.1 Fundamental concepts

Chromatic dispersion (CD) plays a critical role in the propagation of short optical pulses in single mode fibre (SMF). CD manifests itself through the frequency dependence of the refractive index of the optical fibre. Any type of modulated data at a given bit-rate has a non-zero bandwidth which is of the same order of magnitude as the bit-rate. CD causes different spectral components of a propagating optical pulse to travel at different speeds. The propagation speed dependence on the optical frequency causes the optical pulse shape to broaden, as shown in Figure 2-2, which in turn limits the maximum bit-rate that can be transmitted through the fibre. The dispersion parameter *D* is usually measured in picoseconds of delay per nanometre of signal bandwidth per kilometre of transmission (ps/nm/km) and must be compensated for to maintain good signal quality.

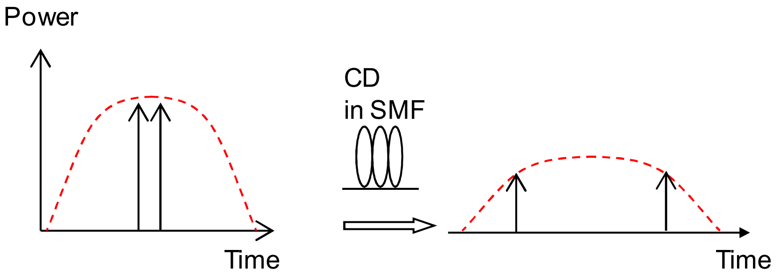

Figure 2-2: CD broadening effect on a propagating optical pulse in single mode fibre (SMF).

The dispersion of the group velocity β_2 is responsible for the pulse broadening. This phenomenon is known as the group velocity dispersion (GVD), and β_2 is the GVD parameter. The propagation constant β_2 is proportional to the dispersion parameter *D* and is defined as [AGR'07]:

$$\beta_2 = -\frac{1}{2\pi}\frac{\lambda^2}{c}D \tag{2.7}$$

where *c* is the light velocity and λ is optical wavelength.

The GVD is equal to the dispersion parameter *D* multiplied by the propagation length *L* and is usually measured in picoseconds per nanometre (ps/nm).

$$GVD = DL \tag{2.8}$$

CD effect on the signal's phase

The proposed CD monitoring technique described in chapter 4 is based on a phase measurement of a spectral tone within the signal bandwidth. For this reason, the following section determines the impact of CD on the signal's phase.

Let us consider *E(t)*, the electric field of a propagating optical pulse. After transmission, the accumulated dispersion introduces a phase shift to the signal proportional to β_2, and is given by [AGR'07]:

$$E(\omega,L) = \mathbb{F}\left(E(t,0)\right)\exp\left(i\frac{1}{2}L\beta_2\omega^2\right) \tag{2.9}$$

Where $E(\omega)$ is the electrical field in the frequency domain, $\mathbb{F}$ is the Fourier transform, L is the propagation length, β_2 is the propagation constant and ω is the optical angular frequency.

The upper sideband (USB) and lower sideband (LSB) of the optical pulse acquire a phase shift due to CD, which can be derived from Eq. (2.9). The frequency of a tone ω_T, within each sideband can be defined as:

$$\omega_{USB} - \omega_0 = \omega_T \tag{2.10}$$

and

$$\omega_{LSB} - \omega_0 = -\omega_T \tag{2.11}$$

Where ω_{USB} and ω_{LSB} are the optical frequencies of the USB and LSB tones, ω_0 is the carrier optical frequency and ω_T is the tone frequency.

From Eq. (2.9), the phase shift of each sideband after propagation through a length of fibre *L* with dispersion relative to the carrier phase is given by:

$$\varphi_{USB}(\omega_{USB} - \omega_0) = \frac{1}{2} L \beta_2 \omega_T^2 \tag{2.12}$$

and

$$\varphi_{LSB}(\omega_{LSB} - \omega_0) = \frac{1}{2} L \beta_2 \omega_T^2 \tag{2.13}$$

Thus the phase shift $\Delta\varphi_{GVD}$ between the two sidebands is then equal to:

$$\Delta\varphi_{GVD} = L \beta_2 \omega_T^2 \tag{2.14}$$

Using Eq. (2.7), the phase shift can be expressed in terms of the dispersion parameter *D*:

$$\Delta\varphi_{GVD} = 2\pi \frac{\lambda^2}{c} f_T^2 DL \tag{2.15}$$

where f_T is the tone frequency.

It can be seen in Eq. (2.15) that the phase shift between two tones within the optical pulse is directly proportional to GVD. This is the phenomena that we make use of in the CD monitoring technique described in subsequent chapters where a maximum phase shift of 2π provides the maximum monitoring range corresponding to:

$$DL_{\max} = \frac{c}{\lambda^2} \frac{1}{f_T^2} \tag{2.16}$$

It is however noted that certain OPM techniques can only unambiguously measure a maximum phase shifts of π, in which case the maximum monitoring range is halved compared to the previous result, and equal to:

$$DL_{\max} = \frac{1}{2}\frac{c}{\lambda^2}\frac{1}{f_T^2} \tag{2.17}$$

2.3.2 System tolerance to chromatic dispersion

As described previously, CD causes a propagating optical pulse to broaden. This phenomenon limits the error-free transmission distance of such an optical pulse. A dispersion-limited distance is defined as the fibre length for which the optical pulse broadening is equal to the bit-time period. Figure 2-3 shows the dispersion-limited distance in single mode fibre as a function of the bit-rate [WIL'02c]. Using a dispersion coefficient *D=17ps/(nm.km)* at a signal wavelength of 1550nm, the maximum transmission distance for 10Gbit/s is 73.4km or 1248ps/nm which also corresponds to a power penalty of around 1dB [WIL'02c]. For a 40Gbit/s signal, this limit decreases to 4.6km of SMF or 78.2ps/nm.

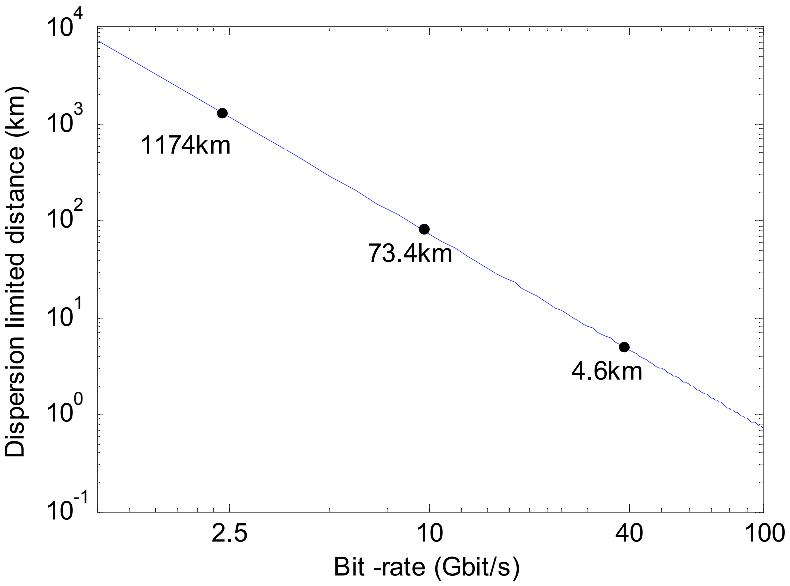

Figure 2-3: Dispersion-limited transmission distance in single-mode fibre as a function of data rate for intensity-modulated optical signals [WIL'02c].

The penalty arising from CD is cumulative and increases linearly with transmission distance and quadratically with the bit-rate. It is noted that regardless of the dispersion-limited distance definition, a four-fold increase in the bit-rate results in a CD limit to decrease by a factor of 16 (see Eq. (2.15)).

Chromatic dispersion management

Various research has shown that chromatic dispersion must be managed rather than eliminated. Zero dispersion is not acceptable in WDM systems due to the fact that nonlinear effects can only be reduced by introducing small amounts of dispersion in the link [WIL'02c].

This can be achieved by creating dispersion maps, in which the dispersion takes positive and negative values at each link. This is done by implementing in each link negative dispersion elements that counteract the positive dispersion effect of the SMF, while insuring that the accumulated dispersion at the receiver is zero. This technique is referred to as dispersion management. A typical negative dispersion element is based on dispersion-compensating fibre (DCF) which is designed to cancel the positive dispersion of the fibre. In addition to the static periodic dispersion compensation, additional tuneable compensation modules (such as chirped gratings, tuneable virtually imaged phased array (VIPA), ring resonators, Mach-Zehnder and planar lightwave circuit (PLC) devices are described in the literature review in chapter 3) can be added in each link, controlled by an OPM device, to provide a fine-tuning of the dispersion, thus improving the performance of the system. This is of a particular interest in dynamically reconfigurable networks, as described in the previous chapter.

2.4 Polarisation mode dispersion

2.4.1 Fundamental concepts

In a waveguide with an ideal symmetric and circular cross-section, there are two orthogonally polarised modes which exist in a single mode fibre which have the same group velocity. However, manufacturing process imperfections cause the fibre to be asymmetric, breaking the degeneracy of the orthogonally polarised modes, resulting in birefringence, causing a difference in phase and group velocities of the two modes. These two modes are referred to as the fast and slow polarisation modes. PMD manifests itself through this birefringence and the random variation of the birefringence axes orientation along the fibre and causes different polarisation modes to travel at different speeds. Similarly to CD, PMD causes the optical pulse to broaden, which in turn also limits the maximum bit-rate that can be transmitted through the fibre. Environmental changes such as temperature and stress cause the PMD to vary stochastically in time, making it particularly difficult to manage [KOG’02]. This represents the key difference between PMD and CD; the latter being considered constant over time. Optical fibre birefringence is caused by both intrinsic and extrinsic perturbations. Imperfections in the manufacturing process set up permanent intrinsic perturbations. When the fibre is embedded in the ground, undersea for submarine systems or in aerial systems, birefringence can be induced from a number of extrinsic perturbations such as lateral stress, bending, twisting or variations in temperature.

In a short section of fibre, the birefringence can be considered uniform. First order PMD, also called differential group delay (DGD) is defined as the difference in group delay between the slow and fast polarisation modes. Figure 2-4 is an illustration of the time domain effect of PMD in a short fibre, where a pulse launched with equal power on the two birefringent axes results in two pulses at the output separated by the DGD ($\Delta\tau$). The linear length dependence of the DGD can be applied when the birefringence is considered uniform.

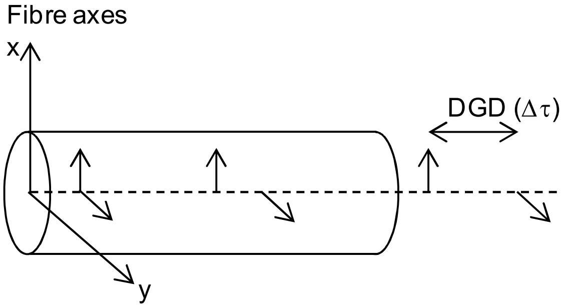

Figure 2-4: Illustration of the time domain effect of PMD in a short fibre, where a pulse launched in equal power on the two birefringent axis, x and y, becomes two pulses at the output, separated by the DGD.

For long-length regime, the birefringence is no longer additive, there are random variations of the axes of the birefringence along the fibre length. Each fibre section causes the birefringence to either add or subtract from the total birefringence, as a result, the DGD does not accumulate linearly for the fibre length and it has been shown that the DGD increases on average with the square-root of the distance. Transmission systems are generally in the long-length regime, so fibre PMD is often specified using a PMD coefficient having units of picoseconds of delay per squared kilometre of transmission ($ps/km^{1/2}$) [KOG'02].

Despite the random variations of the birefringence in long-length regimes, there are two orthogonal polarisation states at the fibre input that result in an output pulse that is undistorted to first order. The principal states model shows that there exists for every frequency a special pair of polarisation states, called the principal states of polarisation (PSP). A PSP is defined as the input polarisation for which the output state of polarisation is independent of frequency to first order, i.e., over a small frequency range. In the absence of polarisation-dependent loss, the PSPs are orthogonal.

In the time domain, the Jones vectors are used to characterise PMD. Using the PSPs as an orthogonal basis set, any polarisation can be expressed as the vector sum of two components, each aligned with a PSP. When considering first order PMD, the output electric field from a fibre with PMD takes the form [KOG'02]:

$$\vec{E}_{out}(t) = a\left|p\right\rangle E_{in}(t-\tau_0-\frac{\Delta\tau}{2}) + b\left|p_-\right\rangle E_{in}(t-\tau_0+\frac{\Delta\tau}{2}) \tag{2.18}$$

where $E_{in}(t)$ is the input electric field, a and b are the complex weighting coefficients indicating the field amplitude launched along the slow and fast PSPs $\left|p\right\rangle$ and $\left|p_-\right\rangle$, and τ_0 is the polarisation-independent transmission delay.

In this equation, $\Delta\tau$ is the difference in arrival time between the two principal states, also referred to as DGD, and is usually given in picoseconds. PMD causes pulse broadening due to DGD, though this broadening may not occur if the input pulse is aligned with a PSP, i.e., when *a* or *b* is zero.

The first-order PMD power splitting ratio, which represents the ratio between the signal power on the fast PSP to the total signal power, may be defined from Eq. (2.18), and is given by:

$$\gamma = \frac{|b|^2}{|a|^2 + |b|^2} \tag{2.19}$$

PMD effect on the signal's phase

The proposed monitoring technique described in chapter 4 is also based on phase measurements for DGD monitoring. For this reason, the following section determines the DGD impact on the signal's phase. It can be noted from Eq. (2.18) that the phase of the electric field on the slow and fast PSPs at ω_T, the monitored tone frequency within each sideband, can be defined as:

$$\varphi_S = \omega_T(t - \tau_0 - \frac{\Delta\tau}{2}) \tag{2.20}$$

and

$$\varphi_F = \omega_T(t - \tau_0 + \frac{\Delta\tau}{2}) \tag{2.21}$$

The phase difference $\Delta\varphi$ is then equal to:

$$\Delta\varphi = \omega_T \Delta\tau \tag{2.22}$$

It can be seen in Eq. (2.22) that the phase shift difference between the fast and slow modes is directly proportional to DGD. This equation is key in understanding the DGD effect on the optical pulse and will be used a number of times in subsequent chapters. A maximum phase shift of 2π provides the maximum monitoring range corresponding to:

$$\Delta\tau_{\max} = 2\pi \frac{1}{\omega_T} \tag{2.23}$$

Similarly to the CD monitoring described in the previous section, it is noted that certain OPM techniques can only unambiguously measure maximum phase shifts of π, in which case the maximum monitoring range is halved compared to the previous result, and equal to:

$$\Delta\tau_{\max} = \pi \frac{1}{\omega_T} \tag{2.24}$$

2.4.2 System tolerance to polarisation mode dispersion

PMD has become a major impediment for network operators seeking to increase the per-channel bit-rate on long-haul fibre links. While the DGD in buried fibre had negligible impact at 2.5Gbit/s bit-rates [IAN'93], upgrades to 10Gbit/s, 40Gbit/s and beyond require increasingly more attention. While there are PMD challenges facing carriers at 10Gbit/s, these challenges are not as severe as originally feared. Major carriers are successfully deploying 10Gbit/s dense-wavelength-division-multiplexed (DWDM) links across the core of their networks. A marked improvement in the DGD tolerance of 10Gbit/s long reach receivers to about 40ps, will likely satisfy most length demands, obviating the need for PMD compensation (PMDC). Signalling rates of 40Gbit/s and beyond will most likely require some form of mitigation in long-haul applications, such as robust modulation schemes or PMDC (as discussed in chapter 3, section 6).

Time evolution of PMD

The time evolution of PMD has previously been investigated for submarine systems [TAK'93] and terrestrial cables [ANG'92] that were found to change in timescales of the order of an hour. Occurrences of high instantaneous DGD may degrade the signal quality to an intolerable level, resulting in a PMD-induced outage. Statistical analysis of the measured DGD data shows that high-DGD episodes are rare and short-lived. Experimental work has also been done to record the PMD transients over a period of 36hours. The measurements were done in a field fibre loop of 52km length deployed in a buried cable selected due to a comparatively high DGD of 6.3ps [BUL'99]. It has been shown that fast PMD transients can occur in time scales of milliseconds. Even though these fast events may occur with low probability, the transients strongly influence the design of monitoring and compensation units.

PMD evolution with temperature

The fluctuations of PMD due to environmental changes are an important issue in fibre optic systems. The time evolution of PMD as a function of temperature for 48.8km installed buried cable has been investigated [CAM'98]. It was shown that a variation in fibre temperature leads to a fluctuation in PMD and that the rate of fluctuation follows the rate of temperature change.

System tolerance to PMD

The DGD length dependence has been experimentally investigated and was found that an optical pulse may broaden by 17ps after traversing 100km of SMF in a 10Gbit/s system [TSU'88]. The maximum DGD a receiver can tolerate before the signal degradation becomes unacceptable depends on a number of factors including the bit-rate, the modulation format, the OSNR and the receiver design. For intensity-modulated direct-detection (IMDD) systems, it was found that when the transmitted signal excites both PSPs equally (a worst case condition), a 1dB receiver sensitivity penalty results when the instantaneous DGD is about 23% of the signal time-period [IAN'93]. Figure 2-5 shows the theoretical sensitivity penalty as a function of the differential group delay for three different bit-rates of 2.5, 5 and 10Gbit/s. For a 10Gbit/s NRZ signal, this corresponds to 23ps and by extrapolation, for a 40Gbit/s, this DGD limit would correspond to 5.7ps. This maximum tolerable DGD level can be increased by using PMD-tolerant signalling formats such as RZ with a 1dB penalty caused by 40ps [KHO'00].

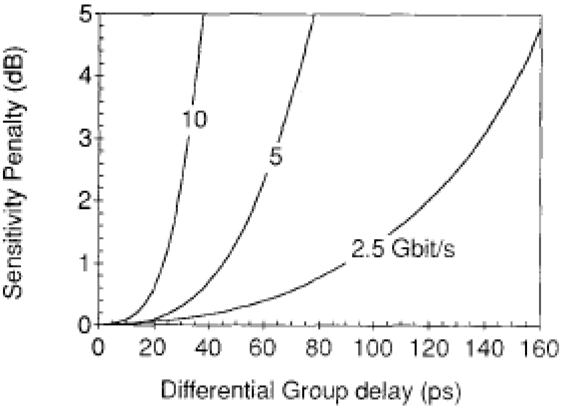

Figure 2-5: Theoretical sensitivity penalty as a function of the differential group delay for three different bit-rates, taken from [IAN'93].

2.5 Optical signal-to-noise ratio

Noise in optical systems, comes from three different sources. The first being the transmitter noise [DER'98], which arises from the intensity fluctuations of the semiconductor laser. The second source of noise is the receiver noise [DER'98], which arises from its output electric current fluctuations, and is due to thermal and shot noise. The last source of noise, which is the optical amplifier noise, characterised by the optical-signal to noise ratio (OSNR), is the dominant noise in WDM networks and is topic of discussion in this section.

2.5.1 Fundamental concepts

The advent of optical amplifiers capable of simultaneously amplifying multiple signal wavelengths was the technological advance that allowed the development of DWDM systems. Optical amplifiers are used at the end of each fibre span to boost the power of the DWDM signal, to compensate for the fibre loss. Unfortunately, optical amplification is not possible without the generation of amplified spontaneous emission (ASE), and the noise resulting from this ASE constitutes a severe impairment that limits the span length of such systems. Each optical amplifier contributes to ASE, and these contributions add cumulatively along the fibre link. This accumulated ASE gives rise to signal-spontaneous beat noise at the receiver, which is the fundamental limit in an optically amplified transmission system. This signal-spontaneous noise can be characterized in terms of the optical-signal to noise ratio (OSNR), defined as the ratio of the signal channel power to the power of the ASE in a specified optical bandwidth, usually equal to 0.1nm for 10Gbit/s systems and 0.5nm for 40Gbit/s systems. The OSNR is defined as:

$$OSNR\ (dB) = 10\log\left(\frac{P_{signal}}{P_{noise}}\right) \tag{2.25}$$

where P_{signal} and P_{noise} are respectively the signal and noise power measured using the same optical bandwidth. Figure 2-6 shows an illustration of an OSNR measured using an optical spectrum.

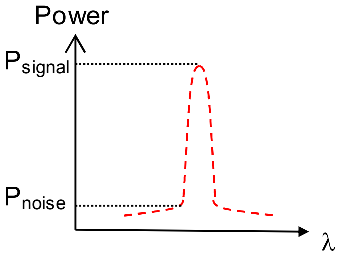

Figure 2-6: Illustration of the OSNR determined from an optical spectrum.

The maximum system length that results for a given OSNR is determined by the characteristics of the fibre network and the optical amplifiers. For a system consisting of N_{amp} fibre spans, each of loss L_{span} (in dB) followed by an optical amplifier with output power P_{out} (in dBm) per channel launched into the span and noise figure NF (in dB), the OSNR (in dB) of a 10Gbit/s signal channel at the end of the system is approximately [ZYS'02]:

$$OSNR = 58 + P_{out} - L_{span} - NF - 10\log(N_{amp}) \tag{2.26}$$

Although the fibre span of commercial fibre networks are typically not uniform, Eq. (2.26) can be used to illustrate some of the constraints placed on system design as a result of amplifier noise. The OSNR can be increased (dB for dB) by increasing the output power or decreasing the fibre span or the noise figure. The OSNR can also be increased by reducing the number of spans, although this dependency is weaker since it is logarithmic. Increasing P_{out} is possible only to a certain extent, since as P_{out} increases, impairments arising from optical nonlinearities become more severe. Reducing L_{span} is also possible, however, this involves reducing the separation between amplifiers, this implies the use of more amplifiers which is an expensive solution. The remaining alternative is to reduce the noise figure of the amplifiers which is typically around 5dB. The noise figure of an EDFA is however limited in principle to values above 3dB.

An approximate expression of the required OSNR to achieve a given bit-error-rate (BER) is given by Eq. (2.27) and Eq. (2.28). The expression in Eq. (2.27) assumes that the main source of noise results from the beating between the signal and the ASE noise and for large duty cycle intensity-modulated formats such as NRZ.

$$OSNR = \frac{Q^2 B_e}{B_0} \frac{1+r}{\left(1-\sqrt{r}\right)^2} \tag{2.27}$$

where B_o is the optical bandwidth (of 12.5GHz, equivalent to 0.1nm optical bandwidth), B_e is the electrical filter's bandwidth of the receiver, r is the transmitter extinction ratio, defined as the ratio between the power of the ones and the zeros, and Q is the parameter linked to the BER such that [ESS'02]:

$$BER = \frac{1}{2} erfc\left(\frac{Q}{\sqrt{2}}\right) \tag{2.28}$$

where *erfc* is the complementary error function [ESS'02].

2.5.2 System tolerance to optical signal-to-noise ratio

The BER is determined using Eq. (2.27) and Eq. (2.28). For a 10Gbit/s signal, the parameters of Eq. (2.27) are chosen such that B_o=12.5GHz, B_e=7.5GHz and r=0, which corresponds to an infinite extinction ratio. Figure 2-7 shows the BER as a function of OSNR. It is noted that a BER of 10^{-9} can be obtained with an OSNR of 13.4dB.

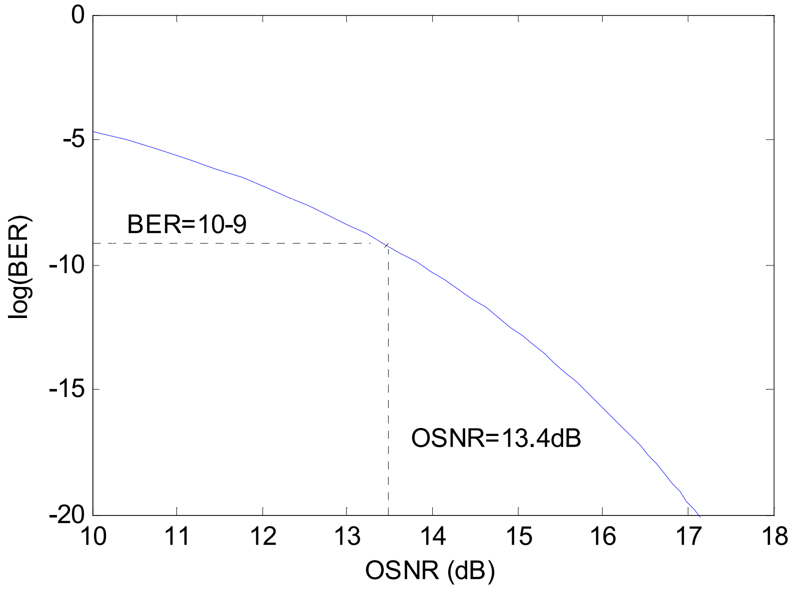

Figure 2-7: BER as a function of OSNR for a 10Gbit/s signal, using the following parameters: B_o=12.5GHz, B_e=7.5GHz, r=0 (infinite extinction ratio).

The OSNR target must be sufficient to achieve the required system performance, which for commercial systems, are most often a BER of 10^{-15}, which is effectively error free. The OSNR target must include sufficient margin to provide for any impairments that may be encountered. These include transmission impairments arising, for example, from chromatic dispersion, PMD, nonlinearities; distortions introduced by the transmitter and receiver; amplifier gain ripple; manufacturing margins to provide for variation in performance of components; and aging both of the system equipments and fibre plant during the expected life of the system. The target OSNR must theoretically increase by 6dB for each increase by a factor of 4 in the channel bit-rate in order to maintain an equivalent noise performance. The maximum un-regenerated reach of an optically amplified system is the length of the system at which the OSNR at its end equals the target OSNR for acceptable system performance.

2.6 Summary

This chapter described the fundamental concepts of optical pulse propagation followed by the description of key propagation impairments which were divided into three effects: chromatic dispersion, polarisation mode dispersion and optical signal-to-noise ratio. The properties of these impairments were discussed and the system tolerance was assessed.

It has been shown that the power spectral density function of a NRZ optical signal has a transmission bandwidth (if measured between the first nulls, on either side of the centre frequency, see Figure 2-1) of twice the bit-rate. It has also been shown that this optical bandwidth is increased with CD and PMD effects, limiting the transmission distance. For a 10Gbit/s system, a 1dB sensitivity penalty was reached with a CD level of 1248ps/nm and a DGD level of 23ps, whereas for a 40Gbit/s system, these limits are reduced respectively for CD and DGD to 78.2ps/nm and 5.7ps. A BER of 10^{-9} can be obtained with an OSNR of, 13.4dB for a 10Gbit/s signal and 19.4dB for a 40Gbit/s signal. These tolerances are compared with the monitoring range and sensitivity achieved by the OPM techniques reported to date, and described in the following chapter, and also with the proposed OPM technique described in chapter 4.

Chapter 3: Literature review of OPM and dispersion compensation schemes

3.1 Introduction

This chapter focuses on the analysis of advanced optical performance monitoring (OPM) and tuneable dispersion compensation devices developed to date. As described in chapter 1, in this thesis, we refer to advanced OPM techniques as OPM techniques that are developed to meet the new requirements of dynamically reconfigurable networks and meet some or all of the following criteria: (1) the OPM is able to measure simultaneously and independently a number of impairments such as OSNR, CD, PMD and channel power; (2) the technique is suitable for WDM networks; (3) it has a suitable measurement range and accuracy to cope with the increasing sensitivity requirements in dynamically reconfigurable networks; (4) its measurement speed is of the same order as that of the network re-configurability time; (5) it is non-intrusive; (6) and finally, it is network agnostic. To reduce cost, the monitor should be bit-rate and modulation format independent and would not require transmitter modification.

The OPM techniques developed to date can be divided into either spectral methods or time domain methods (see Figure 1-2). Spectral methods can be further divided into RF spectrum and optical spectrum measurements whereas time domain monitoring includes sampling methods. RF spectrum analysis can be in turn divided into clock tone and pilot tone monitoring. It is shown in the following sections that none of the OPM techniques developed to date satisfy the first two criteria mentioned above (i.e. multi-impairment and multi-channel operation). As an example, sampling techniques are sensitive to CD, PMD and noise effects. However, they may be costly in WDM networks when implemented in every network element since they need de-multiplexing and opto-electrical conversion of the signal. Similarly, it is shown that OPM techniques based on RF spectrum analysis allow for the simultaneous and independent measurement of CD and PMD, however, their implementation can only be used for single channels, which increases their cost for WDM systems as they also use high speed electronics.

Fixed dispersion maps are only suitable for low bit rates (up to 10Gbit/s) and static networks. For high bit rates (40Bbit/s and above) in dynamically reconfigurable networks, compensation devices must be tuneable for the following reasons: (1) changes in path length: In a reconfigurable network, signals are rerouted to avoid congestion or faulty sections in which the distance and type of fibre may change. The dispersion compensation must follow these changes. (2) Tighter accuracy required: the required accuracy in dispersion compensation increases dramatically with the signal bit-rate (see chapter 2, section 1.3.2) enhancing the need for highly accurate compensation. This could be achieved with the use of custom-made fixed dispersion modules, but would introduce complexity in the module management. Thus the use of tuneable modules seems the only practical solution. (3) Environmental effects: temperature changes can lead to variations in dispersion that may be significant enough to impact the system. Given a temperature change of 25C, a distance of 500km and a SMF dispersion slope of $D''=0.08ps/(nm^2.km)$, the thermally induced variation in dispersion is 30ps/nm, which becomes significant for 40Gbit/s systems, considering that a 1dB tolerance is reached with a dispersion or ~70ps/nm (see chapter 2, section 2.3.2).

Tuneable dispersion compensation devices, such as chirped gratings, tuneable virtually imaged phased array (VIPA), ring resonators, Mach-Zehnder and planar lightwave circuit (PLC) devices are described in section 1.6. Compensation modules can be added in each link, controlled by an OPM device, to provide a fine-tuning of the dispersion, thus improving the performance of the system.

3.2 RF spectrum analysis using clock tone detection techniques

Performance monitoring techniques based on RF spectrum analysis using clock detection are very attractive compared to various other techniques such as the ones based on optical spectrum analysis and on sampling methods which are mentioned in the following sections. OPM based on RF clock detection can monitor either CD or PMD. The clock techniques have achieved ranges, for 10Gbit/s systems, up to ±640ps/nm and 50ps, respectively for CD and PMD monitoring [PAN'01, MOT'02]. The monitor response time can potentially be of a sub-μs order, which may allow for real-time monitoring and compensation in dynamically reconfigurable networks of similar switching time. One of the advantages of these methods is the fact that they are not intrusive, and that they do not require transmitter modification. These techniques are applicable to the most widely used optical modulation formats (NRZ, RZ and CSRZ), and would be suitable for bit-rates beyond 40Gbit/s. However, the monitors based on clock tone detection techniques have some limitations, e.g. they do not allow for OSNR measurements, these implementations can only be used for single channels, which increases their cost for WDM systems as they use high speed electronics, and they are bit-rate and modulation format dependent.

Two methods based on RF spectrum analysis using clock tone measurements are described in this section. The first method, based on clock power detection, has been used to monitor CD [SAN'96, PAN'01, MOT'04] and PMD [MOT'02, MOT'04b, YU'03, LUO'04]; the second method based on clock phase detection technique has been used for CD monitoring [YU'02].

3.2.1 Clock power detection for CD and PMD monitoring

CD monitoring

Chromatic dispersion attenuates the clock tones of a received double side-band (DSB) signal after square law detection in an RZ signal, and regenerates them in an NRZ signal, which is commonly known as RF fading [PAN'01]. This is due to the fact that CD induces a time delay between the two sidebands of the optical signal, since the sidebands are located at a different frequency. This time delay is converted into a phase shift which causes the upper and lower sideband beat terms to interfere with the carrier after square law detection (see chapter 2, section 2.3). The electrical power spectrum of an RZ signal contains a strong component at the clock frequency compared to an NRZ signal [PAN'01]. The relative clock power (RCP) is defined as the ratio, at any given propagation point, of the clock power (at the bit-rate) to the DC term.

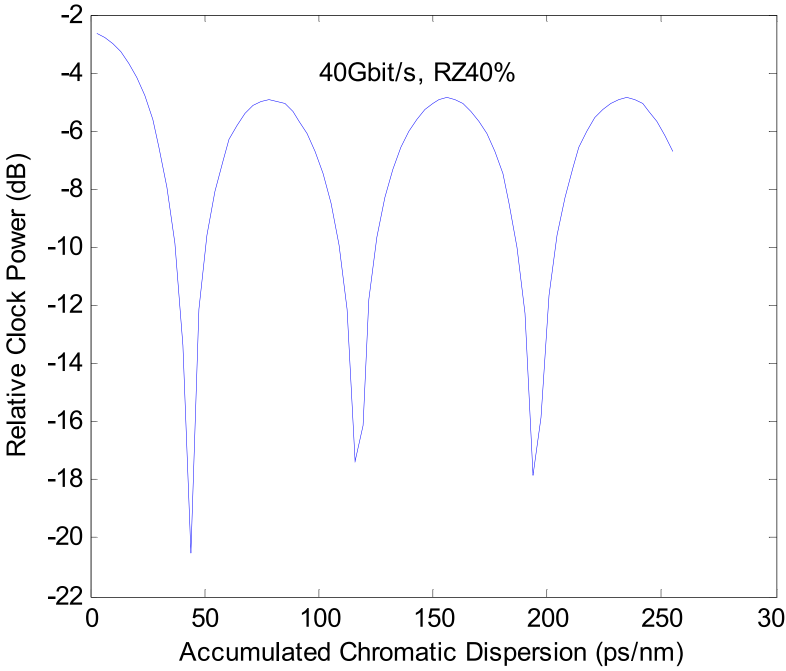

Figure 3-1: Simulation results (using Matlab) of the relative clock power (RCP) at 40GHz varying with CD in a 40Gbit/s RZ system (40% duty cycle).

The transmitted signal in the numerical model (using Matlab) is a 40Gbit/s, 2^7 RZ signal (40% duty cycle). Figure 3-1 shows the simulated RCP as a function of the accumulated chromatic dispersion for an RZ modulation format at 40Gbit/s. The results show that for an RZ signal, the RCP is inversely proportional to the chromatic dispersion over some finite range of dispersion values. Beyond this range, the RCP increases then decreases periodically with the accumulated dispersion. If the difference in phase between both sidebands reaches π, the interference is maximum; and the measured RF clock power reaches its local minimum. The phase shift between two local minima in the RCP curve corresponds to a phase shift of 2π between the two clock signals. It is noted that the measurement range is limited by the accumulated dispersion value over which the RCP signal varies monotonically. A CD monitor can thus only be used in any monotonic range corresponding to a phase shift of π.

The electrical power spectrum of an NRZ signal does not contain any power at the clock frequency (null in the spectrum). This is the case since the Fourier transform of a NRZ rectangular pulse is a sinc function that is equal to zero at all frequency components that are multiple of the bit-rate [MOT'04b]. The clock tone can be regenerated due to dispersion, increasing by more than 30dB over the measurement range. Beyond this range, the clock power decreases then increases periodically with the accumulated dispersion.

The theoretical maximum group velocity dispersion (GVD) monitoring range, for a phase shift of π, is given by (see chapter 2, section 1.3):

$$GVD_{\max} = \frac{1}{2}\frac{c}{\lambda^2}\frac{1}{B^2} \tag{3.1}$$

where B is the bit-rate and λ is the optical wavelength.

For a 10Gbit/s and 40Gbit/s systems (using a 1550nm optical wavelength), the monitoring ranges correspond respectively to 624ps/nm and 39ps/nm. These monitoring ranges have been verified using simulation results.

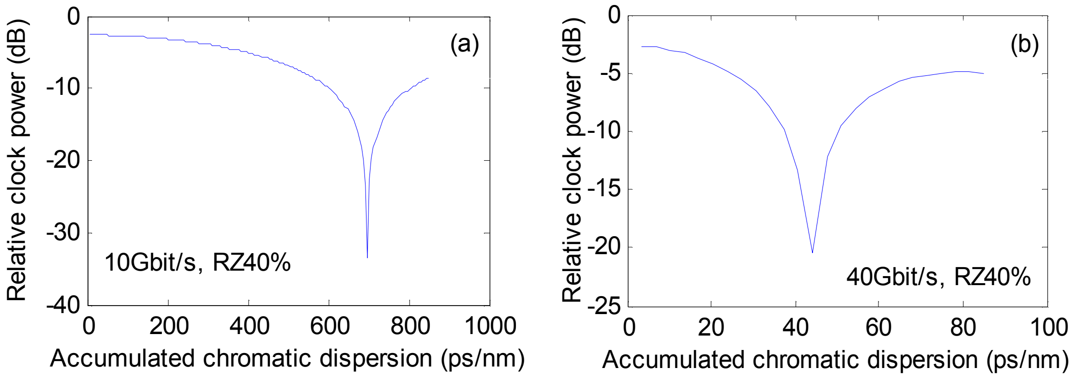

Figure 3-2: Simulation results of the relative clock power (RCP) as a function of chromatic dispersion (CD) for a RZ system with 40% duty cycle, at: (a): 10Gbit/s and (b): 40Gbit/s.

Figure 3-2 shows the RCP as a function of the accumulated chromatic dispersion for an RZ modulation format at 10Gbit/s and 40Gbit/s bit-rates where the measurement range for both 10Gbit/s and 40Gbit/s systems can be extracted. For a 10Gbit/s system, the RCP curve is monotonic between 0 and 700ps/nm; which represents a range of 41km of SMF. For a 40Gbit/s system, the RCP curve is monotonic between 0 and 42ps/nm; which represents a range of 2.5km of SMF (assuming *D=17ps/(nm.km)*, which is in-line with the theoretical expectations and the fact that the fourfold increase in bandwidth decreases the dispersion range by a factor of 16 (see chapter 2, section 1.3).

Figure 3-3 shows the schematic used to monitor the clock tone power as described in [PAR'02b]. A portion of the optical signal is tapped and fed into the CD Monitor. The optical signal is converted into an electrical signal using a high speed photodiode (PD). The electrical signal is split into 2 signals. The low pass filter (LPF) is used to measure the DC component of the signal, while the band-pass filter (BPF) and the high speed power detector are used to measure the power of the clock tone. Each component (LPF and high speed power detector) provides, respectively, an analog DC voltage V_0 and V_1. The comparator determines the relative clock power (RCP), defined as the ratio of the clock power to the DC power (V_1/V_0). The RCP signal, being proportional to the chromatic dispersion of the optical signal, can be fed into a tuneable compensator device (TCD).

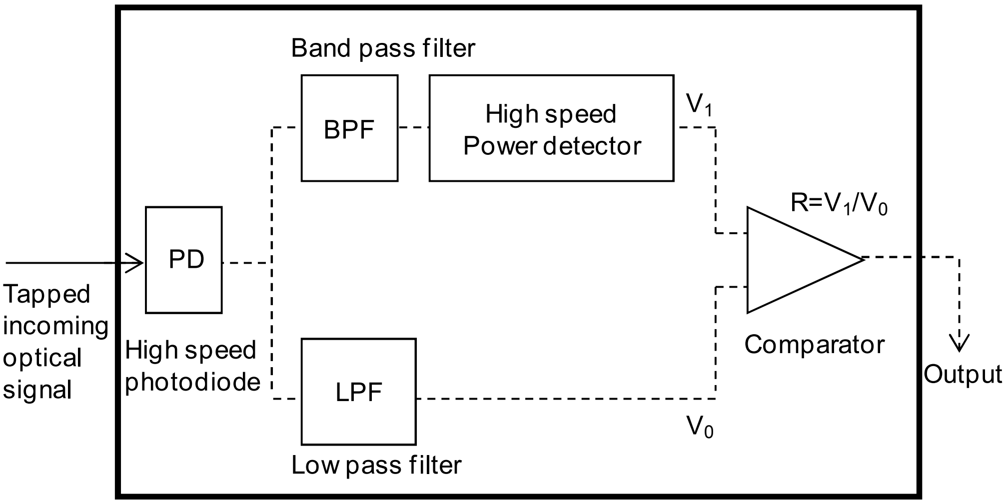

Figure 3-3: Principle of a CD Monitor based on clock power detection. BPF/LPF: band/low pass filter, PD: high speed photodiode, solid line: optical signal, dashed line: electrical signal [PAR'02b].

This technique has been used for various optical formats such as NRZ, RZ and CSRZ. Results show that the range obtained for 10Gbit/s systems is ±640ps/nm for an RZ modulation format, which agrees with the theoretical limit of 624ps/nm [PAN'01].

In an effort to increase the measurement range for 40Gbit/s systems, some research has been carried out on biased CD monitors. This method involves biasing the signal with additional CD inside the monitor (thus not affecting the inline data). The bias amount is chosen such as the measurement range is shifted from the first to the second monotonic segment of the RCP curve (see Figure 3-1). This technique has been applied to a CSRZ modulation format. The monitoring range was extended from 30ps/nm to 48ps/nm which represents a 50% improvement [MOT'04].

PMD monitoring

When transmitting a DSB signal, the detected RF power at the clock frequency results from the beating of both sidebands with the carrier. As seen in the previous section, this phenomenon is used to monitor the accumulated chromatic dispersion in the signal. However, for a single sideband (SSB) signal, the detected RF power at the clock frequency results from the beating of only one side-band with the carrier [MOT’02]. In this case, the RF power is insensitive to the accumulated chromatic dispersion, but is sensitive to the polarisation mode dispersion (PMD) in the link, and can hence be used to detect and measure PMD.

PMD causes different delays for different polarisations. Due to the fibre birefringence, the clock tone splits into two principal states of polarizations (PSPs). Each split tone travels at a different speed, leading to a time delay between them. When analysing a SSB, both split tones interfere with the carrier. The RF power of the clock tone is then proportional to the phase difference between the two split tones, which makes it proportional to the differential group delay (DGD) of the signal. In this scheme, the transmitted signal is DSB, however, in order to suppress the CD impact on the RF clock power, a SSB is analysed in the PMD monitor. The SSB signal is generated by using an optical filter centred at the clock frequency.

The theoretical maximum differential group delay (DGD) monitoring range, for a phase shift of π, is given by (see chapter 2, section 1.4):

$$DGD_{\max} = \frac{1}{2B} \tag{3.2}$$

where B is the bit-rate.

For 10Gbit/s and 40Gbit/s systems, the monitoring ranges correspond respectively to 50ps and 12.5ps. Figure 3-4 shows the schematic used to monitor the clock tone power as described in [LUO’04] for PMD monitoring. A portion of the optical signal is tapped and fed into the PMD Monitor. A single sideband (SSB) optical band-pass filter, centred on the upper clock component, is placed before a photodiode. Higher order Gaussian filters have shown to present better results than a first order filter. The 3dB bandwidth of this filter is around 80% of the bit-rate (e.g. 8GHz for a 10Gbit/s system). The RF power at the bit-rate is measured for a SSB in order to monitor the PMD [YU’03]. It is noted that monitors using notch filters have shown greater suppression of the other side-band than when using SSB filter [MOT’04b].

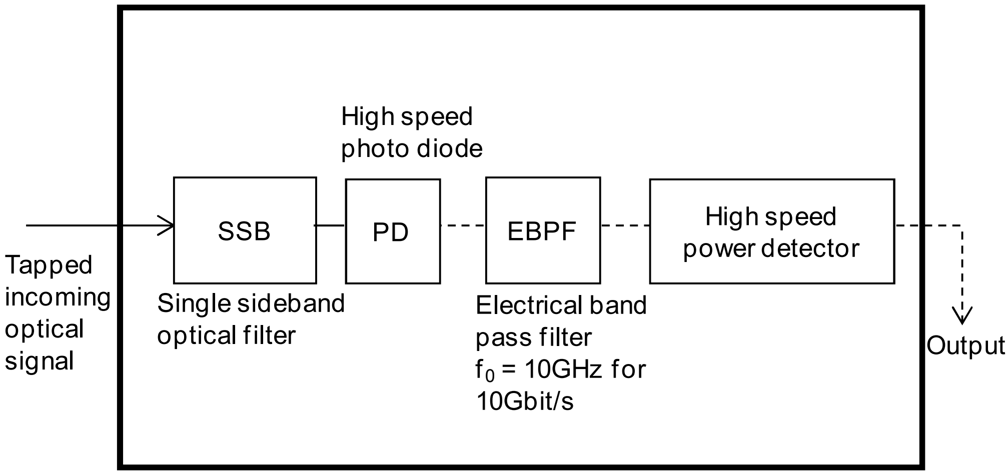

Figure 3-4: Principle of a PMD Monitor based on clock power detection for a 10Gbit/s system, RZ format. Solid line: optical signal, dashed line: electrical signal [LUO'04].

The setup, shown in Figure 3-4, can also be used for an NRZ modulation format. If the incoming signal has been fully compensated for dispersion, the NRZ signal will not have any power at the clock frequency. Chromatic dispersion amplifies the clock in the electrical spectrum of a DSB NRZ signal. Using this property, a linearly chirped fibre Bragg grating (FBG) is added before the SSB filter to regenerate the clock. This method is however sensitive to CD fluctuations. In order to get maximum clock tone generation, the chromatic dispersion of the FBG is chosen using Eq. (3.1). It is noted that this amount is mainly dependent on the bit-rate (B) and wavelength (λ) [MOT'04b]. As an example, in a 10Gbit/s system and considering a wavelength of 1550nm, around 630ps/nm of added dispersion results in a maximally generated clock which makes PMD effect most visible.

These techniques have been used for two optical formats: NRZ and RZ, at 10Gbit/s [MOT'04b]. Simulation results show that these techniques can also be used in 40Gbit/s systems [LUO'04]. Previous results demonstrate a DGD monitoring range in a 10Gbit/s system of 50ps [MOT'04b], which represents 50% of the bit duration (100ps). Another experiment reported a 40±2ps range and accuracy for a 20Gbit/s NRZ signal where the RF power was measured at the frequency of 9.814GHz [PAR'02].

In typical SMF, the PMD parameter (D_p) is around 0.1ps/km$^{0.5}$, whereas in legacy SMF fibre, it can reach 1ps/km$^{0.5}$. In the long-length regime [KOG'02], a transmission link of 250,000km is necessary to accumulate 50ps DGD. The PMD effect changes stochastically with time; this can lead to higher time delay between the 2 polarisation components. However, the measurement range of 50ps is usually sufficient for applications where transmission links are below 500km. For a 40Gbit/s system, simulation results achieved a monitoring range of 8ps [LUO'04]. This range represents 32% of the bit duration (25ps), and is also adequate for applications where transmission links are below 500km.

3.2.2 Clock phase detection for CD monitoring

CD monitoring

The clock phase detection technique has been used for chromatic dispersion monitoring. The accumulated chromatic dispersion induces a time delay between both SSBs. This time delay is translated into a phase difference. The aim of this method is to determine the phase difference between both SSBs in order to determine the chromatic dispersion. This method has been applied to NRZ and RZ modulation formats at 40Gbit/s bit-rates [YU'02].

Figure 3-5 shows the schematic used to monitor the clock tone phase as described in [YU'02] for CD monitoring using a single side-band optical filtering technique. Both NRZ and RZ formats have 2 optical sidebands that carry the same data. A tunable filter is used to extract the upper then lower SSB. The clock, which is always recovered at the receiver, is used as a reference signal for the phase-sensitive detection. This involves measuring the phase difference between each SSB and the recovered clock signal. The cumulated phase difference is proportional to the relative group delay caused by the chromatic dispersion.

A portion of the optical signal is tapped and fed into the CD Monitor. A tuneable SSB filter is first centred near the USB. The frequency detuning can be chosen between 50% and 80% of the bit-rate with a bandwidth equal to the bit-rate. At 40Gbit/s, the filter central frequency is chosen between 20 and 32GHz and its bandwidth equal to 40GHz. This allows the selection of the USB clock tone and the carrier. A phase detector is used to determine the phase difference between the USB and the recovered clock signal. The tuneable SSB filter is detuned to select the LSB. A second phase measurement is done between the LSB and the recovered clock signal. The phase shift between the two SSB signals is proportional to the relative group delay caused by the chromatic dispersion.

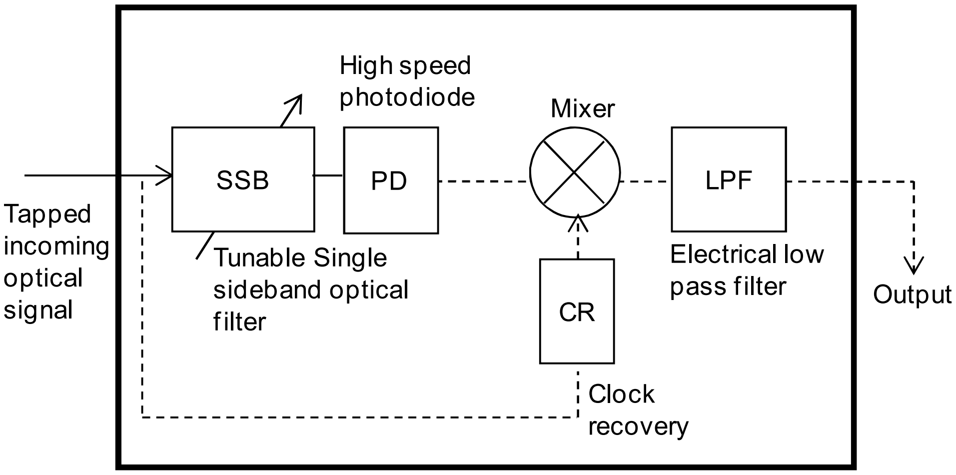

Figure 3-5: Principle of the CD Monitor based on clock phase detection for 40Gbit/s system. Solid line: optical signal, dashed line: electrical signal [YU'02].

The accumulated chromatic dispersion that was monitored using this technique was around 70ps/nm [YU’02]. This range represents 4km of SMF assuming a dispersion value of 17ps/(nm.km).

3.2.3 Comparison between the clock power and phase detection techniques

The RF spectrum analysis techniques based on clock power and phase detection have been investigated. They have both been used for CD monitoring while only the clock power detection technique was used for PMD monitoring.

	RF spectrum analysis using clock tone detection		
	Ck power detection		**Ck phase detection**
Impairment	CD	PMD	CD
WDM	No	No	No
Range at 10Gbit/s	±640 ps/nm [PAN’01]	50ps [MOT’02, MOT’04b, LUO’04, YU’03] 40±2ps [PAR’02]	
Range at 40Gbit/s	48±2ps/nm [MOT’04]	8ps [LUO’04]	70±3ps/nm [YU’02]
Time response	Potentially sub µs	Potentially sub µs	Potentially sub µs
Bit rate dependent	Yes	Yes	Yes
Format dependent	Yes	Yes	Yes
Modulation format used	NRZ, RZ, CSRZ	NRZ, RZ	NRZ, RZ
Require Tx modification	No	No	No

Table 3-1: Summary of the reported results for the RF spectrum analysis techniques using clock power and phase detection.

Table 3-1 shows the summary of the various results presented in the previous section. The CD and PMD can only be monitored independently using a single sideband configuration, although these measurements cannot be done simultaneously. Another limitation is the fact that these techniques can only monitor one wavelength at a time. A WDM link that contains N channels would require N monitors for simultaneous monitoring, which may have a negative impact on the cost. The CD and PMD monitors contain a number of high speed components (PD) which are associated with high cost. In addition, the phase measurements require clock recovery; this method can only be deployed within a node where there is an optical-to-electrical-to-optical (O-E-O) function. Both techniques have large measurement range. Despite the fact that both techniques show similar measurement accuracies, it is expected that the phase measurements provide better accuracies compared to the power measurement. This is due to the fact the clock tone power is not only sensitive to dispersion but also to power fluctuations, which is not the case for the phase measurements. These techniques can also potentially have a very fast response time in the order of sub μs. This is due to the use of high speed components such as a photodiode and a power detector to monitor the clock power which can be at 10Gbit/s or 40Gbit/s. This represents a great advantage over the other monitoring methods such as the optical spectrum and sampling techniques that are considerably slower. They are also non-intrusive and do not require transmitter modification, but are not network agnostic since they are both bit-rate and modulation format dependent. Overall, the phase measurement is a more complex method compared to the power measurement, but should provide a better dispersion accuracy since it is not sensitive to power fluctuations. It is however noted that none of the two methods allow for measurement of the OSNR.

3.3 RF spectrum analysis using pilot tones detection techniques

In this section, we describe RF spectrum analysis techniques using pilot tones for monitoring purposes. A pilot tone is defined as a frequency component that has been added to the modulated signal. Typically, this frequency component has stronger amplitude than the adjacent tones of the signal. When transmitting a DSB signal over a fibre, the frequency dependent fibre dispersion creates a phase shift between both sidebands, thereby causing a RF power fading at the receiver. This fading effect is a function of the pilot tone frequency, the fibre length, the CD and is also a function of PMD. Two methods are described, the first based on amplitude modulation (AM) of the pilot tone [HAM’97,DIM’00, BEN’00, PET’02, MOT’04d, JI’04], the second method based on phase modulation (PM) [TOM’94, TOM’97]. An amplitude modulated pilot tone can be generated by either dithering the bias current of the laser or by biasing the voltage of an intensity modulator; whereas the phase modulated pilot tone is generated using a phase modulator.

Pilot tones can be added to and extracted from any node in the network. The AM pilot tone can be a measure of numerous parameters such as optical power, wavelength, optical path, OSNR, CD [PET’01, KUW’02] and PMD [MOT’04c, JI’04, MOT’04d] whereas the PM pilot tone has been investigated for CD monitoring [JI’04]. The tone follows the optical carrier during the propagation through the fibre and is subject to the same effects as the optical carrier. The tone amplitude is a direct measure of the optical power. In a WDM system, a different tone frequency can be attributed to each channel. At each node, the tone's extraction can be an indication of the channel (wavelength) and the optical path. More complex configurations are used to extract the OSNR, CD and PMD. In the case of dispersion monitoring, the tone amplitude can be used as a feed-back signal to an inline tunable dispersion compensator.

These techniques present several limitations: they require transmitter modification; the pilot tone can superimpose an unwanted modulation on the data and deteriorates the BER at the receiver. In addition, both effects of CD and PMD are not independent in this measurement and thus lead to measurement errors. In order to separate these effects, the use of PM tones for CD measurement has been proposed with a SSB setup to suppress the CD effect on PMD monitoring.

However, the main advantages of the pilot tone techniques rely on the fact that the pilot tone frequency can be chosen (and is bit-rate independent), whereas the clock detection method relies on the clock frequency which is determined by the bit-rate and is format dependent. Choosing the tone frequency gives flexibility in finding a compromise between the monitoring range and the measurement sensitivity.

3.3.1 Pilot tone amplitude modulation for CD, PMD and OSNR monitoring

In this section, the amplitude modulated (AM) pilot tone technique is described. This involves adding an amplitude modulated subcarrier to the base-band data. The RF spectrum of such signal will contain data at the carrier frequency and the pilot tone. This method can be used for optical power, wavelength, OSNR, CD and PMD monitoring. The following sections describe the CD, PMD and noise measurements.

Figure 3-6 shows the general schematic for generating an amplitude modulated pilot tone. The output of the laser is modulated using an intensity modulator. The latter is driven by a signal containing both the data at the bit-rate and the pilot tone. It is noted that the pilot tone does not carry any data.

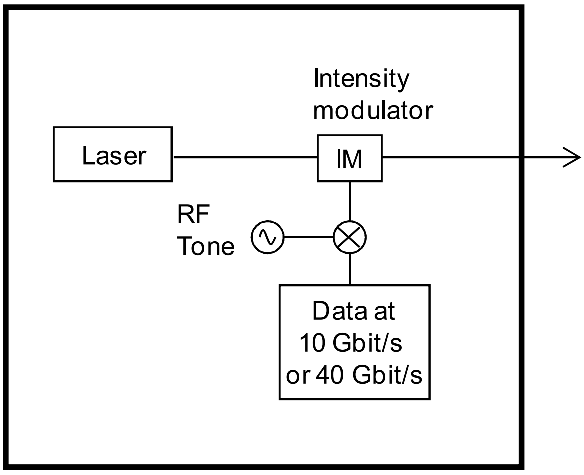

Figure 3-6: General schematic for an amplitude modulated pilot tone generation technique.

CD monitoring

A sinusoidal signal (the tone) is added to the data using an optical intensity modulator such as a Lithium Niobate (LiNbO3) Mach-Zehnder. The tone does not carry any data and its only function is for monitoring. After transmission, the RF tone power is extracted in the monitor. The magnitude of the AM pilot tone is proportional to the accumulated dispersion [DIM'00]. However, the pilot tone amplitude can also be affected by PMD. As shown in Figure 3-7 (see also clock detection techniques), the phase difference between the lower and upper sidebands of the optical signal changes with dispersion. After square law detection, the interference between the two sidebands causes change in amplitude of the RF pilot tone [WIL'99].

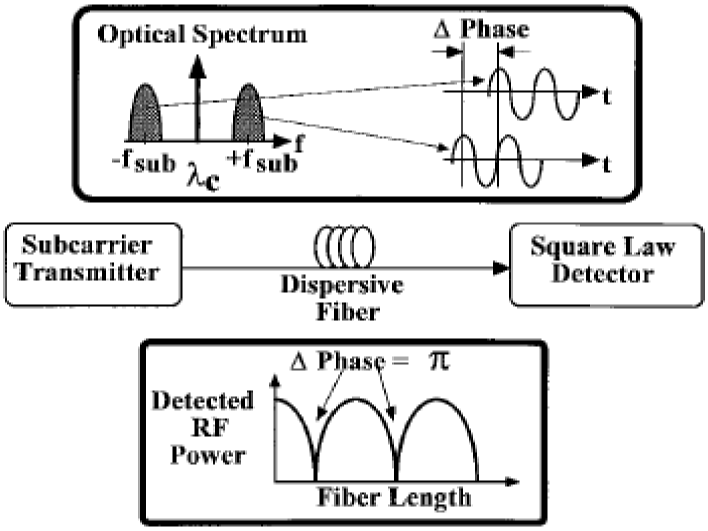

Figure 3-7: RF power fading of double-sideband transmission in a fibre link due to dispersion, taken from [WIL'99].

The electrical power of the received AM tone is a function of dispersion and is described as follows [PAR'03]:

$$P_{AM} \propto m^2 \cos^2(\frac{\pi D L \lambda^2 f_{pt}^2}{c}) \tag{3.3}$$

where m is the intensity modulation index; D the dispersion parameter; L the fibre length; λ the wavelength; f_{pt} the tone frequency and c the light velocity.

This equation shows that the magnitude of the AM pilot tones (which is proportional to the fibre length) decreases as the dispersion increases. The accuracy of this technique ($\Delta P_{AM} / \Delta(DL)$) can be improved by increasing the tone frequency, but this would reduce the measurement range. Thus the tone frequency should be optimized to obtain both acceptable measurement range and accuracy. The received power will reach a null value for a CD value equal to GVD_{max} [ROS'00]:

$$GVD_{\max} = \frac{c}{2\lambda_0^2 f_{pt}^2} \tag{3.4}$$

Where GVD_{max} is the maximum monitoring range.

This value corresponds to the maximum unambiguous monitoring range of the technique. It is noted that this expression is bit-rate independent. It has been shown in [ROS'00, PET'01, PET'02] that using a tone frequency of 8GHz provides a measurement range of 1000ps/nm at 10Gbit/s NRZ system, with a negligible impact on the power penalty (<0.5dB) for data recovery. The dispersion compensation of a CSRZ signal in a 40Gbit/s system has been investigated [KUW'02]. Using a 1GHz tone, a range of approximately -800 to +700ps/nm has been achieved.

PMD monitoring

AM pilot tone methods have been used for PMD monitoring [WIL'99]. It has been shown that the AM pilot tone amplitude is proportional to PMD. The pilot tone frequency is determined at the transmitter level. The maximum DGD measurement range (DGD_{max}), using either DSB or SSB methods, is bit-rate independent and is given by [MOT'04c]:

$$DGD_{\max} = \frac{1}{2f_{pt}} \tag{3.5}$$

where f_{pt} is the pilot tone frequency.

The RF spectrum of a transmitted optical signal through an optical fibre with PMD is detected, and the pilot tone power is described as follows [PAR'02, JI'04].

$$P \propto 1 - 4\gamma(1-\gamma)\sin^2(\pi f_{pt} DGD) \qquad (3.6)$$

where P is the pilot tone power, γ the DGD power ratio between the fast and slow axis and f_{pt} the pilot tone frequency.

This equation shows that the tone amplitude is inversely proportional to the DGD which has been experimentally verified in [JI'04]. Figure 3-8 shows the pilot tone amplitude as a function of the tone frequency for different values of DGD. For a 10GHz pilot tone, the maximum measurement range is 50ps. It has been shown that increasing the tone frequency reduces the monitoring range but improves the resolution (ΔP/Δ(DGD)) of the technique.

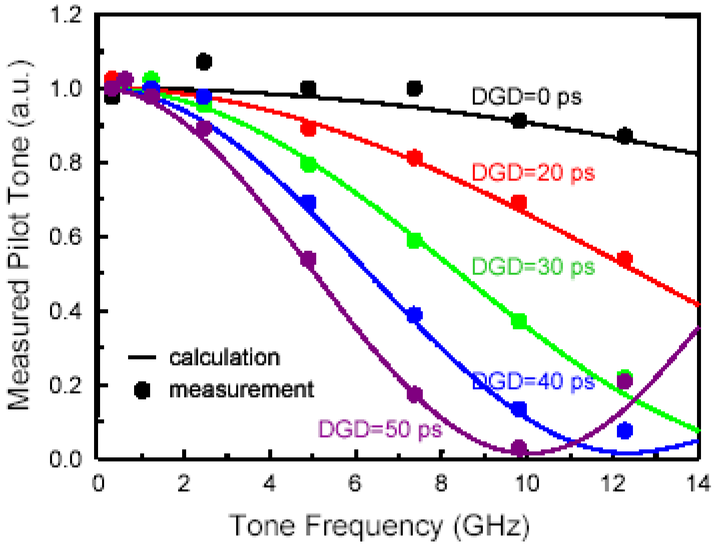

Figure 3-8: Experimental and analytical results of the pilot tone amplitude as a function of the tone frequency for multiple values of DGD, taken from [JI'04].

Pilot tones for PMD monitoring based on DSB setups are very sensitive to CD. The presence of CD changes the phase between both optical sidebands which modifies the tone power and deteriorates the DGD accuracy. This problem can be solved by measuring the tone power of a SSB [MOT'04c]. The SSB pilot tone is then inherently insensitive to CD since it has only one sideband and both polarisation components within the single sideband experience the same CD. The advantage of a SSB implementation over a DSB one has also been experimentally demonstrated in [JI'04]. Figure 3-9 shows the pilot tone amplitude as a function of DGD for both a DSB and SSB implementation. It can be seen that a dispersion of 680ps/nm introduces a 25dB error on the tone power for a DSB setup and only 4dB in a SSB setup.

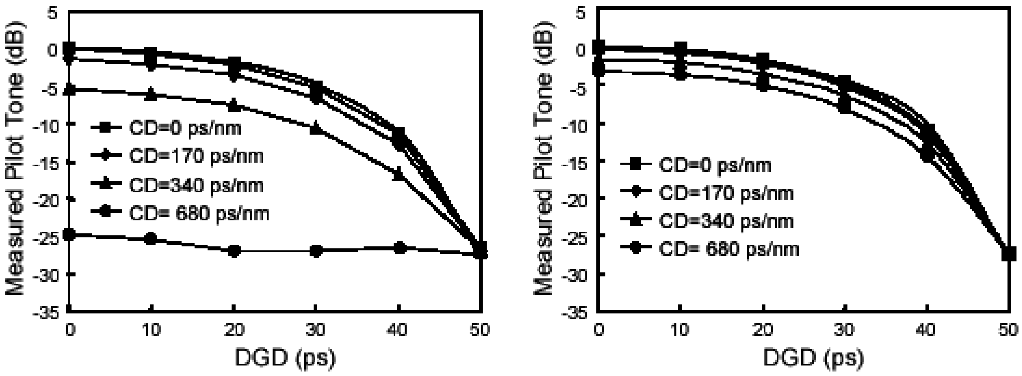

(a) (b)

Figure 3-9:: Experimental results of the pilot tone amplitude as a function of DGD for (a) a DSB implementation and (b) a SSB implementation, taken from [JI'04].

The data and pilot tone are considered to be completely linearly polarised waves with a degree of polarization (DOP) equal to the unity. The presence of PMD will degrade the DOP as the waves propagate along the fibre [KAO'93]. Figure 3-10 shows the DOP as a function of DGD for a 20GHz pilot tone with three different intensity modulations (*m*). The DGD_{max} corresponds to the minimum DOP value obtained in the graph shown below corresponding to the first monotonical segment of the curve, which is equal to 20ps. It is noted that this measurement range is independent of the setup (DSB or SSB). It has also been shown that the DOP sensitivity is dependent on the modulation depth of the tone [MOT'04d].

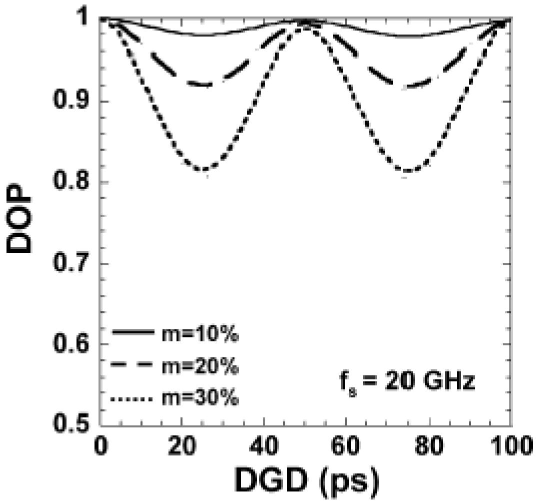

Figure 3-10: Simulation results showing the degree of polarisation (DOP) as a function of DGD for a 20 GHz pilot tone with varying modulation depth, taken from [MOT'04d].

OSNR monitoring

The pilot tone technique is a simple but powerful method to supervise individual wavelength channels along the optical path [HIL'93].

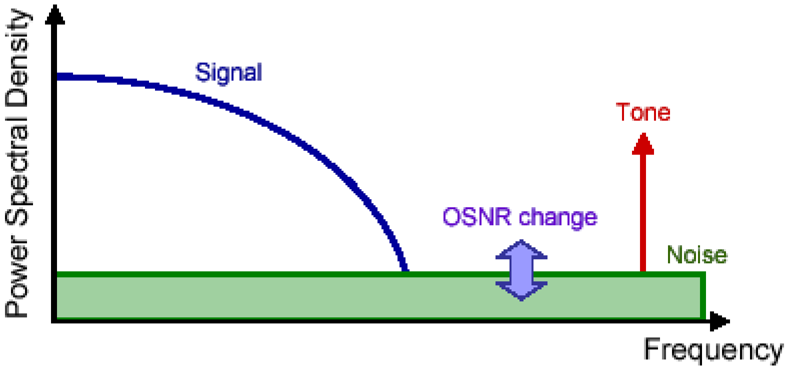

Figure 3-11: Principle of pilot tone based OSNR monitoring technique, taken from [JI'04].

By monitoring the pilot tone's amplitude, parameters such as OSNR can be extracted. This method consists of adding a tone in the tens of kHz to MHz regime [BEN'00] to the optical signal by directly modulating the bias current going to the laser or by adding high frequency pilot tones (GHz) placed outside the data's bandwidth (see Figure 3-11). In this case, the OSNR is estimated by measuring the carrier-to-noise ratio (CNR) of the pilot tone. This is indeed possible as the tone is based outside the signal's bandwidth.

It has been shown that for an OSNR level less than 30dB, the pilot tone method gives the same results as an OSA instrument. However, the pilot tone performance is affected by the number of wavelengths operating in the network, the tone frequencies used and the modulation index [HAM'97]. The most suitable tone frequency is still an open issue. Typically, frequencies from the EDFA cut-off (tens of KHz) to few MHz have been used to minimise the slow dynamic properties of EDFAs and the payload channel penalty [BEN'00]. The OSNR monitoring using high frequencies (GHz) presents two main limitations: The first is that the tone's amplitude (thus the CNR) is affected by chromatic dispersion and PMD, the second limitation is that high frequency tones that are located outside the data's bandwidth can be attenuated by the various optical filters that the signal passes through. Both of these limitations cause inaccuracies of the OSNR measurement.

3.3.2 Pilot tone phase modulation for CD monitoring

In this section, the phase modulated (PM) pilot tone technique is described. This involves adding a phase modulation to the data. This method has been used for CD monitoring. Figure 3-12 shows the general schematic for generating a phase modulated pilot tone. The output of a laser is modulated at the bit-rate using an intensity modulator to generate the data while a phase modulator is used to generate the PM pilot tone. The resultant phase modulation is converted into amplitude modulation

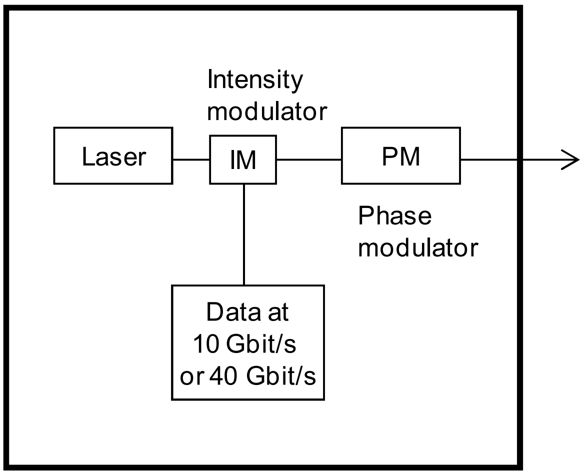

Figure 3-12: General schematic for a phase modulated pilot tone generation technique.

CD monitoring

The phase modulation to amplitude modulation (PM-AM) conversion effect is theoretically described in [CHR'86]. Using a sinusoidally phase modulated data source, this effect can be used for chromatic dispersion measurement [TOM'94]. However, the PM-AM method only gives the absolute value of dispersion; to determine its polarity, some parameters such as the wavelength have to be dithered.

Before transmission, the data phase is modulated at the tone frequency; its electrical field can be described as follows:

$$E(t) = E_0 \exp\left(i\left(2\pi f_0 t + b\sin\left(2\pi f_{pt} t\right)\right)\right) \tag{3.7}$$

where $E(t)$ is the electrical field after the phase modulation; E_0 the electrical field amplitude, f_0 the electrical field optical frequency; b the modulation index and f_{pt} the pilot tone modulation frequency. The power of the tone is proportional to the dispersion following this expression [JI'04]:

$$P_{PM} \propto J_0^2(b) J_1^2(b) \sin^2\left(\frac{\pi D L \lambda^2 f_{pt}^2}{c}\right) \tag{3.8}$$

where J_0 and J_1 are respectively the first kind Bessel functions of order 0 and 1; D the dispersion parameter; L the fibre length, λ the wavelength; f_{pt} the pilot tone frequency and c the light velocity. This equation shows that the magnitude of the AM component generated by the PM-AM conversion increases with CD even when the tone operates in the low frequency region [TOM'97]. As with the AM tones monitoring, the monitoring range may be increased by decreasing the modulation frequency at the expense of worsening the monitoring resolution.

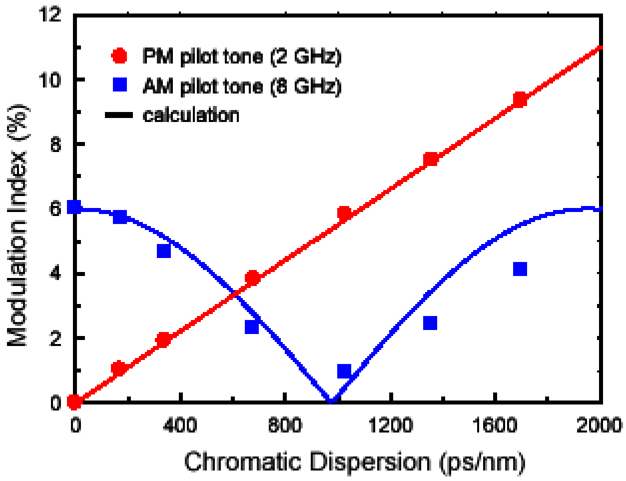

Figure 3-13: Comparison between AM and PM pilot tones methods for CD monitoring. Modulation index of pilot tone measured at the receiver while varying the CD, taken from [JI'04].

Figure 3-13 shows the modulation index as a function of chromatic dispersion for the PM and AM pilot tones. The frequency of the AM pilot tone was set at 8GHz where a measurement range of 1000ps/nm was obtained. By setting the frequency of the PM pilot tone to 2GHz, the accumulated chromatic dispersion that has been monitored using this technique in a 10Gbit/s NRZ system is higher than 15000ps/nm [JI'04].

3.3.3 Comparison between the pilot tone amplitude and phase modulation techniques

The RF spectrum analysis techniques based on pilot tone amplitude and phase modulation have been investigated. They have both been used for CD monitoring while only the pilot tone AM was used for PMD and OSNR monitoring.

Table 3-2 shows the summary of the various results presented in the previous section. Unlike the clock tone techniques where the phase measurements tend to be more accurate than the amplitude measurements, in the pilot tone case, both AM and PM rely on power measurements. This is the case since PM pilot tone techniques rely on PM-AM conversion effect described previously. Both techniques are thus expected to have similar accuracies since they are both sensitive to power fluctuations. Both methods are single channel techniques, while their monitoring range and their time-response is dependent on the pilot tone frequency. They both require transmitter modification, but are network agnostic since they are both bit-rate and modulation format independent. In addition, the phase measurements require time recovery. This method can only be deployed within a node where there is an O-E-O function. Overall, the pilot tone PM is a more complex method compared to the pilot tone AM, and doesn't offer any obvious advantage.

	RF spectrum analysis using pilot tone detection			
	Pilot tone AM			**Pilot tone PM**
Impairment	**CD**	**PMD**	**OSNR**	**CD**
WDM	No	No	No	No
Range at 10Gbit/s	1000ps/nm (f_{pt}=8GHz) [PET'01] -800 to +700ps/nm (f_{pt}=1GHz) [KUW'02]		30dB [BEN'99]	15000±60ps/nm (f_{pt}=2GHz) [JI'04]
Range at 40Gbit/s		75ps (f_{pt}=6.75GHz) [MOT'04c] 50ps (f_{pt}=10GHz) [JI'04] 20ps (f_{pt}=20GHz) [MOT'04d]		
Time response	Dependent on pilot tone freq.	Dependent on pilot tone freq.	Dependent on pilot tone freq.	Dependent on pilot tone freq.
Bit rate dependent	No	No	No	No
Format dependent	No	No	No	No
Require Tx modification	Yes	Yes	Yes	Yes

Table 3-2: Summary of the RF spectrum analysis using pilot tone detection techniques.

3.4 Optical spectrum analysis techniques

Optical methods can provide carrier frequency and optical noise information. The optical spectrum can either be obtained using optical filtering or using homodyne detection. These methods are suitable for multi-channel operation; however, they do not provide any information on CD and PMD. In addition, they tend to be slow; it may take few seconds to obtain the full WDM scan. This is due to the tuning mechanism of the optical filters or of the tuneable laser used in homodyne methods.

3.4.1 Optical spectrum analysis using optical filtering

Optical spectrum analysis using optical filters are mainly based on the approach used in an optical spectrum analysis (OSA). Figure 3-14 shows the general schematic of an OSA based monitor. In this simple technique, the wavelength selection is achieved using a tuneable optical filter, followed by a low-speed photodiode. The filter is tuned over the channels bandwidth while the optical power is recorded. It can be noted that the spectrum resolution is determined by the filter’s bandwidth.

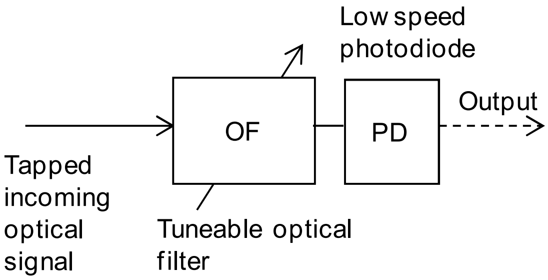

Figure 3-14: General schematic of an OPM based on optical spectrum analysis using optical filtering.

These methods allow for the monitoring of wavelength drift and OSNR. When monitoring a single channel, the out-of-band noise is determined and interpolated to determine the in-band OSNR. This method becomes less accurate as the channel spacing becomes smaller.

3.4.2 Optical spectrum analysis using homodyne techniques

Figure 3-15 shows the general schematic of the homodyne method described in [AMR’00]. The optical spectrum analysis techniques using homodyne technique monitors the same impairments compared to the previous technique using optical filtering. However, unlike with the previous method where the optical spectrum is obtained using simple optical filtering, the homodyne technique is based on the use of a tuneable laser which is mixed with the signal and swept across the channels bandwidth. The interference signal is then detected using low-speed photo-detector generating a pulse signal when both wavelengths (of the tuneable laser and the channel) coincide. The spectrum obtained with this method is proportional to both the optical channel and to the tuneable laser power. The relative power between the optical channel and the adjacent noise level is proportional to OSNR. It is noted that a polarisation scrambler is used after the tuneable laser to avoid any polarisation mismatch with the optical channel. This technique provides a much better resolution compared to the optical filtering technique since the resolution is determined by the laser’s line-width which is few order of magnitude smaller than that of the optical filter’s bandwidth. Its high resolution makes the method suitable for dense WDM systems.

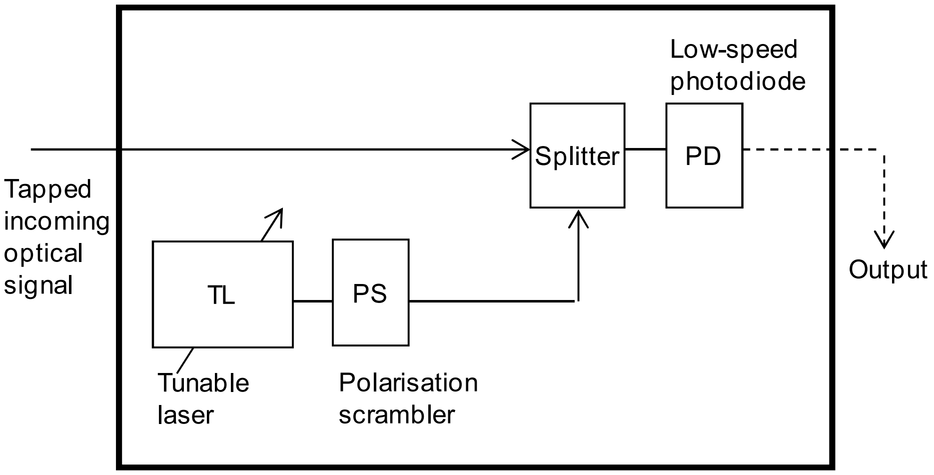

Figure 3-15: General schematic of an OPM based on optical spectrum analysis using homodyne [AMR'00].

3.4.3 Comparison between optical filtering and homodyne techniques

Advantage of the technique

The optical spectrum analysis methods can monitor wavelength drift and OSNR. Among all OPM methods described in this chapter, these methods are the only one that are suitable for WDM systems. This is due to the fact that for both methods, the key optical device (optical filter or laser) is tuneable over the channels bandwidth. In addition, the homodyne method is also applicable to the densely spaced optical channels due to its high spectral resolution. These methods are also network agnostic since they are bit-rate and modulation format independent and do not require transmitter modification.

Limitations of the technique

These techniques do not allow for dispersion measurements, but their key limitation is their speed. The use of a tuneable device provide a full spectrum in a time scale reaching the second, which makes these methods unsuitable for dynamically reconfigurable networks. In addition, the use of a tuneable laser for homodyne methods makes its cost prohibitive.

3.5 Time domain analysis using sampling techniques

Time domain analysis uses sampling techniques and explores the statistical information of an optical signal to derive the histogram and the BER of a transmission channel. Unlike spectral methods, they are sensitive to both distortion and noise effects and can be integrated into a single electronic circuit. However, they may be costly in WDM networks when implemented in every network element since they need demultiplexing and opto-electrical conversion of the signal. In addition, their response time is usually in the order of milliseconds, making these techniques inadequate for future optical packet switching networks.

Sampling methods can be divided into two categories: synchronous and asynchronous. The latter has the advantage of performing sampling without the need for a clock recovery but loses accuracy in impairment monitoring. Synchronous sampling is the closest method to a full BER measurement and can be used to identify and evaluate different sources of degradation such as OSNR, CD and PMD. Sampling can be performed electronically using post-detection decision circuits or optically using an electro-optic sampling module. Post detection (electrical) sampling techniques can be further divided into single decision or dual decision circuits as described below.

It has been shown that the degradation of an optical signal due to dispersion, noise or crosstalk can be detected with high sensitivity by evaluating the amplitude histograms [MUE’98, HAN’99]. It has also been shown that histograms, and especially marks’ histograms, take distinctive shapes (signatures) for each source of degradation. As the perturbations act on the histograms in a distinguishable way, the definition of appropriate signatures should allow fast and reliable estimation of the transmission quality as well as the source of degradation.

The effects of CD, PMD, crosstalk and BER measurements have been confirmed experimentally for synchronous [OHT’99, RIC’01, FIS’01, WRA’02, BEN’05c, BEN’06] and asynchronous techniques [KIK’05, DOD’07] and are discussed in the subsequent sections.

3.5.1 How to generate a histogram

Electrical sampling circuits

Two types of electrical sampling circuits, based on single and dual decision stages, have been used in synchronous sampling techniques.

Single decision electrical sampling circuit

This method derives the mean and standard variation of the marks (ones) and spaces (zeros) of the eye diagram to determine the Q-factor and thus the BER. Histograms can be generated using a single D-type flip-flop as shown in Figure 3-16 [OHT’99]. It consists of a photodiode, a variable decision-threshold circuit and a pulse counter. A clock recovery circuit is used to feed the clock input of the decision circuit. While the threshold level is swept through the eye at decision time (centre of bit), the number of samples that are taken as zeros is counted.

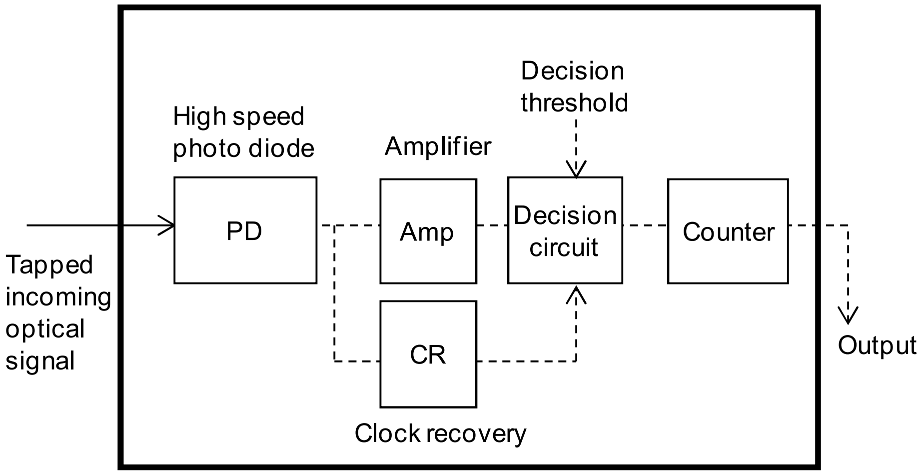

Figure 3-16: Single decision circuit configuration for histogram generation [OHT'99].

Figure 3-17(a) shows the number of samples counted as zero as a function of the decision threshold (v_i). These results have been obtained using a numerical simulation [OHT'99]. It is shown that the result ($F(v_i)$) is a step function whose first derivative ($f(v_i)$) as a function of voltage is taken, also referred to as the probability density function (PDF), and a histogram is obtained.

Figure 3-17(b) shows the signal power distribution $f(v_i)$ as a function of the decision threshold.

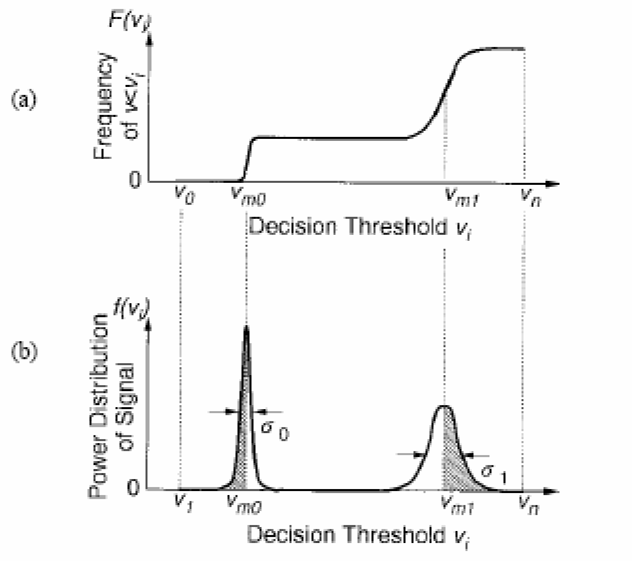

Figure 3-17: (a) Number of spaces against threshold level; (b) Histogram, taken from [OHT'99].

Dual decision electrical sampling circuit

Similarly, the histogram can be obtained using a dual decision circuit [WIE'00] as shown in Figure 3-18. In this configuration, the current from the photodiode is split into two parts; one part is fed into a decision circuit with a fixed (reference) threshold level whereas the other part is fed into a decision circuit that has a variable threshold. The output from the two decision circuits is then fed into an XOR gate. This latter component turns to a high state only when the outputs from the two decision circuits are logically different. Like the single decision circuit, the clock inputs of the two decision circuits are connected to a clock recovery circuit for synchronous sampling.

While the threshold level of one of the decision circuit is swept through the eye, the number of marks (ones) coming from the XOR gate is counted. In other words, the number of times the two decision circuits differ in their judgement (one or zero) is summed over the same decision threshold.

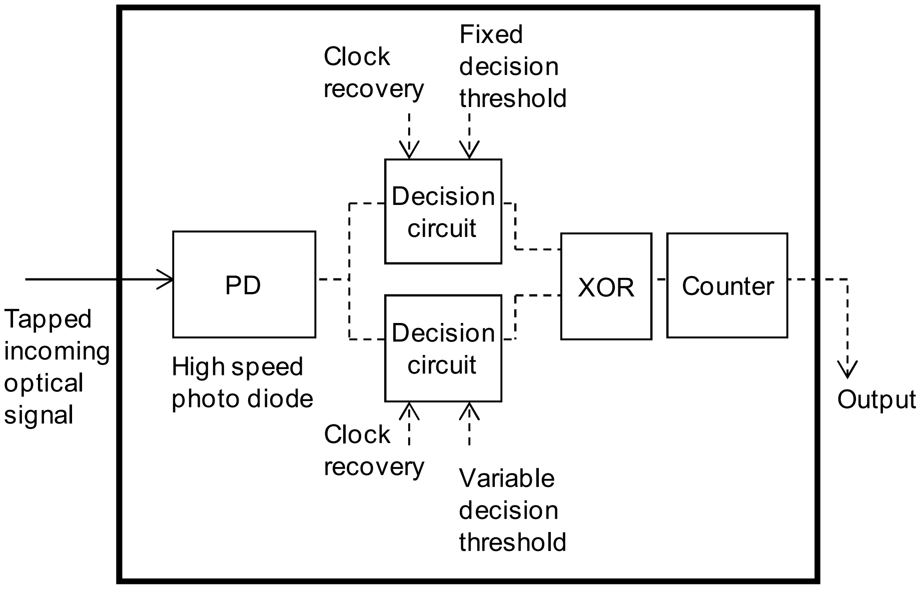

Figure 3-18: Dual decision circuit configuration for histogram generation [WIE'00].

Figure 3-19(b) shows the output of the monitor as a function of the variable threshold. Figure 3-19(a) shows the histogram obtained by taking the absolute value of the first derivative of the graph in Figure 3-19(b).

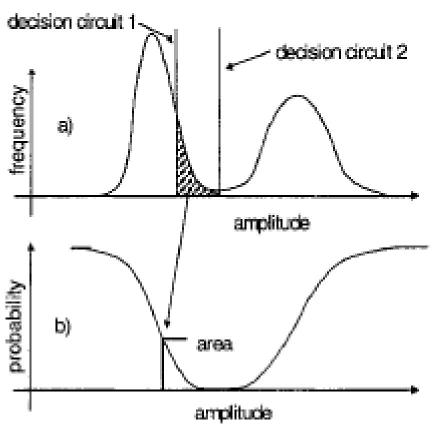

Figure 3-19: (a) Histogram; (b) output measurement of the monitor, taken from [WIE'00].

The advantage of this method over the single decision one is that the number counted by the XOR gate is significantly lower, and therefore a less expensive low frequency counter can be utilised. In addition, the optimum decision level can be determined by extrapolating the graph and the Q-factor and BER can be evaluated using Eq. (3.9) and Eq. (3.10). This method using dual stage decision circuit has been tested to monitor the Q-factor and determine the BER for 10Gbit/s systems [FIS'01, RIC'02] with a measurement time shorter than 1min [RIC'01].

The electrical circuits mentioned in this section, using either a single stage or a dual stage decision circuit, can also be used for asynchronous sampling techniques. This is achieved by replacing the clock signal by an external clock.

Optical sampling circuits

Asynchronous sampling can also be performed in the optical domain by using an electro-optic sampling module. In [SHA'03, SHA'04] an electro-absorption modulator (EAM) was utilised for this purpose.

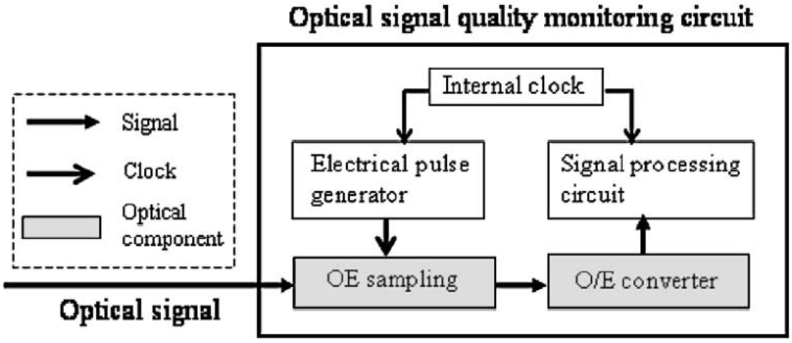

Figure 3-20: Block diagram of an optical sampling circuit, taken from [SHA'03].

Figure 3-20 shows the block diagram of the sampling circuit. The module consists of an EAM, a clock source, an electrical pulse generator, a photo-receiver and a signal processing circuit.

The latter records the amplitude of the signal exiting the optical-to-electrical (O/E) converter against the frequency of occurrence and the histogram is obtained. The advantage of using this technique is that the errors due to the electrical noise of the decision circuits are discarded and a low bandwidth receiver can be used when asynchronous detection is desired.

3.5.2 Synchronous sampling techniques

Bit-error-rate

Using the histograms shown in Figure 3-17(b), the Q-factor can be directly measured. This technique for in-service signal quality monitoring is simple and independent of the signal format. It can be applied to small signal degradation due to coherent crosstalk caused by optical components and to that which cannot be revealed by SNR monitoring [OHT'99]. Using this method, the standard deviation and the mean values of the mark/space rail of the eye pattern are derived. Assuming that the distribution of ASE noise approximates Gaussian distribution, the Q-factor and BER are given by:

$$Q = \frac{\mu_1 - \mu_0}{\sigma_1 + \sigma_0} \tag{3.9}$$

and

$$BER = \tfrac{1}{2} erfc\left(\frac{Q}{\sqrt{2}}\right) \tag{3.10}$$

where μ_1, μ_0 and $\sigma 1$, $\sigma 0$ are the mean and standard deviation of the mark and space levels respectively. However, this method would yield erroneous results in the presence of dominant non-Gaussian degradations, such as crosstalk & inter-symbol interference [LEG'96]. In general these types of impairment are hidden by Gaussian noise and the total PDF appears to be Gaussian. Numerous algorithms were developed to separate these impairments and rectify the BER and Q-factor estimations to take the non-Gaussian components into account.

Chromatic dispersion

The effects of dispersion on synchronous histograms have been investigated. A side sampling technique has been developed to monitor CD independently of PMD (see the following section). Figure 3-21 shows the measured dispersion as a function of the actual dispersion. This method achieved a dispersion range of 1800ps/nm for a 10Gbit/s system and was shown to be resilient to ASE noise [BEN'06].

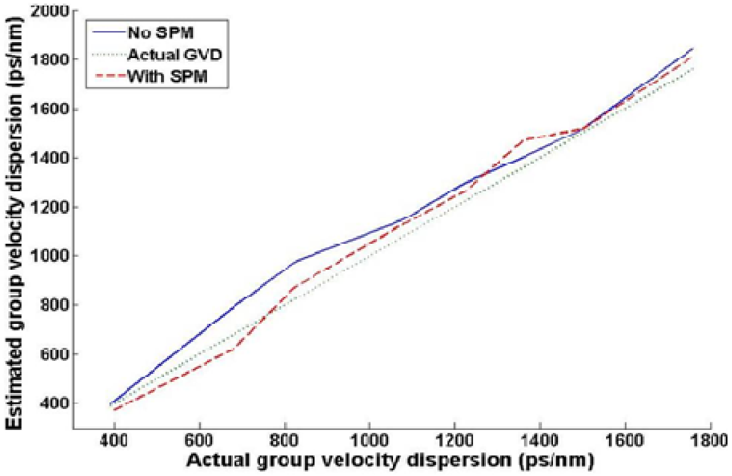

Figure 3-21: Estimated GVD using the side sampling technique, taken from [BEN'06].

Polarisation mode dispersion

The PMD effect on the histogram is very similar to chromatic dispersion and in reality cannot be differentiated. Figure 3-22 shows the observed degradation of the signal eye for a 10Gbit/s NRZ system as the differential group delay is varied between 10 and 40ps [BEN'05]. We note that the PMD effect is, in general, temporally asymmetric where the eye closure of one side is more important than the other one. Only when the power is evenly split between the two principal states of polarisation does the effect become symmetrical and is similar to pulse broadening caused by chromatic dispersion. It can be seen from the above figure that PMD starts by gradually closing one side of the eye before noticing any significant change on the rest of the eye. As the differential group delay increases, the difference in the opening between the left and right hand sides becomes more important and in severe cases DGD will lead to the collapse of the entire eye (Figure 3-22d). In addition, the side of the closure gives further information regarding the distribution of power; if most of the power is travelling in the fast axis then the left side of the eye is affected (our case). Conversely, if most of the power is travelling in the slow axis then the closure comes from the right.

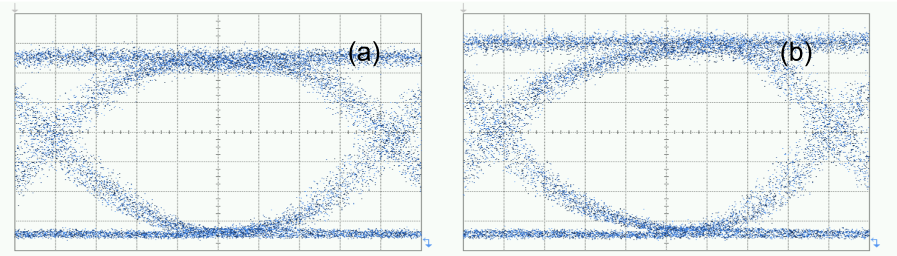

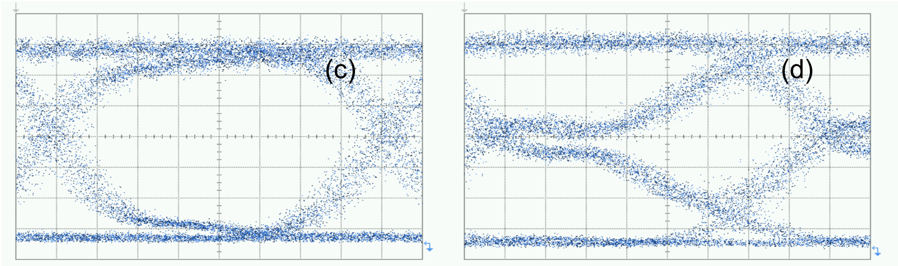

Figure 3-22: Effects of first order PMD on the eye diagram for (a) DGD=10ps, (b) DGD=15ps, (c) DGD=20ps and (d) DGD=40ps, taken from [BEN'05].

Synchronous sampling can be used to detect and estimate PMD by sampling the eye at three different places [BEN'05, BEN'05b]. Based on the observations made in the previous section, a sampling scheme that exploits the distinctive characteristics of the PMD-affected eye was developed in order to monitor PMD in transmission systems. In addition to sampling at the centre of the eye, a fixed delay can be introduced to the clock signal to extract the histograms of both edges as shown in Figure 3-23.

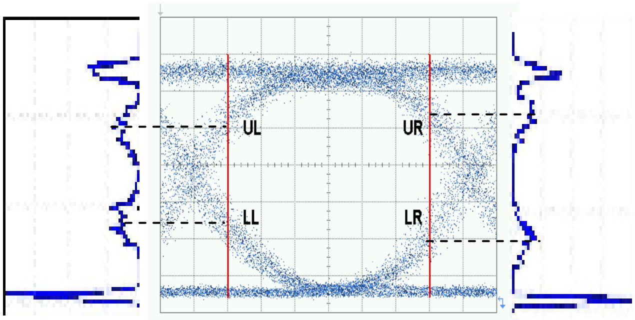

Figure 3-23: Side samplings and histograms of an eye diagram at the upper-left (UL), lower-left (LL), upper-right (UR) and lower-right (LR) points, taken from [BEN'05c].

By performing the three-section eye sampling at both the transmitter and the receiver, information on the differential group delay and power splitting ratio between the two principle states of polarisation can be extracted.

Figure 3-24 shows the measured DGD as a function of the actual DGD [BEN'05c]. The measurement range of this technique was 90ps with a theoretical limit of equal to the bit duration, thus 100ps for 10Gbit/s systems. It can be observed that the error increases when most of the power is concentrated in one state of polarisation, where the power splitting ratio (γ) is equal to 0.1, and decreases when the power is evenly split (γ=0.4-0.5). This is due to the fact that the side samples of the eye diagram, when one polarisation state contains most of the power, change only slightly with increasing DGD, leading to more errors in the estimation. However, when the power is equally split, the rate of change of the side samples, as DGD increases, is important.

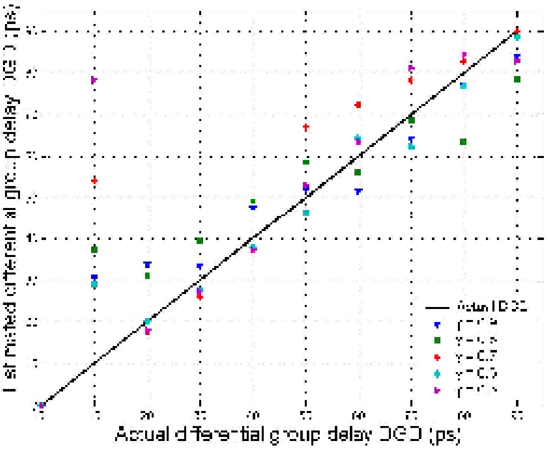

Figure 3-24: DGD measurement using the three-point synchronous sampling technique, taken from [BEN’05c].

This technique has also been used to determine the power splitting ratio in the slow axis. It was observed that for DGD values higher than 20ps, the estimation of the power splitting ratio was very accurate [BEN’05c].

OSNR

OSNR can be obtained from a synchronous histogram by fitting a Gaussian distribution to the PDF of the spaces and the marks [WRA’02]. Figure 3-25 shows the OSNR measured using the proposed technique as a function of the OSNR measured using an OSA. A linear fit of the experimental data provide a slope of 0.98±0.05 for OSNR values ranging from 17 to 32dB after which the distribution of the marks and spaces become too narrow.

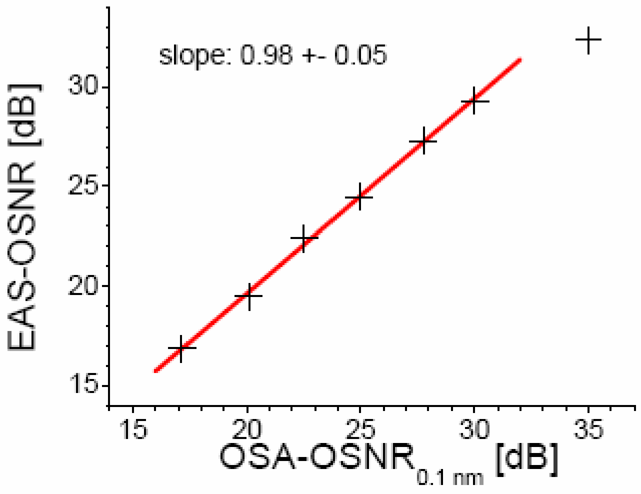

Figure 3-25: OSNR measured using the proposed technique as a function of the OSNR measured using an OSA, taken from [WRA’02].

Crosstalk

The statistical effects of crosstalk on the histogram and especially on the marks' distribution have been extensively studied and lead to an arcsine distribution (U-shape) [LEG'96]. A 5Gbit/s experiment was carried out to determine the effects of in-band crosstalk on the histogram. Figure 3-26 shows the synchronous histogram for different levels of crosstalk [MUE'98]. The crosstalk affects the histogram by introducing a floor around the marks curve.

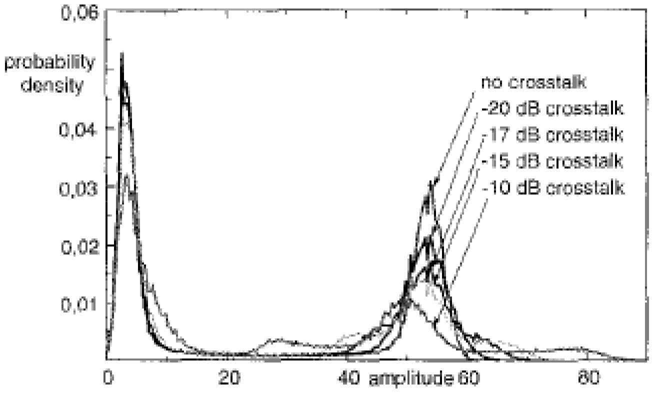

Figure 3-26: Histograms of a 5Gbit/s NRZ signal subject to crosstalk, taken from [MUE'98].

3.5.3 Asynchronous sampling techniques

The key difference in asynchronous sampling compared to synchronous sampling is that the former uses an external clock instead of a clock signal that is recovered from the data signal. This achieves bit-rate transparency and negates the need for an additional clock recovery circuit; however, it has been shown that asynchronous sampling loses monitoring accuracy. The asynchronous histogram is obtained by sampling at a frequency that can either be higher or lower than the bit-rate. In both cases, samples at the transition levels of the eye can be included in the histogram, which creates a floor between the marks and spaces, and is the cause for the loss of monitoring accuracy [AND'04].

Chromatic dispersion

The effects of dispersion on the histogram using a standard single mode fibre in a 5Gbit/s system have been investigated [MUE'98]. The transmitted signal was fed into a recirculating loop of 160km length and the histogram was taken after each round trip. Figure 3-27 shows the histogram of the signal affected by dispersion compared to the signal affected by noise. The effects of dispersion on the distributions are easily observed on the asynchronous histogram. The dominant effect is that the lower peak representing the spaces is shifted to higher amplitudes, and that the range between the marks-mean and spaces-mean is filled due to the increasing intersymbol interference.

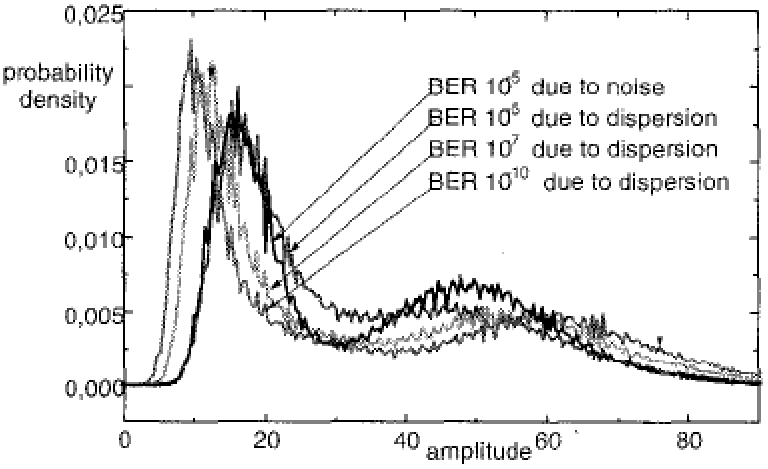

Figure 3-27: Asynchronous histogram of a 5Gbit/s signal affected by dispersion compared to signal affected by noise, taken from [MUE'98].

CD, PMD and OSNR

The effects of dispersion on the histograms using asynchronous sampling techniques in a 10Gbit/s and 40Gbit/s systems have been investigated. It has been shown that histograms derivatives of NRZ based waveforms become minimum and symmetric at zero CD, which can be used as a CD monitoring signals. Figure 3-28 show the third-order derivative of the asynchronous sampled waveform histograms as a function of CD for 10, 20 and 40Gbit/s NRZ signals [KIK'04]. The CD monitoring range achieved in this experiment was equal to ±2000ps/nm for a 10Gbit/s system and ±1300ps/nm for a 40Gbit/s system.

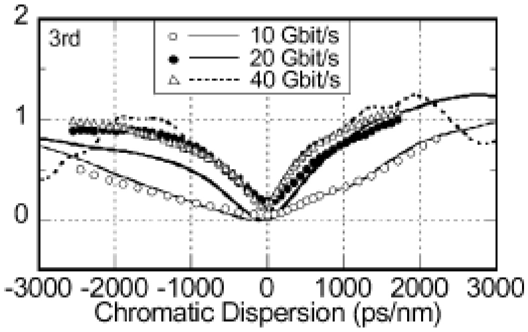

Figure 3-28: Experimental (points) and simulated (curves) of the third order moment of the asynchronous sampled histograms as a function of CD for 10, 20 and 40Gbit's NRZ modulations, taken from [KIK'05].

Various other implementations of asynchronous sampling have been achieved. As an example, one experiments based on asynchronous delay-tap sampling have been investigated in [DOD'07]. By sampling the optical waveform with a known physical delay, information-rich patterns can be extracted without requiring clock recovery. The information content can be further enhanced by varying the delay between the samples. As an example, delays much shorter than the bit period highlight the gradient of the waveform, while delays of around half a bit period emphasize the more general rise and fall times. One bit delays can separate and isolate different bit combinations for analysis. Unique patterns that occur for different ratios of the delay to the bit period offer a means of bit-rate identification. The various amplitude-based modulation formats such as RZ and NRZ also produce different signatures, additionally enabling format identification. By analyzing the phase portraits, what can be extracted not only include the signal quality through Q and jitter, but also the underlying cause of signal degradation, whether it is OSNR, chromatic dispersion, PMD, filter dispersion, or some combination. Figure 3-29 shows the monitoring results for OSNR, CD and first order PMD. The method has demonstrated a CD monitoring range of 1600ps/nm for a 10Gbit/s signal. This technique has also been used for PMD monitoring achieving a 40ps range and for OSNR reaching a 25dB range.

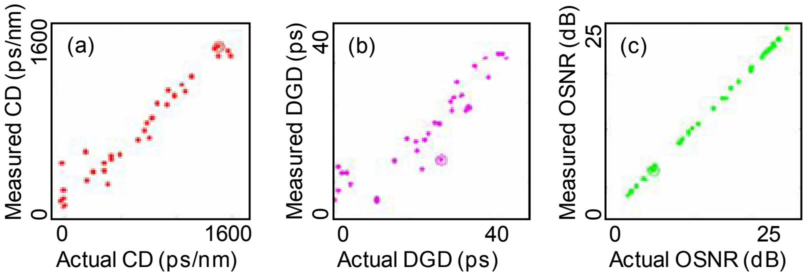

Figure 3-29: Monitor as a function of (a) first order PMD (DGD); (b) CD; (c) OSNR, taken from [DOD'07].

Crosstalk

The effect of crosstalk on histograms obtained with asynchronous sampling techniques has also been investigated [LUI'04]. It has been shown that the crosstalk modify the shape of the marks histogram. By comparing this histogram to a reference one obtained in the absence of impairment, a measure of crosstalk can be achieved.

3.5.4 Comparison between synchronous and asynchronous sampling techniques

The sampling techniques can monitor CD, PMD, OSNR, crosstalk in addition to the BER. CD and PMD can only be monitored independently of each other using the three point sampling technique described previously. The response time of these techniques can be as low as few milliseconds. As a result, these methods are ideal for real-time monitoring in static networks.

	Sampling techniques					
	Synchronous			**Asynchronous**		
Impairment	**CD**	**PMD**	**OSNR**	**CD**	**PMD**	**OSNR**
WDM	No	No	No	No	No	No
Range at 10Gbit/s	1800ps/nm [BEN’06] BER [OHT’99, RIC’01, FIS’01]	90ps [BEN’05c]	17 to 32dB [WRA’02]	±2000ps/nm [KIK’05] 1600ps/nm [DOD’07]	40ps [DOD’07]	25dB [DOD’07]
Range at 40Gbit/s				±1300ps/nm [KIK’05]		
Bit rate dependent	Yes	Yes	Yes	No	No	No
Format dependent	Yes	Yes	Yes	Yes	Yes	Yes
Require Tx modification	No	No	No	No	No	No

Table 3-3: Summary of the monitoring sampling techniques.

The asynchronous sampling techniques retain all advantages of the synchronous sampling techniques; their key advantage is their bit-rate transparency which is achieved by replacing the clock recovery in the monitor with a free running clock which however reduces the impairment accuracy achieved with their counterpart. Both synchronous and asynchronous methods are only able to monitor one single channel, requiring the full duplication of the monitor for additional channels. The measurement range of the PMD with the synchronous method is limited to the bit-rate duration, though this is not considered as a major drawback, in addition, this method is bit-rate and modulation format dependent.

3.6 Tuneable dispersion compensation schemes

Historically, chromatic dispersion has been considered as invariant with time in static networks, for which fixed compensation using, for example, devices such as dispersion compensation fibre (DCF) has been adequate. The use of higher bit-rate (40Gbit/s and above), the increase in the numbers of channels and the migration toward time varying network topologies have all been the major causes in the increase in impairment sensitivity, for which multi-channel and fast tuneable compensation schemes has become relevant.

It is shown in the next section that tuneable compensation schemes go hand-in-hand with OPM devices, the latter providing a control signal for the tuning mechanism of the compensation device. In the subsequent sections, both CD and PMD tuneable compensation devices are described. Their measurement range and tuning speed are also highlighted. It is shown that the compensation schemes are currently less advanced compared to the OPM techniques. This has been the case since most tuneable compensation schemes have a single channel operation, and the ones that achieve multi-channel operation are limited by the same compensation value for all channels (such as with the VIPA). In addition, these schemes possess slow tuning mechanisms (few ms at best) compared to the speed requirements in dynamically reconfigurable networks.

3.6.1 General tuneable compensation scheme

As previously discussed, time-dependent effects, such as network-induced path changes, environmental changes and component changes all contribute to the need for tuneable compensation devices. For changes that occur on the order of milliseconds or faster, a global management system that would tune the compensator remotely may be too slow to react. Instead, each device may require the feedback of a local optical performance monitor (OPM) device, to adapt to new network conditions. The general approach for implementing a dispersion compensator, (either CD or PMD), is based on a feedback signal provided by the OPM, acting on the adaptive compensating element, as shown in Figure 3-30.

It is noted that, unlike for CD and PMD that can be compensated for, impairments due to noise cannot be linearly compensated for, thus OSNR monitoring is often used as an indicator for the signal quality. Depending on the OSNR level, a real-time alarm could be triggered to check the EDFAs, the transmitters and used for intelligent path provisioning and traffic routing.

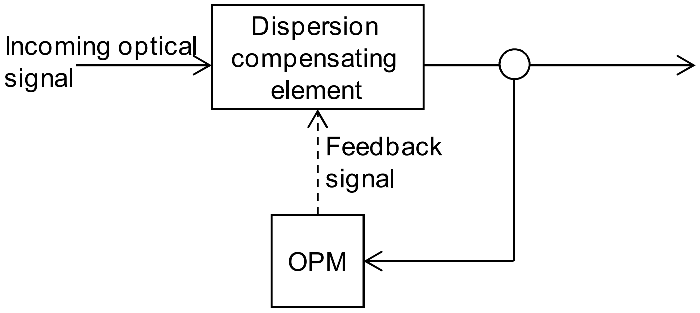

Figure 3-30: General schematic of a dispersion compensating element controlled using a feedback signal from an optical performance monitor (OPM) device. Solid line: optical signal, Dashed line: electrical signal

The following section describes the key mechanisms for CD and PMD compensation, which are thought to be key complementary technologies to OPM techniques.

3.6.2 Chromatic dispersion compensation

Tuneable dispersion compensators are systems that introduce wavelength dependent delays. These devices are used to compensate for the accumulated CD in the network. The implementation of the device can be achieved using multiple Fabry-Perot (FP) cavities, each cavity having a different resonating frequency. Each wavelength travels a different path length to reach its correspondent reflecting cavity. The difference of path length introduces the delay in time and allows for the CD compensation.

Various FP cavities have been implemented to achieve this concept. As an example of the operation of these devices, the commonly used chirped fibre Bragg grating (FBG) is shown in Figure 3-31.

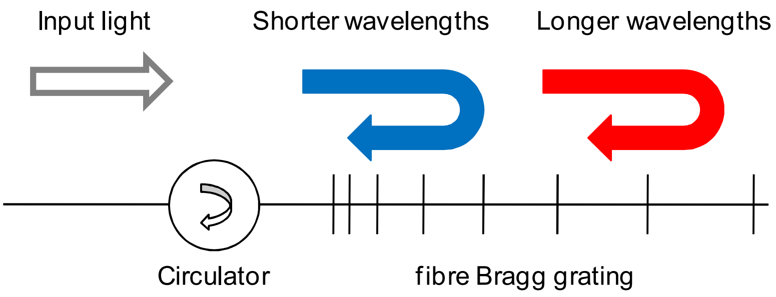

Figure 3-31: Fibre Bragg grating (FBG) diagram depicting the wavelength dependent delay. Each wavelength travels a different path length that introduces a delay in time and allows for the CD compensation.

In a chirped FBG, each wavelength is reflected from a different longitudinal point along the grating structure providing the required wavelength dependent delay. Tuning is achieved by applying strain using a piezo-electric mechanical actuator or thermal gradient which spatially varies the Bragg period. The grating now reflects each wavelength at different points along its length, therefore giving a tuneable wavelength dependent delay.

When assessing the suitability of tuneable dispersion compensators for use in broadband multi-channel and dynamic optical networks, it is necessary to consider the following parameters:

- Single or multi-channel operation and channel spacing
- Tuning speed
- Compensation and tuning range (ps/nm)

- Bandwidth (nm)
- Insertion Loss and PDL

Linearly chirped grating tuning with non-uniform mechanical strain

A linearly chirped grating has a linear response when plotting the delay as a function of wavelength. The concept of this configuration is to change the grating periodicity and the chirp rate, thus changing the dispersion. This is achieved by stretching a uniform grating with a number of independent piezoelectric devices. A linearly increasing voltage is applied to each of these devices. The reported range was from +940 ps/nm to + 8770 ps/nm, with a tuning-speed of the order of ~ 20ms [OHN'97]. Another way to achieve a nonuniform mechanical strain is by bending the uniform grating after having attached it to a cantilever beam. This method presents the advantage of using a single stretching element. The range achieved with this method was -791 ps/nm to +932ps/nm [IMA'98].

Nonlinearly chirped grating tuned with uniform mechanical strain

A nonlinear grating has a chirp represented by a nonlinear curve when plotting the time delay as a function of wavelength. Applying a uniform mechanical strain to such a grating increases the resonant wavelength of each sub cavity; this leads to shifting the chirp curve toward longer wavelengths without altering the grating response. A range of -300 to -1000 ps/nm with a tuning speed of less than 10ms has been reported [FEN'99]. The advantage of this is the use of a single moving part. Similar effect can be obtained by heating uniformly the same type of gratings. A multi-channel dispersion compensator can be obtained using a sampled nonlinearly chirped grating. The sampled grating is obtained by modulating the index of a single channel grating. This device provides an equal dispersion to each channel. The sampled grating preserves all advantages of the single channel grating while allowing multi-channel operation, however, its main disadvantage is the increasing loss (reduced reflectivity) with the number of channels. A multi-channel dispersion compensation has been demonstrated using this device, and a tuning range of -200 to -1200 ps/nm was achieved [CAI'99].

Linearly chirped grating tuning with non-uniform thermal gradients

A thermal heating element with a varying thickness is deposited around and along the grating. The induced thermal gradient will chirp the uniform grating and produce a tunable compensator device [EGG'99]. The reported tuning range is -300 to -1350 ps/nm. The major advantage of this technique is the absence of any moving part. Its main drawback is the slow response (sub second) of the grating to thermal changes.

Tuneable virtually imaged phased array (VIPA)

This solution is a free space device. It contains fixed lenses, one glass plate allowing spatial wavelength distribution and a moving lens and mirror to achieve tuneability. A multi-wavelength light reaches the glass plate, and undergoes multiple reflections inside the plate. A collimated light is formed in the plate, where the output angles depend on the wavelength, thus showing angular dispersion. This output light (with a spatial distribution which is wavelength dependent) is focused via a lens on a moving mirror. The moving mirror creates the relative time delay between all the wavelengths and achieves dispersion compensation. The main advantage of this configuration is that positive or negative dispersion compensation can be achieved. The main disadvantage is the high loss (which can reach 10dB) due to the free space optics. The performance of this method has been demonstrated for 60 channels at 100 GHz spacing and a dispersion range of +/- 2000 ps/nm [SHI'97].

Tuneable ring resonators

Ring resonator of 3.3mm can be used to compensate for up to 15000ps/nm [MAD'98]. The advantage of this technique is that micro ring resonators can be integrated on a chip. However, the main limitations are the free spectral range (FSR) that limits the channel spacing to 10 GHz or less. Increasing the FSR is possible by increasing the ring diameter, which however increases the total loss. This can be overcome by using materials with higher refractive index, thus increasing the FSR without increasing the ring diameter.

Tuneable Mach-Zehnder devices

A tuneable dispersion compensation module was demonstrated using a four-stage Mach-Zehnder (MZ) all-pass architecture. Each MZ contained two phase shifter, one to adjust the power ratio and the other to tune the resonant wavelength. The resulting device had an FSR of 25 GHz, a pass-band of 14 GHz and a dispersion of 1800 ps/nm [MAD'99]. Further improvement of the device provided a dispersion range of +/- 2000 ps/nm [MAD'01].

Planar lightwave circuit (PLC)

Tuneable dispersion compensators can be fabricated on planar lightwave circuits (PLC). One configuration consists in an alternating cascade of symmetrical and asymmetrical Mach-Zehnder interferometers. These interferometers are formed of tuneable couplers and delay arms. This device can compensate for both positive and negative dispersion values and its operational centre frequency can be adjusted to any desirable wavelength. The performance of this configuration has been reported to achieve a range of -681 to +786ps/nm [TAK'96]. Another configuration consists of a PLC containing a high resolution wavelength grating router. A plano-cylindrical lens is attached to the PLC and focuses the light on a deformable mirror. This deformable mirror achieves the dispersion tuneability by changing its curvature. A range of +/- 500 ps/nm has been reported using this configuration [DOE'05].

Electronic compensation

Dispersion compensation devices can be integrated on electronic chips. The signal is detected at the receiver. The dispersion compensation is achieved using electronic filtering and adaptive processing. The electronic equalizers modify the pulse to its initial shape thus compensating for the accumulated dispersion. Electronic compensation is potentially an inexpensive solution for systems with bit rates up to 10 Gbit/s [KIL'05].

Comparison between chromatic dispersion compensation devices

	Tuning range	**Tuning speed**
Linearly chirped grating tuning with non-uniform mechanical strain [OHN'97]	+940 to +8770 ps/nm	~ 20ms
Nonlinearly chirped grating tuned with uniform mechanical strain [FEN'99]	-300 to -1000 ps/nm	< 10ms
Linearly chirped grating tuning with non-uniform thermal gradients [EGG'99]	-300 to -1350 ps/nm	Sub second
Tuneable virtually imaged phased array (VIPA) [SHI'97]	+/-2000 ps/nm	Few seconds
Tuneable ring resonators [MAD'98]	15000 ps/nm	
Tuneable Mach-Zehnder devices [MAD'01]	+/-2000 ps/nm	
Planar lightwave circuit (PLC) [TAK'96]	-681 to +786 ps/nm	

Table 3-4: Summary of the chromatic dispersion compensation devices.

Other tuneable dispersion compensation modules

Several other devices have been investigated to achieve dispersion compensation tuneability:

- All pass optical filter based on Micro-Electro-Mechanical Systems (MEMS) [MAD'00].
- Arrayed waveguide grating [TSU'98].
- Arrayed waveguide devices [TAK'01].

- Mach-Zehnder with thermal phase tuning [TAK'98].
- Chirp tuning of electro-absorption modulators for analog systems [POL'99].
- Spectral holography [AND'01].

3.6.3 Polarisation mode dispersion compensation

Optical fibres manufactured today can have mean PMD coefficients of less than 0.1ps/km$^{1/2}$, however, legacy fibres installed in the 1980s may exhibit PMD coefficients higher than 1ps/km$^{1/2}$ [KOG'02]. Network operators faced with the challenge of upgrading the channel bit-rate on high-PMD links possess a handful of solutions to preserve the signal quality. One solution is to selectively replace those fibre segments in the link, known to be the dominant contributors to the overall link DGD, if they can be identified. A second alternative solution is to regenerate the optical signal by placing back-to-back terminals at the point in the link where the DGD effects approach an intolerable level, thus effectively reducing the optical link length. Another approach is to incorporate an adaptive PMD compensation (PMDC) system. Typical PMDC schemes are effective at minimizing the effects of the first-order PMD and in some cases the second-order PMD. However, both the first and second-order PMDC systems suffer the drawback that they reduce the effects of signal degradation over a very narrow optical bandwidth. This is a significant drawback for DWDM systems. For a long-haul optical link carrying hundreds of wavelengths, a separate PMDC system may be required for each wavelength to provide the desired compensation. PMD compensation can be achieved electrically or optically. One of the electrical methods is based on electronic filtering [WIN'90, BUL'98], which are typically located at the receiver. It is noted that electronic PMDC is not discussed here, this section only provides an overview of the basic building block for optical PMDC scheme that can be located anywhere in the network.

PMDC using polarisation-beam-splitters and a variable time-delay

Optical compensation of first-order PMD can be accomplished by introducing a variable time-delay between two adjustable orthogonal polarisation states in the optical signal [HIE'98, PUA'00, ROS'01]. Figure 2-32 shows the schematic diagram of the PMDC using this technique. The compensator comprises a fast electro-optic polarisation controller (PC) which connects the output of the transmission fibre to the input of a polarisation beam-splitter (PBS). The PC rotates the link's output PSPs to align with the input PSPs of the PBS. The PBS splits the output light into two orthogonally polarised components then a variable delay-line delays these components relative to each other by a variable time $\Delta\tau$ corresponding to the DGD. Finally, a second PBS combines both signals into a single output fibre. If the differential time delay $\Delta\tau$, introduced by the compensator is exactly equal to the DGD of the transmitted signal, then the optical signal after the compensator is completely free of distortions due to first-order PMD.

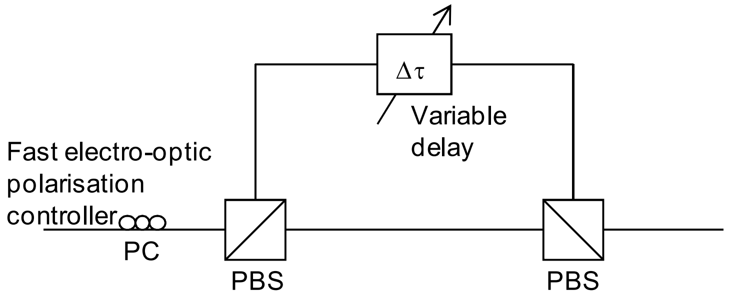

Figure 2-32: PMDC using polarisation-beam-splitters (PBS) and a variable delay [HIE’98].

This scheme is frequency independent and only valid for first-order PMD. For wider bandwidth, higher order effects must be considered resulting in frequency dependent polarisation and dispersion. The bandwidth over which the PSPs can be assumed constant depends on the properties of the fibre and has been shown to vary inversely with the mean DGD [BET’91]. While the minimum bandwidth of the PSPs in SMF was found to always be over 50GHz [BET’91], this bandwidth for standard SMF is of the order of 100GHz [PUA’00].

3.7 Summary

In this chapter, four main advanced OPM techniques have been reviewed. RF spectrum analysis techniques using clock tone and pilot tone detection techniques, optical spectrum analysis techniques and finally sampling techniques.

RF spectrum analysis techniques using clock tone detection present the following characteristics:

- Monitor CD and PMD independently of each other but not simultaneously.
- No OSNR monitoring.
- Posses a large measurements range, dependent on the bit-rate.
- Very fast response time (μs).
- Single channel operation.
- Bit-rate and modulation format dependent.

RF spectrum analysis techniques using pilot tone detection present the following characteristics:

- Monitor CD and PMD independently of each other but not simultaneously.

- Monitor out-of-band OSNR.
- Posses a large measurements range, dependent on the pilot tone frequency.
- Fast response time (μs-ms), dependent on the pilot tone frequency.
- Single channel operation
- Bit-rate independent
- Modulation format independent.
- Require transmitter modification.

Optical spectrum analysis techniques present the following characteristics:

- Monitor OSNR and wavelength drift.
- No CD and PMD monitoring.
- Very slow response time (seconds).
- Multi-channel operation.
- Bit-rate and modulation format independent.

The synchronous and asynchronous sampling methods present the following characteristics:

- Monitor CD, PMD, OSNR, crosstalk and BER.
- Can monitor CD and PMD independently and simultaneously using the three point sampling technique
- Posses a large measurements range.
- Slow response time (sub ms).
- Single channel operation.
- Bit-rate dependent for synchronous sampling.
- Modulation format dependent.

Table 3-5 shows the summary of advanced OPM techniques reported in this chapter. It has been shown that time-dependent effects, such as network-induced path changes, environmental changes and component changes all contribute to the need for tuneable compensation devices. For changes that occur on the order of milliseconds or faster, a global management system that would tune the compensator remotely may be too slow to react. Instead, each device may require the feedback of a local OPM device, to adapt to new network conditions. Both CD and PMD tuneable compensation devices have been described and their measurement range and tuning speed highlighted. It is noted that none of the monitoring techniques and tuneable dispersion compensation devices developed to date have a multi-impairment, multi-channel and fast operation; which is the subject of the work presented in the following chapter that aims at solving the OPM limitations.

	OPM			
	Frequency domain			**Time domain**
	Clock	**Pilot tone**	**OSA**	**Sampling**
Impairments	CD, PMD	CD, PMD, OSNR	OSNR, wavelength drift	CD, PMD, OSNR, Crosstalk, BER
WDM	No	No	Yes	No
Dispersion range	Bit-rate limited For 40Gbit/s: $GVD_{max}=39ps/nm$ $DGD_{max}=12.5ps$	Pilot tone frequency limited	No fundamental limit	Bit-rate limited For 40Gbit/s: $GVD_{max}=39ps/nm$ $DGD_{max}=12.5ps$
Time response	Very fast potentially sub µs	Fast µs - ms	Very slow Few seconds	Slow Potentially sub ms
Bit rate dependent	Yes	No	No	Yes for synch. No for async.
Format dependent	Yes	No	No	Yes
Require Tx modification	No	Yes	No	No

Table 3-5: Summary of advanced OPM techniques reported in chapter 3.

Chapter 4: From prior art to the proposed OPM technique

4.1 Introduction

The RF spectrum phase detection technique has been described in section 3.2.2. It has been shown that this technique presents a number of advantages compared to the other OPM techniques. It has been used to monitor CD (using phase detection) as described in [YU'02] noting that the same setup could have also been used to simultaneously monitor PMD (using amplitude detection). This technique can also potentially have a very fast response time (sub-μs). In addition, the electrical down-conversion using an electrical mixer allows for the use of low speed components after the mixer and finally, this technique does not require transmitter modification. However, the monitors based on this technique have some limitations, e.g. they are bit-rate and modulation format dependent, they do not allow for OSNR measurement and require clock recovery. But most of all, they are only really suited to single-channel operation since they require high bandwidth receivers and RF filters and mixers per WDM channel, thus are not cost effective for multi-channel systems.

The OPM technique we propose here is based on RF spectrum phase detection technique with aim of solving the key limitations of the conventional method. The proposed technique has three key differences bringing three main advantages compared to the prior art: First, the setup has a multi-channel operation; secondly, it was implemented to monitor OSNR in addition to CD; then thirdly, it was adapted to also monitor PMD. In addition, it is bit-rate and modulation format independent.

Multi-channel operation

Figure 4-1 shows the general block diagram of the RF spectrum phase detection using electrical down-conversion and of the proposed OPM technique. The principle of the former method is as follows: The incoming optical signal is first detected using a high-speed detector. The clock phase, proportional to CD, is obtained from the DC power after electrical down-conversion. A mathematical analysis described in section 4.2.2, shows that the square law detection (thus squaring the signal) and the down-conversion (thus multiplying the signal by the modulator transfer function) can be permuted. Doing so would allow, in the physical implementation, for a down-conversion operating in the optical domain. All channels can then be optically down-converted simultaneously which achieves the multi-channel operation.

The proposed novel OPM technique for chromatic dispersion is based on the single sideband (SSB) RF phase detection technique but using electro-optical mixing. This reduces the number of high-bandwidth components to a single electro-optical mixer, allowing for simultaneous multi-channel monitoring.

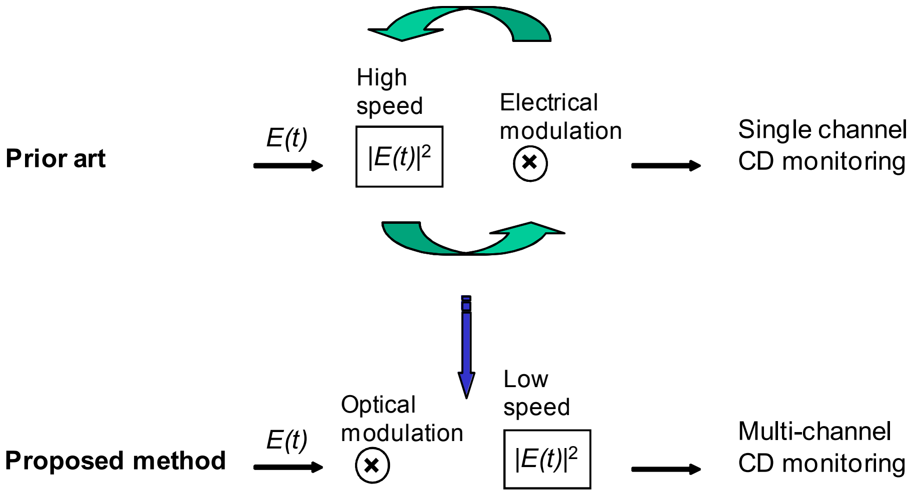

Figure 4-1: General bloc diagram of the RF spectrum phase detection for the prior art and for proposed OPM technique.

OSNR monitoring

The second difference between the proposed OPM and the conventional technique is that the monitored tone is not the clock tone, which does not allow for OSNR monitoring and would require high speed detection, making the setup bit-rate and modulation format dependent; nor is it based on a pilot tone which despite solving all these issues, requires transmitter modification; but is based on an 'in-band' tone monitoring down-converted to an intermediate frequency (IF) as described in the following section. Figure 4-2 illustrates the OSNR monitoring concept. It is shown mathematically in chapter 5 that the DC term I_{DC} in the monitored RF spectrum is proportional to the average intensity I_o and the noise power n_o^2, whereas the IF tone is only proportional to the average intensity I_o. As such, the ratio of the IF tone to the DC term is found to be proportional to the OSNR. It is noted that similarly to the clock phase detection, the IF tone phase is also proportional to GVD.

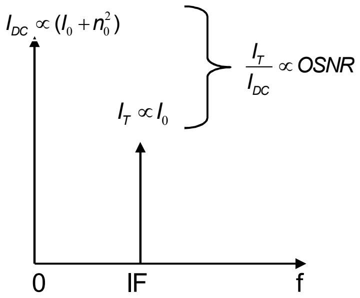

Figure 4-2: Illustration of the OSNR monitoring concept. The monitored RF spectrum allows us to extract the OSNR value from the ratio of the DC term to the IF tone intensity.

PMD monitoring

The proposed OPM technique, described up to now, allows for simultaneous CD and OSNR monitoring. In order to monitor PMD, a polarisation controller (PC) followed by a polarisation beam-splitter (PBS) are used to extract the fast (I_F) and slow (I_S) components of the signal on the principal states of polarisation (PSPs). It is shown mathematically in chapter 5 that the phase difference between these two components is proportional to DGD.

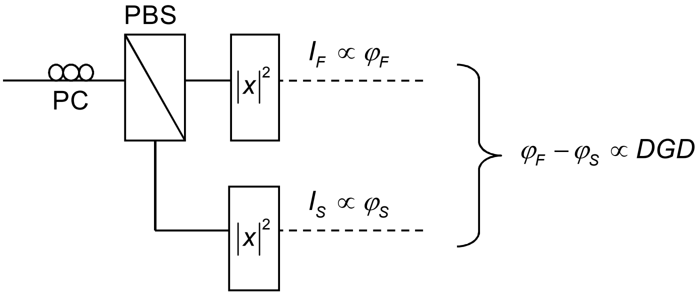

Figure 4-3: Illustration of the DGD monitoring concept. The phase difference between the fast and slow components of the signal is proportional to DGD.

Figure 4-4 shows the evolution of the proposed OPM technique.

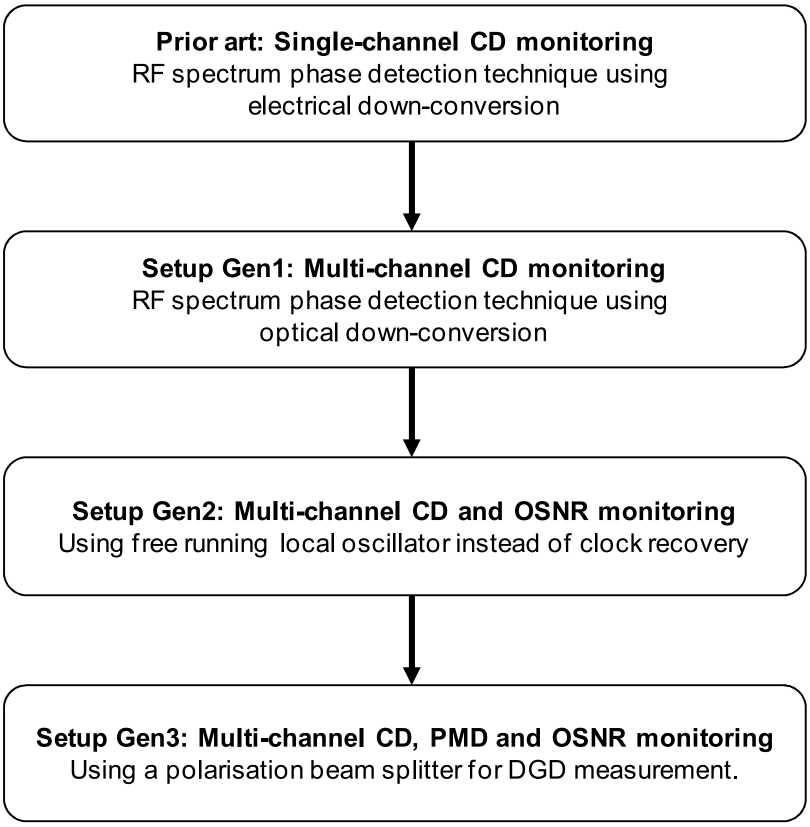

Figure 4-4: General block diagram illustrating the evolution of the proposed OPM technique.

The experimental results of the first and second generations, corresponding respectively to a multi-channel CD monitoring and OSNR, are described in this chapter. The third generation, comprising the final implementation, which allows for multi-channel simultaneous CD, PMD and OSNR monitoring, is described in chapter 5 for the mathematical analysis and in chapter 6 for the experimental results.

4.2 Evolution of the experimental setup

4.2.1 Prior art: Single-channel CD monitoring

Previous work has demonstrated an implementation of RF spectrum clock phase detection for CD monitoring [YU'02]. This technique is based on electrical mixing using an I-Q configuration [DER'07]. Figure 4-5 shows the principle of the CD monitor based on clock phase detection for 40Gbit/s system (see chapter 3, section 3.2.2). The incoming signal, $E_{DSB}(t)$, is an amplitude modulated dual sideband (DSB) signal. A single sideband (SSB) tuneable band-pass optical filter is used to suppress firstly the upper, then the lower sideband of the incoming signal providing consecutively the lower sideband (LSB) signal $E_L(t)$ and the upper sideband (USB) signal $E_U(t)$. RF I-Q mixers are used after high speed square-law detection, driven by a clock signal that has been split into two in-quadrature components. Two signals, in-phase (I_I) and in quadrature (I_Q), are obtained, from which the phase of each side-band is extracted. The chromatic dispersion is then determined from the phase difference between the two sidebands.

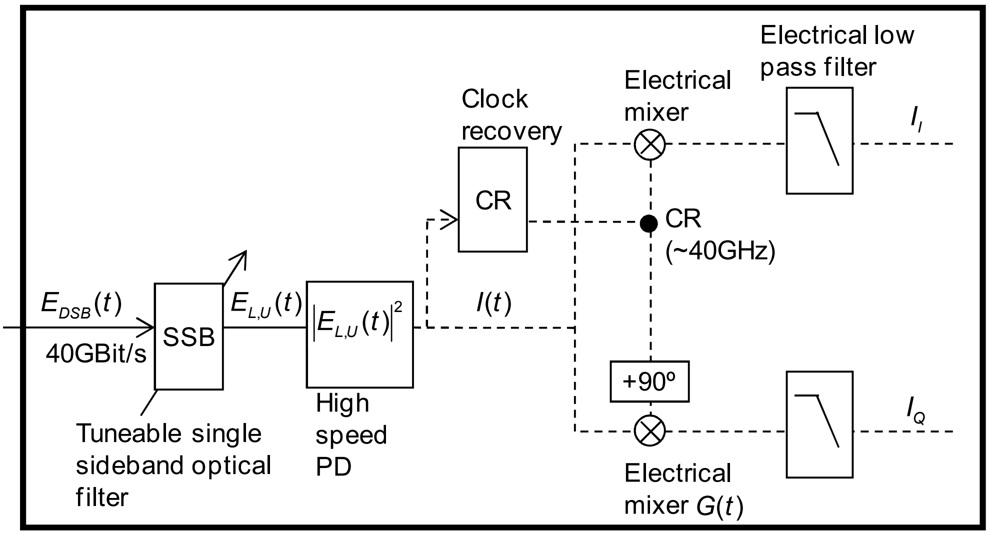

Figure 4-5: Principle of the CD Monitor based on clock phase detection using electrical mixing. Solid line: optical signal, dashed line: electrical signal [YU'02].

Mathematical analysis

After the high-speed detection and the electrical down-conversion, the in-phase and in-quadrature received signals $I_{I,Q}$ for the LSB and USB are given by:

$$\begin{cases} \left(I_{I,Q}\right)_L = \left\langle \left|E_L(t)\right|^2 G_{I,Q}(t) \right\rangle \\ \left(I_{I,Q}\right)_U = \left\langle \left|E_U(t)\right|^2 G_{I,Q}(t) \right\rangle \end{cases} \tag{4.1}$$

where $E_L(t)$ and $E_U(t)$ are the LSB and USB filtered signal and $G_{I,Q}(t)$ are the electrical modulator transfer functions for the in-phase and in-quadrature signals $I_{I,Q}$.

$$\begin{cases} G_I(t) = \cos\left(\omega_{ck} t + \varphi_{ck}\right) \\ G_Q(t) = \cos\left(\omega_{ck} t + \varphi_{ck} + \frac{\pi}{2}\right) \end{cases} \tag{4.2}$$

where ω_{ck} is the modulation clock frequency of the electrical modulator and φ_{ck} is its relative phase to the data clock. It is noted that in theory φ_{ck} is null since both electrical modulators are driven using a signal from a data clock recovery. In practise, this phase might not be null due to the delay caused by the electrical cables used in the experiment. It is shown however in Eq. (4.6), that the effect of φ_{ck} is in all cases eliminated by the phase difference $\Delta\varphi$.

To illustrate the concept, the filtered LSB and USB optical fields $E_L(t)$ and $E_U(t)$ can be modelled as two monochromatic tones, one at the carrier frequency and one at the clock frequency:

$$\begin{cases} E_L(t) = \alpha\sqrt{I_0}\cos\left(\omega_0 t\right) + \beta\sqrt{I_0}\cos\left(\left(\omega_0 - \omega_{ck}\right)t + \varphi_L\right) \\ E_U(t) = \alpha\sqrt{I_0}\cos\left(\omega_0 t\right) + \beta\sqrt{I_0}\cos\left(\left(\omega_0 + \omega_{ck}\right)t + \varphi_U\right) \end{cases} \tag{4.3}$$

where ω_0 and ω_{ck} are, respectively, the optical frequencies of the carrier and the clock tone, and φ_{ck} is the relative optical phase of the clock tone to the carrier, $I_0 =< E_{L,U}^2(t) >$ is the total signal power and α and β determine the amplitude splitting between each tone normalised such that $\frac{1}{2}(\alpha^2 + \beta^2)=1$.

The detected signals I_I and I_Q are determined from Eq. (4.1)-(4.3):

$$\begin{cases} I_I = \dfrac{\alpha\beta I_0}{2}\cos\left(\varphi_{L,U} + \varphi_{ck}\right) \\ I_Q = \dfrac{\alpha\beta I_0}{2}\cos\left(\varphi_{L,U} + \varphi_{ck} + \frac{\pi}{2}\right) \end{cases} \tag{4.4}$$

The relative phase of the carrier and each sideband for the LSB and USB (φ_L and φ_U) are given by:

$$\begin{cases} \varphi_L = Arctg\left(\frac{I_Q}{I_I}\right)_L - \varphi_{ck} \\ \varphi_U = Arctg\left(\frac{I_Q}{I_I}\right)_U - \varphi_{ck} \end{cases} \tag{4.5}$$

It is noted that the phase difference $\Delta\varphi$ is independent of electrical modulator's phase φ_{ck}.

$$\Delta\varphi = \varphi_U - \varphi_L = Arctg\left(\frac{I_Q}{I_I}\right)_U - Arctg\left(\frac{I_Q}{I_I}\right)_L \tag{4.6}$$

The *GVD* is then given by (see chapter 2, section 2.2.1):

$$GVD = \frac{2\pi c}{\lambda_0^2}\frac{1}{\omega_T^2}\Delta\varphi \tag{4.7}$$

4.2.2 Setup Gen1: Multi-channel CD monitoring

It is shown in the following section that the square-law detection and the down-conversion operators from Eq. (4.1) can be permuted; this has led to the proposed OPM technique based on an optical down-conversion followed by square-law detection, that simultaneously down-converts multiple WDM channels and retains the benefits of the conventional RF clock phase detection method whilst being cost effective for multi-channel operation.

In Eq. (4.1), the signals I_I and I_Q were given such that the electrical field *E(t)* was first detected using a high-speed photo-detector, thus squared; then electrically down-converted, thus multiplied by the electrical modulator transfer function *G(t)*.

$$I_{I,Q} = \left\langle \left|E(t)\right|^2 G_{I,Q}(t) \right\rangle \tag{4.8}$$

This equation can also be rewritten as follows:

$$I_{I,Q} = \left\langle \left|E(t)\sqrt{G_{I,Q}(t)}\right|^2 \right\rangle \tag{4.9}$$

The physical interpretation of the new expression can be described by the fact that the electrical field *E(t)* of the optical signal is first optically down-converted, thus multiplied by the optical modulator transfer function $\sqrt{G_{I,Q}(t)}$; then the down-converted optical signal is detected, thus squared. Figure 4-6 shows the principle of the proposed CD monitor based on optical mixing. The main signal is tapped and sent through an optical filter to select a SSB. In a WDM system, a Mach-Zehnder interferometer (MZI) type filter with a free spectral range (FSR) equal to the channel spacing is used. This filter is used in a notch configuration, which simultaneously suppresses one sideband from all channels. The multi-wavelength SSB signal is down-converted using two electro-absorption modulators (EAM) in quadrature driven with a sinusoidal signal at the sideband offset frequency (f_{LO}) equal to half the clock frequency. Each channel is then selected using a wavelength demux (e.g. arrayed waveguide grating (AWG) or WDM channel monitor) and detected using low speed photodiodes. The use of electro-optical down-conversion gives rise to an additional DC component which is proportional to the average signal power (I_0). The average power is detected using an additional wavelength demultiplexer and photodiode and subtracted from the down-converted signals, providing the two in-quadrature signals (I and Q) from which the phase of the sideband beat signal is calculated. The optical filter is simply tuned to suppress the other sideband and the measurement repeated to obtain the phase difference between the sidebands. In a multi-channel system, the only components that must be duplicated are the low speed photodiodes; making this system suitable for multi-wavelength monitoring.

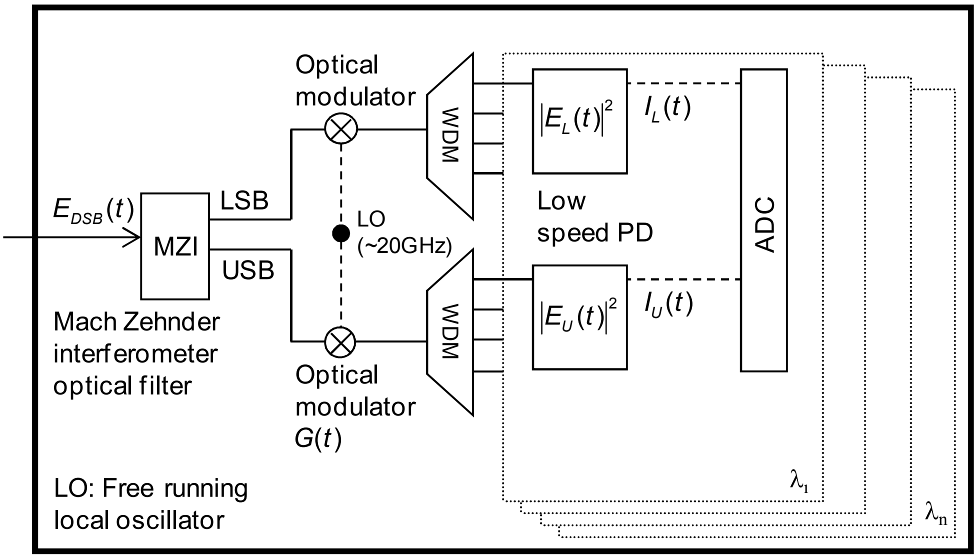

Figure 4-6: Principle of the proposed CD monitor based on optical mixing.

Mathematical analysis

After the optical down-conversion and the low-speed detection, the received signals $I_{I,Q}$ are given by Eq (4.9). Where $E_T(t)$ is the single-channel filtered signal and $G_{I,Q}(t)$ is the optical modulator transfer function for the in-phase and in-quadrature signals $I_{I,Q}$.

$$\begin{cases} G_I(t) = \frac{1}{2}\left(1+\cos\left(\omega_{LO}t+\varphi_{LO}\right)\right) \\ G_Q(t) = \frac{1}{2}\left(1+\cos\left(\omega_{LO}t+\varphi_{LO}+\frac{\pi}{2}\right)\right) \end{cases} \tag{4.10}$$

where ω_{LO} is the modulation frequency of the optical modulator and φ_{LO} is its relative phase to the data clock.

Similarly to the previous technique based on electrical mixing, the electrical field $E_T(t)$ can be modelled as two monochromatic tones given in Eq. (4.3). The detected signals I_I and I_Q are given by:

$$\begin{cases} I_I = \frac{I_0}{2} + \frac{\alpha\beta}{4} I_0 \cos\left(\varphi_{U,L} - \varphi_{LO}\right) \\ I_Q = \frac{I_0}{2} + \frac{\alpha\beta}{4} I_0 \cos\left(\varphi_{U,L} - \varphi_{LO} - \frac{\pi}{2}\right) \end{cases} \tag{4.11}$$

where I_0 is the total signal power, α and β determine the amplitude splitting between each tone normalised such that $\frac{1}{2}(\alpha^2 + \beta^2)=1$, φ_T and φ_{LO} are respectively the phases of the tone and the optical modulator. The relative phase of the carrier and each sideband (φ_L and φ_U) is given by:

$$\begin{cases} \varphi_L = Arctg\left(\frac{I_Q - \frac{I_0}{2}}{I_I - \frac{I_0}{2}}\right)_L + \varphi_{LO} \\ \varphi_U = Arctg\left(\frac{I_Q - \frac{I_0}{2}}{I_I - \frac{I_0}{2}}\right)_U + \varphi_{LO} \end{cases} \tag{4.12}$$

It is noted that the phase difference $\Delta\varphi$ is independent of the optical modulator's phase φ_{LO}.

$$\Delta\varphi = \varphi_U - \varphi_L = Arctg\left(\frac{I_Q - \frac{I_0}{2}}{I_I - \frac{I_0}{2}}\right)_U - Arctg\left(\frac{I_Q - \frac{I_0}{2}}{I_I - \frac{I_0}{2}}\right)_L \tag{4.13}$$

The *GVD* is proportional to $\Delta\varphi$ and given by Eq. (4.7).

Measurement RMS error calculation

In order to assess the accuracy of the experimental results, the measurements root-mean-square (RMS) error was calculated using the following expression:

$$GVD\_RMS\_err = \sqrt{\frac{\sum_i^N \left(GVD_{meas} - GVD_{mean}\right)^2}{N-1}} \tag{4.14}$$

where GVD_{meas} is the measured GVD, GVD_{mean} is the mean GVD corresponding to the actual GVD of the SMF and N is the number of trials. It is noted that due to the slow manual measurement of this implementation, N was chosen to be equal to 10. The subsequent implementations described in sections 4.23 and 4.2.4 were automated which allowed us to use a larger N number equal to 100, thus providing a better confidence in the accuracy measurements.

Experimental results

The initial system implementation has been constructed for a single-channel non-return-to-zero (NRZ) at 40Gbit/s. The optical filter is manually tuned to each side-band. Two EAM have been used for the optical down-conversion driven with a sinusoidal signal, using a clock recovery derived from the pattern generator, of frequency (f_{LO}) corresponding to half the clock frequency (20GHz for 40Gbit/s data). The dispersion is added to the system using various lengths of SMF fibre with a loss that has been compensated for by using a variable optical attenuator. This system has been used to evaluate the dispersion of a number of fibre spans with a residual dispersion varying from 0 to 314ps/nm.

CD monitoring range and system accuracy

The theoretical measurement range can be derived from Eq. (4.7), which corresponds to a phase shift of 2π:

$$GVD_{\max} = \frac{c}{\lambda_0^2 f_T^2} \tag{4.15}$$

where GVD_{max} is the maximum monitoring range.

This expression depends on the frequency tone f_T and is bit-rate independent. In this experiment, the monitored tone is at 20GHz (down-converted to DC), corresponding to a maximum range that can be unambiguously measured of 312ps/nm. It can be noted that this range can be increased by monitoring lower frequency sidebands at the expense of reducing the measurement resolution. The chromatic dispersion has been varied in the system using three spools of SMF of 6km, 12km and 18km, corresponding respectively to 107, 207 and 314ps/nm. Figure 4-7 shows the variation in the measured CD using the proposed technique as a function of the actual CD. The measurement RMS error for a number of 10 trials is calculated to be ±15ps/nm. However it is envisaged that this will be improved with an automated setup that reduces the drifts encountered with slow manual measurements. The signal-to-noise ratio (SNR) of the measured photocurrents is equal to 10dB. Better accuracy could be obtained by improving this SNR, which could be achieved by using low noise photodiodes in the detection system. In this implementation, the EAMs used have a polarisation dependent loss (PDL) of 1dB. One additional measure to improve the accuracy would be to choose devices with lower PDL.

It is noted that some original experiments were conducted using two LiNbO3 Mach-Zehnder optical modulators. The accuracy achieved for CD measurement was of the order of ±60ps/nm. This poor accuracy was due to the high PDL of the modulators (in the order of 20dB) and required manual polarisation alignment prior to each measurement, making them unsuitable for operation in a real system. The use of EAMs, with a PDL of less than 1dB, provided a major accuracy improvement (±15ps/nm), and for that reason, all the work presented in this thesis was conducted using these same EAMs.

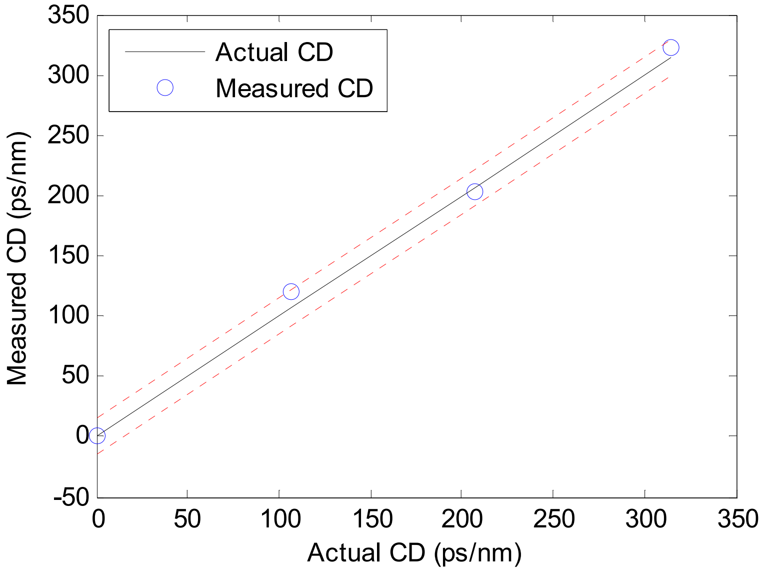

Figure 4-7: Chromatic dispersion monitoring range and accuracy using 3 spools of SMF fibre (6km, 12km and 18km).

In the following experiments, investigating the OSNR, the integration time and the optical filter detuning effects, the CD was fixed at a constant level of 107ps/nm and each measurement was repeated 10 times to calculate the CD RMS error.

Impact of OSNR on the CD measurement

The OSNR of the incoming signal was varied by introducing noise from an ASE source. The measurement RMS error of ±15ps/nm was unchanged as the OSNR was degraded from 40dB to 15dB as shown in Figure 4-8. This emphasises the system's robustness to OSNR, which can be explained by the fact that the phase measurement is derived from the in-quadrature signals that are measured simultaneously and are thus insensitive to the signal and noise fluctuations.

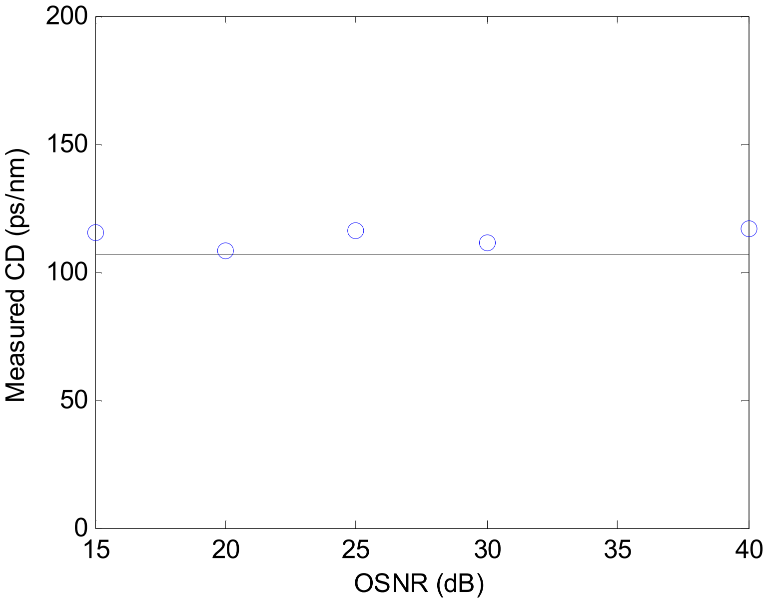

Figure 4-8: OSNR effect on the CD measurement.

Impact of DGD on the CD measurement

The system’s sensitivity to DGD has been investigated by means of simulation using Matlab. To do so, the GVD was fixed at arbitrary constant levels varying between 0 and 300ps/nm in steps of 50ps/nm and the DGD was varied between 0 and 25ps. The simulation results show that the CD measurement is independent of first-order PMD. This is the case as the phase difference between the carrier and the sideband components for both polarisations remain equal with DGD. However, it is expected that higher order mode PMD will have some effect on the measurement due to their wavelength dependence.

Impact of the acquisition time on the CD measurement

An analogue-to-digital card (ADC) with a constant sampling rate of 500kS/s was used to measure the photocurrent. The measurement integration time was reduced from 10ms to 10µs by decreasing the number of samples, required for a single measurement of one SSB phase, from 5000 to 5 respectively. Figure 4-9 shows the increase in the RMS measurement error as the integration time is reduced. The maximum RMS error of 17ps/nm at an integration time of 10µs is in the same order of that of the system error shown in Figure 4-7; thus the performance is not significantly degraded when an integration time of only 10µs is used. The minimum acquisition time in this setup is limited by the maximum sample rate of the ADC (500kS/s). To determine whether sub-microsecond operation is possible will require the use of a faster ADC.

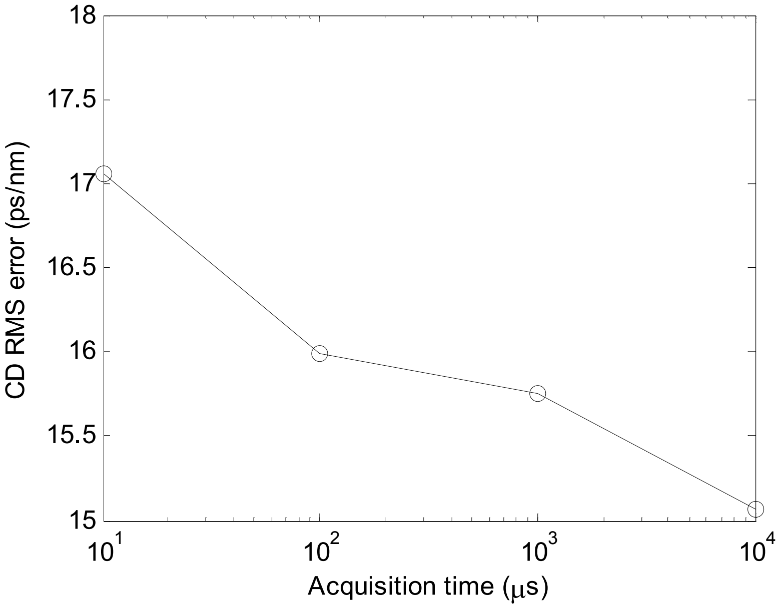

Figure 4-9: Acquisition time effect on the CD measurement.

Impact of the optical filter detuning on the CD measurement

In order to achieve multi-channel monitoring using the proposed configuration, it is necessary to use a periodic filter such as a MZI filter with a FSR chosen to be equal to the channel spacing (e.g. 200GHz).

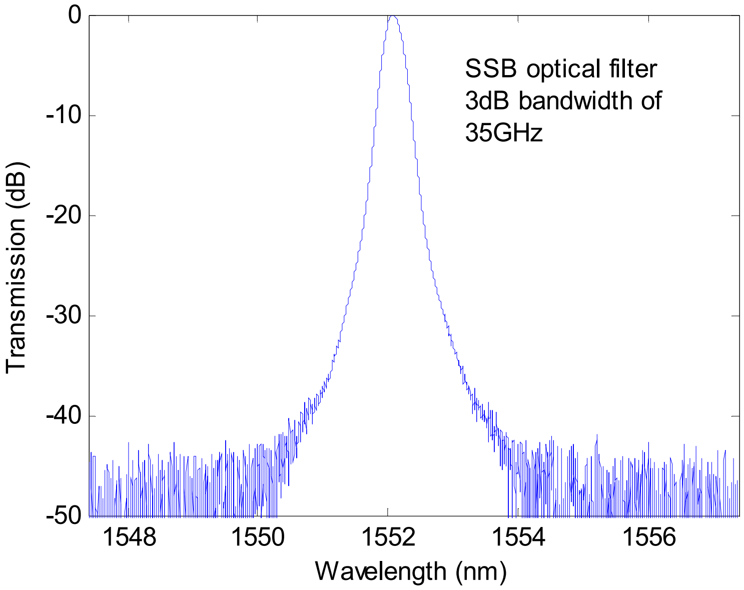

Figure 4-10: Tuneable band-pass optical filter used in the monitoring implementation.

The MZI is used as a notch filter to suppress one side-band component allowing interference between the second side band component and the carrier. This type of filter can easily be tuned to either SSB frequency component by changing the phase on one arm of the MZI. In a single-channel monitoring, it has been shown that better measurement accuracy can be achieved when the band-pass filter bandwidth is close to the modulation frequency (20GHz bandwidth for a 20GHz modulation) [YU'02]. However, such device was not available at the time of the experiment. Figure 4-10 shows the transmission curve of the tuneable optical band pass filter (BPF) used in this experiment. The filter has a 35GHz bandwidth and was manually tuned to each sideband.

By changing the filter detuning from 15GHz to 55GHz and calculating the measurement error, we determine the CD RMS error of this technique caused by the filter detuning as shown in Figure 4-11. An optimum measurement, corresponding to a minimum RMS error, is obtained with a detuning of 35GHz from the carrier. This experiment shows that the CD measurements are sensitive to filter detuning. The system's accuracy of ±15ps/nm can be maintained by keeping the filter detuning at its optimal position within +/-5GHz.

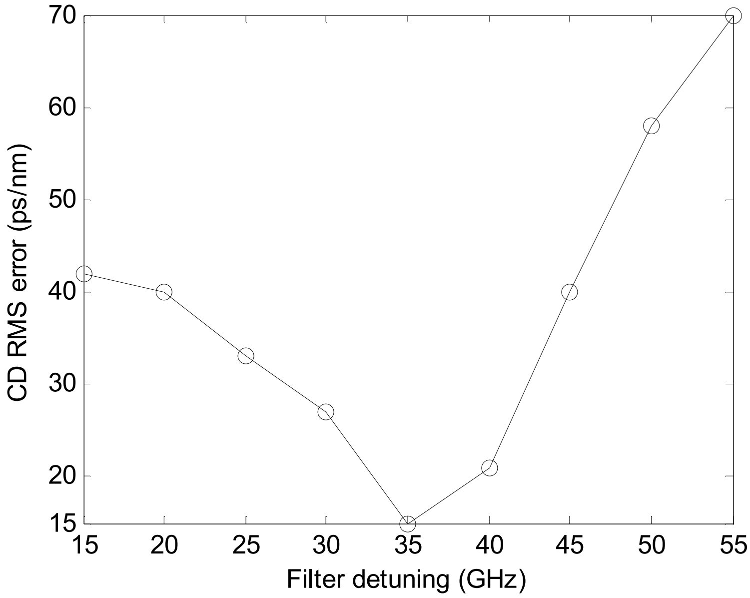

Figure 4-11: Filter detuning effect on the CD measurement.

4.2.3 Setup Gen2: Multi-channel CD and OSNR monitoring

In the previous section, the first generation of the proposed OPM technique has been described. This method was used for CD monitoring, and its key advantage compared to prior-art was its ability to monitor multiple-channels. The version of the OPM technique described in this section presents a main advantage, compared to the first generation, in its ability to monitor OSNR independently and simultaneously to CD monitoring. The in-band monitored tone is electro-optically heterodyned down to an intermediate frequency (IF) of ≈10kHz using a free-running local oscillator. It is shown mathematically in chapter 5 that the DC term of the monitored RF spectrum is proportional to the average intensity and the noise power, whereas the IF tone is only proportional to the average power. As such, the ratio of the tone intensity to the DC term is found to be proportional to the OSNR.

The experimental setup for the simultaneous CD and OSNR measurement is shown in Figure 4-12. The signal and noise are optically filtered to select the optical carrier and a SSB. The SSB signal is then electro-optically heterodyned down to an intermediate frequency (IF) of ≈10kHz which is then detected using a low bandwidth square-law photodetector. The electrical signal is then digitised and the IF tone is extracted in software with a fast Fourier transform (FFT).

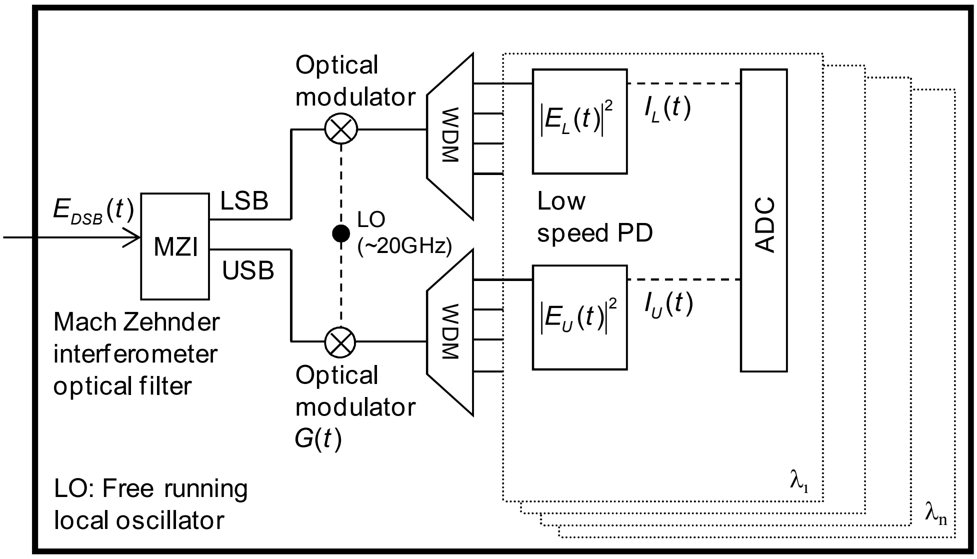

Figure 4-12: Principle of the proposed CD and OSNR monitor using a free running oscillator instead of a clock recovery.

Mathematical analysis

After the optical down conversion and low-speed detection, the received signals for the USB and LSB, $I_U(t)$ and $I_L(t)$, are given by:

$$I_{L,U}(t) = |E(t)_{L,U}|^2 \, G(t) \tag{4.16}$$

where $E_{L,U}(t)$ are the filtered signal and noise for the USB and LSB and $G(t)$ is the optical modulator transfer function such that:

$$G(t) = \frac{1}{2}(1 + \cos(\omega_{LO} t + \varphi_{LO})) \tag{4.17}$$

and

$$\omega_{LO} = \omega_T - \omega_{IF} \tag{4.18}$$

where ω_{LO} and φ_{LO} are respectively the local-oscillator frequency and phase driving the EAMs, ω_T is the monitored tone frequency (~20GHz) and ω_{IF} is the intermediate frequency to which the monitored tone is down-converted to (~10KHz).

CD monitoring

The full analytical derivation for the chromatic dispersion is described in the next chapter (see section 5.2.1). This general model assumes the presence of PMD in the system; however, this assumption does not apply to the experimental setup shown in Figure 4-12. For this reason, the equations developed in the general model are used to describe the GVD when there is no PMD. Similarly to the technique described in the previous section, the phase is extracted from both the USB and LSB IF tones ($I_U(\omega_{IF})$ and $I_L(\omega_{IF})$), and their difference is also proportional to GVD. It is noted that the phase difference $\Delta\varphi$ is independent of the optical modulator's phase φ_{LO}.

$$\Delta\varphi = \left(\varphi_U - \varphi_{LO}\right) - \left(\varphi_L - \varphi_{LO}\right) = \arg\left(I_U(\omega_{IF})\right) - \arg\left(I_L(\omega_{IF})\right) \tag{4.19}$$

where φ_L and φ_U are respectively the phase of the LSB and USB relative to the optical carrier. The *GVD* is proportional to $\Delta\varphi$ and given by Eq. (4.7).

OSNR monitoring

The full analytical derivation for the OSNR is also described in the next chapter (see section 5.2.3). The ratio *R* of the total power ($\left| < I_{L,U}(t) > \right|$ which is proportional to the signal and noise) to the IF tone amplitude ($\left|\hat{I}_{L,U}(\omega_{IF})\right|$ which is proportional to the signal only) is defined such that:

$$R = \frac{\left| < I_L(t) > \right|}{\left|\hat{I}_L(\omega_{IF})\right|} = \frac{\left| < I_U(t) > \right|}{\left|\hat{I}_U(\omega_{IF})\right|} = \frac{1}{\rho}\left(1 + \frac{n^2}{I_0}\right) \tag{4.20}$$

Where I_0 is the signal average power in the absence of noise, n^2 is the noise power and ρ is a constant of proportionality dependent on the modulation format. This ratio *R* is related to the OSNR as follows

$$OSNR = -10log_{10}(\eta \frac{n_0^{\ 2}}{I_0}) = -10log_{10}(\eta(\rho R - 1)) \tag{4.21}$$

where η is a constant of proportionality dependent on the effective measurement bandwidth. The OSNR can then be determined from the measurement of *R* obtained from the ratio of the total power to the IF tone amplitude. It is noted that one sideband measurement is sufficient for the OSNR monitoring. This technique is suitable for intensity modulated formats with a carrier (i.e. NRZ, RZ), and can be adapted to different bit-rates by changing the LO frequency.

Experimental results

An improved setup from the one previously described in section 4.2.2 is proposed. The two key differences are:

- A non-tuneable Mach-Zehnder interferometer (MZI) filter is used to simultaneously select the lower and upper side-bands (LSB and USB) of the channel used (1550.1nm), unlike previously, where the LSB and USB measurements were done sequentially due to the use of a tuneable band-pass optical filter
- Both EAMs are driven with the same local-oscillator providing two in-phase signals, for the simultaneous phase measurement of both sidebands, unlike previously, where the LSB and USB measurements were done sequentially due to the use of in-quadrature signals, requiring two modulators per-sideband.

The proposed OPM technique was setup for a 40Gbit/s multi-channel operation. However, only a single-channel non-return-to-zero (NRZ) with a pseudo-random bit-sequence (PRBS) of 2^{15}-1 was tested. The bit-rate used in the pattern generator is equal to 39.813120GHz, and the monitored tone frequency is f_T=19.907170GHz. The local-oscillator frequency f_{LO}=19.907160GHz is chosen such that the IF is equal to 10KHz (see Eq. (4.18)).

OSNR monitoring range and system accuracy

In order to minimise component loss, the WDM filter (IL=5dB) was replaced by a single channel filter of 3dB insertion loss (IL) and 1.35nm full-width half-maximum (FWHM). The OSNR was varied by keeping the signal at a constant power level and attenuating the ASE source. The effect of varying the OSNR for a constant data signal power, on the amplitude of the extracted IF tone was investigated, it is found that the tone amplitude is constant and independent of the incoming noise. Figure 4-13 shows the comparison between the OSNR measured using this technique and the OSNR measured over a 0.5nm bandwidth (for 40 Gbit/s signals) using an optical spectrum analyser (OSA). The constants α, β, and η in Eq. (4.21), have been experimentally obtained in calibrating the system by fitting Eq. (4.21) to the measured *R* as a function of the independently measured OSNR using an OSA. Further analysis of the value of the constants is performed in the experimental chapter (see section 6.5). The maximum error between the measured and the actual OSNR is 0.6dB over a measurement range of 10dB to 25dB. The standard error arising from the calibration and experimental uncertainty is also shown in Figure 4-13. For OSNR values less than 20dB the standard error is less than 1dB, however, the standard error increases considerably for OSNR values higher than 20dB. The increase in error at large OSNR arises from the error in the measurement of the signal and noise term when the noise is considerably smaller than the signal power. The measurement range could be further improved by reducing the noise in the detection and processing electronics.

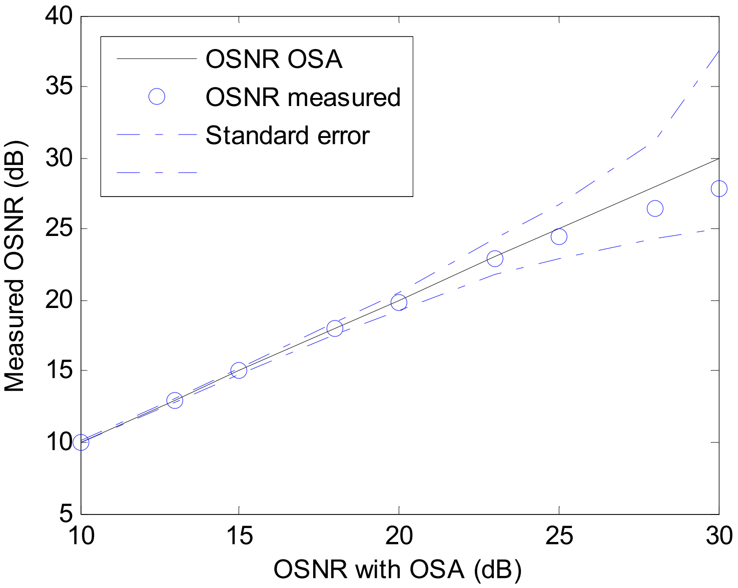

Figure 4-13: OSNR monitoring range and accuracy.

The impact of CD and PMD on the OSNR monitoring have not been verified experimentally for this configuration. However, it is predicted theoretically that the OSNR monitoring is independent of both effects. This can be seen in Eq. (4.21), where the OSNR is independent of the upper and lower sideband phases (φ_U and φ_L). It is noted that the mutual impact of each impairment is experimentally verified for the final implementation which is described in the next section.

Impact of the acquisition time on the OSNR measurement

The acquisition time depends on the averaging time required to achieve an acceptable error in the OSNR measurement. Figure 4-14 shows the effect of reducing the acquisition time from 100ms to 1ms on the RMS error in the OSNR measurement. A 1dB accuracy was achieved for acquisition times of 10ms and above. In addition, a preliminary WDM experiment shows that a 20dB crosstalk does not add any measurable error to the OSNR measurements. This is due to the fact that crosstalk introduces non-coherent light to the channel being measured, which doesn't impact the measurement of the IF tone.

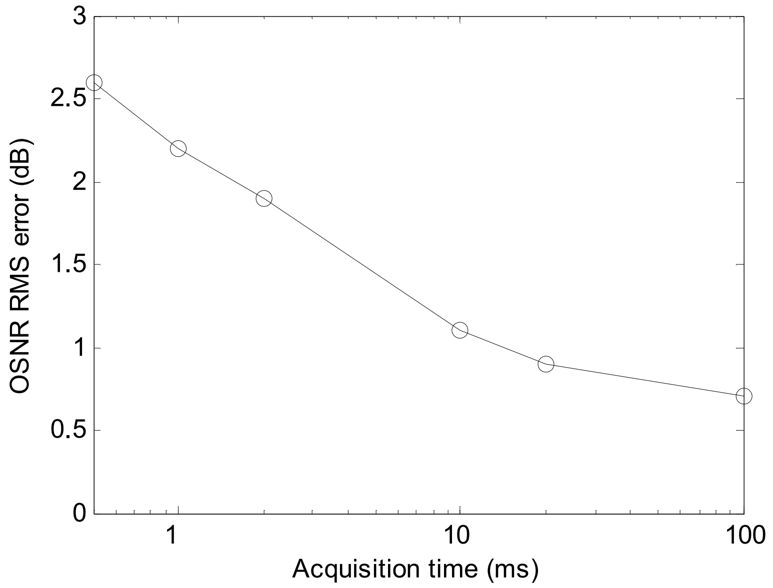

Figure 4-14: Acquisition time effect on the OSNR measurement RMS error.

Impact of the optical filter detuning on the OSNR measurement

Figure 4-15 shows the effect of varying the SSB filter detuning from -10GHz to +20GHz around the optimum position, on the OSNR measurement RMS error. An optimum measurement is obtained with zero detuning corresponding to the minimum error.

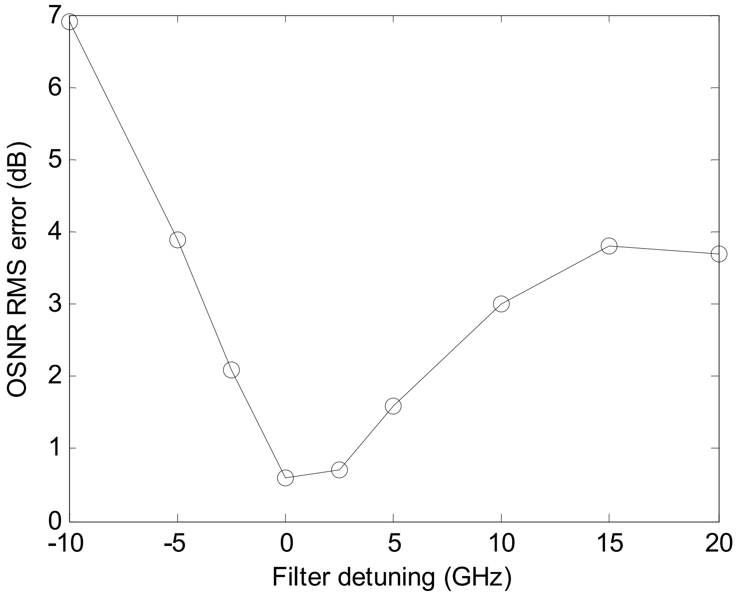

Figure 4-15: Filter detuning effect on the OSNR measurement RMS error.

Impact of the input power on the OSNR measurement

In order to determine the sensitivity of the system, and thus the required tapped power, the optical input power to the photodetectors was varied from -25dBm to -40dBm whilst the OSNR was kept constant at 20dB. Figure 4-16 shows that the RMS error in the measured OSNR increases as the input power decreases. From this result, an error of less than 1dB can be achieved with input powers as low as -30dBm.

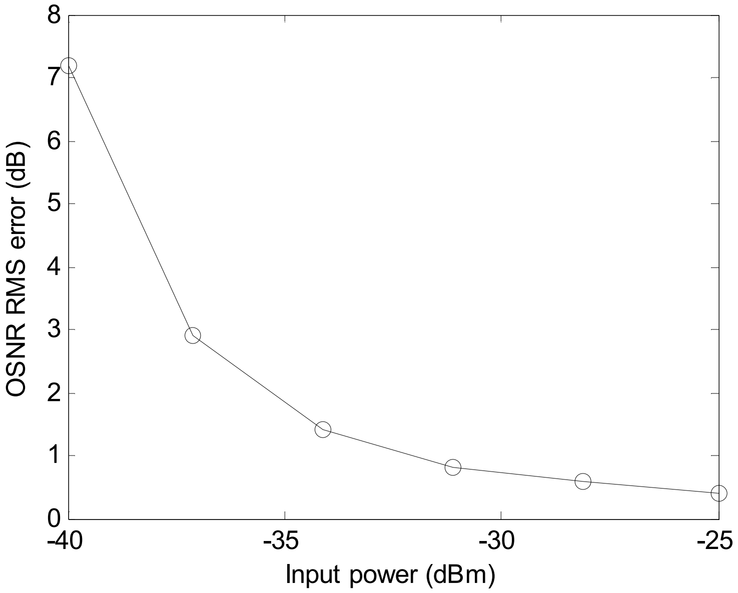

Figure 4-16: Input power effect on the OSNR measurement RMS error.

4.2.4 Setup Gen3: Multi-channel CD, PMD and OSNR monitoring

In the previous section, the second generation of the proposed OPM technique has been described. Its key advantage compared to the first generation was its ability to monitor OSNR. The third and final version of the OPM technique described in this section presents the main advantage of independently and simultaneously monitoring multiple channels with CD, OSNR and PMD impairments. Figure 4-17 shows the principle of the technique; the key difference of this implementation compared to the previous one, used for CD and OSNR measurements, is the use of a polarisation controllers (PC) and polarisation beam-splitters (PBS), which are used to extract the fast (I_F) and slow (I_S) components of the signal. It is shown, mathematically in chapter 5 and experimentally in chapter 6, that the phase difference between these two components is proportional to DGD. It is also shown that CD and OSNR are obtained by the same method than described in the previous implementations. In order to increase the phase-measurement range, thus the GVD and DGD range, a monitored tone of lower frequency (~5GHz) was used compared to the previous implementations (~20GHz).

This has increased the GVD monitoring range by a factor of 16, as expected theoretically (see Eq. (4.15)), while improving the OSNR monitoring range (~25dB).

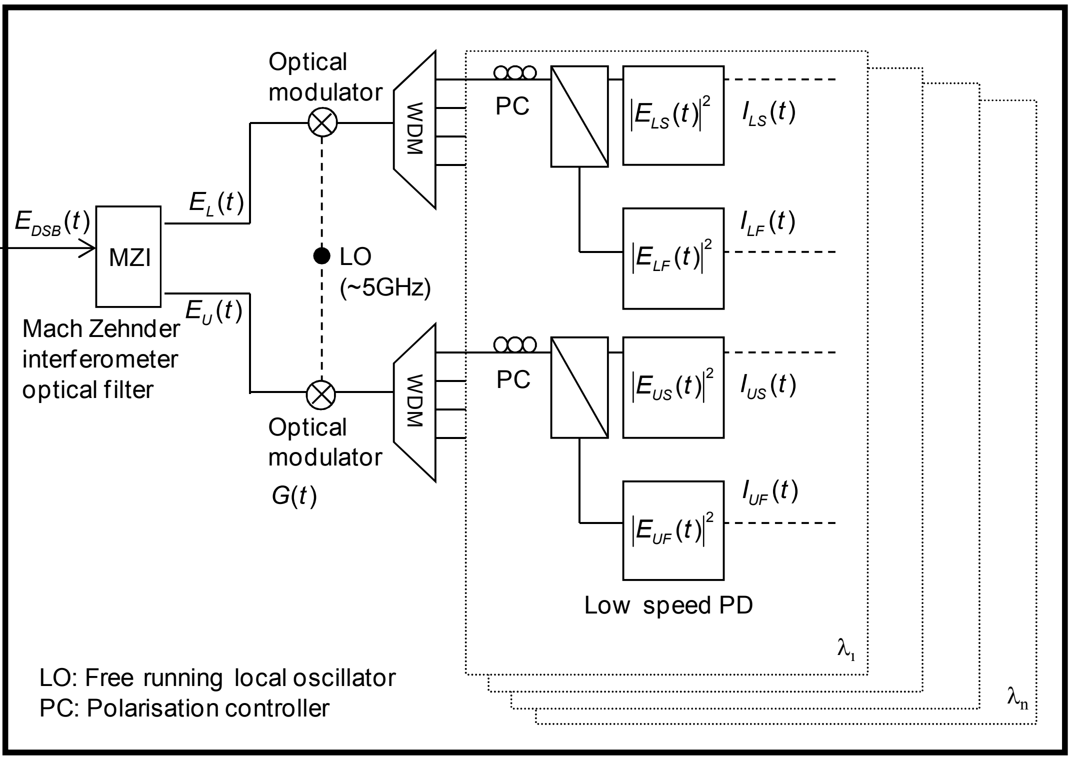

Figure 4-17: Principal of the final implementation of the proposed OPM technique used for simultaneous CD, PMD and OSNR monitoring.

Chapter 5 describes the full mathematical analysis of the final implementation for the proposed OPM technique, and chapter 6 presents all the experimental results.

4.3 Summary

A novel technique for the simultaneous multi-channel monitoring of chromatic dispersion, PMD and OSNR was proposed. This technique was based on the conventional method based on RF spectrum phase detection. The latter method uses electrical mixing providing a single-channel CD monitoring. The proposed technique evolved through 3 generations, each including an additional feature compared to the conventional method. The first generation provided a multi-channel operation through the use of optical mixing. The performance of this technique was experimentally assessed for a single-channel 40Gbit/s NRZ system. A range of +/-156ps/nm was achieved with a measurement accuracy of ±15ps/nm and an acquisition time of 10μs.

The second generation had the added capability of simultaneous CD and OSNR monitoring. The same bit-rate of 40Gbit/s and NRZ modulation format were used in the experimental implementation. The OSNR range was between 10 and 20dB with 1dB accuracy. This measurement accuracy can be maintained for an acquisition time of the order of 10ms. It is noted that the first generation requires a considerably shorter acquisition time compared to second generation. This is due to the fact that the former method extracted DC values, which can be obtained by integrating a very small number of data points (5 data points corresponding to 10μs acquisition-time), whereas the latter method monitored an IF tone of 10kHz, requiring 5000 samples (corresponding to 10ms acquisition-time) to obtain an accurate FFT. Finally, the third generation retained all advantages of the previous implementation, but included DGD monitoring. The experimental implementation was done for a 9 channel 40Gbit/s NRZ system. All the experimental results are described in chapter 6. The three main advantages of final implementation compared to the conventional method are:

- Simultaneous and independent multi-impairment monitoring of CD, PMD and OSNR
- Multi-channel operation
- Bit-rate and amplitude modulation format independent.

Chapter 5: Analytical model

5.1 Introduction

In this chapter, the proposed monitoring technique for chromatic dispersion (CD), polarisation mode dispersion (PMD) and optical signal-to-noise ratio (OSNR) is described and investigated. The aim of this chapter is to derive an analytical expression for the three impairments. The technique's sensitivity to effects such as the optical filter detuning is also investigated. It is noted that all non-linear transmission effects have been neglected and that we equally refer to chromatic dispersion or group velocity dispersion (GVD). Similarly, while first order PMD can be modelled by a vector, with a magnitude corresponding to differential group delay (DGD) and a direction corresponding to the principal states of polarisation (PSPs), we are deliberately focusing exclusively on DGD since this is a readily measured parameter on installed optical networks.

In section 5.2, an analytical model is developed to describe the monitoring technique for GVD, DGD and OSNR. It is shown that both CD and PMD rely on phase measurements whereas the OSNR relies on amplitude measurements of the monitored tone.

- Phase difference between two sidebands → GVD
- Phase difference between two PSPs → DGD
- $\frac{\text{Tone amplitude}}{\text{Average power}}$ → OSNR

The analytical model relies on the use of a Fourier series representation for the optical fields [DES'94, MAR'91]. This allows us to derive a generalised model for all impairments which is then simplified to a two-tone model. The latter allows us to derive a simple expression for the filtering detuning effect. Various assumptions have been made in obtaining the simplified analytical model. These assumptions are both described and justified within this chapter. It is shown that the analytical results presented in this chapter agree very well with the experimental results presented in chapter 6.

In section 5.3, the impact of filter detuning on the monitoring performance is investigated. The method is shown to be insensitive to the filter detuning when monitoring CD or PMD, however, it is not insensitive when monitoring OSNR.

5.2 Generalised multi-tone model

In the previous chapter, we used an analysis for the OSNR monitoring (see section 4.2.3) using a simplified representation of the signal and noise modelled as two monochromatic tones, one at the carrier frequency and the second at the monitored frequency. In this chapter, and in an effort to generalise the model, we describe the optical signal and noise, using a Fourier series representation, as a finite number of tones located within the signal optical bandwidth and separated by a constant frequency spacing. The frequency spacing $\Delta\omega$ between the tones within the data envelope depends on the length of the repeating pseudo-random bit-sequence (PRBS) data signal that is used. In the case of a completely random data stream, $\Delta\omega$ tends to zero and the data tones become a continuum. In deriving the analytical model, it is not necessary to assume that there are discrete tones, however, the experimental results presented in the next chapter use a PRBS with a length equal to 2^{15}-1, and thus discrete tones with a frequency spacing of around 1.2MHz are observed when the data rate is 40Gbit/s. It is noted that for a field implementation monitoring a continuous spectrum generated by a random data stream, the experimental setup would involve a software modification (see section 6.2.4), but the analytical results developed in this chapter using a Fourier series representation of the data would still apply.

The 1st order PMD, CD and OSNR measurement principle is shown schematically in Figure 5-1. The measurement is based on determining the relative phases, of a selected RF tone that is present in the signal due to the data modulation, for PMD and CD measurements; and the tones' amplitude relative to the signal average-power for OSNR measurement. The signal is optically filtered using a partial bit-delay Mach-Zehnder interferometer (MZI) to select the optical carrier and a single sideband. The free spectral range (FSR) of the MZI is chosen to be twice the frequency spacing between the upper and lower sidebands, and tuned so that the filter transmits one sideband in its first output and the other sideband in the its second output. Under these conditions the upper and lower sidebands signals are obtained simultaneously from the two outputs of the MZI. For multi-wavelength operation it is also necessary to ensure that the FSR is a sub-multiple of the WDM channel spacing. Each single sideband (SSB) signal is then electro-optically heterodyned down to an intermediate-frequency (IF) in the order of few kHz (compared to the monitored tone of few GHz). A polarising beam splitter (PBS) is used to separate each SSB signal into two orthogonal polarisation states, which are then detected using four low bandwidth square-law photodetectors (only one sideband is depicted in Figure 5-1). The electrical signals are then digitised and the IF tones are extracted in software with a fast Fourier transform (FFT).

In the following section, it is shown that the phases of the four IF tones (the fast and slow polarisations of both the upper and lower sidebands) are a measure of DGD (see Eq. (5.36)) and CD (see Eq. (5.32)), and that the IF tones' amplitude in conjunction with the total average power is a measure of OSNR (see Eq. (5.53)).

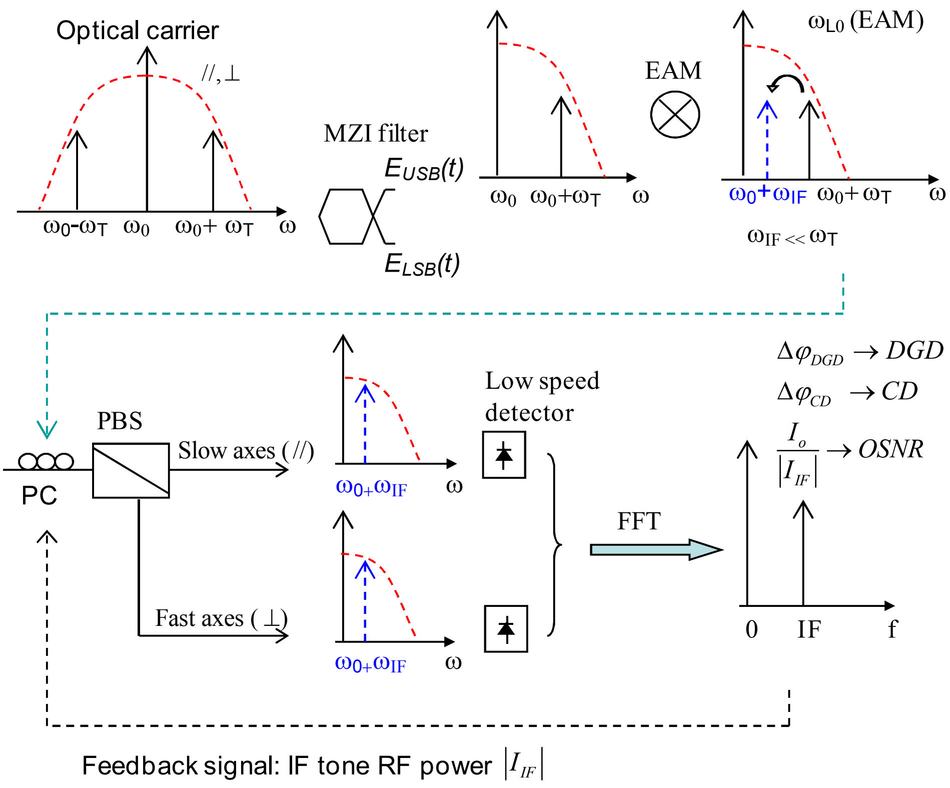

Figure 5-1: Principle of the spectral analysis method after frequency down-conversion (only the USB sideband is depicted for detection). The red line indicates the data spectrum. The blue tone indicates the down-converted tone to the IF frequency. ω_0 represents the carrier optical angular-frequency of the signal. ω_T, ω_{IF} and ω_{LO} represent respectively the angular-frequency of the monitored tone, the intermediate frequency and the local oscillator used to drive the optical modulators.

The envelope of the electric field *E(t)* of a binary optical signal may be described in the time domain as [HO'04]:

$$E(t)=\left(\sum_{k=-\infty}^{\infty} b_k p(t-kT)\right)\alpha\exp\left(i\left(\omega_0 t+\varphi_0\right)\right) \tag{5.1}$$

where $b_k=0,+1$ is the transmitted random data stream, *p(t)* is the pulse shape, *T* is the signal's bit period, and where α, ω_0 and φ_0 are, respectively, the amplitude, the optical angular-frequency and the phase of the signal. Eq. (5.1) can be re-expressed as follows:

$$E(t)=\left(\sum_{k=-\infty}^{\infty} b_k\left(p(t)\otimes\delta(t-kT)\right)\right)\alpha\exp\left(i\left(\omega_0 t+\varphi_0\right)\right) \tag{5.2}$$

where δ represents the Dirac delta function.

The analysis of the monitoring technique simplifies considerably with the use a Fourier series representation for field. Thus *E(t)* is expanded in terms of Fourier series coefficients α_k, the amplified spontaneous emission noise present in the system is also represented in the same way [DES'94, MAR'91, MAR'90]. The dual-sideband electric filed $E_{DSB}(t)$ is then given by:

$$E_{DSB}(t) = \sum_{k=-\infty}^{\infty} \alpha_k \exp\left(i\left(\omega_k t + \varphi_k\right)\right) + \sum_{k=-\infty}^{\infty} n_k \exp\left(i\left(\omega_k t + \varphi_{rk}\right)\right) \tag{5.3}$$

where α_k, ω_k and φ_k are, respectively, the amplitude, the optical angular-frequency and the phase of the signal's k^{th} tone; n_k and φ_{rk} are, respectively, the amplitude and the random phase of the noise's k^{th} tone.

Here we band-limit the signal to twice the signal bit-rate 2/T using an ideal band-pass filter with a unity transfer function inside the band-pass and zero outside it (the phase effect of the filter is neglected). The real-part of the Fourier series representation then becomes:

$$E_{DSB}(t) = \sum_{k=-M}^{M} \alpha_k \cos\left(\omega_k t + \varphi_k\right) + \sum_{k=-M}^{M} n_k \cos\left(\omega_k t + \varphi_{rk}\right) \tag{5.4}$$

where M is defined such that $2M+1$ is the total number of tones present within the considered bandwidth of the signal. Higher order frequency-terms that are beyond the signal's bandwidth have been dropped.

In the presence of first order PMD, the modulated dual-sideband signal $E_{DSB}(t)$ can be modelled within the signal's bandwidth as the sum of monochromatic tones which are all linearly polarised light. Nonlinear transmission effects are neglected here. Without loss of generality, it is assumed that the fast and slow PSPs [POO'86] can be represented by a column vector $\begin{bmatrix} 1 \\ 0 \end{bmatrix}$ and $\begin{bmatrix} 0 \\ 1 \end{bmatrix}$ respectively, such that a linearly polarised signal can be represented as:

$$\overrightarrow{E_{DSB}}(t) = \begin{pmatrix} \cos\phi \sum\limits_{k=-M}^{M} \alpha_k \cos\left(\omega_k\left(t - \dfrac{\Delta\tau}{2}\right) + \varphi_k\right) \\ \sin\phi \sum\limits_{k=-M}^{M} \alpha_k \cos\left(\omega_k\left(t + \dfrac{\Delta\tau}{2}\right) + \varphi_k\right) \end{pmatrix} + \begin{pmatrix} \dfrac{1}{\sqrt{2}} \sum\limits_{k=-M}^{M} n_k \cos\left(\omega_k t + \varphi_{xrk}\right) \\ \dfrac{1}{\sqrt{2}} \sum\limits_{k=-M}^{M} n_k \cos\left(\omega_k t + \varphi_{yrk}\right) \end{pmatrix} \tag{5.5}$$

and

$$\gamma = \sin^2\phi \tag{5.6}$$

where ϕ represents the angle between the linearly polarised signal and the fast principal state; γ represents the 1st order PMD power-splitting-ratio; $\Delta\tau$ is the DGD, defined as the group-delay difference between the slow and fast modes. It is noted that the phase on both principal states of polarization for each tone within the signal bandwidth are equal since the signal is considered as linearly polarized. The noise power is split equally between both PSP. A MZI is used to filter the DSB signal into a lower-sideband (LSB) signal and an upper-sideband (USB) signal. It is shown in the following section that this optical filtering allows CD measurement to be done independently of DGD. Figure 5-2 shows the power spectrum diagram of the incoming NRZ DSB signal, and the LSB and USB after the sinusoidal transfer function of the MZI filter. In deriving the model, we assume an ideal sideband filter and thus the only tones that are considered are from –M to 0 for the LSB and from 0 to M for the USB where k_T is the monitored tone index.

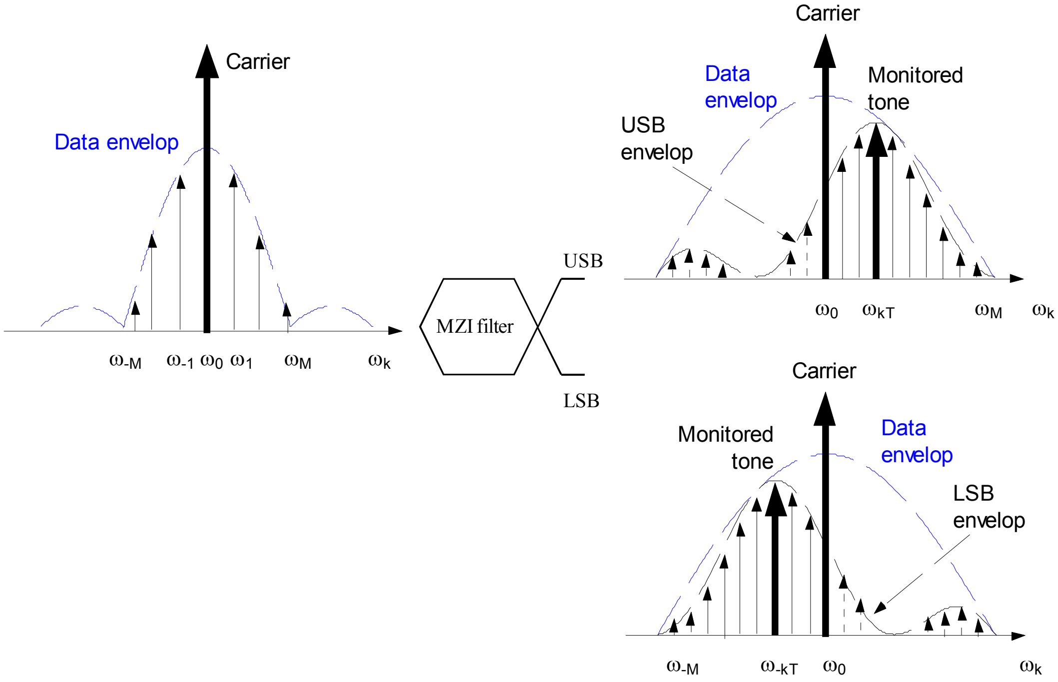

Figure 5-2: Power spectrum diagram of a NRZ DSB input signal centred around the carrier optical frequency ω_0, LSB and USB output signals after an MZI filter (k is the tone index).

The expression of each sideband is given by:

$$\overrightarrow{E_{USB}}(t)=\begin{pmatrix}\cos\phi\sum_{k=0}^{M}T_k\alpha_k\cos\left(\omega_k\left(t-\frac{\Delta\tau}{2}\right)+\varphi_k\right)\\ \sin\phi\sum_{k=0}^{M}T_k\alpha_k\cos\left(\omega_k\left(t+\frac{\Delta\tau}{2}\right)+\varphi_k\right)\end{pmatrix}+\begin{pmatrix}\frac{1}{\sqrt{2}}\sum_{k=0}^{M}T_kn_k\cos\left(\omega_kt+\varphi_{xrk}\right)\\ \frac{1}{\sqrt{2}}\sum_{k=0}^{M}T_kn_k\cos\left(\omega_kt+\varphi_{yrk}\right)\end{pmatrix} \tag{5.7}$$

and

$$\overrightarrow{E_{LSB}}(t)=\begin{pmatrix}\cos\phi\sum_{k=-M}^{0}T_k\alpha_k\cos\left(\omega_k\left(t-\frac{\Delta\tau}{2}\right)+\varphi_k\right)\\ \sin\phi\sum_{k=-M}^{0}T_k\alpha_k\cos\left(\omega_k\left(t+\frac{\Delta\tau}{2}\right)+\varphi_k\right)\end{pmatrix}+\begin{pmatrix}\frac{1}{\sqrt{2}}\sum_{k=-M}^{0}T_kn_k\cos\left(\omega_kt+\varphi_{xrk}\right)\\ \frac{1}{\sqrt{2}}\sum_{k=-M}^{0}T_kn_k\cos\left(\omega_kt+\varphi_{yrk}\right)\end{pmatrix} \tag{5.8}$$

where T_k is the filter's amplitude of the k^{th} tone. In a WDM system, each channel is simultaneously optically down-converted using two EAMs (one for each sideband). The two polarisation components of each of the down-converted signals are then extracted using a PBS which is preceded by a polarisation-controller as shown in Figure 5-1.

Figure 5-3 shows the arbitrary orientation of the down-converted signals PSPs onto the PBS PSPs.

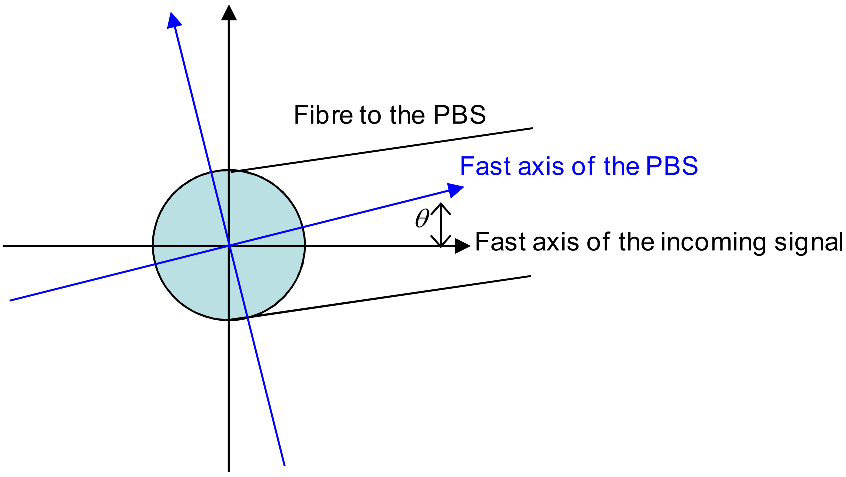

Figure 5-3: Diagram showing the arbitrary orientation (θ) of the incoming signals PSPs onto the PBS PSPs.

The fields at the output of the two PBS are referenced as (E_{UF}, E_{US}) for the fast and slow polarisations of the USB, and (E_{LF}, E_{LS}) for the fast and slow polarisations of the LSB in the reference frame of the PBS.

$$\begin{pmatrix} \mathrm{E_{UF}} \\ \mathrm{E_{US}} \end{pmatrix} = \sqrt{G_U(t)} \begin{pmatrix} \cos\theta_U & \sin\theta_U \\ -\sin\theta_U & \cos\theta_U \end{pmatrix} \overrightarrow{E_{USB}}(t) \tag{5.9}$$

and

$$\begin{pmatrix} \mathrm{E_{LF}} \\ \mathrm{E_{LS}} \end{pmatrix} = \sqrt{G_L(t)} \begin{pmatrix} \cos\theta_L & \sin\theta_L \\ -\sin\theta_L & \cos\theta_L \end{pmatrix} \overrightarrow{E_{LSB}}(t) \tag{5.10}$$

where θ_U and θ_L represent, respectively, the orientation angles of the PBS on the upper and lower sidebands with respect to the PSP of the signal; $G_U(t)$ and $G_L(t)$ represent, respectively, the EAM transfer function on the upper and lower sidebands. Here we assume that the transfer functions of the two EAMs are identical and they are driven by the same local-oscillator (LO):

$$G_U(t) = G_L(t) = G(t) \tag{5.11}$$

If we assume that the EAM is operated in the linear part of its transfer function and driven by a sinusoidal voltage, then the transfer function can be approximated by a raised cosine. Further justification of this approximation is shown in the experimental chapter (see Chap 6 section 6.2.3):

$$G(t)=\frac{1}{2}\left(1+\cos\left(\omega_{LO}t+\varphi_{LO}\right)\right) \tag{5.12}$$

where ω_{LO} is the modulation frequency of the optical modulator and φ_{LO} is its relative phase to the data clock. It is noted that non-identical EAM transfer functions would introduce a different phase-shift to the upper and lower down-converted sidebands (see Eq.(5.28)), introducing an error in the chromatic dispersion monitoring, which requires a double sideband measurement (see Eq.(5.31)); but would not have any impact on the DGD monitoring since the later only requires a single sideband measurement (see Eq.(5.36)).

The four signals at the output of the two PBS are detected using low-speed detectors. Their intensities are referenced as (I_{UF}, I_{US}) for the fast and slow polarisations of the USB, and (I_{LF}, I_{LS}) for the fast and slow polarisations of the LSB:

$$\begin{cases} I_{UF}(t)=G(t)\left(\cos\theta_U E_{Ux}+\sin\theta_U E_{Uy}\right)^2 \\ I_{US}(t)=G(t)\left(-\sin\theta_U E_{Ux}+\cos\theta_U E_{Uy}\right)^2 \end{cases} \tag{5.13}$$

and

$$\begin{cases} I_{LF}(t)=G(t)\left(\cos\theta_L E_{Lx}+\sin\theta_L E_{Ly}\right)^2 \\ I_{LS}(t)=G(t)\left(-\sin\theta_L E_{Lx}+\cos\theta_L E_{Ly}\right)^2 \end{cases} \tag{5.14}$$

where (E_{Ux}, E_{Uy}) and (E_{Lx}, E_{Ly}) are, respectively, the two polarisation components on the x-y axis, the reference frame of the USB and LSB fields before the PBS.

$$I_{UF}(t)=G(t)\begin{pmatrix} \cos\phi\cos\theta_U\sum_{k=0}^{M}T_k\alpha_k\cos\left(\omega_k(t-\frac{\Delta\tau}{2})+\varphi_k\right) \\ +\frac{1}{\sqrt{2}}\cos\theta_U\sum_{k=0}^{M}T_k n_k\cos\left(\omega_k t+\varphi_{xrk}\right) \\ +\sin\phi\sin\theta_U\sum_{k=0}^{M}T_k\alpha_k\cos\left(\omega_k(t+\frac{\Delta\tau}{2})+\varphi_k\right) \\ +\frac{1}{\sqrt{2}}\sin\theta_U\sum_{k=0}^{M}T_k n_k\cos\left(\omega_k t+\varphi_{yrk}\right) \end{pmatrix}^2 \tag{5.15}$$

and

$$I_{US}(t)=G(t)\begin{pmatrix} -\cos\phi\sin\theta_U\sum_{k=0}^{M}T_k\alpha_k\cos\left(\omega_k(t-\frac{\Delta\tau}{2})+\varphi_k\right) \\ -\frac{1}{\sqrt{2}}\sin\theta_U\sum_{k=0}^{M}T_k n_k\cos\left(\omega_k t+\varphi_{xrk}\right) \\ +\sin\phi\cos\theta_U\sum_{k=0}^{M}T_k\alpha_k\cos\left(\omega_k(t+\frac{\Delta\tau}{2})+\varphi_k\right) \\ +\frac{1}{\sqrt{2}}\cos\theta_U\sum_{k=0}^{M}T_k n_k\cos\left(\omega_k t+\varphi_{yrk}\right) \end{pmatrix}^2 \tag{5.16}$$

where $\omega_k = \omega_0 + k\Delta\omega$ and $\omega_0, \Delta\omega$ are respectively the central optical angular-frequency of the data signal and the frequency spacing between the data tones which depends on the length of the repeating PRBS data signal that is used. Further development of Eq (5.15) and Eq. (5.16) is given in appendix 1.

As shown in the following sections, depending on the relative value of *l* and *k*, we will be able to greatly simplify $I_{UF}(t)$ and $I_{US}(t)$. We show (see appendix 1) that $I_{UF}(t)$ and $I_{US}(t)$ can be expressed as the sum of a first term proportional to the average power and a second term proportional to the IF tone:

$$I_{UF}(t) = \text{Average Power}\big|_{UF} + \text{IF Tone}\big|_{UF} \tag{5.17}$$

and:

$$I_{US}(t) = \text{Average Power}\big|_{US} + \text{IF Tone}\big|_{US} \tag{5.18}$$

The components of $I_{US,UF}(t)$ at the IF are extracted experimentally in software, after analogue to digital conversion, using a FFT. The IF tone, is the sum of the beating terms between all the signal-tones that are separated by the monitored tone-frequency ω_T.

The two IF tone's expressions are given by:

$$\hat{I}_{US,UF}(\omega_{IF}) = \left\langle I_{US,UF}(t)\exp\left(i\omega_{IF}t\right)\right\rangle \tag{5.19}$$

where the intermediate frequency to which the SSB tones are down-converted to is ω_{IF}.

$$\omega_T = \omega_{LO} + \omega_{IF} \tag{5.20}$$

The intermediate frequency (ω_{IF}~10kHz) is chosen to be much lower than the monitored tone frequency (ω_T~5GHz):

$$\omega_{IF} << \omega_T \tag{5.21}$$

This allows the detection of the IF tones using low-speed detection system and an ADC of low sampling rate (the experimental work was done using a maximum sampling rate of 500kS/s per channel). The IF tones are a result of the beating terms between two tones separated by ω_T . The first tone having an index *k* and the second tone having an index *l* such that $l=k+k_T$. We define k_T. such that (see Figure 5-2):

$$\omega_T = k_T\Delta\omega \tag{5.22}$$

In this case, the expression of the IF tones is obtained for an index $l = k + k_T$ and null for $l \neq k + k_T$. From Eq. (5.17), Eq. (5.18) and further development presented in appendix 1, we obtain:

for $l = k + k_T$

$$\hat{I}_{UF}(\omega_{IF}) = \frac{1}{16}\left(\begin{array}{l} \cos^2\phi\cos^2\theta_U \exp\ i\left(\varphi_{USB} - \varphi_{LO} - \dfrac{k_T\Delta\omega\Delta\tau}{2}\right) \\ \sum\limits_{k=0}^{M}\sum\limits_{l=k+k_T}^{M} T_k T_l \alpha_k \alpha_l \\ +\sin^2\phi\sin^2\theta_U \exp\ i\left(\varphi_{USB} - \varphi_{LO} + \dfrac{k_T\Delta\omega\Delta\tau}{2}\right) \\ \sum\limits_{k=0}^{M}\sum\limits_{l=k+k_T}^{M} T_k T_l \alpha_k \alpha_l \\ +2\sin\phi\cos\phi\sin\theta_U\cos\theta_U \exp\ i\left(\varphi_{USB} - \varphi_{LO} - (\omega_{k+\Delta k} + \omega_k)\dfrac{\Delta\tau}{2}\right) \\ \sum\limits_{k=0}^{M}\sum\limits_{l=k+k_T}^{M} T_k T_l \alpha_k \alpha_l \end{array}\right) \tag{5.23}$$

for $l \neq k + k_T$

$$\hat{I}_{UF}(\omega_{IF}) = 0$$

and

for $l = k + k_T$

$$\hat{I}_{US}(\omega_{IF}) = \frac{1}{16}\left(\begin{array}{l} \cos^2\phi\sin^2\theta_U \exp\ i\left(\varphi_{USB} - \varphi_{LO} - \dfrac{k_T\Delta\omega\Delta\tau}{2}\right) \\ \sum\limits_{k=0}^{M}\sum\limits_{l=k+k_T}^{M} T_k T_l \alpha_k \alpha_l \\ +\sin^2\phi\cos^2\theta_U \exp\ i\left(\varphi_{USB} - \varphi_{LO} + \dfrac{k_T\Delta\omega\Delta\tau}{2}\right) \\ \sum\limits_{k=0}^{M}\sum\limits_{l=k+k_T}^{M} T_k T_l \alpha_k \alpha_l \\ -2\sin\phi\cos\phi\sin\theta_U\cos\theta_U \exp\ i\left(\varphi_{USB} - \varphi_{LO} - (\omega_{k+\Delta k} + \omega_k)\dfrac{\Delta\tau}{2}\right) \\ \sum\limits_{k=0}^{M}\sum\limits_{l=k+k_T}^{M} T_k T_l \alpha_k \alpha_l \end{array}\right) \tag{5.24}$$

for $l \neq k + k_T$

$$\hat{I}_{US}(\omega_{IF}) = 0$$

The previous Eqs (5.23) and (5.24) are obtained given that terms containing $\left\langle \cos\left(\omega t\right)\right\rangle = 0$ and $\left\langle \cos\varphi_r \right\rangle = \left\langle \sin\varphi_r \right\rangle = 0$ when φ_r is random, time-average to zero.

From Eqs. (5.23) and (5.24), it can be seen that the phase and amplitude of the IF tones on the slow and fast PSPs will depend on the PBS orientation angles (θ_U). In order to suppress this dependency, θ_U must be adjusted to zero, which can be achieved by tuning the polarisation controller (PC) placed before each PBS (see Figure 5-1). The RF power of each IF tone is used as a control feed-back to tune the PCs. Within one sideband, the maximum RF power of the fast polarisation IF tone (corresponding to the minimum RF power of the slow polarisation IF tone) coincide with the alignment of the PBS and signal's PSPs (θ_U=0) (see simulation results in section 6.2.4):

$$\theta_U = n\pi : \begin{cases} \left|\hat{I}_{UF}(\omega_{IF})\right|^2 = Max\left|\hat{I}_{UF}(\omega_{IF})\right|^2 \\ \left|\hat{I}_{US}(\omega_{IF})\right|^2 = Min\left|\hat{I}_{US}(\omega_{IF})\right|^2 \end{cases} \tag{5.25}$$

In this configuration where θ_U=0, the full expression of the USB IF tones is derived from Eqs. (5.23)-(5.24), and is given by:

for $l = k + k_T$:

$$\hat{I}_{UF}(\omega_{IF}) = \frac{\cos^2\phi}{16}\exp\ i\left(\varphi_{USB} - \varphi_{LO} - \frac{k_T\Delta\omega\Delta\tau}{2}\right)\sum_{k=0}^{M}\sum_{l=k+k_T}^{M} T_k T_l \alpha_k \alpha_l$$

$$\hat{I}_{US}(\omega_{IF}) = \frac{\sin^2\phi}{16}\exp\ i\left(\varphi_{USB} - \varphi_{LO} + \frac{k_T\Delta\omega\Delta\tau}{2}\right)\sum_{k=0}^{M}\sum_{l=k+k_T}^{M} T_k T_l \alpha_k \alpha_l \tag{5.26}$$

for $l \neq k + k_T$:

$$\hat{I}_{UF}(\omega_{IF}) = 0$$

$$\hat{I}_{US}(\omega_{IF}) = 0$$

Similar analysis shows that for θ_L*=0*, the full expression of the LSB IF tones $\hat{I}_{LF}(\omega_{IF})$ and $\hat{I}_{LS}(\omega_{IF})$ are given by:

for $l = k + k_T$:

$$\hat{I}_{LF}(\omega_{IF}) = \frac{\cos^2\phi}{16}\exp\ i\left(\varphi_{LSB} - \varphi_{LO} - \frac{k_T\Delta\omega\Delta\tau}{2}\right)\sum_{k=-M}^{0}\sum_{l=k-k_T}^{0} T_k T_l \alpha_k \alpha_l$$

$$\hat{I}_{LS}(\omega_{IF}) = \frac{\sin^2\phi}{16}\exp\ i\left(\varphi_{LSB} - \varphi_{LO} + \frac{k_T\Delta\omega\Delta\tau}{2}\right)\sum_{k=-M}^{0}\sum_{l=k-k_T}^{0} T_k T_l \alpha_k \alpha_l \tag{5.27}$$

for $l \neq k + k_T$:

$$\hat{I}_{LF}(\omega_{IF}) = 0$$

$$\hat{I}_{LS}(\omega_{IF}) = 0$$

The phases of the four IF tones (the fast and slow polarisations of the USB and LSB) are extracted from Eq. (5.26) and (5.27) in order to measure GVD and DGD as shown in the next sections.

$$\begin{pmatrix} \varphi_{UF} & \varphi_{US} \\ \varphi_{LF} & \varphi_{LS} \end{pmatrix} = \begin{pmatrix} \varphi_{USB} - \varphi_{LO} - \dfrac{k_T\Delta\omega\Delta\tau}{2} & \varphi_{USB} - \varphi_{LO} + \dfrac{k_T\Delta\omega\Delta\tau}{2} \\ \varphi_{LSB} - \varphi_{LO} - \dfrac{k_T\Delta\omega\Delta\tau}{2} & \varphi_{LSB} - \varphi_{LO} + \dfrac{k_T\Delta\omega\Delta\tau}{2} \end{pmatrix} \tag{5.28}$$

It is also shown in the next sections that the amplitude of each IF tone can be extracted from Eq. (5.15) and (5.26) in order to determine the OSNR.

5.2.1 Analytical model for CD monitoring

From Eq. (5.28), the phase difference between the IF tones from the upper and lower sidebands for each polarisation state is defined by:

$$\Delta\varphi_{GVD\_F} = \varphi_{\mathrm{UF}} - \varphi_{\mathrm{LF}} = \varphi_{USB} - \varphi_{LSB} \tag{5.29}$$

and

$$\Delta\varphi_{GVD\_S} = \varphi_{\mathrm{US}} - \varphi_{\mathrm{LS}} = \varphi_{USB} - \varphi_{LSB} \tag{5.30}$$

It is clearly shown that both phase differences $\Delta\varphi_{GVD\_F}$ and $\Delta\varphi_{GVD\_S}$ measured respectively, on the fast and slow polarisation states, are equal:

$$\Delta\varphi_{GVD\_F} = \Delta\varphi_{GVD\_S} = \Delta\varphi_{GVD} \tag{5.31}$$

As described in section 2.3, the CD induces a time delay between the upper and lower sidebands of the optical signal, this time delay is converted into a phase shift $\Delta\varphi_{GVD}$. After transmission, the accumulated dispersion is given by:

$$GVD = \frac{1}{2\pi}\frac{c}{\lambda_T^2}\frac{1}{\omega_T^2}\Delta\varphi_{GVD} \tag{5.32}$$

where c is the light velocity, λ_T and ω_T are, respectively, the optical wavelength and angular frequency of the monitored tone.

It is shown analytically in Eq. (5.32) (and experimentally in chapter 6) that $\Delta\varphi_{GVD}$ is proportional to GVD and is independent of DGD. This is the case since the DGD will introduce the same amount of phase shift to both (φ_{UF}, φ_{LF}) and (φ_{US}, φ_{LS}) since PMD is, to the first order, wavelength independent. It is also noted that $\Delta\varphi_{GVD}$ is independent of noise and therefore independent of the OSNR. This is the case since the time-averaged IF tones are independent of the optical noise, as shown in Eq. (5.26) and (5.27).

The maximum measurement range GVD_{max} is defined such that $\Delta\varphi_{GVD} = 2\pi$:

$$GVD_{\max} = \frac{c}{\lambda_T^2}\frac{1}{\omega_T^2} \tag{5.33}$$

For an optical signal of 1550nm and a 5GHz monitored tone, the maximum monitoring range is equal to 4995ps/nm. A larger range can be obtained by reducing the monitored tone frequency at the expense of degrading the measurement accuracy (further analysis on the accuracy is conducted in the experimental chapter). Similarly, a smaller range can be obtained by increasing the monitored tone frequency which would need the use of higher bandwidth electronics but would achieve better measurement accuracy.

5.2.2 Analytical model for PMD monitoring

From Eq. (5.28), the phase difference between the slow and fast polarisation-components of the IF tones from each sideband is defined by:

$$\Delta\varphi_{DGD\_U} = \varphi_{US} - \varphi_{UF} = k_T \Delta\omega\Delta\tau = \omega_T \Delta\tau \tag{5.34}$$

and

$$\Delta\varphi_{DGD\_L} = \varphi_{LS} - \varphi_{LF} = k_T \Delta\omega\Delta\tau = \omega_T \Delta\tau \tag{5.35}$$

It is shown analytically in Eq. (5.34) and (5.35) that $\Delta\varphi_{DGD\_U}$ and $\Delta\varphi_{DGD\_L}$ are proportional to DGD and are independent of GVD. Since both sidebands are monitored at the same frequency, it is also shown that both phase differences, $\Delta\varphi_{DGD\_U}$ and $\Delta\varphi_{DGD\_L}$ are equal, thus it is sufficient to conduct measurements on one sideband to extract DGD:

$$\Delta\varphi_{DGD\_U} = \Delta\varphi_{DGD\_L} = \Delta\varphi_{DGD} = \omega_T \Delta\tau \tag{5.36}$$

Similarly to the CD measurement, it is noted that $\Delta\varphi_{DGD}$ is independent of the optical noise terms, and therefore independent of the OSNR.

The maximum measurement range $\Delta\tau_{\max}$ is defined such that $\Delta\varphi_{DGD} = 2\pi$:

$$\Delta\tau_{\max} = \frac{2\pi}{\omega_{\mathrm{T}}} \tag{5.37}$$

For a 5GHz monitored tone, the maximum monitoring range is equal to 200ps. Similarly to the CD range analysis mentioned above, a larger DGD range can be obtained by reducing the monitored tone frequency at the expense of degrading the measurement accuracy (further analysis on the accuracy is conducted in the experimental chapter).

5.2.3 Analytical model for OSNR monitoring

In this section, it is shown that the USB signal average-power in conjunction with the USB IF tone amplitude measurement provides a measure of OSNR. Identical results can also be obtained for the LSB, thus the OSNR measurement can be made using only one sideband signal. The signals average power is the result of the beating terms between any two tones of equal optical frequency. In this case, the expression of the signals average power is obtained from $I_{UF}(t)$ for an index $l = k$ and null for $l \neq k$. This can be demonstrated as follows: For $\theta_{\mathrm{U}} = \theta_{\mathrm{L}} = 0$ and $l = k$, $I_{UF}(t)$ and $I_{US}(t)$ are simplified to (see appendix 1):

for $l = k$

$$
\begin{aligned}
I_{\mathrm{UF}}(t) = {} & \frac{1}{4}\left(\begin{array}{l}
\cos^2\phi \sum_{k=0}^{M} T_k^2 \alpha_k^2 \\
+\frac{1}{2}\sum_{k=0}^{M} T_k^2 n_k^2 \\
+\frac{2}{\sqrt{2}}\cos\phi \sum_{k=0}^{M} T_k^2 \alpha_k n_k \cos\left(\omega_k \frac{\Delta\tau}{2} + (\varphi_{xrk} - \varphi_k)\right)
\end{array}\right) \\
& + \frac{1}{8}\left(\begin{array}{l}
\cos^2\phi \sum_{k=0}^{M} T_k^2 \alpha_k^2 \cos\left(\omega_{LO} t + \varphi_{LO}\right) \\
+\frac{1}{2}\sum_{k=0}^{M} T_k^2 n_k^2 \cos\left(\omega_{LO} t + \varphi_{LO}\right) \\
+\frac{2}{\sqrt{2}}\cos\phi \sum_{k=0}^{M} T_k^2 \alpha_k n_k \cos\left(\omega_{IF} t + \omega_k \frac{\Delta\tau}{2} + \varphi_{LO} - (\varphi_{xrk} - \varphi_k)\right)
\end{array}\right)
\end{aligned}
\tag{5.38}
$$

for $l \neq k$

$$I_{\mathrm{UF}}(t) = 0$$

and

for $l = k$

$$
\begin{aligned}
I_{\mathrm{US}}(t) = {} & \frac{1}{4}\left(\begin{array}{l}
\sin^2\phi \sum_{k=0}^{M} T_k^2 \alpha_k^2 \\
+\frac{1}{2}\sum_{k=0}^{M} T_k^2 n_k^2 \\
+\frac{2}{\sqrt{2}}\sin\phi \sum_{k=0}^{M} T_k^2 \alpha_k n_k \cos\left(-\omega_k \frac{\Delta\tau}{2} + (\varphi_{yrk} - \varphi_k)\right)
\end{array}\right) \\
& + \frac{1}{8}\left(\begin{array}{l}
\sin^2\phi \sum_{k=0}^{M} T_k^2 \alpha_k^2 \cos\left(\omega_{LO} t + \varphi_{LO}\right) \\
+\frac{1}{2}\sum_{k=0}^{M} T_k^2 n_k^2 \cos\left(\omega_{IF} t + \varphi_{LO}\right) \\
+\frac{2}{\sqrt{2}}\sin\phi \sum_{k=0}^{M} T_k^2 \alpha_k n_k \cos\left(\omega_{LO} t - \omega_k \frac{\Delta\tau}{2} + \varphi_{LO} - (\varphi_{yrk} - \varphi_k)\right)
\end{array}\right)
\end{aligned}
\tag{5.39}
$$

for $l \neq k$

$$I_{\mathrm{US}}(t) = 0$$

Since $\left\langle \cos\left(\omega t\right)\right\rangle = 0$ and $\left\langle \cos\varphi_r \right\rangle = \left\langle \sin\varphi_r \right\rangle = 0$, it is shown that the time-averaged detected signals $\left\langle I_{UF}\left(t\right)\right\rangle$ and $\left\langle I_{US}\left(t\right)\right\rangle$ are linearly proportional to the sum of the USB signal average-power $\sum_{k=0}^{M} T_k^2 \alpha_k^2$ and the noise power $\sum_{k=0}^{M} T_k^2 n_k^2$:

$$
\begin{cases}
< I_{UF}(t) >= \frac{1}{4}\left(\cos^2\phi \sum_{k=0}^{M} T_k^2 \alpha_k^2 + \frac{1}{2}\sum_{k=0}^{M} T_k^2 n_k^2\right) \\
< I_{US}(t) >= \frac{1}{4}\left(\sin^2\phi \sum_{k=0}^{M} T_k^2 \alpha_k^2 + \frac{1}{2}\sum_{k=0}^{M} T_k^2 n_k^2\right)
\end{cases}
\tag{5.40}
$$

However, both signals $\langle I_{UF}(t)\rangle$ and $\langle I_{US}(t)\rangle$ are dependent on ϕ, the angle between the linearly polarised signal and the fast principal state, which would make the OSNR measurement dependent on the incoming signal polarisation state. In order to suppress this dependency, the sum of both signals $\langle I_{UF}(t)\rangle$ and $\langle I_{US}(t)\rangle$ is calculated to be:

$$< I_U(t) >=< I_{UF}(t) > + < I_{US}(t) >= \frac{1}{4}\sum_{k=0}^{M} T_k^2\left(\alpha_k^2 + n_k^2\right) \tag{5.41}$$

The signal $\langle I_U(t)\rangle$ becomes solely dependent on the incoming signal average-power and noise power, and independent of PMD and CD. We define I_0 as the time-averaged signal power in the absence of noise:

$$I_0 = < I_U(t) >\big|_{n=0} = \frac{1}{4}\sum_{k=0}^{1} T_k^2 \alpha_k^2 \tag{5.42}$$

and the total noise power n^2 is defined as:

$$n^2 = \frac{1}{4}\sum_{k=0}^{1} T_k^2 n_k^2 \tag{5.43}$$

Such that the time-averaged detected signal $< I_U(t) >$ can be expressed by (see Eq. (5.41)):

$$< I_U(t) >= I_0 + n^2 \tag{5.44}$$

It is shown from Eq. (5.26) that the amplitude of the IF tones $\left|\hat{I}_{UF}(\omega_{IF})\right|$ and $\left|\hat{I}_{US}(\omega_{IF})\right|$, depends on the quantity $\sum_{k=0}^{M}\sum_{l=k+k_T}^{M} T_k T_l \alpha_k \alpha_l$ which is independent of the noise power:

$$\begin{cases} \left|\hat{I}_{UF}(\omega_{IF})\right| = \dfrac{\cos^2\phi}{16}\displaystyle\sum_{k=0}^{M}\sum_{l=k+k_T}^{M} T_k T_l \alpha_k \alpha_l \\ \left|\hat{I}_{US}(\omega_{IF})\right| = \dfrac{\sin^2\phi}{16}\displaystyle\sum_{k=0}^{M}\sum_{l=k+k_T}^{M} T_k T_l \alpha_k \alpha_l \end{cases} \tag{5.45}$$

However, both quantities $\left|\hat{I}_{UF}(\omega_{IF})\right|$ and $\left|\hat{I}_{US}(\omega_{IF})\right|$ are dependent on ϕ, which would also make the OSNR measurement dependent on the incoming signal polarisation state. In order to suppress this dependency, the sum of both quantities $\left|\hat{I}_{UF}(\omega_{IF})\right|$ and $\left|\hat{I}_{US}(\omega_{IF})\right|$ is calculated to be:

$$\left|\hat{I}_U(\omega_{IF})\right| = \left|\hat{I}_{UF}(\omega_{IF})\right| + \left|\hat{I}_{US}(\omega_{IF})\right| = \frac{1}{16}\sum_{k=0}^{M}\sum_{l=k+k_T}^{M} T_k T_l \alpha_k \alpha_l \tag{5.46}$$

The quantity $\left|\hat{I}_U(\omega_{IF})\right|$ is proportional to the sum of all beating terms between any two tones separated by the monitored tone frequency (i.e. for $l=k+k_T$) and is independent of the noise power, the PMD and CD.

It can easily be seen that the IF tone amplitude defined in Eq. (5.46) is linearly proportional to the signal power I_0. This can be demonstrated as follows: Let us consider that I_0 is amplified by a gain factor *G*. In this case, both I_0 and $\left|\hat{I}_U(\omega_{IF})\right|$ can be written as follows:

$$\begin{cases} \dfrac{1}{4}\sum\limits_{k=0}^{1}\left(\sqrt{G}T_k\alpha_k\right)^2 = G\dfrac{1}{4}\sum\limits_{k=0}^{1}T_k^2\alpha_k^2 = GI_0 \\ \sum\limits_{k=0}^{M}\sum\limits_{l=k+k_T}^{M}\left(\sqrt{G}T_k\alpha_k\right)\left(\sqrt{G}T_l\alpha_l\right) = G\sum\limits_{k=0}^{M}\sum\limits_{l=k+k_T}^{M}T_kT_l\alpha_k\alpha_l = G\left|I_U(\omega_{IF})\right| \end{cases} \tag{5.47}$$

Thus the IF tone amplitude can be written as a function of I_0 as follows:

$$\left|\hat{I}_U(\omega_{IF})\right| = \rho^2 I_0^2 \tag{5.48}$$

where ρ is a constant of proportionality dependent on the shape of the signal spectrum.

The ratio (R_U) of the USB signal average-power (signal and noise) from Eq. (5.41) to the USB IF tone amplitude (signal only) from Eq. (5.46), is inversely proportional to the signal-to-noise ratio, and is defined as:

$$R_U(M) = \frac{<I_U(t)>}{\left|\hat{I}_U(\omega_{IF})\right|} = \frac{1}{4}\frac{\sum\limits_{k=0}^{M}T_k^2\left(\alpha_k^2+n_k^2\right)}{\sum\limits_{k=0}^{M}\sum\limits_{l=k+k_T}^{M}T_kT_l\alpha_k\alpha_l} \tag{5.49}$$

Similar analysis can be done for the LSB. The ratio R_L can be derived from the previous equation by considering tones with negative indeces:

$$R_L(M) = \frac{<I_L(t)>}{\left|\hat{I}_L(\omega_{IF})\right|} = \frac{1}{4}\frac{\sum\limits_{k=-M}^{0}T_k^2\left(\alpha_k^2+n_k^2\right)}{\sum\limits_{k=-M}^{0}\sum\limits_{l=k-k_T}^{0}T_kT_l\alpha_k\alpha_l} \tag{5.50}$$

It is assumed that the power spectrum of the LSB and USB are symmetrical around the carrier (see Figure 5-2) which is justified by the use of a MZI filter with a symmetrical transfer function. In this case, the sum $\sum\limits_{-M}^{0}$ in Eq. (5.50) can be replaced by $\sum\limits_{0}^{M}$ leading to the ratio R_L being equal to R_U which will show in the following equations that one sideband measurement is sufficient for the OSNR monitoring.

$$R_U(M) = R_L(M) = R(M) \tag{5.51}$$

In order to illustrate the relationship of *R* to OSNR, the total signal power, *R* can be expressed as:

$$R = \frac{I_0 + n^2}{\rho I_0} = \frac{1}{\rho}\left(1 + \frac{n^2}{I_0}\right) \tag{5.52}$$

This ratio *R* is related to the OSNR as follows

$$OSNR = -10\log_{10}\left(\eta \frac{n^2}{I_0}\right) = -10\log_{10}\left(\eta\rho R - \eta\right) \tag{5.53}$$

where η is a constant of proportionality, dependent on the effective measurement bandwidth. The OSNR can then be determined from the measurement of *R* obtained from the ratio of the total power to the IF tone amplitude. It is noted that one sideband measurement is sufficient for the OSNR monitoring.

5.3 MZI filter detuning effect

The MZI filter used in these experiments is an integrated optical device with a 20GHz FSR. This filter is tuned and centred around one sideband to transmit either the lower or upper sidebands on either outputs of the device. Figure 5-4 shows the diagram of the filter, based on a Mach-Zehnder interferometer structure. The phase-shift $\varphi_{\mathrm{MZI}}(f)$ introduced in one arm of the interferometer is given by:

$$\varphi_{\mathrm{MZI}}(f) = 2\pi\left(\frac{f - f_T}{f_{FSR}}\right) \tag{5.54}$$

where f_T is the monitored tone frequency and f_{FSR} is the filter's FSR.

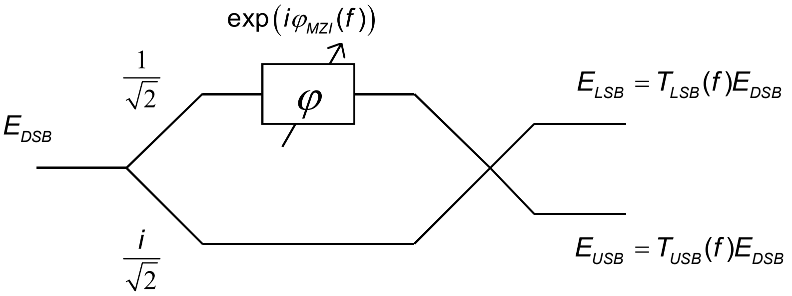

Figure 5-4: Diagram of the MZI filter device structure.

In order to transmit one sideband and suppress the other, an inherent relationship between f_T and f_{FSR} is such that (see Figure 5-5):

$$f_{FSR} = 4f_T \tag{5.55}$$

In a WDM system, the MZI FSR is chosen as a sub-multiple of the channel spacing in order to transmit the USB and suppress the LSB of all channels simultaneously. In the experimental work described in the next chapter, f_T was equal to ~5GHz, f_{FSR} equal to

20GHz with a WDM channel spacing of 100GHz. The MZI amplitude transfer-function for both the lower and upper sidebands can be modelled as follows:

$$\begin{cases} T_{LSB}(f) = \cos\left(\frac{1}{2}\varphi_{\mathrm{MZI}}(f)\right)\exp\left(\frac{i}{2}\varphi_{\mathrm{MZI}}(f)\right) \\ T_{USB}(f) = i\sin\left(\frac{1}{2}\varphi_{\mathrm{MZI}}(f)\right)\exp\left(\frac{i}{2}\varphi_{\mathrm{MZI}}(f)\right) \end{cases} \tag{5.56}$$

Figure 5-5 shows the diagram of the filter's detuning direction in relation to the data signal. In order to illustrate the effect of the filter's detuning on the proposed monitoring technique, the filtered SSB optical field can be modelled as two monochromatic tones where *M=1* and $k_T = 1$, referred to as a two-tone model, as described in the section 6.5, thus greatly simplifying the filter detuning analytical results.

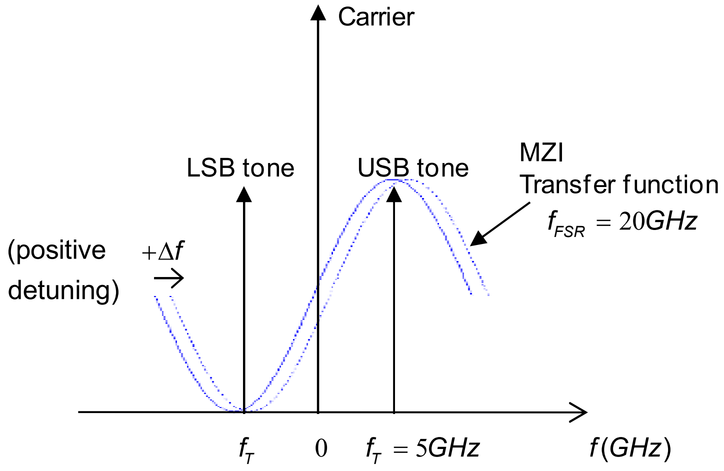

Figure 5-5: Diagram of the MZI filter detuning.

Using the two-tone model, the expression of the IF tones, is then given by Eq. (5.26):

$$\begin{cases} \hat{I}_{UF}(\omega_{IF}) = \frac{\cos^2\phi}{16}\exp\, i\left(\varphi_{USB} - \varphi_{LO} - \frac{k_T\Delta\omega\Delta\tau}{2}\right)T_0T_1\alpha_0\alpha_1 \\ \hat{I}_{US}(\omega_{IF}) = \frac{\sin^2\phi}{16}\exp\, i\left(\varphi_{USB} - \varphi_{LO} + \frac{k_T\Delta\omega\Delta\tau}{2}\right)T_0T_1\alpha_0\alpha_1 \end{cases} \tag{5.57}$$

where $T_0 = T(0)$ and $T_1 = T(f_T)$, the filter's transfer-function, respectively, at the carrier and the monitored tone frequency. In order to assess the filter's detuning effect on PMD and CD monitoring, the phase of the four monitored tones is reassessed taking into account the filter's phase contribution. The phases of the two USB IF tones are:

$$\begin{cases} \varphi_{UF} = \varphi_{USB} - \varphi_{LO} - \frac{k_T\Delta\omega\Delta\tau}{2} + \frac{1}{2}\varphi_{\mathrm{MZI}}(0) + \frac{1}{2}\varphi_{\mathrm{MZI}}(f_T) + \frac{\pi}{2} \\ \varphi_{US} = \varphi_{USB} - \varphi_{LO} + \frac{k_T\Delta\omega\Delta\tau}{2} + \frac{1}{2}\varphi_{\mathrm{MZI}}(0) + \frac{1}{2}\varphi_{\mathrm{MZI}}(f_T) + \frac{\pi}{2} \end{cases} \tag{5.58}$$

And the phases of the two LSB IF tones are:

$$\begin{cases} \varphi_{LF} = \varphi_{LSB} - \varphi_{LO} - \dfrac{k_T \Delta\omega \Delta\tau}{2} + \dfrac{1}{2}\varphi_{MZI}(0) + \dfrac{1}{2}\varphi_{MZI}(f_T) + \dfrac{\pi}{2} \\ \varphi_{LS} = \varphi_{LSB} - \varphi_{LO} + \dfrac{k_T \Delta\omega \Delta\tau}{2} + \dfrac{1}{2}\varphi_{MZI}(0) + \dfrac{1}{2}\varphi_{MZI}(f_T) + \dfrac{\pi}{2} \end{cases} \tag{5.59}$$

From the equations above, it is show that Eq. (5.36) and Eq. (5.31) remain valid, where $\Delta\varphi_{DGD} = k_T \Delta\omega \Delta\tau$ and $\Delta\varphi_{GVD} = \varphi_{USB} - \varphi_{LSB}$ are both independent of the filter's phase impact. This is the case since the MZI filter introduces the same phase shift for each monitored tone.

The MZI filter's detuning effect on OSNR is also assessed. With no detuning, the ratio *R* for the USB can be derived from Eq. (5.49) when considering a two-tone model (*M=1*):

$$R(\Delta f = 0) = \frac{< I_U(t) >}{|I_U(\omega_{IF})|} = \frac{1}{4} \frac{|T(0)|^2 \left(\alpha_0^2 + n_0^2\right) + |T(f_T)|^2 \left(\alpha_1^2 + n_1^2\right)}{|T(0)||T(f_T)|\alpha_0 \alpha_1} \tag{5.60}$$

where $T_0 = T\left(f = 0\right)$ and $T_1 = T\left(f = f_T\right)$.

By introducing a filter detuning Δf, the expression of R becomes:

$$R(\Delta f) = \frac{< I_U(t) >}{|I_U(\omega_{IF})|} = \frac{1}{4} \frac{|T(\Delta f)|^2 \left(\alpha_0^2 + n_0^2\right) + |T(f_T + \Delta f)|^2 \left(\alpha_1^2 + n_1^2\right)}{|T(\Delta f)||T(f_T + \Delta f)|\alpha_0 \alpha_1} \tag{5.61}$$

It is shown from Eq. (5.61) that the ratio R, thus the OSNR measurement, is affected by the filter's detuning, since $|T(0)| \neq |T(\Delta f)|$ and $|T(f_T)| \neq |T(f_T + \Delta f)|$. This is the case since detuning the filter changes both the USB average-power and the IF tone's amplitude. Experimental and simulation results quantifying the OSNR measurement error and the filter's detuning are given in the next chapter.

5.4 Summary

In this chapter, we have derived an analytical model for the proposed OPM technique used to simultaneously and independently measure chromatic dispersion, PMD and OSNR. This analytical model relies on the use of a Fourier series representation for the optical fields. This allows us to derive a generalised model for all impairments which is then simplified to a two-tone model. The latter allows us to derive a simple expression for the filter detuning effect. We have shown that both CD and PMD rely on phase measurements whereas the OSNR relies on amplitude measurements of the monitored tone. The analytical expressions for the three impairments have shown that they are independent of each other, which represent a major technological achievement compared to the OPM techniques described to date. The impact of the filter detuning on the monitoring performance has also been investigated. The method is shown to be insensitive to the filter's detuning when monitoring CD or PMD, however, it is not insensitive when monitoring OSNR. The required filter detuning to achieve given accuracy for each impairment is experimentally obtained and presented in the next chapter. It is shown that the analytical results presented in this chapter agree very well with the experimental results presented in chapter 6.

Chapter 6: Experimental and simulation results

6.1 Introduction

In this chapter, the experimental and simulation results of the proposed optical performance monitoring (OPM) technique are given for chromatic dispersion (CD), first-order polarisation mode dispersion (PMD) and optical signal-to-noise ratio (OSNR) measurements. The analysis of the results is based on the equations developed in the previous chapter. In section 6.2, the experimental implementation is described alongside key components of the setup such as the electronic detection stage, the EAMs transfer function and the adjustment of the polarisation controllers, are also presented in more detail in order to allow the reader to duplicate any result. In sections 6.3 to 6.5, the results for the group velocity dispersion (GVD), differential group delay (DGD) and OSNR measurement are presented and the impact that each impairment has on the measurement of the others is also investigated. The performance of the proposed method for a particular impairment monitoring can be expressed in terms of measurement range and accuracy, defined as the root mean square (RMS) error. The measurement range achieved with this method is equal to 4742±100ps/nm for GVD, 200±4ps for DGD and 25±1dB for OSNR. It is also shown that these three impairment measurements are independent of each other.

In sections 6.6 to 6.8, the impact of acquisition-time, filter detuning and wavelength division multiplexing (WDM) crosstalk are demonstrated. As predicted by the theory, longer acquisition-time has no effect on the maximum measurement range but reduces the measurement error for all impairments. The acquisition-time is then chosen as a compromise between the required measurement accuracy and the required measurement-time. The filter detuning is shown to have no impact on the GVD and DGD measurements, which are based on the phase detection, but is shown to deteriorate the OSNR measurement, which is based on the power detection. The crosstalk from adjacent WDM channels is shown to have no impact on any of the three impairment measurements, making this method suitable for multi-channel operation. It is noted that in the experimental results, all non-linear transmission effects have been neglected, to this effect, we equally refer to CD or GVD and to PMD or DGD.

6.2 Experimental implementation

6.2.1 Setup

The experimental setup for the simultaneous GVD, DGD and OSNR measurement is shown in Figure 6-1. The data signal is a multi-channel 39.81312Gbit/s, 2^{15}-1 pseudorandom binary sequence (PRBS) non-return-to-zero (NRZ). There are nine channels centered around 1553.228nm with 100GHz channel-spacing. Four spools of SMF are used to vary the CD, a 1st order PMD emulator is used to introduce a variable DGD and the OSNR is varied with a variable noise loading stage using an ASE source.

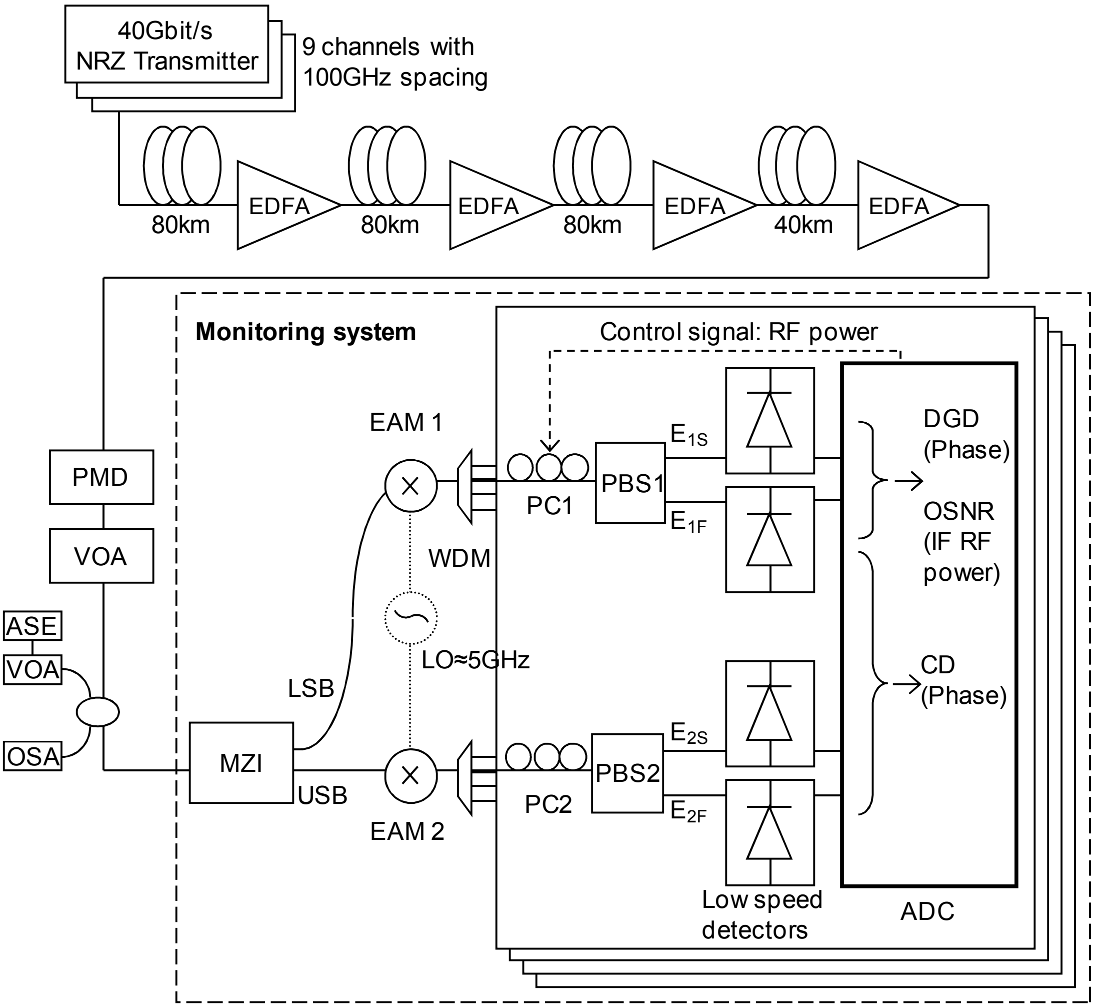

Figure 6-1: 40Gbit/s multi-channel GVD, DGD and OSNR monitoring system based on electro-optical mixing.

The main signal is tapped and sent through an optical filter to select the SSB signals. In a WDM system, a Mach-Zehnder interferometer (MZI) filter with a free spectral range (FSR) equal to a sub-multiple of the channel spacing can be used, as an e.g., a MZI filter with 50GHz FSR (thus monitoring the 12.5GHz tone where the monitored tone is ¼ of the FSR, as shown in section 5.3) could be used for a 100GHz or 200GHz channel spacing. In this multi-channel experiment, the MZI filter used has a FSR of 20GHz with a channel spacing of 100GHz. Each output port of the MZI filter transmits one side-band and suppresses the other side-band. In this experiment, using a 39.81312Gbit/s bit-rate and a PRBS of 2^{15}-1, the monitored tone frequency (f_T) is equal to:

$$f_T = 4.977250 GHz \tag{6.1}$$

Nine WDM channels have been used with wavelengths ranging from 1550.048nm to 1556.508nm. The two outputs of the MZI filter simultaneously provide both the filtered upper and lower sidebands of the multi-channel signal. The lower sideband (LSB) and upper sideband (USB) signals of the monitored channel are down-converted in the optical domain using two EAMs (Oki OM5521W-200X) with a 22GHz bandwidth, and 8dB insertion-loss (IL). The EAMs are driven with a free running local oscillator (LO) using a sinusoidal signal at a frequency (f_{LO}):

$$f_{LO} = 4.977240GHz \tag{6.2}$$

f_{LO} is shifted from the monitored tone frequency by ~10kHz corresponding to the down-converted intermediate frequency (f_{IF}):

$$f_{IF} = 10kHz \tag{6.3}$$

The individual channels are then separated by two wavelength-demultiplexer (WDM) filters of 100 GHz spacing. Each down-converted optical signal is filtered using a polarization beam splitter (PBS) separating the signal into two components along the two orthogonal polarisation states (PSPs) of the PBS, which are then detected using two low-speed photo-detectors. The signals are digitized for further processing using an analogue-to-digital card (ADC) with a maximum sampling rate of 1.25MS/s, 32 channels and 16bit resolution (National Instruments NI 6259). In these experiments, and due to the limited maximum sampling-rate of the ADC, only one optical channel (the central channel at 1553.228nm) was monitored using four channels (the fast and slow polarisation axis of the USB and LSB) of the ADC at a sampling rate of 300kS/s. In software a fast Fourier transform (FFT) is applied to the four signals, and the amplitude and phase of the tone at the IF of 10kHz is extracted for each signal. The phase and amplitude of the IF tones on the slow and fast principal PSPs will depend on the PBS orientation angles of the USB and LSB (θ_U, θ_L respectively). In order to suppress this dependency, θ_U and θ_L must be adjusted to zero (see section 5.3.5), which can be achieved by tuning a polarisation controller (PC) placed before each PBS. It is noted that the use of a PBS is necessary for PMD measurements but not required for CD and OSNR measurements as shown in section 4.2.4. The RF power of the IF tones is used as a control feedback to tune the polarisation controller (PC1) placed before PBS1 (see Figure 6-1). Within one sideband, the maximum RF power of one IF tone (corresponding to the minimum RF power of the second IF tone) coincide with the alignment of the PBS and signal's PSPs. In this experiment, PC1 and PC2 were adjusted manually, however, in the field; the control system could be automated. Once the PCs are adjusted, the phase measurement of these four IF tones is extracted to provide a measurement of CD and DGD, as shown analytically in sections 5.2.1 and 5.2.2, whereas their amplitudes in conjunction with the total average power provides a measure of OSNR , as shown analytically in section 5.2.3. It is noted that all measurements of CD, DGD and OSNR are independent of the arbitrary polarisation power splitting-ratio of the monitored optical signal.

6.2.2 Low-speed detection circuit

Each monitored channel requires four low-speed photo-detectors that are in turn connected to an ADC. The responsivity of these photo-detectors (JDS Uniphase EPM 605 LL-250) for wavelengths around 1550nm is 0.88A/W. Figure 6-2 shows the electronic stage connecting the photodiodes to the ADC. A 100kΩ resistor is used in series to the photodiode in order to keep the cut-off frequency above 100kHz (a higher resistor of 1MΩ would have reduced this cut-off frequency to 10KHz, making the 10kHz tone monitoring difficult to achieve). In order to increase the voltage from the photodiode and the resistor of100kΩ, an additional voltage gain of 10 is introduced using an inverting amplifier. A voltage-follower stage in a unity configuration with high input impedance is inserted as a buffer before the ADC to isolate the impedance change that occurs on the multiplexing card of the ADC. The overall electronic stage connecting the photodiodes to the ADC has an equivalent-impedance of 1MΩ. A typical detected optical power is around -30dBm, providing a photo-current of around 0.88μA and an electrical signal of around 0.88V.

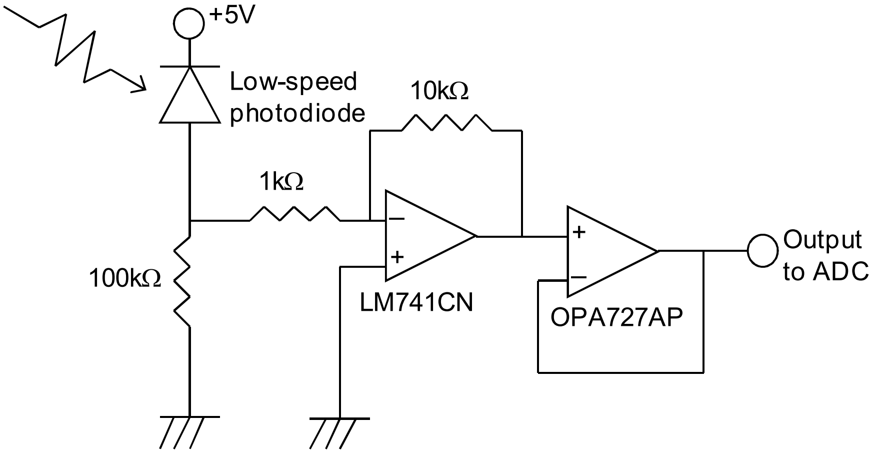

Figure 6-2: Electronic circuit of the low-speed detectors.

Figure 6-3 shows a typical measured power-spectrum of the received electrical signal when an input optical signal with 20dB OSNR is incident on the monitoring system. The input optical power is around -33dBm (measured at the photo-diode input), the average detected signal is equal to 0.4V and the IF tone is equal to 1.3mV. The IF tone frequency is around 10kHz; other tones can also be observed above 30kHz. These spurious signals, also observed without any optical signal and without powering ON the photodiode electronic stage, come from the ADC. The spurious signals could be suppressed with additional electrical filtering although it is noted that they had no impact on the 10kHz tone detection.

In order to determine the sensitivity of the system, and thus the required tapped power from the network's main line, the optical input power to the photo-detectors is varied from -25dBm to -45dBm whilst the GVD, DGD and OSNR are kept at constant levels of 2685ps/nm, 100ps and 20dB respectively. Experimental results show that all levels of GVD, DGD and OSNR remain constant for an input power higher than -40dBm. Performance deterioration is however observed for optical power levels below -40dBm. -40dBm optical signal corresponds to an average electrical signal of 0.08V and an IF tone amplitude as low as 0.2mV for 30dB OSNR level. It is noted that the electronic noise-floor of the system coming from the electronic stage and ADC is measured to be around 0.03mV. In a network implementation, the required amount of tapped signal will depend on the OPM total loss, thus the need for an appropriate choice of each component loss.

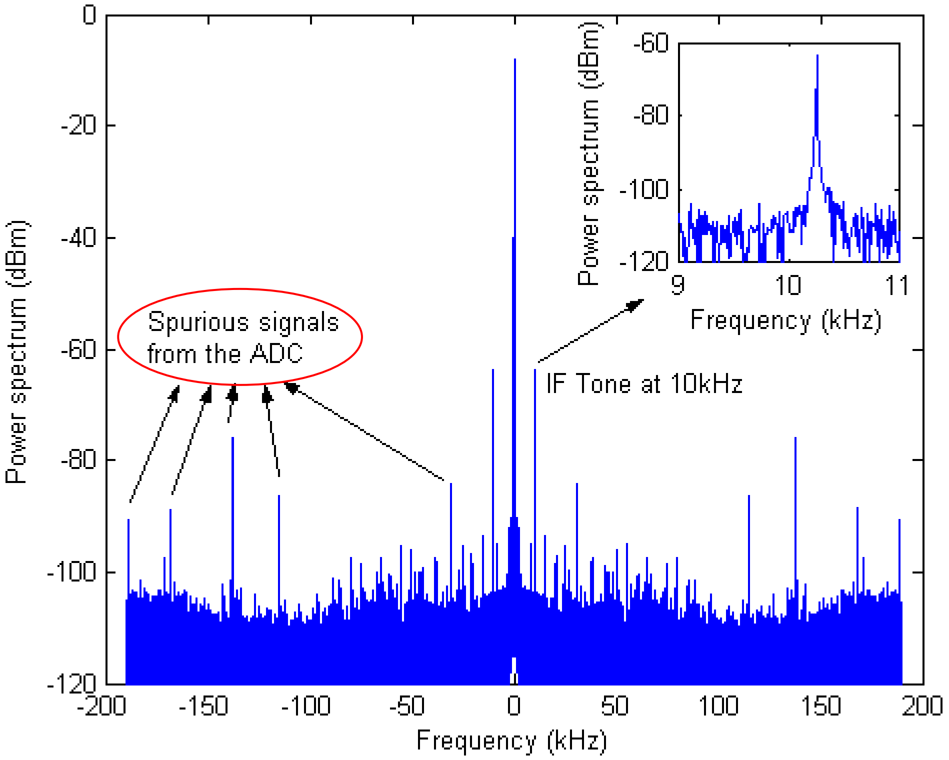

Figure 6-3: Typical power spectrum of a detected signal with 20dB OSNR (LSB, fast axis). The average signal is around 0.4V and the IF tone around 1.3mV.

It is noted that drifts of the local oscillator relative to the signal carrier will vary the IF, but will not have an impact on the monitoring technique since the peak of the IF tone is tracked in the software. However, drifts in the IF will limit the integration time. In this experiment the IF is observed to drift by only 0.1Hz/s observed over a period of 4 hours. In these experiments, the maximum integration time used is 100ms and so will not be significantly affected by the IF drift.

6.2.3 EAM transfer function

In the previous chapter, the analytical development of the monitoring technique was done using the assumption that the EAMs used for the optical down-conversion had a raised-cosine transfer function. This assumption allowed us to extract simplified expressions for the

GVD, DGD and OSNR monitoring. This section aims to justify the use of a raised-cosine transfer function. The intensity transfer function of an EAM can be represented in terms of the reversed applied voltage *V* by the expression [MIT'92]:

$$G(V) = \exp\left(-\left(\frac{V}{V_0}\right)^a\right) \tag{6.4}$$

where *G* is the EAM's transmission function, *a* and V_0 are two constants that can be determined experimentally.

Figure 6-4 shows the experimental data of the transmission of both EAMs used for the upper and lower side-bands as a function of the reversed bias voltage (*V*). A least-squares-fit of the experimental data points to the analytical function given in Eq (6.4) is used to determine the value of the constants *a* and V_0. The constants *a* and V_0 for the upper side-band (EAM1) are equal to:

$$V_0 = 1.02 \qquad a = 1.82 \tag{6.5}$$

and for the lower side-band (EAM2):

$$V_0 = 1.09 \qquad a = 1.90 \tag{6.6}$$

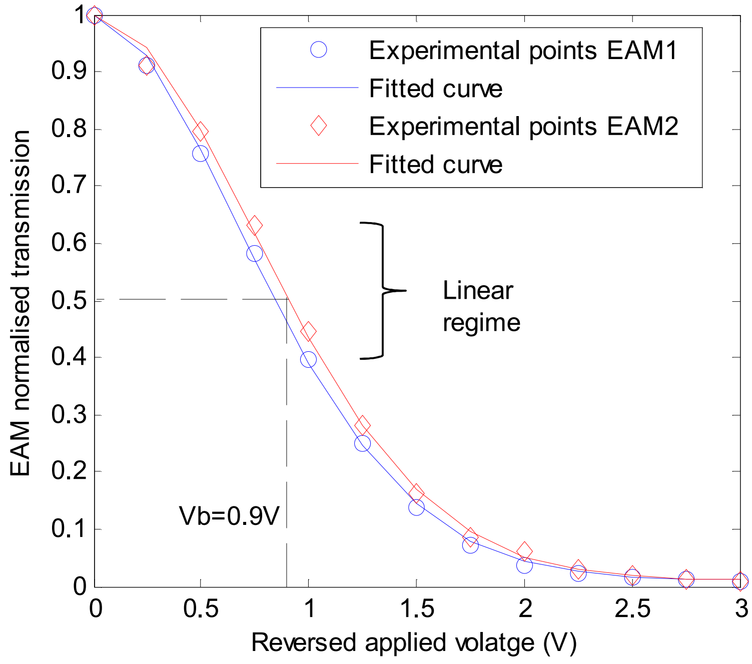

Figure 6-4: Experimental data and analytical curve showing the normalised transmission of the upper and lower side-bands EAMs as a function of the reversed bias voltage.

In the experiment, the EAM modulator is biased at a voltage V_b and driven with a modulating voltage V_m for a total applied voltage of:

$$V = V_b + V_m \tag{6.7}$$

and

$$V_m(t) = V_A \cos(\omega_{LO} t + \varphi_{LO}) \tag{6.8}$$

where V_A is the modulation voltage amplitude, ω_{LO} and φ_{LO} are, respectively, the local oscillator angular frequency and phase. The bias voltage ($V_b = 0.9V$) is experimentally chosen at the inflection point of the transmission curve where the EAM's transmission is equal to 50%. The EAM transfer function *G* as a function of *V* can be expanded in a Taylor series around V_b; *G(V)* is then given by [HAL'90, LEE'99]:

$$G(v) = G(v_b) + \left.\frac{dG}{dv}\right|_{v_b} v_m + \frac{1}{2!}\left.\frac{d^2G}{dv^2}\right|_{v_b} v_m^2 + \ldots \tag{6.9}$$

where

$$v = \frac{V}{V_0} \qquad v_m = \frac{V_m}{V_0} \qquad v_b = \frac{V_b}{V_0} \tag{6.10}$$

and

$$G(v) = c_0 + c_1 v_m + c_2 v_m^2 + \ldots \tag{6.11}$$

where c_n are the Taylor series coefficients. Each term of Eq. (6.11) expresses the specific order distortion of the transfer function at the specific DC bias. For a bias voltage at the inflection point, the coefficient c_0 , which represents the normalised intensity at the bias point, is equal to 0.5 ($c_0 = \frac{1}{2}$) and the second-order coefficient corresponding to the second derivative, is eliminated ($c_2 = 0$) at this inflection point [WIL'97]. Using a small-signal approximation, a first order approximation of the Taylor series can then be considered where the second order is null and the third order and higher are neglected:

$$G(v) = c_0 + c_1 v_m \tag{6.12}$$

thus

$$G(t) = \frac{1}{2}\left(1 + 2c_1 \frac{V_A}{V_0} \cos(\omega_{LO} t + \varphi_{LO})\right) \tag{6.13}$$

The analytical expressions of c_1 is derived:

$$c_1 = -a v_b^{a-1} \exp\left(-v_b^a\right) \tag{6.14}$$

c_1 can be calculated using Eq. (6.5) and the value of V_b (*c_1=0.7*). The modulation voltage amplitude V_A is chosen such that $2c_1 \frac{V_A}{V_0} = 1$ (thus *V_A=0.7V*), in which case the transfer function *G* can then be modelled as a raised cosine, and used in the analytical model to help obtain simpler analytical solutions, and is given by:

$$G(t) = \frac{1}{2}\left(1 + \cos(\omega_{LO} t + \varphi_{LO})\right) \tag{6.15}$$

Experimentally, the modulation voltage amplitude V_A is chosen such that only the linear part of the EAM transfer function is used. When using a CW optical input to the EAM, modulated at the LO frequency, the RF spectrum of the output signal is measured. The restriction to the linear part of the EAM transfer function corresponds to an RF spectrum of the output optical signal containing only one peak at the LO frequency with no visible higher order harmonics. In this configuration, the experimental result was $V_A=1V$. It is noted that there is a discrepancy in value between the theoretical value of $V_A=0.7V$ calculated with a static transfer function and the experimental value of $V_A=1.1V$, obtained in a dynamic regime (when the EAM is modulated at the LO frequency). This discrepancy corresponds to a 2dB loss (0.7/1.1) at the LO frequency of 5GHz. This is indeed expected since the EAM used has a 22GHz bandwidth corresponding to a 3dB loss in transmission at 22GHz and a 2dB loss at 5GHz, which is caused by the 50Ω impedance match circuit used in the EAM. In summary, we have shown that the raised cosine transfer function used in Eq. (6.15) is an acceptable model for an EAM when biasing the EAM at the inflection point of its transfer function and using an RF signal within the linear part of the transfer function.

6.2.4 Adjustment of the polarisation controllers

We've shown in the analytical chapter that the phase and amplitude of the IF tones on the slow and fast PSPs depend on the PBS orientation angles (θ). In order to suppress this dependency, θ must be adjusted to zero, which can be achieved by tuning a polarisation controller (PC) placed before each PBS. The RF power of each IF tone is used as a control feed-back to tune the PCs. This can be demonstrated by plotting the amplitude of the fast and slow USB IF tone ($\hat{I}_{UF}(\omega_{IF})$ and $\hat{I}_{US}(\omega_{IF})$) as a function of the angle θ. The expressions for $\hat{I}_{UF}(\omega_{IF})$ and $\hat{I}_{US}(\omega_{IF})$ are given in the following equations (see section 5.2):

$$\hat{I}_{UF}(\omega_{IF})=\frac{1}{16}\left(\begin{array}{l}\cos^2\phi\cos^2\theta_U \exp\, i\left(\varphi_{USB}-\varphi_{LO}-\dfrac{k_T\Delta\omega\Delta\tau}{2}\right)\sum\limits_{k=0}^{M}\sum\limits_{l=k+k_T}^{M}T_kT_l\alpha_k\alpha_l\\ +\sin^2\phi\sin^2\theta_U \exp\, i\left(\varphi_{USB}-\varphi_{LO}+\dfrac{k_T\Delta\omega\Delta\tau}{2}\right)\sum\limits_{k=0}^{M}\sum\limits_{l=k+k_T}^{M}T_kT_l\alpha_k\alpha_l\\ +2\sin\phi\cos\phi\sin\theta_U\cos\theta_U \exp\, i\left(\varphi_{USB}-\varphi_{LO}-(\omega_{k+\Delta k}+\omega_k)\dfrac{\Delta\tau}{2}\right)\\ \sum\limits_{k=0}^{M}\sum\limits_{l=k+k_T}^{M}T_kT_l\alpha_k\alpha_l\end{array}\right) \qquad (6.16)$$

and

$$\hat{I}_{US}(\omega_{IF}) = \frac{1}{16}\left(\begin{array}{l} \cos^2\phi \sin^2\theta_U \exp\ i\left(\varphi_{USB} - \varphi_{LO} - \frac{k_T \Delta\omega\Delta\tau}{2}\right)\sum_{k=0}^{M}\sum_{l=k+k_T}^{M} T_k T_l \alpha_k \alpha_l \\ + \sin^2\phi \cos^2\theta_U \exp\ i\left(\varphi_{USB} - \varphi_{LO} + \frac{k_T \Delta\omega\Delta\tau}{2}\right)\sum_{k=0}^{M}\sum_{l=k+k_T}^{M} T_k T_l \alpha_k \alpha_l \\ -2\sin\phi\cos\phi\sin\theta_U\cos\theta_U \exp\ i\left(\varphi_{USB} - \varphi_{LO} - (\omega_{k+\Delta k} + \omega_k)\frac{\Delta\tau}{2}\right) \\ \sum_{k=0}^{M}\sum_{l=k+k_T}^{M} T_k T_l \alpha_k \alpha_l \end{array}\right) \qquad (6.17)$$

Figure 6-5 shows the normalised IF tone amplitude of $\hat{I}_{UF}(\omega_{IF})$ and $\hat{I}_{US}(\omega_{IF})$ as a function of the PBS orientation angles (θ). As the angle θ varies from 0 to 2π, it can be seen that both amplitudes follow a sinusoidal function. It can also be seen that both functions are in quadrature, when $\hat{I}_{UF}(\omega_{IF})$ reaches a maximum level, $\hat{I}_{US}(\omega_{IF})$ reaches a minimum level. In the experiment, a polarisation controller is placed before each PBS and tuned to maximise the tone $\hat{I}_{UF}(\omega_{IF})$ such that $\theta=0$, which coincide with the alignment of the PBS and the signal's PSPs. This allowed us to derive expressions of the IF tones which are independent of the angle θ, thus independent of the signal's polarisation incident angle. It can be noted that in a field implementation, the polarisation controllers would be automated thus reducing the current monitoring time required to do a measurement.

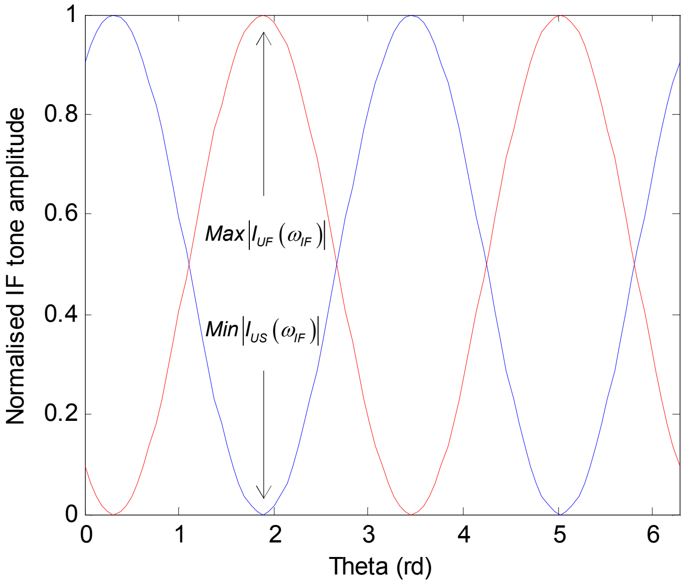

Figure 6-5: Simulation results showing the normalised IF tone amplitude as a function of the PBS orientation angles (θ).

6.2.5 Continuum spectrum generated by a random data stream

In these experiments, a 40Gbit/s, 2^{15}-1 PRBS signal was used. This pattern length provides a frequency-separation between the data tones within the data bandwidth of around 1.22MHz. The presence of these data tones was the basis of a Fourier representation of the signal used in the analytical model described in the previous chapter. Due to the low sampling rate used in the ADC (300kS/s per channel), only one down-converted data tone was observed in each power spectrum. Increasing the pattern length to for example 2^{31}-1 PRBS would have provided a frequency-separation of around 18Hz, approaching a continuum spectrum. In this configuration, tracking the IF tone would not be possible. To alleviate this problem, a software modification for the data processing is required. Rather than simply monitoring the amplitude at a discrete tone, the software would simply integrate the signal over a fixed bandwidth around the nominal IF tone. The calibration of the system would result in different calibration constants but it is expected that none of the results obtained in this chapter would change with the use of higher PRBS sequences.

6.3 CD monitoring

Chromatic dispersion was added to the signal using four spools of SMF of 80, 160, 240 and 280km corresponding respectively to 1350, 2685, 4035 and 4742ps/nm. At first we only consider the effect of CD, by having no PMD added to the system and an OSNR level of 30dB, in order to determine the CD range and accuracy of the system. Then the impact of DGD and OSNR on the CD measurement is investigated. Each measurement is repeated 100 times and the RMS error is calculated in order to determine the monitoring accuracy.

6.3.1 Range and accuracy

Figure 6-6 shows the comparison between the CD measured using this technique and the actual CD measured with a dispersion test set. When measuring the CD, the values obtained for each polarisation state are averaged to improve the accuracy. The RMS error in the measured CD is calculated to be ±100ps/nm over the range of 4742ps/nm, which corresponds to a 2% error. This measurement range of 4742ps/nm corresponds to the predicted theoretical value of 4992ps/nm, corresponding to a phase difference φ_{CD} of 2π (see section 2.3). It is noted that better measurement accuracy can be achieved using higher monitoring tone frequency at the expense of reducing the monitoring range (since the maximum range is inversely proportional to the frequency). This can intuitively be understood by the fact that for a given monitored frequency, a maximum phase range of 2π will correspond to a given maximum GVD range, while reducing the latter will reduce (thus improve) the measurement sensitivity.

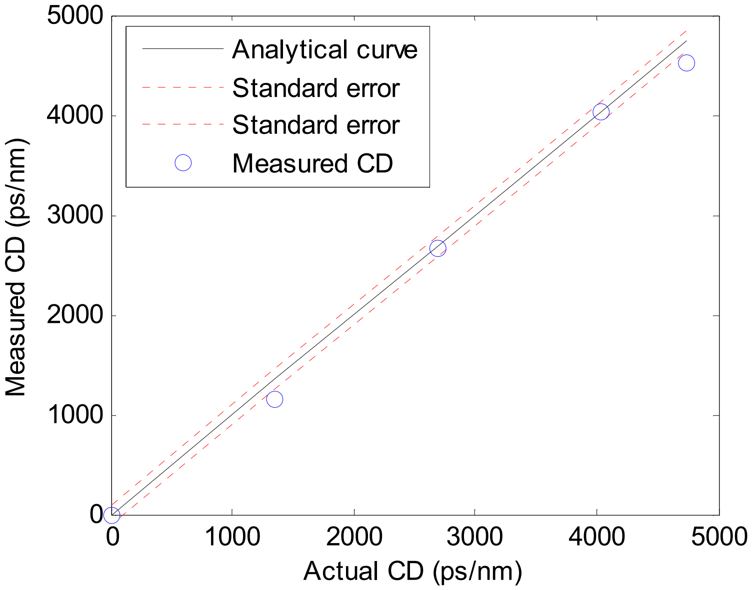

Figure 6-6: CD monitoring range (DGD=0ps/nm, OSNR=30dB).

6.3.2 Impact of PMD on the CD measurement

The level of CD was maintained at an arbitrary constant level of 2685ps/nm while varying the DGD from 0 to 200ps. Figure 6-7 shows the comparison between the CD measured using this technique and the actual DGD. It is shown that the CD measurement is insensitive to DGD, as predicted theoretically. It can be observed that few measurement points are outside the ±100ps/nm measurement error. This can be attributed to the manual adjustment of the PC for both the USB and LSB, which lead to a residual misalignment of the signal PSPs onto the PBS PSPs as described in section 5.2.

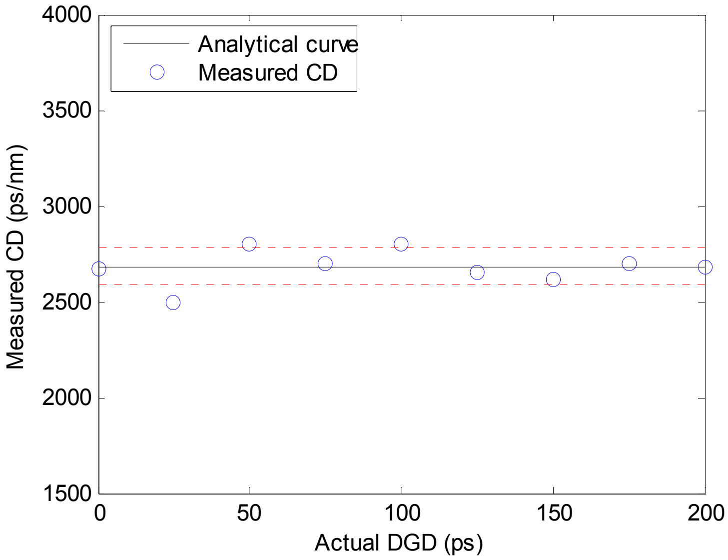

Figure 6-7: Impact of DGD on the CD measurement (CD=2685ps/nm, OSNR=30dB).

This experiment has been repeated for other CD values (1350ps/nm and 4035ps/nm); as expected theoretically, none of the CD measurements were sensitive to DGD. As such, we have shown that a SSB measurement (using a MZI filtering effect) allows for CD monitoring independently of DGD.

6.3.3 Impact of OSNR on the CD measurement

The level of CD was maintained at an arbitrary constant level of 2685ps/nm while varying the OSNR from 10dB to 30dB and neglecting any PMD effect (DGD=0ps). Figure 6-8 shows the comparison between the CD measured using this technique and the actual OSNR. It is shown that the CD measurement is insensitive to OSNR, as predicted theoretically.

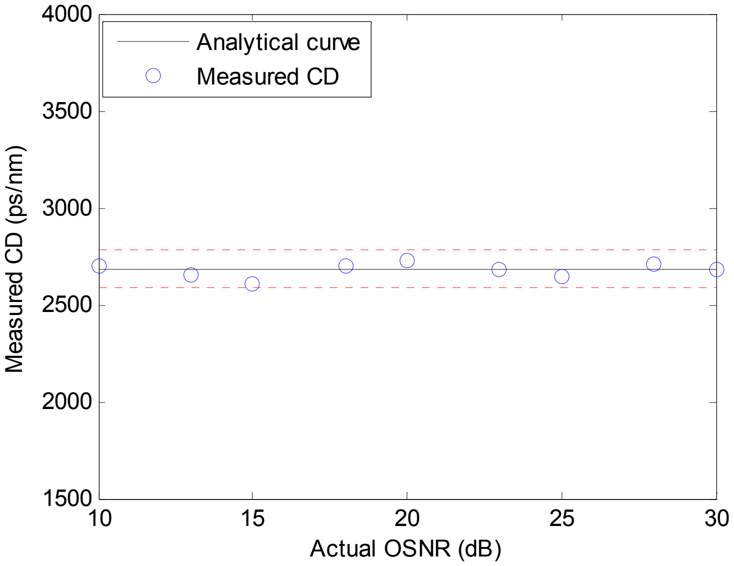

Figure 6-8: Impact of OSNR on the CD measurement (CD=2685ps/nm, DGD=0ps).

6.4 PMD monitoring

The DGD measurement is initially tested without introducing any chromatic dispersion and with a constant OSNR level of 30dB. A 1st order PMD emulator is used to vary the DGD value from 0 to 200ps with a step of 25ps. The polarisation power splitting-ratio of the monitored optical signal takes an arbitrary value, but doesn't require to be controlled since the DGD measurement is independent of it. It is necessary to use a PBS at each sideband in order to achieve DGD measurement as shown on Figure 6-1. It has been shown that the DGD is proportional to the difference between the two phases of the IF tone on the slow and fast PSPs of a one sideband, it is thus noted that a single sideband monitoring is sufficient to achieve this measurement. The phase measurements of the IF tones on the slow and fast PSPs will depend on the PBS orientation angles of the USB and LSB (θ_U, θ_L respectively). As seen previously, in order to suppress this dependency, θ_U and θ_L must be adjusted to zero (see section 5.2) which can be achieved by tuning a polarisation controller (PC) placed before each PBS, providing a DGD measurement independently of the signal polarisation orientation angle. The impact of varying CD and OSNR on the DGD measurement is also investigated. Each measurement is repeated 100 times and the RMS error is calculated in order to determine the monitoring accuracy for each measurement.

6.4.1 Range and accuracy

The DGD measurement is initially tested without introducing any chromatic dispersion, with an OSNR level of 30dB. A 1st order PMD emulator was used to vary the DGD value from 0 to 200ps with in steps of 25ps. Figure 6-9 shows the comparison between the measured DGD obtained using this technique for both the upper and lower sidebands and the actual DGD. The DGD measurement RMS error is calculated to be ±4ps over the measurement range of 200ps, also corresponding to a 2% error. This measurement range corresponds to the predicted theoretical value of 203ps, corresponding to a phase difference φ_{DGD} of 2π (see section 2.4). It is noted that the DGD measurement can be obtained from one sideband measurement and that both sidebands display the same range and accuracy, they can thus be averaged in order to improve the accuracy.

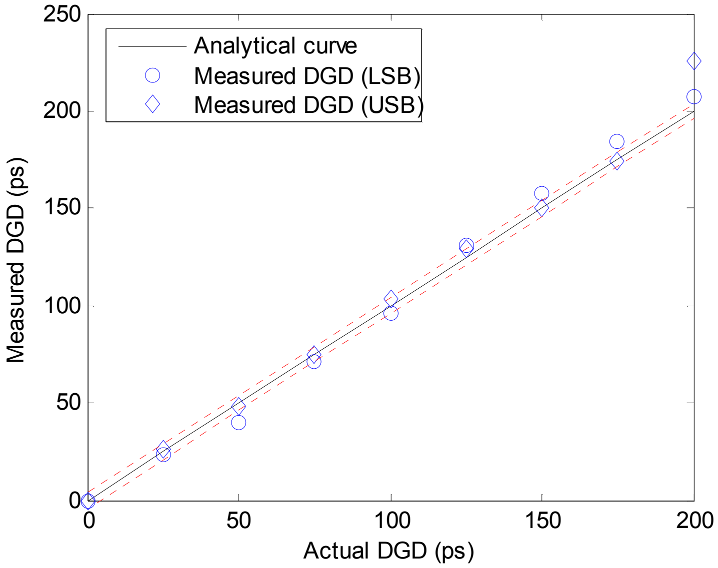

Figure 6-9: DGD monitoring range (CD=0ps/nm, OSNR=30dB).

6.4.2 Impact of CD on the PMD measurement

Chromatic dispersion was added to the signal using four spools of SMF of 80, 160, 240 and 280km corresponding respectively to 1350, 2685, 4035 and 4742ps/nm. The level of DGD was maintained at an arbitrary constant level of 100ps while varying the CD from 0 to 4742ps/nm. Figure 6-10 shows the comparison between the DGD measured using this technique and the actual CD. It is shown that the DGD measurement is insensitive to CD, as predicted theoretically in section 5.2. The use of PBS after the optical down-conversion allows for PMD monitoring independently of CD.

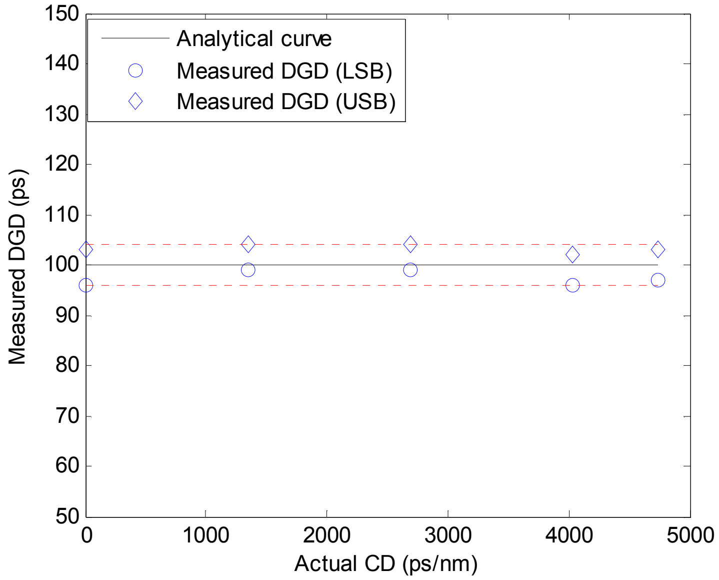

Figure 6-10: Impact of CD on the DGD measurement (DGD=100ps, OSNR=30dB).

6.4.3 Impact of OSNR on the PMD measurement

The OSNR was varied from 10db to 30dB by keeping the signal at a constant power level and attenuating the ASE source as shown in Figure 6-1. Figure 6-11 shows the comparison between the DGD measured using this technique and the actual OSNR. It is shown that the DGD measurement is insensitive to OSNR, as predicted theoretically.

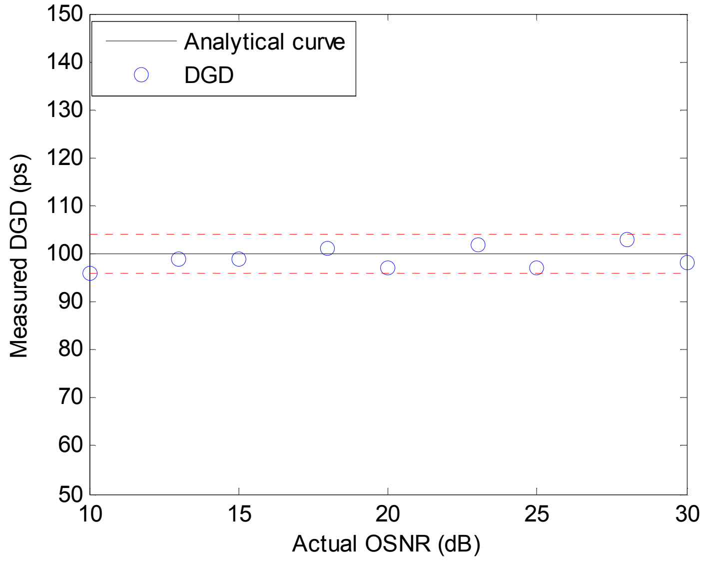

Figure 6-11: Impact of OSNR on the DGD measurement (DGD=100ps, CD=0ps/nm).

6.5 OSNR monitoring

It has been shown in the analytical chapter that a single sideband measurement is sufficient to perform an OSNR measurement. As a result, only the USB tone is detected to monitor the OSNR. A data acquisition of the USB signals on the fast and slow polarisation axis is experimentally taken for an OSNR level of 20dB. Figure 6-12 shows the power spectrum of both signals.

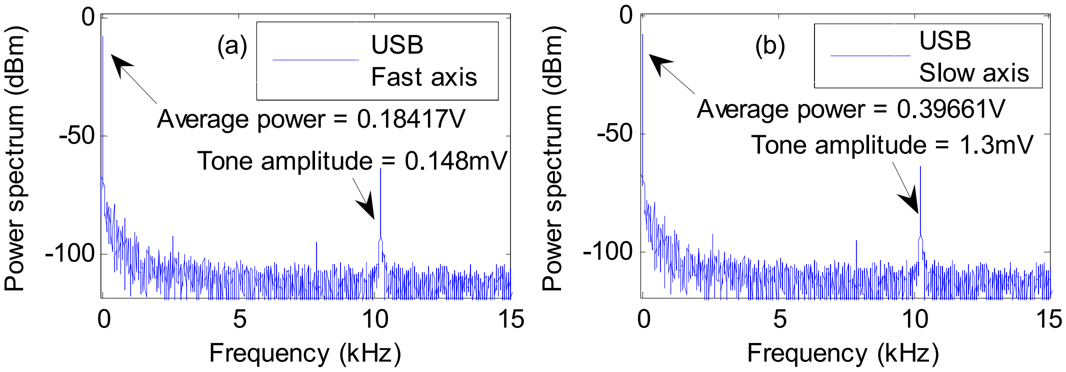

Figure 6-12: Measured power spectrum of the detected USB signals. (a) Fast axis, (b) Slow axis (OSNR=20dB, CD=0ps/nm, DGD=100ps).

The time-averaged detected signal and the IF tone amplitude are extracted from the power spectrum where:

$$\begin{aligned} &< I_{UF}(t) >= 0.18417V, \qquad \left|\hat{I}_{UF}(\omega_{IF})\right| = 0.148mV \\ &< I_{US}(t) >= 0.39661V, \qquad \left|\hat{I}_{US}(\omega_{IF})\right| = 1.3mV \end{aligned} \tag{6.18}$$

It is noted that for this particular measurement, the IF tones on the slow and fast PSP axis vary from each other by an order of magnitude, which is caused by the arbitrary polarisation power splitting-ratio.

Two-tone model approximation

As explained in the analytical chapter, in order to make the OSNR measurement independent of the signal's polarisation state, the sum of the average power and amplitude tone on both the fast and slow PSP axis are calculated and used to determine the factor R which will in turn allow us to calculate the OSNR value.

$$\begin{aligned} < I_U(t) > &= < I_{UF}(t) > + < I_{US}(t) > \\ &= \frac{1}{4}\left(\left|T(0)\right|^2\left(\alpha_0^2 + n_0^2\right) + \left|T(f_T)\right|^2\left(\alpha_1^2 + n_1^2\right)\right) \\ &= 0.58078V \end{aligned} \tag{6.19}$$

and

$$\begin{aligned}\left|\hat{I}_U(\omega_{IF})\right| &= \left|\hat{I}_{UF}(\omega_{IF})\right| + \left|\hat{I}_{US}(\omega_{IF})\right| \\ &= \left|T(0)\right|\left|T(f_T)\right|\alpha_0\alpha_1 \\ &= 1.448mV\end{aligned} \tag{6.20}$$

Where α_0 and α_1 are, respectively, the field amplitude of the optical signal at the carrier and tone frequencies; n_0 and n_1 are, respectively, the field amplitude of the optical noise at the carrier and tone frequencies; and $T(f)$ is the MZI transfer function which is given by (see section 5.3):

$$\left|T(f)\right| = \cos\left(\frac{\pi}{8}\left(\frac{f}{f_T}-1\right)\right) \tag{6.21}$$

From which we can extract the transmission value at the carrier and tone frequencies, T(0) and $T(f_T)$:

$$\left|T(0)\right| = \cos\left(\frac{\pi}{8}\right), \qquad \left|T(f_T)\right| = 1 \tag{6.22}$$

It is noted that a filter's maximum transmission is obtained at the monitored frequency ($f_T \approx 5GHz$). It is assumed that the noise is white and thus has constant spectral density within the bandwidth of the signal (therefore $n_0=n_1$) and that it can be approximated in relation to the signal, for an OSNR of 20dB, as follows:

$$n_0^2 + n_1^2 = 0.01\left(\alpha_0^2 + \alpha_1^2\right) \tag{6.23}$$

From Eq. (6.19) and Eq. (6.20):

$$\begin{cases}\dfrac{1}{4}\left(\cos\left(\dfrac{\pi}{8}\right)^2\left(\alpha_0^2 + 0.005\left(\alpha_0^2+\alpha_1^2\right)\right) + \left(\alpha_1^2 + 0.005\left(\alpha_0^2+\alpha_1^2\right)\right)\right) = 0.58078V \\ \cos\left(\dfrac{\pi}{8}\right)\alpha_0\alpha_1 = 1.448mV\end{cases} \tag{6.24}$$

We can then extract the values of α_0 and α_1 which will be used in section 6.7 to calculate the impact of filter detuning on the OSNR measurement:

$$\alpha_0 = 1.6498\sqrt{V}, \qquad \alpha_1 = 0.95e-3\sqrt{V} \tag{6.25}$$

The carrier amplitude is three orders of magnitude larger than that of the 5GHz tone amplitude, for an NRZ signal modulated at 40Gbit/s. Despite this large ratio, the 5GHz tone can easily be detected, after down-conversion to the 10kHz intermediate-frequency, due to its high signal-to-noise ratio (SNR) which is in the order of 40dB as shown in Figure 6-12. A much stronger carrier in relation to the monitored tone also justifies the use of the two-tone model as described in section 5.2.3.

Gaussian approximation of the R measurement distribution

The OSNR is varied from 10db to 30dB by keeping the signal at a constant power level and attenuating the ASE source as shown in Figure 6-1. No CD or PMD is introduced into the system. It shown in section 5.2.3 that within one sideband, the ratio (*R*) of the signal average-power (signal and noise) to the IF tone amplitude (signal only) is inversely proportional to the OSNR. The *R* measurement was repeated 100 times for each OSNR value. Figure 6-13 shows a typical distribution of *R*. It is observed that this distribution follows a Gaussian curve. The mean value of each set of measurement of *R* is used to determine the mean OSNR used for the system calibration, whereas the standard variation of *R* is used to determine the standard error of the OSNR measurement as shown in the following section.

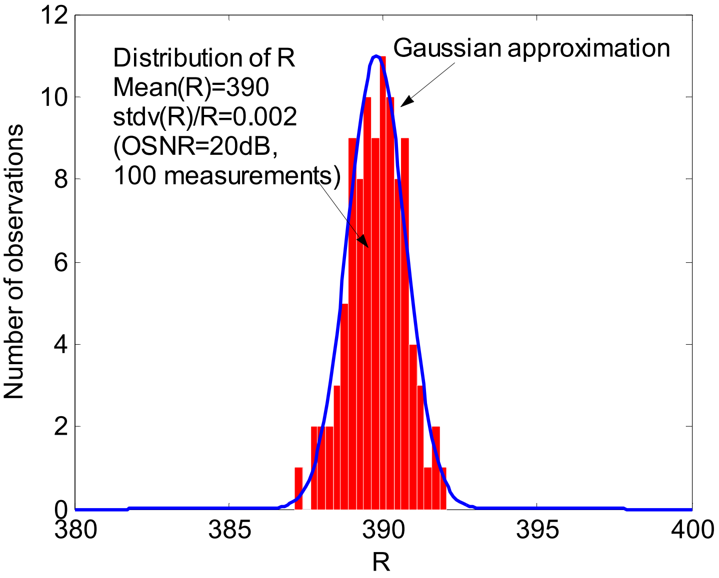

Figure 6-13: Histogram of the R factor distribution over 100 measurements (OSNR=20dB).

6.5.1 Range and accuracy

It has been shown in the analytical chapter that the OSNR can be derived from the ratio *R* as follows:

$$OSNR = -10\log_{10}\left(\eta\rho R - \eta\right) \tag{6.26}$$

where both η and ρ are constants of proportionality. As such, the linear OSNR can also be expressed as a function of *R* as follows:

$$OSNR_{lin} = \frac{1}{\eta\rho R - \eta} \tag{6.27}$$

Figure 6-14 shows the comparison between the *R* measurement and the linear OSNR measured over a 0.5nm bandwidth (for 40Gbit/s signals) using an optical spectrum analyser (OSA) for OSNR values ranging between 10dB and 30dB. It is observed that *R* is inversely proportional to OSNR, as predicted by Eq. (6.27). The constants η and ρ, have been experimentally obtained in calibrating the system by fitting Eq. (6.27) to the measured *R* as a function of the independently measured OSNR using an OSA. The values of these constants are equal to $\eta=0.0209$ and $\rho=3.676e\text{-}3$. Figure 6-14 also shows that a given *R* measurement error is expected to cause larger OSNR measurement error for low R values and thus for high levels of OSNR.

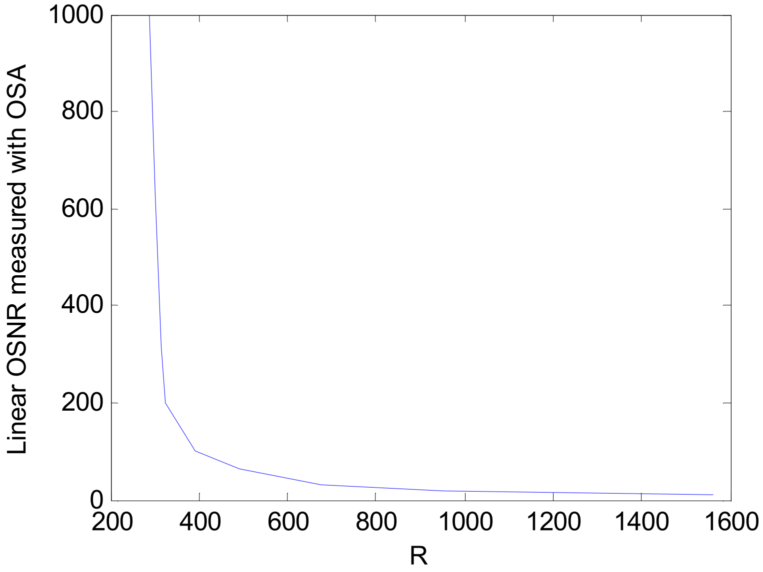

Figure 6-14: The linear OSNR is inversely proportional to the R measurement.

The standard variation of *R* is used to determine the standard error in the linear OSNR measurement.

$$\sigma^2\left(OSNR_{lin}^{-1}\right)=Slope^2\sigma^2\left(R\right)+R^2\sigma^2\left(Slope\right)+\sigma^2\left(Intercept\right) \tag{6.28}$$

where

$$Slope=\eta\rho \tag{6.29}$$

and

$$Intercept=-\eta \tag{6.30}$$

The normalised standard error of the *R* measurement is experimentally determined and found equal to 0.2% ($\frac{\sigma^2\left(R\right)}{R}=0.002$). The standard error of the slope and the intercept ($\sigma^2\left(Slope\right)$ and $\sigma^2\left(Intercept\right)$) are derived from the squares least fitting formulae. Figure 6-15 shows the comparison between the OSNR measured using this technique (using the results shown in the previous figure) and the OSNR measured using an OSA. The standard error arising from the calibration and experimental uncertainty is also shown in Figure 6-15. For OSNR values less than 25dB the standard error is less than 1dB, however, the standard error increases considerably for OSNR values higher than 25dB. The increase in error at large OSNR arises from the error in the measurement of the signal and noise term when the noise power is considerably smaller than that of the signal power. The measurement range could be further improved by reducing the noise in the detection and processing electronics. This limitation, for higher OSNR values, remains inconsequential for most applications where OSNR levels of 20dB and below are critical to detect.

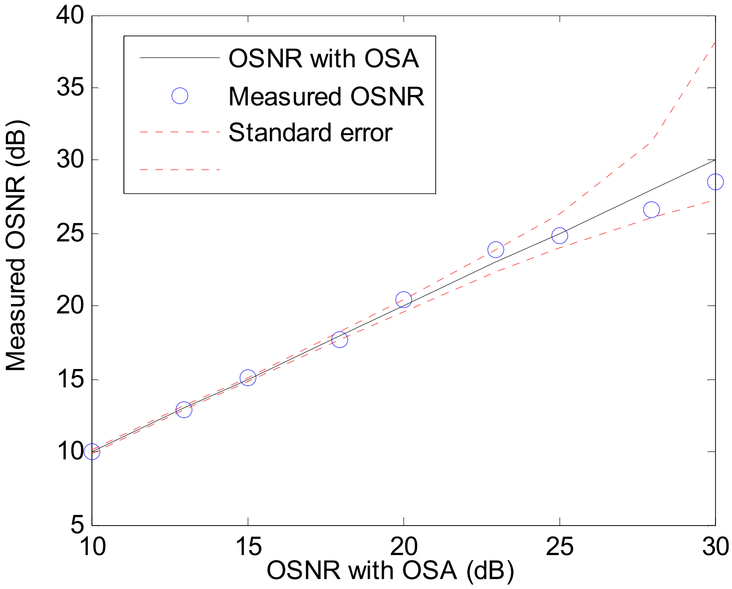

Figure 6-15: OSNR monitoring range and accuracy (CD=0ps/nm, DGD=0ps).

6.5.2 Impact of CD on the OSNR measurement

The level of OSNR was maintained at an arbitrary constant level of 20dB while varying the CD from 0 to 4742ps/nm.

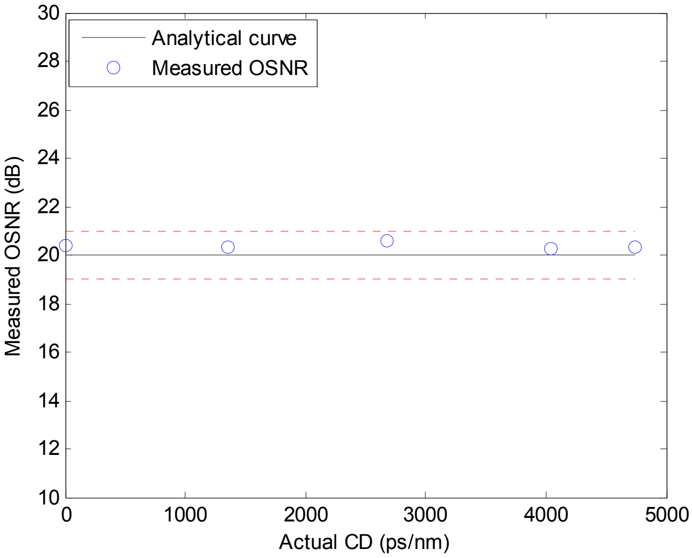

Figure 6-16: Impact of CD on the OSNR measurement (OSNR=20dB, DGD=0ps).

Figure 6-16 shows the comparison between the OSNR measured using this technique and the actual CD. It is shown that all data points lie within the 1dB accuracy, and thus the OSNR measurement is insensitive to CD, as predicted theoretically.

6.5.3 Impact of PMD on the OSNR measurement

The level of OSNR was maintained at an arbitrary constant level of 20dB while varying the DGD from 0 to 200ps. Figure 6-17 shows the comparison between the OSNR measured using this technique and the actual DGD. Similarly to the previous conclusion related to GVD, all data points lie within the 1dB accuracy, as such, it is shown that the OSNR measurement is insensitive to DGD, as predicted theoretically.

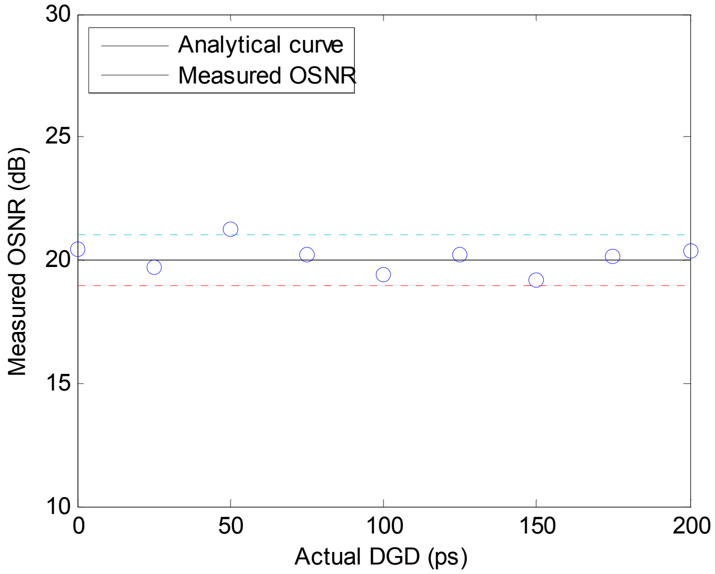

Figure 6-17: Impact of DGD on the OSNR measurement (OSNR=20dB, CD=0ps/nm).

6.6 Acquisition-time effect

The monitoring-time is the time required to complete a measurement. This time is particularly important when monitoring dynamically reconfigurable networks. If we ignore the travel-time of the optical signal within the setup, the monitoring-time is primarily due to three parts:

$$\textit{Monitoring-time} = \textit{PC adjustment-time} + \textit{Acquisition-time} + \textit{Processing-time} \quad (6.31)$$

Where PC adjustment-time is the time required to mechanically tune the polarisation controllers (PC), using a feed-back signal as shown in Figure 6-1, in order to adjust the PBS polarisation orientation angle to zero which is necessary to do any of the impairment measurements, as shown in chapter 5. The acquisition-time is the time required to acquire a set number of data-points and the processing-time is the time required to process these data-points using an FFT, in order to complete the measurement. This experiment focuses on the effect of the acquisition-time on the measurements accuracy. The impairments are fixed at a constant level equal to 2685ps/nm (corresponding to 160km) for CD, 100ps for DGD and 25dB for OSNR. With a sampling rate of 380kS/s, a single scan of 100ms (thus 38,000 data-points) is acquired and processed for each of the four signals at the output of the two PBS (see Figure 6-1). Shorter acquisition-times are obtained by processing a smaller number of data-points from the original scans.

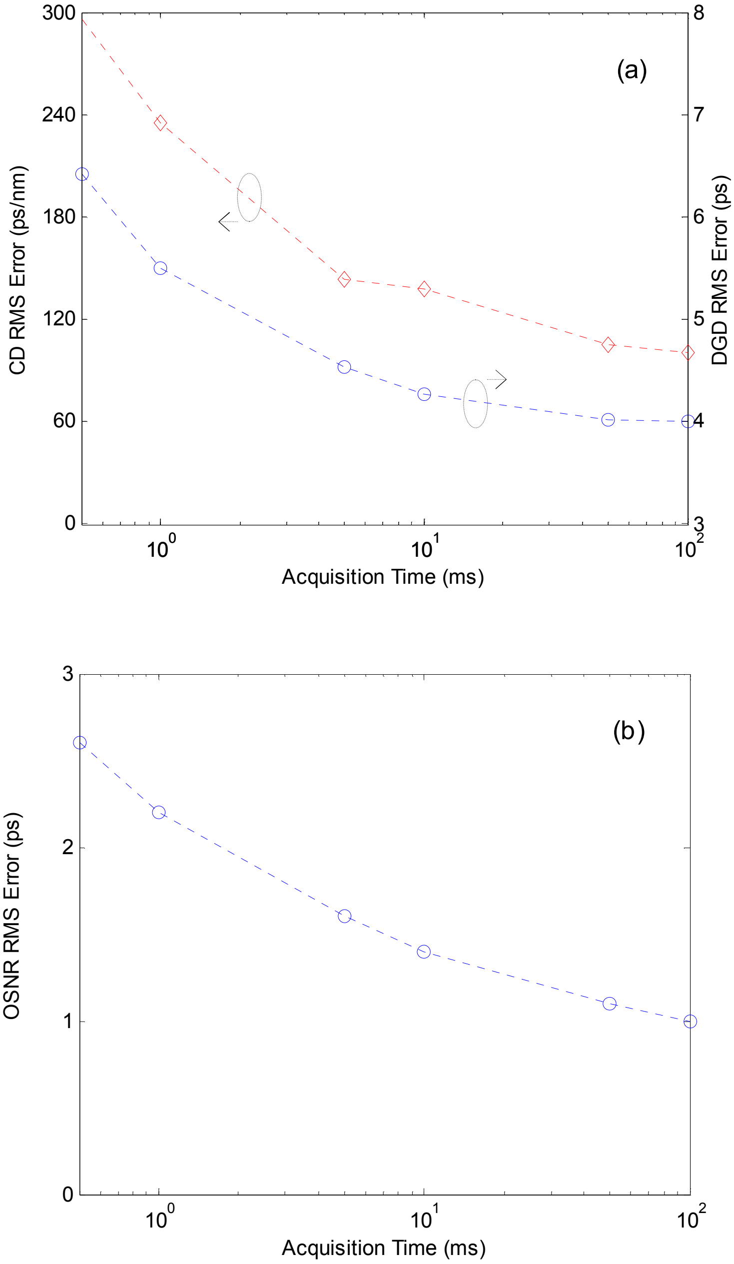

Figure 6-18: Acquisition-time effect on (a) CD (GVD=2685ps/nm) and DGD (DGD=100ps) measurement, (b) OSNR (OSNR=25dB) measurement.

Figure 6-18(a) shows the effect of reducing the acquisition-time from 100ms to 0.5ms on the RMS error in the CD and DGD measurement and Figure 6-18(b) shows the effect of reducing the acquisition-time on the RMS error in the OSNR measurement. The accuracy, achieved for acquisition times of 100ms for GVD, DGD and OSNR, is respectively 100ps/nm, 4ps and 1dB which corresponds to the acquisition time used in all experiments presented in this chapter. For 10ms acquisition-time, the RMS errors increase to 155ps/nm, 4.6ps and 1.5dB. It can be observed from the results above that better accuracy is achieved with longer acquisition-time where the averaging is done over more periods of the monitored tone. This is due to the fact that for a given sampling rate, a longer acquisition-time equates to a larger number of acquired points, which provides a better frequency resolution of the FFT, thus a smaller RMS error [JAC'07]. It is however expected that above a certain acquisition-time value, the accuracy doesn't improve anymore as it reaches the system's accuracy threshold. This threshold is due to various effects such as the PC adjustment accuracy and the noise floor of the electronic stage. In a real implementation, the choice of the parameters will be a compromise between the monitoring-time (thus the acquisition-time) and the required measurement accuracy.

6.7 Optical filter detuning effect

The MZI filter is used to filter each sideband from the dual-sideband incoming signal. The filter is tuned and maintained at a given tuning position such that each output port passes one sideband and suppresses the other sideband. It is under this configuration, corresponding to zero detuning, where the setup calibration is performed for all impairment monitoring. If the filter drifts from its desired position of zero detuning, the amplitude and phase of the monitored tones can be altered due to the amplitude and phase response of the filter. The filter has been detuned experimentally by 5GHz, in 2.5GHz steps, from either side of the zero detuning position in order to assess the impact this has on the GVD, DGD and OSNR measurements. For this investigation the GVD, DGD and OSNR are set to 2685ps/nm, 100ps and 20dB respectively. Figure 6-19(a) shows the MZI filter detuning effect on the CD and DGD measurement. As expected, both impairments remain constant within their measurement error of ±100ps/nm and ±4ps for CD and DGD respectively. This has been demonstrated analytically in the previous chapter and can be explained by the fact that the MZI filter has a linear phase-shift response introducing the same phase error for each of the four measured phases on the fast and slow polarisation axis of the USB and LSB, and is thus cancelled when calculating the phase-difference for either GVD or DGD. Clearly, as the filter detuning increases such that the IF tone power is fully attenuated, the measurement uncertainty increases due to a degraded SNR.

The analytical model described in the previous chapter (see section 5.3) has been used to calculate the change in the ratio *R* as a function of the filter detuning (Δf):

$$R(\Delta f) = \frac{1}{4}\frac{\left|T(\Delta f)\right|^2\left(\alpha_0^2 + n_0^2\right) + \left|T(f_T + \Delta f)\right|^2\left(\alpha_1^2 + n_1^2\right)}{\left|T(\Delta f)\right|\left|T(f_T + \Delta f)\right|\alpha_0\alpha_1} \tag{6.32}$$

Where the MZI transfer function is given by:

$$\left|T(\Delta f)\right| = \cos\left(\frac{\pi}{8}\left(\frac{\Delta f}{f_T}-1\right)\right) \tag{6.33}$$

A filter detuning of 0GHz, ±2.5GHz and ±5GHz correspond to a ratio $\frac{\Delta f}{f_T}$ of 0, 0.5 and 1 ($f_T \approx 5GHz$). Assuming again that the noise is white and thus has constant amplitude within the bandwidth of the signal, then:

$$n_0 = n_1 \tag{6.34}$$

In this case, R can be expressed as:

$$R(\Delta f) = \frac{1}{4}\frac{\cos^2\left(\frac{\pi}{8}\left(\frac{\Delta f}{f_T}-1\right)\right)\left(\alpha_0^2+n_0^2\right)+\cos^2\left(\frac{\pi}{8}\frac{\Delta f}{f_T}\right)\left(\alpha_1^2+n_0^2\right)}{\sqrt{\cos\left(\frac{\pi}{8}\left(\frac{\Delta f}{f_T}-1\right)\right)\cos\left(\frac{\pi}{8}\frac{\Delta f}{f_T}\right)\alpha_0\alpha_1}} \tag{6.35}$$

The values of $\alpha_0 = 1.6498\sqrt{V}$ and $\alpha_1 = 0.95e-3\sqrt{V}$ are experimentally extracted (see Eq. (6.25)) and used to simulate Eq.(6.35). For an OSNR level of 20dB, the noise power can be approximated such that $n_0^2 + n_1^2 = 0.01\left(\alpha_0^2+\alpha_1^2\right)$. Figure 6-19(b) shows the MZI filter detuning effect on the ratio R and the OSNR measurement. This figure shows that the ratio R increases between 336 and 470 with a detuning of +/-5GHz. This corresponds to an OSNR value decreasing from 23 to 18.3dB with an actual value of 20dB at zero detuning.

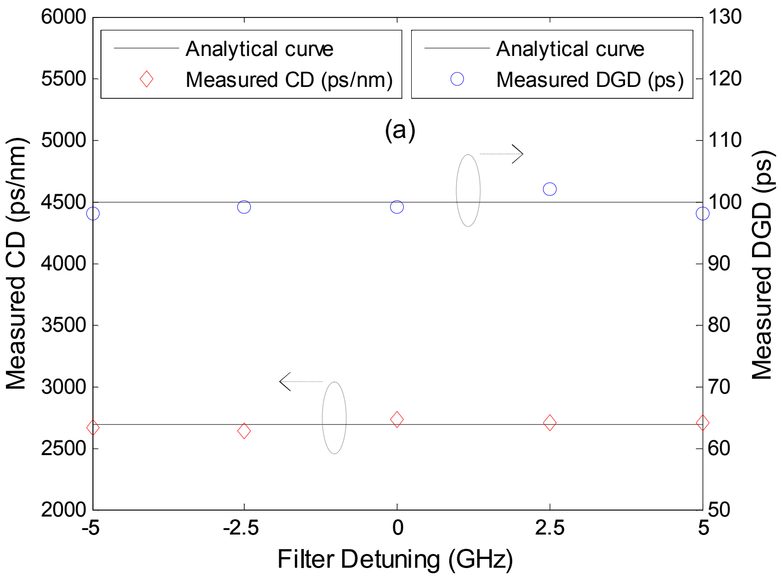

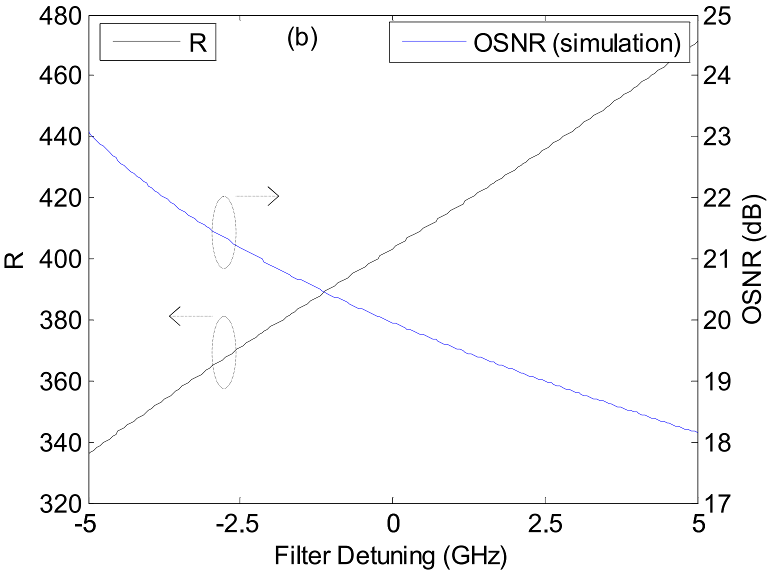

Figure 6-19: Simulation results showing the filter detuning effect on the factor *R* and OSNR (OSNR=20dB).

These experiments show that phase-based measurements (thus CD and PMD) are insensitive to filter detuning; however, amplitude-based measurements (thus OSNR) are very sensitive to the filter detuning. In a field deployment, such monitoring technique would have to maintain the filter detuning stability at ±2GHz to achieve an OSNR accuracy of ±1dB.

6.8 WDM crosstalk effect

In this experiment, the input optical signal is a WDM signal of 9 channels spaced at 100GHz. The simultaneous down-conversion of multi-wavelength tones using a single EAM was assessed by turning-off two channels at a time, symmetrically around a central channel, leaving the system with 9, 7, 5, 3 and 1 channel. The central channel was monitored keeping the CD, DGD and OSNR at a constant arbitrary level, respectively equal to 2685ps/nm, 100ps and 20dB. The monitored channel was attenuated by the appropriate amount at each measurement, in order to retain a constant OSNR level of 20dB. Figure 6-20(a) shows the RMS error in the CD and DGD measurements as a function of the number of channels present in the system and Figure 6-20(b) shows the RMS error in the OSNR measurement. All impairments remain constant within their measurement error, the use of a single EAM is thus resilient to the number of channels to be down-converted. This is due to the fact that both CD and DGD monitoring are based on a phase determination principle which is inherently a narrow-band measurement. The OSNR is also shown to be insensitive to crosstalk from adjacent WDM channels. This is due to the fact that the interfering signal is not coherent with the measured channel and thus the interfering term time-averages to zero and so doesn’t effect the measurement of the IF tone amplitude.

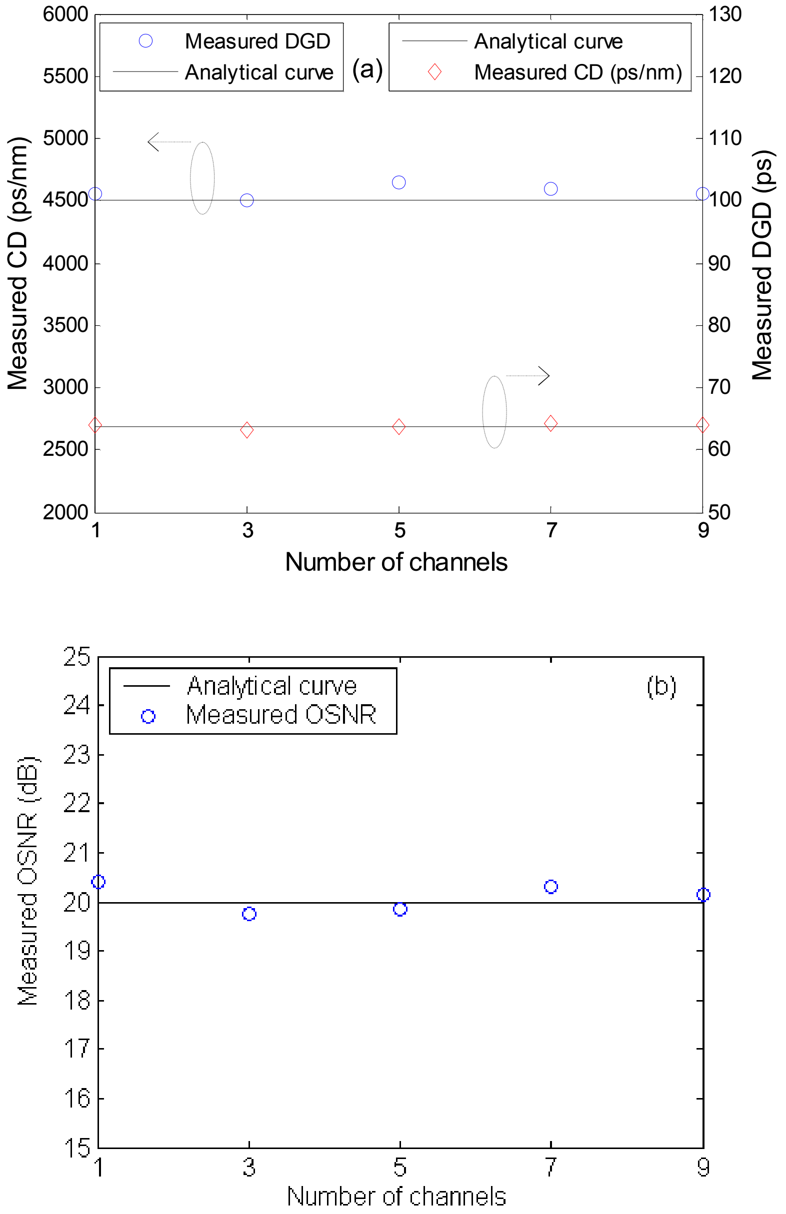

Figure 6-20: WDM crosstalk effect on (a) CD and DGD measurement, (b) OSNR measurement.

6.9 Summary

In this chapter, the experimental results for the proposed OPM technique have been presented for a NRZ modulation format at 40Gbit/s bit rate. This monitoring technique allows for GVD, DGD and OSNR measurements. A novel approach of optically down-converting an in-band data tone to an intermediate frequency has been developed within the work of this thesis. It has been show analytically and verified experimentally that the GVD and DGD measurements are based on the phase measurement of the IF tone whereas the OSNR measurement is based on the amplitude measurement of the IF tone in conjunction with the average power. It has been experimentally demonstrated that the proposed OPM technique allows for simultaneous and independent measurement of these impairments. We have shown that chromatic dispersion and PMD effects can be isolated from each other with the use of a MZI optical filter which allowed us to conduct the measurements for each sideband. It is noted that this method of isolating GVD from DGD, using single sideband measurements, was developed in prior art as described in charter 3. We have shown that a single sideband measurement is sufficient for DGD and OSNR monitoring while GVD required both sidebands. We have also shown that the IF tone amplitude is independent of the phase of the signal, which made the OSNR independent of GVD and DGD. These results were achieved for a WDM system with nine channels spaced at 100GHz. This has been possible with the use of optical modulators (EAMs) which down-converted all channels simultaneously. We consider this novel OPM technique suitable for WDM systems since all components are shared but the low-speed electronics that are required for each channel. The range and accuracies achieved for GVD, DGD and OSNR are respectively 4742±100ps/nm, 200±4ps and 25±1dB for an acquisition time of 100ms. It has been shown that reducing the acquisition time did not have any impact on the measurements ranges but affected the accuracies where the acquisition-time is a trade-off between the measurement accuracies and the monitoring speed. Detuning the MZI optical filter by ±5GHz from its optimum position did not have any effect on the phase measurements, thus on the CD and DGD monitoring; but had an impact on the amplitude measurement, thus on the OSNR monitoring. A filter detuning stability of ±2GHz was required to keep an OSNR accuracy of ±1dB. It has also been shown that the monitoring technique is resilient to the number of channels present in the system. In chapter 3 describing the literature review we have seen that none of the OPM techniques developed to date have achieved the performance of the proposed OPM technique for amplitude modulated signals at 40Gbit/s bit rates.

Chapter 7: Conclusions and future work

7.1 Summary and Conclusions

Dynamically reconfigurable networks introduce greater complexity that may demand new forms of physical layer functionalities, such as real-time impairment monitoring and compensation (i.e. monitoring and compensation performed on the network switching timescales). This has created the need for sophisticated optical performance monitoring (OPM) to track the quality of the optical signal throughout the network. An OPM device, deployed at each link, would provide physical layer fault management by identifying discontinuities in parameters such as OSNR; and the diagnosis of impairments such as chromatic dispersion (CD) and polarisation mode dispersion (PMD) would provide a mechanism to trigger alarms or provide feedback for active dispersion compensation. In such networks, each channel is dynamically added and dropped, and has a different transport history which may include different paths and different optical elements, in addition to changes in environment such as temperature. This prevents network management based on statically mapped network elements and fibre properties, and drives the need for dynamic OPM and compensation. Other potential applications of OPM in dynamically reconfigurable networks may include impairment based routing capabilities where high capacity and priority-traffic that requires high-performance, can be dynamically tuned to the appropriate optical channels. As such, research on OPM has been the topic of discussion in this thesis. The OPM technique proposed in this thesis is based on RF spectrum analysis using in-band tone monitoring, and the following key achievements have been made in the course of this research:

Novel OPM technique

A novel approach of optically down-converting a high-frequency in-band data tone to an intermediate frequency of 10kHz has been developed in the course of this work. It has been shown analytically and verified experimentally that the GVD and DGD parameters can be determined from the phase of the IF tone, whereas the OSNR is obtained from an amplitude measurement of the IF tone, in conjunction with the average power.

Simultaneous multi-impairment monitoring

The proposed OPM method is capable of simultaneous monitoring multiple impairments including chromatic dispersion, PMD and in-band OSNR. The measurement range achieved with this method was equal to 4742±100ps/nm for CD, 200±4ps for DGD and 25±1dB for OSNR. To the knowledge of the author, these dispersion monitoring ranges are the largest reported to date for the bit-rate of 40Gbit/s using amplitude modulation formats.

Independent monitoring of all impairments

It has been experimentally demonstrated that the proposed OPM technique allows for independent measurement of these impairments. We have shown that chromatic dispersion and PMD effects can be isolated with the use of a Mach-Zehnder interferometer (MZI) optical filter which allowed us to conduct the measurements on each sideband. It is noted that this method of isolating GVD from DGD, using single sideband measurements, was developed in prior art as described in chapter 3, however, this implementation is the first to use a phase measurement technique to determine PMD independently of CD. We have shown that a single sideband measurement was sufficient for DGD and OSNR monitoring while GVD required both sidebands. We have also shown that the IF tone amplitude was independent of the phase of the signal, which made the OSNR independent of GVD and DGD.

Multi-channel monitoring

Multichannel operation is achieved with fewer high bandwidth components by using Electro-optical down conversion to simultaneously down-convert all the WDM channels. The feasibility of this was demonstrated in a WDM system with nine channels spaced at 100GHz using an electro absorption modulator (EAM) to down-convert all channels simultaneously and a MZI optical filter which also filtered out the single sideband signal of all channels simultaneously. Multi-channel operation does not lead to any additional degradation in performance over that of a single channel. The sharing of the high bandwidth components across multiple channels makes this technique much more cost effective than the traditional RF monitoring techniques that require duplicated setups for each channel.

CD and PMD monitoring technique insensitive to filter optical detuning

Detuning the MZI optical filter from its optimum position did not have any effect on the phase measurements, thus on the CD and DGD monitoring which represents a major advantage over the OPM techniques using band-pass filters. This has also been demonstrated analytically and can be explained by the fact that the MZI filter has a linear phase-shift response introducing the same phase error for each of the four measured phases on the fast and slow polarisation axis of the USB and LSB, and is thus cancelled when calculating the phase-difference for either GVD or DGD. Clearly, as the filter detuning increases such that the IF tone power is fully attenuated, the measurement uncertainty increases due to a degraded SNR. However, the filter detuning does have an impact on the amplitude measurement and thus on the OSNR monitoring. A filter detuning stability of ±2GHz was required to keep an OSNR accuracy of ±1dB. Such stability can easily be maintained using conventionally available non-tuneable MZI optical filters.

Fastest response time for CD monitoring

As can be seen from Table 7.1, the first generation achieved an acquisition time of 10μs making this scheme the fastest RF spectrum monitoring technique published to date. This acquisition time was considerably shorter than the subsequent generations. This is due to the fact that the former method extracted DC values using an I-Q mixer (see chapter 4), which can be obtained by integrating a very small number of data points (5 data points corresponding to 10μs acquisition-time), whereas the latter methods monitored an IF tone of 10kHz, requiring 38000 samples (corresponding to 100ms acquisition-time) to obtain a sufficient SNR.

Network agnostic

It has been shown that the monitoring technique is resilient to the number of channels present in the system and is bit-rate and amplitude modulation independent (subject to the system's calibration). The proposed OPM technique has a number of advantages compared to the state-of-the-art OPM techniques, published to date, as shown in Table 7.1:

	OPM				
	Time domain	**Frequency domain**			
	Sampling	**Opt. spectrum**	**RF spectrum**		
Criteria	**Sync. & Async.**	**Optical filter & Homodyne**	**Clock tone**	**Pilot tone**	**In-band tone (proposed method)**
Impairments	CD, PMD OSNR, BER	OSNR Wavelength drift	CD, PMD	CD, PMD OSNR	CD, PMD OSNR
Simultaneous	No	No	No	No	Yes
Independent	No	No	No	No	Yes
WDM	No	Yes	No	No	Yes
Dispersion Range	Bit-rate limited for PMD	No fundamental limit	Bit-rate limited	No fundamental limit	No fundamental limit
Speed	Slow (ms)	Very slow (s)	Very fast (μs)	Fast (μs-ms)	Fast (μs-ms) Gen1: 10μs Gen2: 100ms
Bit-rate independent	No	Yes	No	Yes	Yes
Mod. Format independent	No	Yes	No	Yes	Yes

Table 7.1: Comparison between the OPM techniques presented to date and the proposed method.

We have seen that none of the OPM techniques developed to date have achieved the performance of the proposed OPM technique for amplitude modulated signals at 40Gbit/s bit rates. The three main advantages of the final implementation compared to the conventional methods are in:

- Simultaneous and independent multi-impairment monitoring of CD, PMD and OSNR
- Multi-channel operation
- Bit-rate and amplitude modulation format independence.

7.2 Future work

A number of areas remain open to further investigations, these include the following points:

The use of a higher pseudo-random bit-sequence (PRBS)

In all the experiments presented in this thesis, a 40Gbit/s, 2^{15}-1 PRBS signal was used. As mentioned in chapter 6, this pattern length provided a frequency-separation between the data tones within the data bandwidth of around 1.22MHz. The presence of these data tones was the basis of a Fourier representation of the signal used in the analytical model described in the analytical chapter. Increasing the pattern length to 2^{31}-1 would have provided a frequency-separation of around 18Hz, approaching a continuum spectrum. In this configuration, a software modification for the data processing would be required. This would involve the use of a higher integration bandwidth used in the FFT. We have claimed that the calibration of the system would result in different calibration constants but that we would expect that all results obtained in this chapter would not change. Since a field implementation transmit data signals that are comparable to higher PRBS sequences (such as 2^{31}-1), it is essential that the claimed assumption is verified experimentally to fully validate the suitability of this technique to field implementations.

Speed

In chapter 4, we have shown that the initial implementation (Gen 1) required a 10μs acquisition time to provide for multi-channel chromatic dispersion monitoring. This initial implementation evolved to the final proposed OPM technique that had the ability to simultaneously and independently monitor multiple channels and multiple impairments (GVD, DGD and OSNR). These added features have come at the expense of increasing the acquisition time to 100ms. Depending on the dynamically reconfigurable networks, faster OPM techniques may be required. We foresee that an improvement on the acquisition time can be achieved by optically down-converting the in-band tone toward a higher intermediate frequency (IF). For example, using a 1MHz IF instead of 10kHz (as done in this thesis) could potentially improve the acquisition time by a factor of 100, which should be verified experimentally.

Non-linearities

In the mathematical development presented in chapter 5, we have neglected all non-linear effects. This is not foreseen as a major cause of error but should be incorporated into the analytical model for completeness. It might also be possible to measure these non-linear effects from the phase measurements, which would represent an additional impairment monitoring.

Other modulation formats

The experimental work presented in this thesis has been achieved with a non-return-to-zero (NRZ) modulation format. We have claimed that the proposed OPM technique is independent of the amplitude modulation format used. This should be verified experimentally for other modulation formats such as return-to-zero (RZ). A large number of investigations, in the field of OPM, have been recently conducted for phase modulation formats. This represents a very interesting field which would require the development of a new analytical model, with some modifications in the experimental implementation.

Chapter 8: Appendix 1

We have shown in section 5.2 that the four signals at the output of the two PBS are detected using low-speed detectors. Their intensities are referenced as (I_{UF}, I_{US}) for the fast and slow polarisations of the USB, and (I_{LF}, I_{LS}) for the fast and slow polarisations of the LSB:

$$\begin{cases} I_{UF}(t) = G(t)\left(\cos\theta_U E_{Ux} + \sin\theta_U E_{Uy}\right)^2 \\ I_{US}(t) = G(t)\left(-\sin\theta_U E_{Ux} + \cos\theta_U E_{Uy}\right)^2 \end{cases} \tag{8.1}$$

and

$$\begin{cases} I_{LF}(t) = G(t)\left(\cos\theta_L E_{Lx} + \sin\theta_L E_{Ly}\right)^2 \\ I_{LS}(t) = G(t)\left(-\sin\theta_L E_{Lx} + \cos\theta_L E_{Ly}\right)^2 \end{cases} \tag{8.2}$$

where (E_{Ux}, E_{Uy}) and (E_{Lx}, E_{Ly}) are, respectively, the two polarisation components on the x-y axis, the reference frame of the USB and LSB fields before the PBS.

$$I_{UF}(t) = G(t)\begin{pmatrix} \cos\phi\cos\theta_U \sum_{k=0}^{M} T_k\alpha_k \cos\left(\omega_k(t-\frac{\Delta\tau}{2})+\varphi_k\right) \\ +\frac{1}{\sqrt{2}}\cos\theta_U \sum_{k=0}^{M} T_k n_k \cos\left(\omega_k t+\varphi_{xrk}\right) \\ +\sin\phi\sin\theta_U \sum_{k=0}^{M} T_k\alpha_k \cos\left(\omega_k(t+\frac{\Delta\tau}{2})+\varphi_k\right) \\ +\frac{1}{\sqrt{2}}\sin\theta_U \sum_{k=0}^{M} T_k n_k \cos\left(\omega_k t+\varphi_{yrk}\right) \end{pmatrix}^2 \tag{8.3}$$

and

$$I_{US}(t) = G(t)\begin{pmatrix} -\cos\phi\sin\theta_U \sum_{k=0}^{M} T_k\alpha_k \cos\left(\omega_k(t-\frac{\Delta\tau}{2})+\varphi_k\right) \\ -\frac{1}{\sqrt{2}}\sin\theta_U \sum_{k=0}^{M} T_k n_k \cos\left(\omega_k t+\varphi_{xrk}\right) \\ +\sin\phi\cos\theta_U \sum_{k=0}^{M} T_k\alpha_k \cos\left(\omega_k(t+\frac{\Delta\tau}{2})+\varphi_k\right) \\ +\frac{1}{\sqrt{2}}\cos\theta_U \sum_{k=0}^{M} T_k n_k \cos\left(\omega_k t+\varphi_{yrk}\right) \end{pmatrix}^2 \tag{8.4}$$

where $\omega_k = \omega_0 + k\Delta\omega$ and $\omega_0, \Delta\omega$ are respectively the central optical angular-frequency of the data signal and the frequency spacing between the data tones which depends on the length of the repeating PRBS data signal that is used. Further development of Eq. (8.3) and Eq. (8.4) lead to the following expressions:

$$
\begin{gathered}
I_{UF}(t) = \frac{1}{4}\left(1 + \cos(\omega_{LO} t + \varphi_{LO})\right) \\
\left(
\begin{aligned}
&\cos^2 \phi \cos^2 \theta_U \sum_{k=0}^{M} \sum_{l=0}^{M} T_k T_l \alpha_k \alpha_l \cos\left((\omega_l - \omega_k)(t - \frac{\Delta\tau}{2}) + (\varphi_l - \varphi_k) \right) \\
&+ \frac{1}{2} \cos^2 \theta_U \sum_{k=0}^{M} \sum_{l=0}^{M} T_k T_l n_k n_l \cos\left((\omega_l - \omega_k) t + (\varphi_{xrl} - \varphi_{xrk}) \right) \\
&+ \frac{2}{\sqrt{2}} \cos\phi \cos^2 \theta_U \sum_{k=0}^{M} \sum_{l=0}^{M} T_k T_l \alpha_k n_l \cos\left((\omega_l - \omega_k) t + \omega_k \frac{\Delta\tau}{2} + (\varphi_{xrl} - \varphi_k) \right) \\
&+ \sin^2 \phi \sin^2 \theta_U \sum_{k=0}^{M} \sum_{l=0}^{M} T_k T_l \alpha_k \alpha_l \cos\left((\omega_l - \omega_k)(t + \frac{\Delta\tau}{2}) + (\varphi_l - \varphi_k) \right) \\
&+ \frac{1}{2} \sin^2 \theta_U \sum_{k=0}^{M} \sum_{l=0}^{M} T_k T_l n_k n_l \cos\left((\omega_l - \omega_k) t + (\varphi_{yrl} - \varphi_{yrk}) \right) \\
&+ \frac{2}{\sqrt{2}} \sin\phi \sin^2 \theta_U \sum_{k=0}^{M} \sum_{l=0}^{M} T_k T_l \alpha_k n_l \cos\left((\omega_l - \omega_k) t - \omega_k \frac{\Delta\tau}{2} + (\varphi_{yrl} - \varphi_k) \right) \\
&+2 \sin\phi \cos\phi \sin\theta_U \cos\theta_U \\
&\sum_{k=0}^{M} \sum_{l=0}^{M} T_k T_l \alpha_k \alpha_l \cos\left((\omega_l - \omega_k) t + (\omega_l + \omega_k) \frac{\Delta\tau}{2} + (\varphi_l - \varphi_k) \right) \\
&+ \frac{2}{\sqrt{2}} \cos\phi \sin\theta_U \cos\theta_U \sum_{k=0}^{M} \sum_{l=0}^{M} T_k T_l \alpha_k n_l \cos\left((\omega_l - \omega_k) t + \omega_k \frac{\Delta\tau}{2} + (\varphi_{yrl} - \varphi_k) \right) \\
&+ \frac{2}{\sqrt{2}} \sin\phi \sin\theta_U \cos\theta_U \sum_{k=0}^{M} \sum_{l=0}^{M} T_k T_l \alpha_k n_l \cos\left((\omega_l - \omega_k) t - \omega_k \frac{\Delta\tau}{2} + (\varphi_{xrl} - \varphi_k) \right) \\
&+ \sin\theta_U \cos\theta_U \sum_{k=0}^{M} \sum_{l=0}^{M} T_k T_l n_k n_l \cos\left((\omega_l - \omega_k) t + (\varphi_{yrl} - \varphi_{xrk}) \right) \\
&
\end{aligned}
\right)
\end{gathered}
\tag{8.5}
$$

and

$$
\begin{aligned}
I_{US}(t) = \frac{1}{4}\left(1+\cos(\omega_{LO}t+\varphi_{LO})\right)\\
\left(\begin{aligned}
&\cos^2\phi\sin^2\theta_U\sum_{k=0}^{M}\sum_{l=0}^{M}T_kT_l\alpha_k\alpha_l\cos\left((\omega_l-\omega_k)(t-\frac{\Delta\tau}{2})+(\varphi_l-\varphi_k)\right)\\
&+\frac{1}{2}\sin^2\theta_U\sum_{k=0}^{M}\sum_{l=0}^{M}T_kT_ln_kn_l\cos\left((\omega_l-\omega_k)t+(\varphi_{xrl}-\varphi_{xrk})\right)\\
&-\frac{2}{\sqrt{2}}\cos\phi\sin^2\theta_U\sum_{k=0}^{M}\sum_{l=0}^{M}T_kT_l\alpha_kn_l\cos\left((\omega_l-\omega_k)t+\omega_k\frac{\Delta\tau}{2}+(\varphi_{xrl}-\varphi_k)\right)\\
&+\sin^2\phi\cos^2\theta_U\sum_{k=0}^{M}\sum_{l=0}^{M}T_kT_l\alpha_k\alpha_l\cos\left((\omega_l-\omega_k)(t+\frac{\Delta\tau}{2})+(\varphi_l-\varphi_k)\right)\\
&+\frac{1}{2}\cos^2\theta_U\sum_{k=0}^{M}\sum_{l=0}^{M}T_kT_ln_kn_l\cos\left((\omega_l-\omega_k)t+(\varphi_{yrl}-\varphi_{yrk})\right)\\
&+\frac{2}{\sqrt{2}}\sin\phi\cos^2\theta_U\sum_{k=0}^{M}\sum_{l=0}^{M}T_kT_l\alpha_kn_l\cos\left((\omega_l-\omega_k)t-\omega_k\frac{\Delta\tau}{2}+(\varphi_{yrl}-\varphi_k)\right)\\
&-2\sin\phi\cos\phi\sin\theta_U\cos\theta_U\\
&\sum_{k=0}^{M}\sum_{l=0}^{M}T_kT_l\alpha_k\alpha_l\cos\left((\omega_l-\omega_k)t+(\omega_l+\omega_k)\frac{\Delta\tau}{2}+(\varphi_l-\varphi_k)\right)\\
&-\frac{2}{\sqrt{2}}\cos\phi\sin\theta_U\cos\theta_U\sum_{k=0}^{M}\sum_{l=0}^{M}T_kT_l\alpha_kn_l\cos\left((\omega_l-\omega_k)t+\omega_k\frac{\Delta\tau}{2}+(\varphi_{yrl}-\varphi_k)\right)\\
&-\frac{2}{\sqrt{2}}\sin\phi\sin\theta_U\cos\theta_U\sum_{k=0}^{M}\sum_{l=0}^{M}T_kT_l\alpha_kn_l\cos\left((\omega_l-\omega_k)t-\omega_k\frac{\Delta\tau}{2}+(\varphi_{xrl}-\varphi_k)\right)\\
&-\sin\theta_U\cos\theta_U\sum_{k=0}^{M}\sum_{l=0}^{M}T_kT_ln_kn_l\cos\left((\omega_l-\omega_k)t+(\varphi_{yrl}-\varphi_{xrk})\right)
\end{aligned}\right)
\end{aligned}
\tag{8.6}
$$

It is noted that an index *l* is introduced in the double sum $\sum_{k=0}^{M}\sum_{l=0}^{M}$ highlighting the product of two sums $\sum_{k=0}^{M}X\sum_{k=0}^{M}$. In an effort to keep this model concise, only the USB will be analysed in this chapter. However, it is noted that the expressions of $I_{LF}(t)$ and $I_{LS}(t)$ can be derived from Eq. (8.3) and Eq. (8.4) respectively, by replacing θ_U by θ_L and $\sum_{k=0}^{M}$ by $\sum_{k=-M}^{k}$.

As shown in the following sections, depending on the relative value of *l* and *k*, we will be able to greatly simplify Eq. (8.5) and Eq. (8.6). We will show that a further development of these equations shows that $I_{UF}(t)$ can be expressed as the sum of a first term proportional to the average power and a second term proportional to the IF tone:

$$
I_{UF}(t) = \text{Average Power}\Big|_{UF} + \text{IF Tone}\Big|_{UF} \tag{8.7}
$$

where

$$\text{Average Power}\Big|_{UF} =$$

$$\frac{1}{4}\left(\begin{array}{l}
\cos^2\phi\cos^2\theta_U\sum_{k=0}^{M}\sum_{l=0}^{M}T_kT_l\alpha_k\alpha_l\cos\left((\omega_l-\omega_k)(t-\frac{\Delta\tau}{2})+(\varphi_l-\varphi_k)\right)\\
+\frac{1}{2}\cos^2\theta_U\sum_{k=0}^{M}\sum_{l=0}^{M}T_kT_l n_k n_l\cos\left((\omega_l-\omega_k)t+(\varphi_{xrl}-\varphi_{xrk})\right)\\
+\frac{2}{\sqrt{2}}\cos\phi\cos^2\theta_U\sum_{k=0}^{M}\sum_{l=0}^{M}T_kT_l\alpha_k n_l\cos\left((\omega_l-\omega_k)t+\omega_k\frac{\Delta\tau}{2}+(\varphi_{xrl}-\varphi_k)\right)\\
+\sin^2\phi\sin^2\theta_U\sum_{k=0}^{M}\sum_{l=0}^{M}T_kT_l\alpha_k\alpha_l\cos\left((\omega_l-\omega_k)(t+\frac{\Delta\tau}{2})+(\varphi_l-\varphi_k)\right)\\
+\frac{1}{2}\sin^2\theta_U\sum_{k=0}^{M}\sum_{l=0}^{M}T_kT_l n_k n_l\cos\left((\omega_l-\omega_k)t+(\varphi_{yrl}-\varphi_{yrk})\right)\\
+\frac{2}{\sqrt{2}}\sin\phi\sin^2\theta_U\sum_{k=0}^{M}\sum_{l=0}^{M}T_kT_l\alpha_k n_l\cos\left((\omega_l-\omega_k)t-\omega_k\frac{\Delta\tau}{2}+(\varphi_{yrl}-\varphi_k)\right)\\
+2\sin\phi\cos\phi\sin\theta_U\cos\theta_U\sum_{k=0}^{M}\sum_{l=0}^{M}T_kT_l\alpha_k\alpha_l\cos\left((\omega_l-\omega_k)t+(\omega_l+\omega_k)\frac{\Delta\tau}{2}+(\varphi_l-\varphi_k)\right)\\
+\frac{2}{\sqrt{2}}\cos\phi\sin\theta_U\cos\theta_U\sum_{k=0}^{M}\sum_{l=0}^{M}T_kT_l\alpha_k n_l\cos\left((\omega_l-\omega_k)t+\omega_k\frac{\Delta\tau}{2}+(\varphi_{yrl}-\varphi_k)\right)\\
+\frac{2}{\sqrt{2}}\sin\phi\sin\theta_U\cos\theta_U\sum_{k=0}^{M}\sum_{l=0}^{M}T_kT_l\alpha_k n_l\cos\left((\omega_l-\omega_k)t-\omega_k\frac{\Delta\tau}{2}+(\varphi_{xrl}-\varphi_k)\right)\\
+\sin\theta_U\cos\theta_U\sum_{k=0}^{M}\sum_{l=0}^{M}T_kT_l n_k n_l\cos\left((\omega_l-\omega_k)t+(\varphi_{yrl}-\varphi_{xrk})\right)
\end{array}\right) \tag{8.8}$$

$$\text{IF Tone}\big|_{UF} =$$

$$\frac{1}{8}\left(\begin{array}{l}
\cos^2\phi\cos^2\theta_U\sum_{k=0}^{M}\sum_{l=0}^{M}T_kT_l\alpha_k\alpha_l\cos\left(\omega_{LO}t-(\omega_l-\omega_k)(t-\frac{\Delta\tau}{2})+\varphi_{LO}-(\varphi_l-\varphi_k)\right)\\
+\frac{1}{2}\cos^2\theta_U\sum_{k=0}^{M}\sum_{l=0}^{M}T_kT_ln_kn_l\cos\left(\omega_{LO}t-(\omega_l-\omega_k)t+\varphi_{LO}-(\varphi_{xrl}-\varphi_{xrk})\right)\\
+\frac{2}{\sqrt{2}}\cos\phi\cos^2\theta_U\sum_{k=0}^{M}\sum_{l=0}^{M}T_kT_l\alpha_kn_l\cos\left(\omega_{LO}t-(\omega_l-\omega_k)t+\omega_k\frac{\Delta\tau}{2}+\varphi_{LO}-(\varphi_{xrl}-\varphi_k)\right)\\
+\sin^2\phi\sin^2\theta_U\sum_{k=0}^{M}\sum_{l=0}^{M}T_kT_l\alpha_k\alpha_l\cos\left(\omega_{LO}t-(\omega_l-\omega_k)(t+\frac{\Delta\tau}{2})+\varphi_{LO}-(\varphi_l-\varphi_k)\right)\\
+\frac{1}{2}\sin^2\theta_U\sum_{k=0}^{M}\sum_{l=0}^{M}T_kT_ln_kn_l\cos\left(\omega_{LO}t-(\omega_l-\omega_k)t+\varphi_{LO}-(\varphi_{yrl}-\varphi_{yrk})\right)\\
+\frac{2}{\sqrt{2}}\sin\phi\sin^2\theta_U\sum_{k=0}^{M}\sum_{l=0}^{M}T_kT_l\alpha_kn_l\cos\left(\omega_{LO}t-(\omega_l-\omega_k)t-\omega_k\frac{\Delta\tau}{2}+\varphi_{LO}-(\varphi_{yrl}-\varphi_k)\right)\\
+2\sin\phi\cos\phi\sin\theta_U\cos\theta_U\\
\sum_{k=0}^{M}\sum_{l=0}^{M}T_kT_l\alpha_k\alpha_l\cos\left(\omega_{LO}t-(\omega_l-\omega_k)t+(\omega_l+\omega_k)\frac{\Delta\tau}{2}+\varphi_{LO}-(\varphi_l-\varphi_k)\right)\\
+\frac{2}{\sqrt{2}}\cos\phi\sin\theta_U\cos\theta_U\sum_{k=0}^{M}\sum_{l=0}^{M}T_kT_l\alpha_kn_l\cos\left(\omega_{LO}t-(\omega_l-\omega_k)t+\omega_k\frac{\Delta\tau}{2}+\varphi_{LO}-(\varphi_{yrl}-\varphi_k)\right)\\
+\frac{2}{\sqrt{2}}\sin\phi\sin\theta_U\cos\theta_U\sum_{k=0}^{M}\sum_{l=0}^{M}T_kT_l\alpha_kn_l\cos\left(\omega_{LO}t-(\omega_l-\omega_k)t-\omega_k\frac{\Delta\tau}{2}+\varphi_{LO}-(\varphi_{xrl}-\varphi_k)\right)\\
+\sin\theta_U\cos\theta_U\sum_{k=0}^{M}\sum_{l=0}^{M}T_kT_ln_kn_l\cos\left(\omega_{LO}t-(\omega_l-\omega_k)t+\varphi_{LO}-(\varphi_{yrl}-\varphi_{xrk})\right)
\end{array}\right) \tag{8.9}$$

Similar analysis can be done for $I_{US}(t)$:

$$I_{US}(t) = \text{Average Power}\big|_{US} + \text{IF Tone}\big|_{US} \tag{8.10}$$

where

$$\text{Average Power}\Big|_{US} =$$

$$\frac{1}{4}\left(\begin{array}{l}
\cos^2\phi\sin^2\theta_U\sum_{k=0}^{M}\sum_{l=0}^{M}T_kT_l\alpha_k\alpha_l\cos\left((\omega_l-\omega_k)(t-\frac{\Delta\tau}{2})+(\varphi_l-\varphi_k)\right)\\
+\frac{1}{2}\sin^2\theta_U\sum_{k=0}^{M}\sum_{l=0}^{M}T_kT_ln_kn_l\cos\left((\omega_l-\omega_k)t+(\varphi_{xrl}-\varphi_{xrk})\right)\\
-\frac{2}{\sqrt{2}}\cos\phi\sin^2\theta_U\sum_{k=0}^{M}\sum_{l=0}^{M}T_kT_l\alpha_kn_l\cos\left((\omega_l-\omega_k)t+\omega_k\frac{\Delta\tau}{2}+(\varphi_{xrl}-\varphi_k)\right)\\
+\sin^2\phi\cos^2\theta_U\sum_{k=0}^{M}\sum_{l=0}^{M}T_kT_l\alpha_k\alpha_l\cos\left((\omega_l-\omega_k)(t+\frac{\Delta\tau}{2})+(\varphi_l-\varphi_k)\right)\\
+\frac{1}{2}\cos^2\theta_U\sum_{k=0}^{M}\sum_{l=0}^{M}T_kT_ln_kn_l\cos\left((\omega_l-\omega_k)t+(\varphi_{yrl}-\varphi_{yrk})\right)\\
+\frac{2}{\sqrt{2}}\sin\phi\cos^2\theta_U\sum_{k=0}^{M}\sum_{l=0}^{M}T_kT_l\alpha_kn_l\cos\left((\omega_l-\omega_k)t-\omega_k\frac{\Delta\tau}{2}+(\varphi_{yrl}-\varphi_k)\right)\\
-2\sin\phi\cos\phi\sin\theta_U\cos\theta_U\sum_{k=0}^{M}\sum_{l=0}^{M}T_kT_l\alpha_k\alpha_l\cos\left((\omega_l-\omega_k)t+(\omega_l+\omega_k)\frac{\Delta\tau}{2}+(\varphi_l-\varphi_k)\right)\\
-\frac{2}{\sqrt{2}}\cos\phi\sin\theta_U\cos\theta_U\sum_{k=0}^{M}\sum_{l=0}^{M}T_kT_l\alpha_kn_l\cos\left((\omega_l-\omega_k)t+\omega_k\frac{\Delta\tau}{2}+(\varphi_{yrl}-\varphi_k)\right)\\
-\frac{2}{\sqrt{2}}\sin\phi\sin\theta_U\cos\theta_U\sum_{k=0}^{M}\sum_{l=0}^{M}T_kT_l\alpha_kn_l\cos\left((\omega_l-\omega_k)t-\omega_k\frac{\Delta\tau}{2}+(\varphi_{xrl}-\varphi_k)\right)\\
-\sin\theta_U\cos\theta_U\sum_{k=0}^{M}\sum_{l=0}^{M}T_kT_ln_kn_l\cos\left((\omega_l-\omega_k)t+(\varphi_{yrl}-\varphi_{xrk})\right)
\end{array}\right) \tag{8.11}$$

$$\text{IF Tone}\Big|_{US} = \frac{1}{8}\left(\begin{array}{l}
\cos^2\phi\sin^2\theta_U\sum_{k=0}^{M}\sum_{l=0}^{M}T_kT_l\alpha_k\alpha_l\cos\left(\omega_{LO}t-(\omega_l-\omega_k)(t-\frac{\Delta\tau}{2})+\varphi_{LO}-(\varphi_l-\varphi_k)\right)\\
+\frac{1}{2}\sin^2\theta_U\sum_{k=0}^{M}\sum_{l=0}^{M}T_kT_ln_kn_l\cos\left(\omega_{LO}t-(\omega_l-\omega_k)t+\varphi_{LO}-(\varphi_{xrl}-\varphi_{xrk})\right)\\
-\frac{2}{\sqrt{2}}\cos\phi\sin^2\theta_U\sum_{k=0}^{M}\sum_{l=0}^{M}T_kT_l\alpha_kn_l\cos\left(\omega_{LO}t-(\omega_l-\omega_k)t+\omega_k\frac{\Delta\tau}{2}+\varphi_{LO}-(\varphi_{xrl}-\varphi_k)\right)\\
+\sin^2\phi\cos^2\theta_U\sum_{k=0}^{M}\sum_{l=0}^{M}T_kT_l\alpha_k\alpha_l\cos\left(\omega_{LO}t-(\omega_l-\omega_k)(t+\frac{\Delta\tau}{2})+\varphi_{LO}-(\varphi_l-\varphi_k)\right)\\
+\frac{1}{2}\cos^2\theta_U\sum_{k=0}^{M}\sum_{l=0}^{M}T_kT_ln_kn_l\cos\left(\omega_{LO}t-(\omega_l-\omega_k)t+\varphi_{LO}-(\varphi_{yrl}-\varphi_{yrk})\right)\\
+\frac{2}{\sqrt{2}}\sin\phi\cos^2\theta_U\sum_{k=0}^{M}\sum_{l=0}^{M}T_kT_l\alpha_kn_l\cos\left(\omega_{LO}t-(\omega_l-\omega_k)t-\omega_k\frac{\Delta\tau}{2}+\varphi_{LO}-(\varphi_{yrl}-\varphi_k)\right)\\
-2\sin\phi\cos\phi\sin\theta_U\cos\theta_U\\
\sum_{k=0}^{M}\sum_{l=0}^{M}T_kT_l\alpha_k\alpha_l\cos\left(\omega_{LO}t-(\omega_l-\omega_k)t+(\omega_l+\omega_k)\frac{\Delta\tau}{2}+\varphi_{LO}-(\varphi_l-\varphi_k)\right)\\
-\frac{2}{\sqrt{2}}\cos\phi\sin\theta_U\cos\theta_U\sum_{k=0}^{M}\sum_{l=0}^{M}T_kT_l\alpha_kn_l\cos\left(\omega_{LO}t-(\omega_l-\omega_k)t+\omega_k\frac{\Delta\tau}{2}+\varphi_{LO}-(\varphi_{yrl}-\varphi_k)\right)\\
-\frac{2}{\sqrt{2}}\sin\phi\sin\theta_U\cos\theta_U\sum_{k=0}^{M}\sum_{l=0}^{M}T_kT_l\alpha_kn_l\cos\left(\omega_{LO}t-(\omega_l-\omega_k)t-\omega_k\frac{\Delta\tau}{2}+\varphi_{LO}-(\varphi_{xrl}-\varphi_k)\right)\\
-\sin\theta_U\cos\theta_U\sum_{k=0}^{M}\sum_{l=0}^{M}T_kT_ln_kn_l\cos\left(\omega_{LO}t-(\omega_l-\omega_k)t+\varphi_{LO}-(\varphi_{yrl}-\varphi_{xrk})\right)
\end{array}\right) \qquad (8.12)$$

Chapter 9: References

[AGR'07] Govind P. Agrawal, "Nonlinear fiber optics," *Academic press Inc. (London)*, ISBN: 0-12-045143-3, 2007.

[AMR'00] A. Amrani*,* G. Junyent, J. Prat*,* J. Comellas, I. Ramdani, V. Sales, J. Roldán, and A. Rafel, "Performance Monitor for All-Optical Networks Based on Homodyne Spectroscopy," *IEEE Photon. Technol. Lett*., vol. 12, no. 11, pp. 1564-1566, 2000.

[AND'01] K. E. Anderson, K.H. Wagner, "Chromatic and polarisation mode dispersion compensation using spectral holography," in *Conf. Optical Fiber Communication (OFC)*, paper TuH2, 2001.

[AND'04] Paulo S. André, António Luís J. Teixeira, Mário J. Lima, Paulo N. Monteiro, "Asynchronous sampled amplitude histogram models for optical performance monitoring in high-speed networks," *Journal of Optical Networking*, vol. 3, no. 8, pp. 636-642, 2004

[AND'07] T.B. Anderson, Ken Clarke, Sarah D. Dods, and Masuduzzaman Bakaul , "Robust, Low Cost, In-Band Optical Signal to Noise Monitoring Using Polarization Diversity ," *in Conf. Optical Fiber Communication (OFC),* paper OMM3, 2007.

[ANG'92] C. De Angelis, A. Galtarossa, G. Gianello, F. Mater, M. Schiano, "Time evolution of polarization mode dispersion in long terrestrial links," *IEEE Journal of Lightwave Technol.*, vol. 10, no. 5, pp. 552-555, 1992.

[BAR'97] Stefano Baroni, Polina Bayvel, "Wavelength Requirements in Arbitrarily Connected Wavelength-Routed Optical Networks," *IEEE Journal of Lightwave Technol.,* vol. 15, no. 2, pp. 242-251, Feb. 1997.

[BEN'00] G. Bendelli, C. Cavazzoni, R. Girardi, R. Lano. "Optical performance monitoring techniques," in *European Conf. Opt. Comm. (ECOC),* vol.4, pp. 113-114, Munich 2000.

[BEN'05] Y. Benlachtar, M. Scopes, R. I. Killey, P. Bayvel, "Novel Eye Monitoring Technique for Detection of First Order PMD," in *Conf. Quantum Electronics and Laser Science (QELS)*, vol. 3, paper JThE77, pp. 1789-1791, 2005.

[BEN’05b] Y. Benlachtar, R.I. Killey, P. Bayvel, “Novel Three-Point Sampling Technique for Detection of First Order PMD,” *Winter school e-Photon One*. Aveiro, Portugal, pp. C81-C84, Feb. 2005.

[BEN’05c] Y. Benlachtar, R.I. Killey and P. Bayvel, “Experimental investigation of three-point sampling technique for the estimation of first order PMD’” in *European Conf. Opt. Comm. (ECOC)*, vol. 3, paper We4.P.100, pp. 701-702, 2005.

[BAN’06] Y. Benlachtar, R. I. Killey, P. Bayvel, “Chromatic Dispersion Monitoring Using Synchronous Sampling,” *in Conf. Optical Fiber Communication (OFC),* Paper OWK4, 2006.

[BET’91] S. Betti, F. Curti, B. Daino, G. De Marchis, E. Iannone, and F. Matera, “Evolution of the bandwidth of the principal states of polarization in single-mode fibers,” *Optics Lett.*, vol. 16, no. 7, pp. 467-469, 1991.

[BUL’98] H. Bulow, D. Schlump, J. Weber, B. Wedding, R. Heidemann, “Electronic equalization of fibre PMD-induced distortion at 10 Gbit/s,” in *Conf. Optical Fiber Communication (OFC)*, paper WI1, pp. 151-152, 1998.

[BUL’99] H. Bulow, W. Baumert, H. Schmuck, “Measurement of the Maximum Speed of PMD Fluctuation in Installed Field Fiber,” in *Conf. Optical Fiber Communication (OFC)*, vol. 2, paper WE4-1, pp. 83-85, 1999.

[CAI’99] J. X. Cai, K.-M. Feng, A.E. Willner, V. Grubsky, D.S. Starodubov, J. Feinberg, “Simultaneous tunable dispersion compensation of many WDM channels using a sampled nonlinearly chirped fibre Bragg grating” *IEEE Photon. Technol. Lett.*, vol. 11, no. 11, pp. 1455-1457, November 1999.

[CAM’98] John Cameron, Liang Chen, Xiaoyi Bao, John Stears, “Time evolution of polarization mode dispersion in optical fibres,” *IEEE Photon. Technol. Lett.*, vol. 10, no. 9, pp. 1265-1267, 1998.

[CAR’02] A. B. Carlson, P. B. Crilly, J. C. Rutledge, “Communication systems,” *McGraw-Hill Higher Education*, ISBN: 0-07-011127-8, 2002.

[CHA’04] G. Charlet, E. Corbel, J. Lazaro, A. Klekamp, R. Dischler, P. Tran, W. Idler, H. Mardoyan, A. Konczykowska, F. Jorge, and S. Bigo, “WDM Transmission at 6-Tbit/s Capacity Over Transatlantic Distance, Using 42.7-Gb/s Differential Phase-Shift Keying Without Pulse Carver,” *IEEE Journal of Lightwave Technol.*, vol. 23, no. 1, pp. 104-107, Jan. 2004.

[CHR’86] A. R. Chraplyvy, R. W. Tkach, L. L. Buhl, R. C. Alferness, “ Phase modulation to amplitude modulation conversion of CW laser light in optical fibres,” *IEE Electronics Lett.*, vol. 22, no. 8, pp. 409-411, 1986.

[CON’02] Jan Conradi, “Bandwidth-effiicient modulation formats for digital fibre transmission systems,” in “Optical fiber telecommunications systems IV-B,” *Academic press Inc. (London)*, ISBN: 0-12-395173-9, 2002.

[DER’98] Dennis Derickson, “Fibre optic test and measurement,” *Hewlett Packard professional books, Prentice hall PTR*, ISBN: 0-13-534330-5, 1st edition, January 15, 1998.

[DER’07] Dennis Derickson, Marcus Muller, “Digital communications test and measurements,” Prentice hall, ISBN-13: 978-0-13-220910-6, 2007.

[DES’94] Emmanuel Desurvire, “Erbium-doped fibre amplifiers,” John Wiley & Sons, ISBN: 0-471-58977-2, 1994.

[DIM’00] T. E. Dimmick, G. Rossi, D.J. Blumenthal, “Optical dispersion monitoring technique using double sideband subcarriers,” *IEEE Photon. Technol. Lett.*, vol. 12, no. 7, pp. 900-902, July 2000.

[DOD’07] Sarah D. Dods, Trevor B. Anderson, Ken Clarke, Masudazzaman Bakaul, and Adam Kowalczyk, “Asynchronous Sampling for Optical Performance Monitoring,” *in Conf. Optical Fiber Communication (OFC),* Paper OMM5, 2007.

[DOE’05] C. R. Doerr, D.M. Marom, M.A. Cappuzzo, E.Y. Chen, A. Wong-Foy, L.T. Gomez, S. Chandrasekhar, “40 Gb/s colorless tunable dispersion compensator with 1000 ps/nm tuning range employing a planar lightwave circuit and a deformable mirror,” in *Conf. Optical Fiber Communication (OFC)*, vol. 5, paper PDP5, 2005.

[DUS’05] M. Duser, “Investigation of the impact of traffic growth and variability on future network architectures ,” in *European Conf. Opt. Comm. (ECOC),* vol. 5, Paper Tu. 4.1.2, 2005.

[EGG’99] B.J. Eggleton, J.A. Rogers, P.S. Westbrook, T.A. Strasser, “Electronically tunable power efficient dispersion compensating fibre bragg grating,” *IEEE Photon. Technol. Lett.*, vol. 11, no. 7, pp 854-856, July 1999.

[ESS’02] Rene-Jean Essiambre, Gregory Raybon and Benny Mikkelsen, “Pseudo-linear transmission of high-speed TDM signals: 40 and 160Gb/s,” *in Optical* *fiber telecommunications systems IV-B*, Academic press Inc. (London), ISBN: 0-12-395173-9, 2002.

[FEN’99] K.-M. Feng, J.-X. Chai, V. Grubsky, D.S. Starodubov, M.I. Hayee, S. Lee, X. Jiang, A.E. Willner, J. Feinberg, “Dynamic dispersion compensation in a 160 Gbit/s optical system using a novel voltage tuned nonlinearly chirped fibre bragg grating,” *IEEE Photon. Technol. Lett.*, vol. 11, no. 3, pp. 373-375, March 1999.

[FIS’01] Fischler, W.; Richter, A.; Bock, H.; Elbers, J.-P.; Glingener, C., “Monitoring the optical performance in a transparent and configurable metro area network,” in *Conf. Lasers and Electro-Optics Society (LEOS)*, vol. 2, paper WK2, pp. 479-480, 12-13 Nov. 2001.

[FRI’02] Robert Friskney , Kevin Warbrick , Simon Poliakoff , Richard Heath, “Link-based photonic path performance prediction and control,” *Network Management and control*, Paper 7.4.3, 2002.

[GER’03] O. Gerstel, H. Raza, “On the synergy between the electrical and photonic switching,” *IEEE Communications magazine*, pp. 98-104, April 2003.

[HAL’90] T.R. Halemane, S. K. Korotky, “Distorsion characteristics of optical directional coupler modulators,” *IEEE Transactions on Microwave Theory and Techniques,* vol. 38, no. 5, pp. 669, 1990.

[HAM’97] Y. Hamazuni, M. Koga, “Transmission capacity of optical path overhead transfer scheme using pilot tone for optical path network,” *IEEE Journal of Lightwave Technol.*, vol. 15, no. 12, pp. 2197-2205, 1997.

[HAN’99] N. Hanik, A. Gladisch, C. Caspar and B. Strebel, “Application of amplitude histograms to monitor performance of optical channels’” *IEE Electronics Lett.*, vol. 35, no. 5, pp. 403-404, March 4th 1999.

[HIE’98] Fred Heismann, Daniel A. Fishman, and David L. Wilson, “ Automatic compensation of first-order polarisation mode dispersion in 10Gb/s transmission system,” in *European Conf. Opt. Comm. (ECOC)*, pp. 529-530, 1998.

[HIL’93] G.R. Hill, ”A transport network layer based on optical network elements,” *IEEE Journal of Lightwave Technol.*, vol. 11, no. 5, 1993.

[HO’04] Keang-Po Ho, Joseph M. Kahn, ”Spectrum of Externally Modulated Optical Signals,” *IEEE Journal of Lightwave Technol.*, vol. 22, no. 2, 2004.

[HOF'05] P. Hofmann, E.E. Basch, S. Gringeri, R. Egorov, D.A. Fishman, W.A. Thompson, "DWDM long haul network deployment for the Verizon GNI nationwide network," in Conf. Optical Fiber Communication (OFC), vol. 2, paper OTuP5, Mar. 2005.

[HUN'00] David K. Hunter, Ivan Andonovic, "Approaches to Optical Internet Packet Switching," IEEE Communications magazine, pp. 116-122, Sept. 2000.

[IAN'93] E. Iannone, F. Matera, A. Galtarossa, G. Gianello, M. Schiano, "Effect of polarization dispersion on the performance of IM-DD communication systems," *IEEE Photon. Technol. Lett.*, vol. 5, no. 10, pp. 1247-1249, 1993.

[IMA'98] T. Imai, T. Komukai, M. Nakazawa, "Dispersion tuning of a linearly chirped fibre Bragg grating without a centre wavelength shift by applying a strain gradient," *IEEE Photon. Technol. Lett.*, vol. 10, no. 6, pp. 845-847, 1998.

[JI'04] H. C. Ji, K. J. Park, J. H. Lee, H. S. Chung, E. S. Son, K. H. Han, S. B. Jun, and Y. C. Chung, "Optical performance monitoring techniques based on pilot tones for WDM network applications," in *Journal of Optical Networking (JON)*, vol. 3, no. 7, pp. 510-533, 2004.

[KAO'93] Ming-Seng Kao, Jinshown Wu, "Effect of polarization mode dispersion on a coherent optical system with pilot carrier," *IEEE Journal of Lightwave Technol.*, vol. 11, no. 2, pp. 303-308, February 1993.

[KHO'00] R. Khosravani, A.E. Willner, "Comparison of different modulation formats in terrestrial systems with high polarization mode dispersion," in *Conf. Optical Fiber Communication (OFC)*, vol. 2, paper WL5-2, pp. 201-203, 2000.

[KIK'05] Nobuhiko Kikuchi, Shigenori Hayase, Kenro Sekine, Shinya Sasaki, "Performance of Chromatic Dispersion Monitoring Using Statistical Moments of Asynchronously Sampled Waveform Histograms," *IEEE Journal of Lightwave Technol.,* vol. 17, no. 5, pp. 1103-1105, May 2005.

[KIL'03] D. C. Kilper, W. Weingartner, "Monitoring Optical Network Performance Degradation Due to Amplifier Noise," IEEE Journal of Lightwave Technol., vol. 21, no. 5, pp. 1171-1178, May 2003.

[KIL'04] D. C. Kilper, R. Bach, D. J. Blumenthal, D. Einstein, T. Landolsi, L. Ostar, M. Preiss, A. E. Willner, "Optical Performance Monitoring," *IEEE Journal of Lightwave Technol.*, vol. 22, no. 1, pp. 294-304, Jan. 2004.

[KIL'05] R. I. Killey, P. M. Watts, V. Mikhailov, M. Glick, and Polina Bayvel, "Electronic Dispersion Compensation by Signal Predistortion Using Digital Processing and a Dual-Drive Mach–Zehnder Modulator," *IEEE Photon. Technol. Lett.*, vol. 17, no. 3, pp. 714-716, March 2005.

[KOG'02] H. Kogelnik, R. M. Jopson, "Polarisation mode dispersion," *in Optical fiber telecommunications systems IV-B*, Academic press Inc. (London), ISBN: 0-12-395173-9, 2002.

[KUW'02] S. Kuwahara, A. Hirano, Y. Miyamoto, K. Murata, "Automatic dispersion compensation for WDM system by mode-splitting of tone-modulated CS-RZ signal," in *European Conf. Opt. Comm. (ECOC)*, Rimini, vol. 3, paper 6.1.3, 2002.

[LEE'99] Gyu-Woong Lee, Sang-Kook Han, "Linear dual electroabsorption modulator for analog optical transmission," *Microwave and Optical Technology Letter,* vol. 22, no. 6, pp. 369, September 1999.

[LEG'96] Legg, P.J.; Tur, M.; Andonovic, I., "Solution paths to limit interferometric noise induced performance degradation in ASK/direct detection lightwave networks," *IEEE Journal of Lightwave Technol.*, vol. 14 , no. 9, pp. 1943-1954, Sept. 1996.

[LEL'06] Helen-C. Leligou, Konstantinos Kanonakis, John Angelopoulos, Ioannis Pountourakis, Theofanis Orphanoudakis, "Efficient burst aggregation for QoS-aware slotted OBS systems," *European Transactions on Telecommunications*, 2006.

[LU'05] Guo-Wei Lu, Man-Hong Cheung, Lian-Kuan Chen, Chun-Kit Chan, "Simultaneous PMD and OSNR onitoring by Enhanced RF Spectral Dip Analysis Assisted With a Local Large-DGD Element," *IEEE Photon. Technol. Lett.*, vol. 17, no. 12, pp. 2790-2792, Dec. 2005.

[LUI'04] R. Luís, P. André, A. Teixeira, P. Monteiro, "Performance Monitoring in Optical Networks Using Asynchronously Acquired Samples With Nonideal Sampling Systems and Intersymbol Interference*," IEEE Journal of Lightwave Technol.,* vol. 22 , no. 11, pp. 2452-2459, Nov. 2004.

[LUO'04] T. Luo, 'PMD monitoring by tracking the chromatic-dispersion-insensitive RF power of the vestigial sideband', *IEEE Photon. Technol. Lett.*, vol. 12, no. 9, pp. 2177-2179, July 2004.

[MAD'98] C. K. Madsen, G. Lenz, "Optical all-pass filters for phase response design with applications for dispersion compensation," *IEEE Photon. Technol. Lett.*, vol. 10, no. 7, pp. 994-996, July 1998.

[MAD'99] C. K. Madsen, G. Lenz, A.J. Bruce, M.A. Cappuzzo, L.T. Gomez, R.E. Scotti, "Integrated all-pass filters for tunable dispersion and dispersion slope compensation," *IEEE Photon. Technol. Lett.*, vol. 11, no. 12, pp. 1623-1625, December 1999.

[MAD'00] C. K. Madsen, J.A. Walker, J.E. Ford, K.W. Goossen, T.N. Nielsen, G. Lenz, "A tunable dispersion compensating MEMS all-pass filetr," *IEEE Photon. Technol. Lett.*, vol. 12, no. 6, pp. 651-653, June 2000.

[MAD'01] C. K. Madsen, S. Chandrasekhar, E.J. Laskowski, K. Bogart, M. A. Cappuzzo, A. Paunescu, L. W. Stulz, L. T. Gomez, "Compact integrated tunable chromatic dispersion compensator with a 4000 ps/nm tuning range," in *Conf. Optical Fiber Communication (OFC)*, vol. 4, paper PD9, 2001.

[MAH'01] M.J. O'Mahony, D. Simeonidou, D.K. Hunter, A. Tzanakaki, "The Application of Optical Packet Switching in Future Communication Networks," *IEEE Communications magazine*, pp. 128-135, March 2001.

[MAL'05] Sireen Malik, Ulrich Killat, "Impact of burst aggregation time on performance in optical burst switching networks," *Optical Switching and Networking*, pp. 230-238, 2005.

[MAR'90] Dietrich Marcuse, "Derivation of Analytical Expressions for the Bit-Error Probability in Lightwave Systems with Optical Amplifiers," *IEEE Journal of Lightwave Technol.*, vol. 8, no. 12, pp. 1816-1823, 1990.

[MAR'91] Dietrich Marcuse, 'Calculation of Bit-Error Probability for a Lightwave System with Optical Amplifiers and Post-Detetection Gaussian Noise', *IEEE Journal of Lightwave Technol.*, vol. 9, no. 4, pp. 505-513, 1991.

[MEF'05] Lamia Meflah, Benn Thomsen, John Mitchell, Polina Bayvel, Gottfried Lehmann, Stefano Santoni, Bernd Bollenz, "Advanced Optical Performance Monitoring for Dynamically Reconfigurable Networks," *Proceedings Networks Optical Communications (NOC) conference*, London, 2005.

[MEF'05b] Lamia Meflah, Benn Thomsen, John Mitchell, Polina Bayvel, "Chromatic Dispersion Monitoring using RF Spectrum Analysis," *Proceedings London Conference Symposium (LCS)*, London, p251, 2005.

[MEF'05c] Lamia Meflah, Benn Thomsen, John Mitchell, Polina Bayvel, "Chromatic Dispersion Monitoring of a Multi-Channel 40 Gbit/s System for Dynamically Reconfigurable Networks," *Proceedings European Conference on Optical Communication (ECOC)*, Glasgow, paper Th3.2.5, 2005.

[MEF'06] Lamia Meflah, Benn Thomsen, John Mitchell, Polina Bayvel, "Fast residual chromatic dispersion monitoring for dynamic burst networks," *Proceedings Optical Fiber Communication Conf./National Fiber Optic Engineers Conf. (OFC/NFOEC)*, vol. 2, paper OWK2, pp. 456-457, Anaheim, 2006.

[MEF'06b] Lamia Meflah, Benn Thomsen, Seb Savory, John Mitchell, Polina Bayvel, "Single Technique for Simultaneous Monitoring of OSNR and Chromatic Dispersion at 40Gbit/s," *Proceedings European Conference on Optical Communication (ECOC)*, Cannes, 2006.

[MEF'08] Lamia Baker-Meflah, Benn Thomsen, John Mitchell, Polina Bayvel, "Simultaneous chromatic dispersion, polarization-mode-dispersion and OSNR monitoring at 40Gbit/s," submitted to *Optics Express*, 2008.

[MIT'92] Osamu Mitomi, Shunji Nojima, Isamu Kotaka, Koichi Wakita, Kenji Kawano, Mitsuru Naganuma, "Chirping characteristics and frequency response of MQW optical intensity modulator," *IEEE Journal of Lightwave Technol.*, vol. 10, no. 1,pp. 71, 1992.

[MOR'07] Toshio Morioka, "Ultrafast optical technologies for large-capacity TDM/WDM photonic networks," *in Journal Optical Fiber Communications,* Rep. 4, pp. 14-40, 2007.

[MOT'02] S. M. Reza Motaghian Nezam, "PMD monitoring in WDM systems for NRZ data using a chromatic-dispersion-regenerated clock," in *Conf. Optical Fiber Communication (OFC)*, Paper WE5, 2002.

[MOT'04] S. M. Reza Motaghian Nezam, Ting Luo, J.E. McGeehan; A.E. Willner "Enhancing the monitoring range and sensitivity in CSRZ chromatic dispersion monitors using a dispersion-biased RF clock tone," *IEEE Photon. Technol. Lett.*, vol. 16, no. 5, pp. 1391-1393, 2004.

[MOT'04b] S. M. Reza Motaghian Nezam, 'First-order PMD monitoring for NRZ data using RF clock regeneration techniques', *IEEE Journal of Lightwave Technol.*, vol. 22, no. 4, pp. 1086, 2004.

[MOT’04c] S. M. Reza Motaghian Nezam, “Measuring fibre and component DGD using polarized limited-bandwidth optical sources and monitoring the DOP,” *IEEE Photon. Technol. Lett.*, vol. 16, no. 7, pp. 1694, July 2004.

[MOT’04d] S. M. Reza Motaghian Nezam, J.E. McGeehan; A.E. Willner, “Degree of polarization based PMD monitoring for subcarrier-multiplexed signals via equalized carrier/sideband filtering,” *IEEE Journal of Lightwave Technol.*, vol. 22, no. 4, pp. 1078-1085, April 2004.

[MUE’98] K. Mueller, N. Hanik, A. Gladisch, H. M. Foisel, C. Caspar “Application of amplitude histograms for quality of service measurements of optical channels and fault identification,” in *European Conf. Opt. Comm. (ECOC),* Madrid, vol. 1, pp. 707-708, Sept. 1998.

[NEI’05] D.T. Neilson, D. Stiliadis, “Ultra-high capacity IP routers for the routers of tomorrow: IRIS projects,” in *European Conf. Opt. Comm. (ECOC),* vol. 5, paper, We 1.1.4, 2005.

[OHN’97] M. Ohn, A. Alavie, R. Maaskant, M. Xu, F. Bilodeau, K. Hill, “Tunable fiber grating dispersion using a piezoelectric stack,” in *Conf. Optical Fiber Communication (OFC)*, pp. 155-156, 1997.

[OHT’99] S. Ohtero and N Takachio, “Optical signal quality monitor using direct Q-factor measurement,” *IEEE Photon. Technol. Lett.*, vol.11, no.10, pp. 1307-1309, October 1999.

[PAN’01] Z. Pan, Q. Yu, Y. Xie, S.A. Havstad, A.E. Willner, D.S. Starodubov, J. Feinberg, “Chromatic dispersion monitoring and automated compensation for NRZ and RZ data using clock regeneration and fading without adding signalling,” in *Conf. Optical Fiber Communication (OFC)*, vol. 3, paper WH5,. 2001.

[PAR’02] K. J. Park, H. Kim, J.H. Lee, C.J. Youn, S.K. Shin, Y.C. Chung, “Polarisation-mode dispersion monitoring technique based on polarisation scrambling,” *IEE Electronics Lett.*, vol. 38, no. 2, pp. 83-85, 2002.

[PAR’02b] K. J. Park, J. H. Lee, C. J. Youn and Y. C. Chung, “A simultaneous monitoring technique for polarisation-mode dispersion and group velocity dispersion,” in *Conf. Optical Fiber Communication. (OFC)*, paper WE4, pp. 199-200, 2002.

[PAR'03] K. J Park, "Performance comparisons of chromatic dispersion-monitoring techniques using pilot tones," *IEEE Photon. Technol. Lett.*, vol. 15, no. 6, pp. 873-875, 2003.

[PET'01] M. N. Petersen, Z. Pan, S. Lee, S.A. Havstad, A.E. Willner, "Dispersion monitoring and compensation using single in-band subcarrier tone," in *Conf. Optical Fiber Communication (OFC)*, vol. 3, paper WH4, 2001.

[PET'02] M M. N. Petersen, Z. Pan, S. Lee, S.A. Havstad, A.E. Willner, "Online chromatic dispersion monitoring and compensation using a single inband subcarrier tone," *IEEE Photon. Technol. Lett.*, vol. 14, no. 4, pp. 570-572, 2002.

[POL'99] V. Polo, J. Marti, E. Ramos, D. Moodie, "Mitigation of chromatic dispersion effects employing electro-absorption modulator based transmitters," *IEEE Photon. Technol. Lett.*, vol. 11, no. 7, pp. 883-885, July 1999.

[POO'86] C. D. Poole, R. E. Wagner, "Phenomenological Approach to Polarisation Dispersion in Long Single-Mode Fibres," *IEE Electronics Lett.*, vol. 22 , no. 19, pp. 1029, September 1986.

[PUA'00] Hok Yong Pua, Kumar Peddanarappagari, Benyuan Zhu, Christopher Allen, Kenneth Demarest, and Rongqing Hui, "An Adaptive First-Order Polarization-Mode Dispersion Compensation System Aided by Polarization Scrambling: Theory and Demonstration," *IEEE Journal of Lightwave Technol.*, vol. 18, no. 6, pp. 832-841, 2000.

[RAM'99] Byrav Ramamurthy, Debasish Datta, Helena Feng, Jonathan P. Heritage, Biswanath Mukherjee, "Impact of Transmission Impairments on the Teletraffic Performance of Wavelength-Routed Optical Networks ," *IEEE Journal of Lightwave Technol.*, vol. 17, no. 10, pp. 1713-1723, Oct. 1999.

[RIC'01] Richter, A.; Bock, H.; Fischler, W.; Elbers, J.-P.; Glingener, C.; Bach, R.; Grupp, W., "Field trial of optical performance monitor in dynamically configurable DWDM network," *IEEE Photon. Technol. Lett.,* vol. 37, no. 6, pp. 370-371, March 2001.

[RIC'02] A. Richter, W. Fischler, H. Bock, R. Bach, W. Grupp, "Optical performance monitoring in transparent and configurable DWDM networks," *Optoelectronics IEE Proceedings*, vol. 149 , no. 1, pp. 1-5, Feb. 2002.

[ROS'00] G. Rossi, "Optical performance monitoring in reconfigurable WDM optical networks using subcarrier multiplexing," *IEEE Journal of Lightwave Technol.*, vol. 18, no. 12, pp. 1639, December 2000.

[ROS'01] H. Rosenfeldt, Ch. Knothe, R. Ulrich, E. Brinkmeyer, "Automatic PMD Compensation at 40 Gbit/s and 80 Gbit/s Using a 3-Dimensional DOP Evaluation for Feedback," in *Conf. Optical Fiber Communication (OFC)*, vol. x, paper PD27, 2001.

[SAL'91] B.E.A. Saleh, M.C. Teich, "Photonics," *John Wiley and Sons Inc.*, ISBN: 0-471-83965-5, 1991.

[SAN'96] A. Sano, T. Kataoka, M. Tomizawa, K. Hagimoto, K. Sato, K. Wakita, K. Kato, "Automatic dispersion equalization by monitoring extracted-clock power level in a 40Gb/s, 200km transmission line," in *European Conf. Opt. Comm. (ECOC)*, vol. 2, paper TuD.3.5, pp. 207-210, 1996.

[SEN'03] S. Senjupta, V. Kumar, D. Saha, "Switched optical backbone for cost-effective scalable core IP networks," *IEEE Communications magazine*, pp. 60-70, June 2003.

[SHA'03] Shake, I.; Takara, H.; Kawanishi, S., "Simple Q factor monitoring for BER estimation using opened eye diagrams captured by high-speed asynchronous electrooptical sampling," *IEEE Photon. Technol. Lett.*, vol. 15, no. 4, pp. 620-622, April 2003.

[SHA'04] Shake, I.; Takara, H.; Kawanishi, S., "Simple measurement of eye diagram and BER using high-speed asynchronous sampling," *IEEE Journal of Lightwave Technol.*, vol. 22, no. 5, pp. 1296-1302, May 2004.

[SHI'97] M. Shirasaki, "Chromatic dispersion compensator using virtually imaged phase array," *IEEE Photon. Technol. Lett.*, vol. 9, no. 12, pp. 1598-1600, December 1997.

[TAK'93] T. Takahashi, T. Imai, M. Aiki, "Time evolution of polarisation mode dispersion in 120 km installed optical submarine cable," *IEE Electronics Lett.*, vol. 29, no. 18, pp. 1605-1606, 1993.

[TAK'96] K. Takiguchi, K. Jinguji, K. Okamoto, Y. Ohmori, "Cariable group delay dispersion equalizer using lattice-form programmable optical filter on planar lightwave circuit," *IEEE Journal of Selected Topics in Quantum Electronics,* vol. 2, no. 2, June 1996.

[TAK'98] K. Takiguchi, S. Kawanishi, H. Takara, A. Himeno, K. Hattori, "Dispersion slope equalizer for dispersion shifted fibre using a lattice-form programmable optical filter on a planar Lightwave circuit," *IEEE Journal of Lightwave Technol.*, vol. 16, no. 9, pp. 1647-1656, September 1998.

[TAK'01] H. Takenouchi, T. Goh, T. Ishii, "2X40 channel dispersion slope compensator for 40 Gb/s WDM transmission systems covering entire C and L bands," in *Conf. Optical Fiber Communication (OFC)*, paper TuS2, 2001.

[TAN'06] J. M. Tang, K. Alan Shore, "Wavelength-Routing Capability of Reconfigurable Optical Add/Drop Multiplexers in Dynamic Optical Networks," *IEEE Journal of Lightwave Technol.,* vol. 24, no. 11, pp. 4296-4303, 2006.

[TOM'94] M. Tomizawa, Y. Yamabayashi, I. Sato, T. Kataoka, "Nonlinear influence on PM-AM conversion measurement of group velocity dispersion in optical fibres," *IEE Electronics Lett.*, vol. 30, no. 17, pp. 1434-1435, 1994.

[TOM'97] M. Tomizawa, "Automatic dispersion equalization by tunable laser for installation of high-speed optical transmission system'" in *Conf. Optical Fiber Communication (OFC)*, Paper TuT2, pp. 96-98, 1997.

[TSU'98] H. Tsuda, T. Kurokawa, K. Okamoto, T. Ishii, K. Naganuma, Y. Inoue, H. Takenouchi, "Second and third order dispersion compensation using a high resolution arrayed waveguide grating," in *European Conf. Opt. Comm. (ECOC)*, vol. 1, pp. 533-534, 1998.

[WAG'06] J. Wagener and T. Strasser, "Characterization of the economic impact of stranded bandwidth in fixed OADM relative to ROADM networks," in Conf. Optical Fiber Communication (OFC), Paper OthM6, 2006.

[WAL'91] G. R. Walker, D. M. Spirit, D. L. Williams, S. T. Davey, "Noise Performance of distributed Fibre Amplifiers," *IEE Electronics Lett.*, vol. 27, no. 15, pp. 1390-1391, July 1991.

[WIE'00] R. Wiesmann, O. Bleck, H. Heppner, "Cost effective performance monitoring in WDM systems," in *Conf. Optical Fiber Communication (OFC)*, vol. 2 , pp. 171-173, March 2000.

[WIL'97] G.C. Wilson, T.H. Wood, M. Gans, J.L. Zyskind, J.W. Sulhoff, J.E. Johnson, T. Tanbun-Ek, P.A. Morton, "Predistorsion of electroabsorption modulators for analog CATV systems at 1.55um," *IEEE Journal of Lightwave Technol.,* vol. 15, no. 9, pp. 1654, 1997.

[WIL'99] A. E. Willner, 'Tunable compensation of channel degrading effects using nonlinear chirped passive fibre Bragg gratings', *IEEE Journal of Selected Topics in Quantum Electronics,* vol. 5, no. 5, pp. 1298, Sept. 1999.

[WIL'02b] A. E. Willner, B. Hoanca, "Fixed and tunable management of fibre chromatic dispersion," *in Optical Fibre Telecommunications IVB systems and impairments*, Academic press, 2002.

[WIL'02c] Alan E. Willner, Bogdan Hoanca, "Fixed and tunable management of fibre chromatic dispersion," *in Optical fiber telecommunications systems IV-B*, Academic press Inc. (London), ISBN: 0-12-395173-9, 2002.

[WIN'90] J. H. Winters, Mario Santoro, "Experimental equalization of polarization dispersion," *IEEE Photon. Technol. Lett.*, vol. 2, no. 8, pp. 591-593, 1990.

[WRA'02] M. Wrage, M. Wolf, R.E. Neuhauser, S. Spälter, B. Lankl, "Optical Performance Monitoring by Electrical Amplitude Sampling in Transparent Optical Networks," in *Networks & Optical Communications (NOC)*, A75, 2002.

[YU'02] Q. Yu, L.S. Yan, Z. Pan, A.E. Willner, "Chromatic dispersion monitor for WDM systems using vestigial-sideband optical filtering," in *Conf. Optical Fiber Communication (OFC)*, paper WE3, pp. 197-199, 2002.

[YU'03] C. Yu, 'Chromatic-dispersion-insensitive PMD monitoring for NRZ data based on clock power measurement using a narrowband FBG notch filter', in *European Conf. Opt. Comm. (ECOC)*, vol. 2, pp. 290-291, Paper Tu4.2.3, 2003.

[ZAN'01] H. Zang, J.P. Jue, L. Sahasrabuddhe, R. Ramamurthy, B. Mukherjee," Dynamic Lightpath Establishment in Wavelength-Routed WDM Networks," *IEEE Communications magazine*, pp. 100-108, Sept. 2001.

[ZYS'02] John Zyskind, Rick Barry, Graeme Pendock, Michael Cahill, Jinendra Ranka, "High-capacity, ultra-long-haul networks," *in Optical fiber telecommunications systems IV-B*, Academic press Inc. (London), ISBN: 0-12-395173-9, 2002.